UNIVERSIDADE DE COIMBRA

Study of the *Wtb* Vertex Structure in Top Quark Decays with the ATLAS experiment and Future Prospects

Miguel Castro Nunes Fiolhais

2012

Dissertação de Doutoramento em Física, Especialidade de Física Experimental
Faculdade de Ciências e Tecnologia da Universidade de Coimbra

Orientador:	Professor Doutor Juan Antonio Aguilar Saavedra
Co-orientador:	Professor Doutor António Onofre de Abreu Ribeiro Gonçalves

Coimbra, 2012

Abstract

In this thesis, the ATLAS sensitivity to the Wtb vertex structure was studied in top quark decays. Measurements were performed on the polarization of $W^{\pm}$ bosons, derived from top quark pairs events ($t\bar{t}$) with single lepton and dilepton topologies. The results were obtained with data from pp collisions at a center-of-mass energy of 7 TeV, collected by the ATLAS experiment at the Large Hadron Collider (LHC), corresponding to an integrated luminosity of 1.04 fb^{-1}. The measured fractions of the longitudinal, left-handed and right-handed helicities are $F_0 = 0.67 \pm 0.07$, $F_{\mathrm{L}} = 0.32 \pm 0.04$ and $F_{\mathrm{R}} = 0.01 \pm 0.05$, which can be translated into angular asymmetries yielding $A_+ = 0.53 \pm 0.02$ and $A_- = -0.84 \pm 0.02$. These results are in good agreement with the Standard Model predictions, and correspond in the present date to the most precise published results. As the polarization of the $W^{\pm}$ bosons in top quark decays is sensitive to the Lorentz structure and couplings of the Wtb vertex, the measurements were used to set limits on anomalous contributions to the Wtb couplings. These results obtained at the LHC were compared with the expected results in a possible future linear collider, such as the International Linear Collider (ILC). The sensitivity to these anomalous couplings may largely surpass the one achievable by the LHC either in neutral or charged current processes.

Resumo

Na presente tese é discutida a sensibilidade de ATLAS à estrutura do vértice Wtb em decaimentos de quarks top. Para tal, realizaram-se medidas da polarização de bosões $W^{\pm}$, a partir de eventos de pares de quarks top ($t\bar{t}$) com topologias de um e dois leptões no estado final. Os resultados foram obtidos com dados de colisões pp, recolhidos pela experiência ATLAS do *Large Hadron Collider* (LHC), correspondentes a uma luminosidade integrada de 1.04 fb^{-1}, a uma energia de centro-de-massa de 7 TeV. As frações de helicidade longitudinal, esquerda e direita, foram medidas a $F_0 = 0.67 \pm 0.07$, $F_{\text{L}} = 0.32 \pm 0.04$ e $F_{\text{R}} = 0.01 \pm 0.05$, e podem ser traduzidas em assimetrias angulares $A_+ = 0.53 \pm 0.02$ e $A_- = -0.84 \pm 0.02$. Estes resultados encontram-se em bom acordo com as previsões do Modelo Padrão, e correspondem aos resultados mais precisos publicados até à presente data. Como a polarização dos bosões $W^{\pm}$ em decaimentos de quarks top é sensível à estrutura de Lorentz e aos acoplamentos do vértice Wtb, as medidas foram utilizadas para estabelecer limites nas contribuições dos acoplamentos anómalos do vértice Wtb. Estes resultados obtidos em LHC foram comparados com os resultados esperados num possível colisionador linear futuro, tal como o *International Linear Collider* (ILC). A sensibilidade a estes acoplamentos anómalos poderá ultrapassar largamente a sensibilidade atingível em LHC, tanto em processos de corrente carregada como em processos de corrente neutra.

Acknowledgements

First of all, I would like to thank my supervisors, Professors António Onofre and Juan Antonio Aguilar Saavedra, for their outstanding guidance and dedication through the completion of this thesis. I would also like to thank to Nuno Castro, for his friendship, partnership and availability along the years.

I would also like to thank to the Laboratório de Instrumentação e Física Experimental de Partículas, and, in particular, to Amélia Maio, Team Leader of the Portuguese ATLAS group, for providing me the conditions which allowed to fully achieve the goals I was challenged to. I acknowledge the support from Fundação para a Ciência e Tecnologia, through the grant SFRH/BD/48680/2008.

I would like to thank to Ana Henriques and Irene Vichou for welcoming me in the ATLAS Tile Calorimeter group, where I completed the technical part of the doctoral program. I would also like to thank the collaboration of João Carvalho, Luca Fiorini, Sasha Solodkov, Shimpei Yamamoto, Luís Gurriana and Filipe Veloso, during this period.

A special word is due to Satoshi Hasegawa, with whom I worked in close collaboration in the W helicity measurements. His devotion and team spirit were inspirational to accomplish all our goals in the due deadlines. I would like to thank to the ATLAS Top Working Group and the Top Properties Subgroup members, in particular, to Andrea Knue, Kevin Kroeninger, Ki Lie, Lisa Shabalina and Lucia Masetti for all the discussions and collaboration on the Wtb analyses.

I would also like to thank to Miguel Oliveira, Helmut Wolters and Henrique Matos for managing the computational facilities used in the work of this thesis. Part of the computational work was also performed in the Milipeia supercomputer at the Laboratório de Computação Avançada of the University of Coimbra.

I would also like to thank to all my working colleagues, in particular, to Bruno Galhardo and Juan Pedro Araque, for their friendship. A special word is due to Susana Santos for her friendship and support along the years. I would also like to thank to Burt Betchard, Charilaos Tsarouchas, Elisa Piccaro, Florian Teischinger, Javier Santaolalla, Joana Miguéns, José Melo, Matilde Castanheira and Raffaele Giordano, for their friendship and for making life at CERN a lot better.

I would also like to thank to Professors Francisco del Aguila Giménez and Fernando Cornet for receiving me in Departamento de Física Teórica y del Cosmos of the University of Granada, where I spent several periods. In particular, I would like to thank to Miki Rodriguez, Rafael Cerezo and Jordi Hidalgo for their friendship and hospitality in Granada.

Last but not least, I thank my family and friends for their affection and support.

Contents

List of Figures

List of Tables

Chapter 1

Introduction

The Large Hadron Collider started its operation in September 2008, when the proton beams were successfully circulated in the main ring. However, nine days later, a serious magnet quench incident damaged over 50 superconducting magnets and forced to cease operations. The halt would last more than one year, until the proton beams were successfully circulated again in November 2009. In March 2010, the first proton-proton collisions at 3.5 TeV per beam took place, breaking the world record for the highest-energy man-made particle collisions. Currently operating at an energy of 4 TeV per beam until the beginning of 2013, the LHC has become a top quark factory, which allows to perform precision measurements of the top quark properties.

The top quark is the most massive elementary particle discovered to date, approximately as heavy as a gold atom. With a mass of $m_t = 173.2 \pm 0.9$ GeV [1], measured at the Tevatron with a precision of $\sim 0.5\%$, the top quark is a natural candidate for the search of new physics beyond the Standard Model of particle physics (SM), as it may play an important role in the electroweak spontaneous symmetry breaking mechanism. The top quark decays almost exclusively to a bottom quark and a W boson (both on-shell), with a mean lifetime of the order of 10^{-25} s, one order of magnitude smaller than the typical hadronization time scale. Therefore, the top quark decays before hadronization takes place and, consequently, its spin information is transfered to the decay products, which allows to probe the Wtb vertex and the top quark production mechanisms. The Tevatron and LHC results on top quark physics are, so far, in agreement with the SM. However, the increase of luminosity and the better understanding of the ATLAS and CMS detectors expected in the near future at the LHC, shall improve the precision measurements of the top quark properties, enhancing the tests for new physics beyond the SM.

This thesis comprises the work developed in three different stages, essential for the understanding of top quark physics, the main subject of the thesis. Given the

number of $t\bar{t}$ events produced at the LHC, a significant improvement is expected on the precision of the top quark properties, other than the mass (the only parameter known with great precision). The decays of the W boson (to a quark and an anti-quark, or to a lepton and a neutrino), define the final state topology: hadronic, single lepton, and dilepton channels. The single lepton and dilepton channels are characterized by one charged lepton and at least four jets, or two charged leptons and at least two jets, respectively, and missing transverse energy (associated with the undetected neutrinos). In the first stage of the doctoral program, the jet environment was studied, in particular, the noise present in the hadronic calorimeter of the ATLAS detector (TileCal). The TileCal electronic noise plays a direct role on the reconstruction of jets and missing transverse energy ($E_{\mathrm{T}}^{\mathrm{miss}}$), used in the selection and reconstruction of events with top quarks. These studies improved the performance of this subsystem, and consequently, the general performance of the ATLAS experiment [2–4]. The second stage consisted in the study of the Wtb vertex through the measurement of helicity fractions and angular asymmetries of the W boson in top quark decays [5–8]. The data collected from pp collisions at a center-of-mass energy of 7 TeV with the ATLAS experiment at the LHC were used, corresponding to an integrated luminosity of 1.04 fb^{-1}. The measurements of the W boson polarizations are in good agreement with the SM, and are currently the world's most precise published results [8]. As the polarization of the W boson in top quark decays is sensitive to the Wtb vertex structure itself, the measurements were used to set limits on anomalous contributions to the Wtb couplings. Finally, in the last stage of the doctoral program, these studies were extended to a possible ILC, that may be available in the future, as an attempt to infer the improvement on the precision of measurements obtained at the LHC and discussed in this thesis. In fact, the Wtb, $Zt\bar{t}$ and $\gamma t\bar{t}$ vertices are all sensitive to the top trilinear operators, which can be tested at the ILC and compared with the LHC [9]. The sensitivity to these operators may largely surpass the one achievable by the LHC, both in neutral or charged current processes, extending the new physics scales up to 4.5 TeV, for a center-of-mass energy of 500 GeV. It was shown how the beam polarization and a possible energy upgrade from 500 GeV to 1 TeV would allow to disentangle all effective operator contributions to the $Zt\bar{t}$ and $\gamma t\bar{t}$ vertices. The work developed in this thesis was also useful in the search for flavor changing neutral currents in top quark decays [10] and in the search for events with two same charge leptons [11] at the ATLAS experiment.

Chapter 2

The Standard Model of Particle Physics

In this chapter, the Standard Model of particle physics is presented. The electromagnetic, weak and strong interactions of subatomic particles are discussed. Several properties of the top quark are also discussed in the scope of the latest experimental results.

2.1 Overview

The Standard Model of particle physics is a $SU(3)_c \times SU(2)_L \times U(1)_Y$ relativistic Quantum Field Theory (QFT) developed to describe the electroweak and strong interactions of elementary particles in a single framework. The theory was initially designed to combine electrodynamics with the weak interaction by Sheldon Glashow in 1960 [12] and later in 1967 by Steven Weinberg [13] and Abdus Salam [14], who incorporated the Higgs mechanism [15–17]. As a result of their work, the three shared the Nobel Prize in Physics in 1979 *"for their contributions to the theory of the unified weak and electromagnetic interaction between elementary particles, including, inter alia, the prediction of the weak neutral current"*. In addition, the theory of strong interaction, Quantum Chromodynamics (QCD), was developed in parallel through the 60s and 70s. In 1964, Murray Gell-Mann and George Zweig independently suggested the existence of quarks with different flavors as the components of hadrons [18] and, in 1965, Moo-Young Han with Yoichiro Nambu [19] and Oscar W. Greenberg [20] proposed an additional $SU(3)$ gauge degree of freedom, the color charge. The theory reached its present form in 1973 with the discovery of asymptotic freedom of strong interactions by David Politzer [21, 22] and David Gross together with Frank Wilczek [23] allowing perturbation theory techniques to be applied. The three were awarded the Nobel Prize in Physics in 2004 *"for the*

discovery of asymptotic freedom in the theory of the strong interaction".

In the Standard Model of particle physics, all elementary particles are classified in two categories: bosons and fermions. The fermions are half-integer spin particles obeying the Pauli Exclusion Principle and a total of twelve fermions are known to date, apart from the antiparticle partners. Fermions are divided in two categories: quarks (up, down, charm, strange, top, bottom) and leptons (electron, muon, tau, and their corresponding neutrinos). Quarks hold electric charge, weak isospin, color charge and, therefore, interact through both electroweak and strong forces. Due to confinement (a property of strong interaction), quarks have never been observed as free particles, forming instead bound states of color-neutral particles, the hadrons, which are divided into baryons (three quarks) and mesons (quark-antiquark systems). Leptons have zero color charge, therefore can only interact through the electroweak force. As neutrinos also do not have electric charge, only interact via the weak force. On the other hand, bosons are integer spin particles with spin 1 for all force mediating particles, excluding gravitation, and spin 0 in the case of Higgs boson. There are three kinds of force mediating particles: photons, massive bosons and gluons. The photon is a massless particle and, together with the three massive bosons (W^+, W^- and Z), mediates the electroweak interaction. The Z boson is electrically neutral and more massive than the W boson ($m_W = 80.399 \pm 0.023$ GeV and $m_Z = 91.1876 \pm 0.0021$ GeV) [24]. According to QCD, there are eight different massless and color charged gluons, mediators of the strong force, that can also interact with themselves. Finally, the Higgs boson, theorized in 1964 [15–17] to explain the spontaneous breaking of electroweak symmetry, or in other words, how the other elementary particles acquire mass. The Higgs particle is a massive scalar boson, with zero electric charge and is its own anti-particle.

The Standard Model of particle physics is the most successful theory of elementary particles and interacting fields built to date. The development of renormalization in Quantum Electrodynamics (QED) by Ernst Stueckelberg [25], Julian Schwinger [26, 27], Richard Feynman [28–30], Sin-Itiro Tomonaga [31] and Freeman Dyson [32, 33], led to an outstanding agreement between theory and experiment. The discovery of the massive gauge bosons in 1983 by UA1 and UA2 collaborations established the Glashow-Weinberg-Salam model as one of the pillars of the SM [34, 35], for which Carlo Rubbia and Simon van der Meer were laureated with the Nobel Prize in Physics in 1984. Furthermore, several tests have been performed on perturbative QCD throughout the years, such as the jet production cross sections, Drell-Yan processes, the running QCD coupling, the production of heavy flavors, among others [36].

A summary of the SM is presented in the following sections, with particular

emphasis on the electroweak interaction and the top quark.

2.2 Electroweak Interaction

The electroweak interaction is formulated as a $SU(2)_L \times U(1)_Y$ gauge theory that unifies the electromagnetic and weak interactions. The electromagnetic interaction alone is described by the quantum electrodynamics, a relativistic quantum field theory that describes how electrically charged particles interact by means of exchange of photons. The weak interaction was first theorized by Fermi as a four fermion contact interaction [37], and is nowadays described as a short-ranged field. The weak interaction comprises several unique features not found in any other interaction, such as the violation of parity symmetry (P), conserved in the electromagnetic interaction, the violation of charge conjugation symmetry (C), the violation of the combination of charge conjugation and parity symmetries (CP), the capacity of changing quark flavors, *i.e.* changing one quark into another of a different kind, the existence of massive gauge bosons, and therefore, the need for a spontaneous symmetry breaking mechanism.

Even though the electromagnetic and the weak interactions do not seem to be related at low energies, the two are unified around the order of the electroweak energy scale, $\nu = 246$ GeV. The formulation of the electroweak unification under the $SU(2)_L \times U(1)_Y$ gauge group is presented in the next sections.

2.2.1 Quantum Electrodynamics

The interaction between a Dirac fermion and the electromagnetic field is derived in this section using the gauge principle, *i.e.* by requiring local $U(1)$ gauge invariance on the Lagrangian for a free Dirac fermion. The Lagrangian for a free Dirac massive fermion is:

$$\mathcal{L} = i\bar{\psi}(x)\gamma^\mu\partial_\mu\psi(x) - m\bar{\psi}(x)\psi(x), \tag{2.1}$$

where $\psi(x)$ is the Dirac field, m is the field mass, γ^μ represent the gamma matrices[1], and $\bar{\psi}(x) = \psi^\dagger\gamma^0$. The free Dirac Lagrangian is invariant under global $U(1)$ gauge transformations:

$$\psi(x) \rightarrow \psi'(x) \equiv e^{iQ\theta}\psi(x), \tag{2.2}$$

where Q is the electric charge in units of the elementary charge e, and θ is an arbitrary real constant value. However, the same Lagrangian is not invariant under local $U(1)$ gauge transformations, *i.e.* in case the phase depends on the space-time

[1]The gamma matrices satisfy the algebraic relation: $\{\gamma^\mu, \gamma^\nu\} = \gamma^\mu\gamma^\nu + \gamma^\nu\gamma^\mu = 2g^{\mu\nu}$.

coordinates ($\theta = \theta(x)$):

$$\partial_\mu \psi(x) \rightarrow \partial_\mu \psi'(x) \equiv e^{iQ\theta} \left(\partial_\mu + iQ\partial_\mu \theta\right) \psi(x). \tag{2.3}$$

In order to preserve the $U(1)$ gauge invariance locally, an additional spin-1 field $A_\mu(x)$ must be introduced, transforming as:

$$A_\mu(x) \rightarrow A'_\mu(x) \equiv A_\mu(x) - \frac{1}{e}\partial_\mu \theta(x). \tag{2.4}$$

The gauge invariant Lagrangian under local $U(1)$ transformations is therefore:

$$\begin{aligned} \mathcal{L} &= i\bar{\psi}(x)\gamma^\mu D_\mu \psi(x) - m\bar{\psi}(x)\psi(x) \\ &= i\bar{\psi}(x)\gamma^\mu \partial_\mu \psi(x) - m\bar{\psi}(x)\psi(x) - eQA_\mu \bar{\psi}(x)\gamma^\mu \psi(x), \end{aligned} \tag{2.5}$$

where the covariant derivative is defined as $D_\mu \psi(x) = \left(\partial_\mu + ieA_\mu(x)\right)\psi(x)$. An additional gauge invariant kinetic term needs to be included to complete the QED Lagrangian and to make $A_\mu(x)$ a propagating field:

$$\mathcal{L}_K = -\frac{1}{4} F^{\mu\nu}(x) F_{\mu\nu}(x), \tag{2.6}$$

where $F^{\mu\nu} = \partial^\mu A^\nu - \partial^\nu A^\mu$. Since the mass term for the gauge field $\mathcal{L}_m = \frac{1}{2}m^2 A_\mu A^\mu$ violates the local $U(1)$ gauge invariance, the photon must be massless. As a result, the Maxwell equations can be derived using eqs. (2.5) and (2.6):

$$\partial_\mu F^{\mu\nu} = j^\nu = eQ\bar{\psi}(x)\gamma^\nu \psi(x), \tag{2.7}$$

where j^ν represents the electromagnetic current.

QED has been tested throughout the years with an unprecedented precision. In particular, the high-precision measurement of the electron anomalous magnetic moment provides the most accurate determination of the fine structure constant [38]:

$$\alpha^{-1} = 137.035\,999\,084 \pm 0.000\,000\,051. \tag{2.8}$$

2.2.2 Weak Interaction

The weak interaction manifests itself in two different forms, through the charged and neutral currents, by means of the $W^\pm$ bosons and the Z boson, respectively. The experimental results obtained for more than one century, from early studies on the β-decay to modern neutrino scattering experiments, provide information on the nature of these currents, indispensable to build a successful theory of the weak interaction. In particular, the charged current exhibits the following features:

- Only left-handed (right-handed) fermions (anti-fermions) couple with the $W^{\pm}$ bosons, and therefore, the weak interaction violates parity conservation [39,40].

- All fermion doublets couple to the $W^{\pm}$ bosons with the same strength, also known as the "weak universality" [41].

- The weak eigenstates of the three generation of quarks are different from the mass eigenstates. The weak eigenstates of the three down-type quarks, $|d_i'\rangle$, are related to the mass eigenstates, $|d_j\rangle$, as [42]:

$$|d_i'\rangle = \sum_j \mathbf{V}_{ij}|d_j\rangle, \tag{2.9}$$

  where $\mathbf{V}$ is the Cabibbo-Kobayashi-Maskawa matrix, a 3×3 unitary matrix, *i.e.* $\mathbf{V}\mathbf{V}^{\dagger} = \mathbf{V}^{\dagger}\mathbf{V} = 1$.

- Neutrinos change their flavor as they propagate, an effect known as neutrino oscillation, and suggested by Bruno Pontecorvo [43] to explain the solar neutrino problem. The neutrino oscillation has been experimentally confirmed [44–47], and implies non-massless neutrinos as the weak eigenstates differ from the mass eigenstates [48]. Nonetheless, the neutrinos masses are tiny, and therefore not considered here.

On the other hand, the neutral current also exhibits peculiar properties that characterize the weak interaction:

- The Z boson and the photon couple to a fermion and its own anti-fermion at tree level. Flavor changing neutral currents are absent at tree level and strongly suppressed in higher order processes in the SM through the GIM mechanism [49].

- The fermionic couplings with the Z boson depend on the electric charge and the weak isospin of the fermions.

- Unlike the photon, the Z boson couplings are different for left-handed and right-handed fermions. The Z boson does not couple with right-handed neutrinos.

- The Z boson lineshape at LEP reveals the existence of three families of light neutrinos [50].

In the previous section, the QED Lagrangian was simply derived using the local $U(1)$ gauge invariance. For the electroweak interaction, the unification between the weak and the electromagnetic interactions is accomplished under the $SU(2)_L \times U(1)_Y$

symmetry group. The $SU(2)$ notation represents the group of 2×2 unitary matrices with determinant 1, *i.e.* the group of matrices that can be written as $U = e^{i\vec{\alpha}\cdot\vec{\tau}/2}$, where $\vec{\tau}$ represents the Pauli matrices:

$$\tau_1 = \begin{pmatrix} 0 & 1 \\ 1 & 0 \end{pmatrix} \quad \tau_2 = \begin{pmatrix} 0 & -i \\ i & 0 \end{pmatrix} \quad \tau_3 = \begin{pmatrix} 1 & 0 \\ 0 & -1 \end{pmatrix}. \tag{2.10}$$

The Pauli matrices are traceless and hold the following properties: $[\tau_i, \tau_j] = 2i\epsilon_{ijk}\tau_k$, $\{\tau_i, \tau_j\} = 2\delta_{ij}$ and $\mathrm{Tr}(\tau_i\tau_j) = 2\delta_{ij}$, where δ_{ij} and ϵ_{ijk} represent the Kronecker delta and the Levi-Civita symbol, respectively. Thus, for a generic family with up and down quarks, the fermion fields are written as:

$$\psi_1(x) = \begin{pmatrix} u \\ d \end{pmatrix}_L, \quad \psi_2(x) = u_R, \quad \psi_3(x) = d_R, \tag{2.11}$$

or for a family of leptons:

$$\psi_1(x) = \begin{pmatrix} \nu_l \\ l^- \end{pmatrix}_L, \quad \psi_2(x) = (\nu_l)_R, \quad \psi_3(x) = \ell^-_R, \tag{2.12}$$

where L and R represent the left-handed and right-handed chiralities. The free Dirac Lagrangian for massless fermions,

$$\mathcal{L} = \sum_{j=1}^{3} i\bar{\psi}_j(x)\gamma^\mu\partial_\mu\psi_j(x), \tag{2.13}$$

is invariant under global gauge transformation, as in QED,

$$\psi_1(x) \rightarrow \psi_1'(x) \equiv e^{i\vec{\alpha}\cdot\vec{\tau}/2}e^{iy_1\beta}\psi_1(x), \tag{2.14}$$

$$\psi_2(x) \rightarrow \psi_2'(x) \equiv e^{iy_2\beta}\psi_2(x), \tag{2.15}$$

$$\psi_3(x) \rightarrow \psi_3'(x) \equiv e^{iy_3\beta}\psi_3(x), \tag{2.16}$$

where y_j is the weak hypercharge, a conserved quantum number relating the electrical charge and the third component of the weak isospin. In order to preserve the local gauge invariance ($\vec{\alpha} = \vec{\alpha}(x)$ and $\beta = \beta(x)$), the covariant derivative is defined with four gauge fields, one for each gauge parameter, $\vec{\alpha}(x)$ and $\beta(x)$,

$$D_\mu\psi_1(x) = \left(\partial_\mu - i\frac{g}{2}\vec{\tau}\cdot\vec{W}_\mu(x) - ig'y_1B_\mu\right)\psi_1(x), \tag{2.17}$$

$$D_\mu\psi_2(x) = \left(\partial_\mu - ig'y_2B_\mu\right)\psi_2(x), \tag{2.18}$$

$$D_\mu\psi_3(x) = \left(\partial_\mu - ig'y_3B_\mu\right)\psi_3(x), \tag{2.19}$$

transforming as,

$$B_\mu(x) \rightarrow B_\mu'(x) \equiv B_\mu(x) + \frac{1}{g'}\partial_\mu\beta(x), \tag{2.20}$$

$$\vec{\tau}\cdot\vec{W}_\mu \rightarrow \vec{\tau}\cdot\vec{W}_\mu'(x) \equiv U(x)\vec{\tau}\cdot\vec{W}_\mu(x)U^\dagger(x) + \frac{2i}{g}U(x)\partial_\mu U^\dagger(x), \tag{2.21}$$

where $U(x) = e^{i\vec{\alpha}(x)\cdot\vec{\tau}/2}$. As in QED, the couplings to the B_μ field are arbitrary, however, since the $SU(2)$ commutation relation is non-linear, the constant g must be the same for every coupling. The remaining gauge invariant kinetic terms are given by:

$$\mathcal{L}_K = -\frac{1}{4}B^{\mu\nu}(x)B_{\mu\nu}(x) - \frac{1}{4}\vec{W}^{\mu\nu}(x)\cdot\vec{W}_{\mu\nu}(x), \tag{2.22}$$

where $B^{\mu\nu} = \partial^\mu B^\nu - \partial^\nu B^\mu$ and $\vec{W}^{\mu\nu} = \partial^\mu\vec{W}^\nu - \partial^\nu\vec{W}^\mu + g\vec{W}^\nu \times \vec{W}^\mu$. The gauge invariant Lagrangian under local $SU(2)_L \times U(1)_Y$ transformations,

$$\mathcal{L} = \sum_{j=1}^{3} i\bar{\psi}_j(x)\gamma^\mu D_\mu\psi_j(x) - \frac{1}{4}B^{\mu\nu}(x)B_{\mu\nu}(x) - \frac{1}{4}\vec{W}^{\mu\nu}(x)\cdot\vec{W}_{\mu\nu}(x), \tag{2.23}$$

only contains massless gauge fields and massless fermions at this point, because the mass terms explicitly violate the gauge symmetry. The Higgs mechanism, which generates the mass of particles through electroweak symmetry breaking, is explained in section 2.2.4.

2.2.3 Gauge Bosons

The interaction between fermions and the gauge bosons is included in Lagrangian (2.23):

$$\mathcal{L} = \sum_{j=1}^{3} \frac{g}{2}\bar{\psi}_j(x)\gamma^\mu(\vec{\tau}\cdot\vec{W}_\mu)\psi_j(x) + g' y_j B_\mu \bar{\psi}_j(x)\gamma^\mu\psi_j(x), \tag{2.24}$$

and,

$$\vec{\tau}\cdot\vec{W}_\mu = \begin{pmatrix} W_\mu^3 & W_\mu^1 - iW_\mu^2 \\ W_\mu^1 + iW_\mu^2 & -W_\mu^3 \end{pmatrix}, \tag{2.25}$$

where the gauge field representing the $W^\pm$ bosons is defined as $W_\mu = (W_\mu^1 - iW_\mu^2)/\sqrt{2}$, and the respective hermitian conjugate. Therefore, the charged current sector of the weak interaction for three families of quarks and leptons is written as:

$$\mathcal{L}_{\mathrm{CC}} = \frac{g}{2\sqrt{2}}W_\mu^\dagger\left(\sum_j \bar{u}_j\gamma^\mu(1-\gamma_5)d_j + \bar{\nu}_{l_j}\gamma^\mu(1-\gamma_5)l_j\right) + h.c., \tag{2.26}$$

except for the quark mixing matrix, addressed in section 2.2.5. The charged current interaction vertices are shown in Figure 2.1. The remaining gauge fields, W_μ^3 and B_μ, can be written as:

$$\begin{pmatrix} W_\mu^3 \\ B_\mu \end{pmatrix} = \begin{pmatrix} \cos\theta_W & \sin\theta_W \\ -\sin\theta_W & \cos\theta_W \end{pmatrix}\begin{pmatrix} Z_\mu \\ A_\mu \end{pmatrix}, \tag{2.27}$$

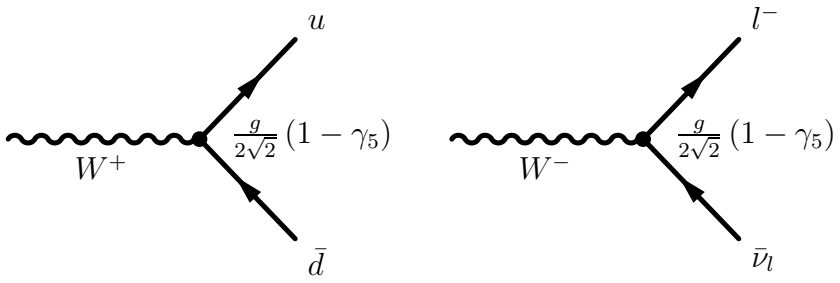

Figure 2.1: Charged current interaction vertices.

where Z^μ and A^μ represent the Z boson and photon fields, respectively, and θ_W is the weak mixing angle. As a result, the Lagrangian for the neutral current sector of the weak interaction is given by:

$$\begin{aligned}\mathcal{L}_{\rm NC} &= \sum_j \bar{\psi}_j \gamma^\mu \left(\frac{g}{2}\tau_3 \sin\theta_W + g' y_j \cos\theta_W\right) A_\mu \psi_j \\ &+ \sum_j \bar{\psi}_j \gamma^\mu \left(\frac{g}{2}\tau_3 \cos\theta_W - g' y_j \sin\theta_W\right) Z_\mu \psi_j + h.c., \end{aligned} \tag{2.28}$$

which successfully recreates QED if, and only if, $g \sin\theta_W = g' \cos\theta_W = e$, and $Y = Q - T_3$, where $T_3 = \tau_3/2$ and Q is the electromagnetic charge operator,

$$Q_1 = \begin{pmatrix} Q_{u/\nu} & 0 \\ 0 & Q_{d/e} \end{pmatrix}, \quad Q_2 = Q_{u/\nu}, \quad Q_3 = Q_{d/e}. \tag{2.29}$$

The electroweak charges Q, Y, and the third component of the weak isospin, T_3, for leptons and quarks are collected in Table 2.1. As the right-handed neutrino has no electric charge nor weak hypercharge (sterile neutrino), it is not considered. The neutral current interaction vertices are shown in Figure 2.2. The final Lagrangian

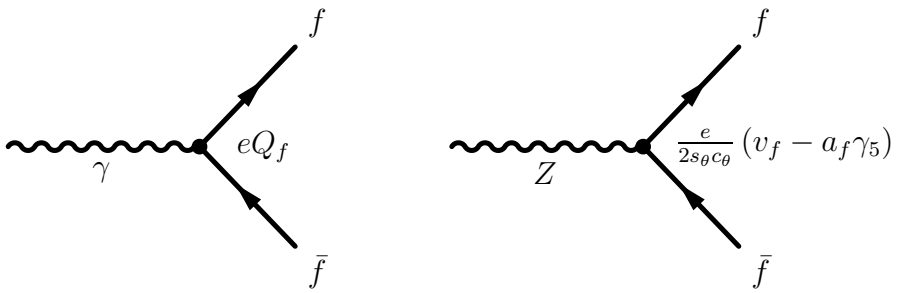

Figure 2.2: Neutral current interaction vertices.

	ν_L^l	l_L^-	l_R^-	u_L	d_L	u_R	d_R
Q	0	-1	-1	2/3	-1/3	2/3	-1/3
T_3	1/2	-1/2	0	1/2	-1/2	0	0
Y	-1/2	-1/2	-1	1/6	1/6	2/3	-1/3

Table 2.1: Electroweak charges Q, Y and the third component of the weak isospin T_3 for quarks and leptons in the SM.

for the neutral current can be written as:

$$\begin{aligned}\mathcal{L}_{\rm NC} &= \mathcal{L}_{\rm QED} + \mathcal{L}_{\rm Z} \\ &= eA_\mu \sum_f \bar{f}\gamma^\mu Q_f f + \frac{e}{2\sin\theta_W \cos\theta_W} Z_\mu \sum_f \bar{f}\gamma^\mu (v_f - a_f\gamma_5) f,\end{aligned} \tag{2.30}$$

where the vectorial and axial couplings, v_f and a_f, respectively, are presented in Table 2.2 for quarks and leptons. In addition, the electroweak interaction is charac-

	u	d	ν_l	l
v_f	$(1 - \frac{8}{3}\sin^2\theta_W)/2$	$(-1 + \frac{4}{3}\sin^2\theta_W)/2$	1/2	$(-1 + 4\sin^2\theta_W)/2$
a_f	1/2	−1/2	1/2	−1/2

Table 2.2: Neutral current couplings

terized by the self-interaction terms among the gauge fields. The kinetic Lagrangian (2.22) generates cubic and quadratic terms:

$$\begin{aligned}\mathcal{L}_3 &= -ie\cot\theta_W \left((\partial^\mu W^\nu - \partial^\nu W^\mu) W_\mu^\dagger Z_\nu - (\partial^\mu W^{\nu\dagger} - \partial^\nu W^{\mu\dagger}) W_\mu Z_\nu\right) \\ &- ie\cot\theta_W W_\mu W_\nu^\dagger (\partial^\mu Z^\nu - \partial^\nu Z^\mu) - ie(\partial^\mu W^\nu - \partial^\nu W^\mu) W_\mu^\dagger A_\nu \\ &+ ie(\partial^\mu W^{\nu\dagger} - \partial^\nu W^{\mu\dagger}) W_\mu A_\nu - ieW_\mu W_\nu^\dagger (\partial^\mu A^\nu - \partial^\nu A^\mu), \qquad (2.31) \\ \mathcal{L}_4 &= -\frac{e^2}{2\sin^2\theta_W} \left((W_\mu^\dagger W^\mu)^2 - W_\mu^\dagger W^{\mu\dagger} W_\nu W^\nu\right) \\ &- e^2\cot^2\theta_W \left(W_\mu^\dagger W^\mu Z_\nu Z^\nu - W_\mu^\dagger Z^\mu W_\nu Z^\nu\right) \\ &- e^2\cot\theta_W \left(2W_\mu^\dagger W^\mu Z_\nu A^\nu - W_\mu^\dagger Z^\mu W_\nu A^\nu - W_\mu^\dagger A^\mu W_\nu Z^\nu\right) \\ &- e^2 \left(W_\mu^\dagger W^\mu A_\nu A^\nu - W_\mu^\dagger A^\mu W_\nu A^\nu\right), \qquad (2.32)\end{aligned}$$

corresponding to the Feynman diagrams shown in Figure 2.3.

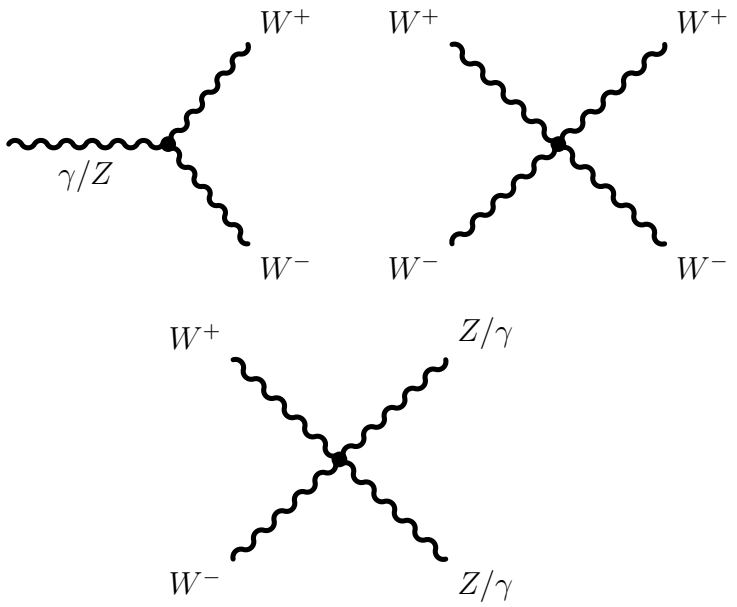

Figure 2.3: Gauge boson self-interaction vertices.

2.2.4 Higgs Mechanism

The electroweak interaction Lagrangian (2.23), derived in the previous sections, is still far from reality since it only contains massless gauge fields and fermions. The relativistic mechanism that generates the masses of the $W^{\pm}$ and Z gauge bosons through spontaneous symmetry breaking, also known as Higgs mechanism, is presented and discussed in this section. The Higgs mechanism was independently suggested in 1964 by Robert Brout and François Englert [15], Peter Higgs [16], and Gerald Guralnik, C. R. Hagen, and Tom Kibble [17], and is the generally accepted renormalizable model which spontaneously breaks the electroweak symmetry. The six authors of the 1964 PRL symmetry breaking papers were awarded the J. J. Sakurai Prize for Theoretical Particle Physics in 2010, by the American Physical Society, "for elucidation of the properties of spontaneous symmetry breaking in four-dimensional relativistic gauge theory and of the mechanism for the consistent generation of vector boson masses".

For a complex scalar field $\phi(x)$, the Lagrangian,

$$\mathcal{L} = \frac{1}{2}\partial_\mu\phi^\dagger\partial^\mu\phi - \frac{1}{2}\mu^2\phi^\dagger\phi - \frac{\lambda}{4}(\phi^\dagger\phi)^2, \tag{2.33}$$

with $\lambda > 0$, is invariant under global gauge transformations:

$$\phi(x) \rightarrow \phi'(x) = e^{i\theta}\phi(x). \tag{2.34}$$

The ground state of the potential, $V(\phi) = \frac{1}{2}\mu^2\phi^\dagger\phi + \frac{\lambda}{4}(\phi^\dagger\phi)^2$, is particularly interesting if $\mu^2 < 0$. The minimum of the potential is obtained for an infinite number

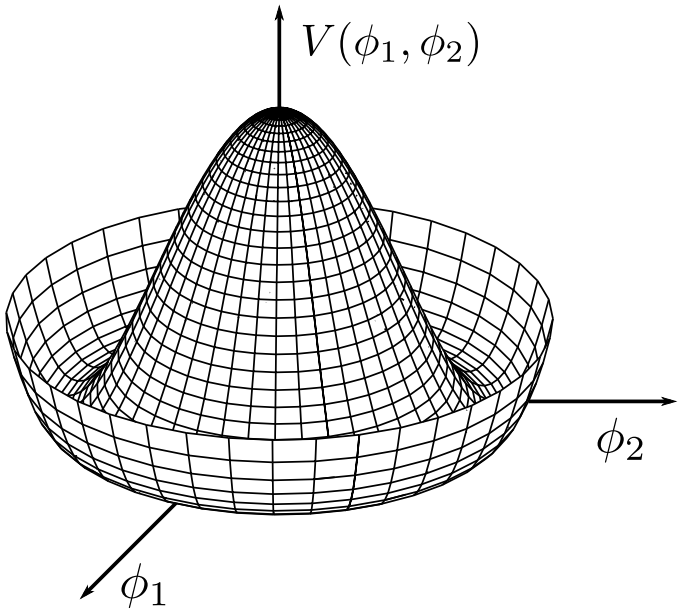

Figure 2.4: Graph of a mexican hat potential function.

of degenerate states satisfying:

$$|\phi_0| = \sqrt{-\frac{\mu^2}{\lambda}} = \nu, \tag{2.35}$$

for any $U(1)$ gauge phase θ. The complex scalar field, in this 2D example of the Higgs mechanism, can be parameterized using two real fields, ϕ_1 and ϕ_2,

$$\phi(x) = \frac{1}{\sqrt{2}} \left(\phi_1(x) + i\phi_2(x)\right), \tag{2.36}$$

which leads to,

$$\mathcal{L} = \frac{1}{2} \left(\partial_\mu \phi_1\right)^2 + \frac{1}{2} \left(\partial_\mu \phi_2\right)^2 - \frac{1}{2}\mu^2 \left(\phi_1^2 + \phi_2^2\right) - \frac{\lambda}{4} \left(\phi_1^2 + \phi_2^2\right)^2. \tag{2.37}$$

Thus, the minimum of the potential, $\phi_0 = \nu e^{i\theta}$, can be represented as a circle of minima of the potential in the ϕ_1-ϕ_2 complex plane,

$$\phi_1^2 + \phi_2^2 = \nu^2, \tag{2.38}$$

represented in Figure 2.4. If a particular solution, $\phi_1 = \nu$ and $\phi_2 = 0$ for example, is chosen as the ground state, the symmetry is spontaneously broken, and the complex scalar field can be expanded around the vacuum in terms of real fields, $\eta(x)$ and $\zeta(x)$:

$$\phi(x) = \nu + \eta(x) + i\zeta(x). \tag{2.39}$$

The Lagrangian becomes,

$$\mathcal{L} = \frac{1}{2} \left(\partial_\mu \eta\right)^2 + \frac{1}{2} \left(\partial_\mu \zeta\right)^2 - \mu^2\eta^2 + \text{cubic and quadratic terms in } \eta \text{ and } \zeta, \tag{2.40}$$

which comprises a massless field, corresponding to excitations into states with the same energy around the flat direction $\zeta(x)$, and a massive field, $\eta(x)$, with mass $m_\eta = \sqrt{-2\mu^2}$. In conclusion, the spontaneous symmetry breaking generated a massless scalar, also known as Goldstone boson [51, 52]. However, this result is still far away from the desired outcome. For the $SU(2)_L \times U(1)_Y$ symmetry, the local gauge invariant Lagrangian of the Goldstone model is,

$$\mathcal{L} = \left(D^\mu \phi\right)^\dagger \left(D_\mu \phi\right) - \mu^2 \phi^\dagger \phi - \lambda \left(\phi^\dagger \phi\right)^2, \tag{2.41}$$

where $D^\mu \phi = \left(\partial_\mu + ig\vec{\tau} \cdot \vec{W}_\mu(x) + ig' y_\phi B_\mu\right) \phi$, and ϕ represents a $SU(2)_L$ doublet of scalar fields,

$$\phi(x) = \frac{1}{\sqrt{2}} \begin{pmatrix} \phi_1(x) + i\phi_2(x) \\ \phi_3(x) + i\phi_4(x) \end{pmatrix}. \tag{2.42}$$

Likewise the previous case, for $\mu^2 < 0$, the potential has its minimum for an infinite set of degenerate states:

$$\phi_1^2 + \phi_2^2 + \phi_3^2 + \phi_4^2 = -\frac{\mu^2}{\lambda} = \nu. \tag{2.43}$$

If a particular solution is chosen, *i.e.* the symmetry is spontaneously broken,

$$\phi_1 = \phi_2 = \phi_4 = 0, \qquad \phi_3^2 = -\frac{\mu^2}{\lambda} = \nu^2, \tag{2.44}$$

the scalar field ϕ can be expanded around the minimum in the most general form,

$$\phi(x) = e^{i\vec{\tau} \cdot \vec{\theta}(x)/2} \frac{1}{\sqrt{2}} \begin{pmatrix} 0 \\ \nu + h(x) \end{pmatrix}, \tag{2.45}$$

with four real fields, $\vec{\theta}(x)$ and $h(x)$. By taking the gauge $\vec{\theta}(x) = 0$, the kinetic term of the Lagrangian becomes,

$$\left(D^\mu \phi\right)^\dagger \left(D_\mu \phi\right) = \frac{1}{2} \partial^\mu h \partial_\mu h + (\nu + h)^2 \left(\frac{g^2}{4} W_\mu^\dagger W^\mu + \frac{g^2}{8 \cos^2 \theta_W} Z_\mu Z^\mu\right). \tag{2.46}$$

That is, the Lagrangian describes the three massive gauge bosons, $W^\pm$ and Z, and a massive scalar field $h(x)$, which represents the Higgs boson. The vacuum expectation value of the neutral scalar has generated a quadratic term for the $W^\pm$ and Z bosons:

$$M_Z \cos \theta_W = M_W = \frac{1}{2} \nu g. \tag{2.47}$$

The fermionic masses are also allowed after the spontaneous symmetry breaking, and the Yukawa-type Lagrangian takes the following form:

$$\mathcal{L}_Y = -\left(1 + \frac{h}{\nu}\right) \left(m_u \bar{u} u + m_d \bar{d} d + m_e \bar{e} e\right). \tag{2.48}$$

The Higgs boson is the ultimate missing piece of the SM. On 4th July 2012, the CMS and ATLAS experiments announced the discovery of a new boson, compatible with the SM Higgs boson, at $125.3 \pm 0.4\,(\text{stat.}) \pm 0.5\,(\text{sys.})$ GeV (CMS) and $126 \pm 0.4\,(\text{stat.}) \pm 0.4\,(\text{sys.})$ GeV (ATLAS), with global statistical significances of 5.8 sigma (CMS) [53] and 5.9 sigma (ATLAS) [54]. No significant deviation from the prediction for a SM Higgs boson was discovered so far, however, an extensive research program is underway to probe the properties of the new boson observed by the ATLAS and CMS experiments [55].

2.2.5 CP Violation and the CKM Matrix

The CP-symmetry corresponds to the combination of the C-symmetry, and the P-symmetry. Since the discovery of parity violation in the 1950s [39, 40], the CP-symmetry was believed to be the true symmetry of the Standard Model. However, the discovery of the CP violation in the weak decays of neutral kaons, by James Cronin and Val Fitch in 1964 [56], forced a reformulation of the electroweak sector of the Standard Model. The Cabibbo-Kobayashi-Maskawa (CKM) matrix, which contains the information on the strength of flavor-changing weak decays, and explains the observed CP violation in the context of a renormalizable theory of the weak interaction, is presented in this section.

It is now almost fifty years since the publication of Nicola Cabibbo's famous letter "Unitary Symmetry and Leptonic Decays" [41], which provided the basic foundation for quark mixing in the weak interaction sector of the Standard Model. Ten years later, Makoto Kobayashi and Toshihide Maskawa extended the work of Cabibbo to three generations of quarks and established the unitary CKM matrix [42]. The work of Kobayashi and Maskawa became notorious for explaining CP violation in the Standard Model, and for predicting the existence of the bottom and top quarks [57–59]. In recognition of their work, the two japanese physicists were laureated with the Nobel Prize in Physics in 2008 *"for the discovery of the origin of the broken symmetry which predicts the existence of at least three families of quarks in nature"*.

The charged current sector for the quarks in the Standard Model Lagrangian, *i.e.* the V-A coupling to the W boson, can be written in terms of mass eigenstates as

$$\mathcal{L}_{CC} = -\frac{g}{2\sqrt{2}} W_\mu^\dagger \sum_{i,j} \bar{u}_i \gamma^\mu (1-\gamma_5) \mathbf{V}_{ij} d_j + h.c., \tag{2.49}$$

where i and j are the quark generation indices and $\mathbf{V}$ is the CKM matrix. As previously discussed, the down-type weak eigenstates, $|d_i'\rangle$, are related to the mass

eigenstates, $|d_j\rangle$, through

$$|d_i'\rangle = \sum_j \mathbf{V}_{ij}|d_j\rangle, \tag{2.50}$$

or, in a different nomenclature,

$$\begin{pmatrix} |d'\rangle \\ |s'\rangle \\ |b'\rangle \end{pmatrix} = \begin{pmatrix} V_{ud} & V_{us} & V_{ub} \\ V_{cd} & V_{cs} & V_{cb} \\ V_{td} & V_{ts} & V_{tb} \end{pmatrix} \begin{pmatrix} |d\rangle \\ |s\rangle \\ |b\rangle \end{pmatrix}, \tag{2.51}$$

so that each up-type quark couples with every down-type quark by means of the CKM matrix. The CKM matrix is a 3×3 unitary matrix with four independent parameters. The unitarity constraints are given by

$$\sum_i |\mathbf{V}_{ij}|^2 = \sum_j |\mathbf{V}_{ij}|^2 = 1, \tag{2.52}$$

for each generation of quarks, and by the orthogonality relations:

$$\sum_k \mathbf{V}_{ik}\mathbf{V}_{jk}^* = 0, \tag{2.53}$$

for any $i \neq j$. The CKM matrix can be parameterized in many different ways, such as the standard parametrization [60],

$$\mathbf{V} = \begin{pmatrix} c_{12}c_{13} & s_{12}c_{13} & s_{13}e^{-i\delta_{13}} \\ -s_{12}c_{23} - c_{12}s_{23}s_{13}e^{i\delta_{13}} & c_{12}c_{23} - s_{12}s_{23}s_{13}e^{i\delta_{13}} & s_{23}c_{13} \\ s_{12}s_{23} - c_{12}c_{23}s_{13}e^{i\delta_{13}} & -c_{12}s_{23} - s_{12}c_{23}s_{13}e^{i\delta_{13}} & c_{23}c_{13} \end{pmatrix}, \tag{2.54}$$

comprising three mixing angles, $c_{ij} = \cos\theta_{ij}$ and $s_{ij} = \sin\theta_{ij}$, where θ_{12} represents the Cabibbo angle, and a CP-violating phase δ_{13}. Another common parametrization of the CKM matrix was introduced by Wolfenstein [61],

$$\mathbf{V} = \begin{pmatrix} 1-\lambda^2 & \lambda & A\lambda^2(\rho - i\eta) \\ -\lambda & 1-\lambda^2 & A\lambda^2 \\ A\lambda^3(1-\rho-i\eta) & -A\lambda^2 & 1 \end{pmatrix}, \tag{2.55}$$

up to order λ^3. The currently most precise values for the Wolfenstein parameters are [24]:

$$\begin{aligned} \lambda &= 0.2246 \pm 0.0011, \quad A = 0.832 \pm 0.017, \\ \rho &= 0.130 \pm 0.018, \quad \eta = 0.350 \pm 0.013, \end{aligned} \tag{2.56}$$

and the Jarlskog invariant [62], a phase-convention-independent measure of CP violation defined as $\Im(V_{ij}V_{kl}V_{il}^*V_{kj}^*)$, is $J = (2.19^{+0.19}_{-0.11}) \times 10^{-5}$. Finally, assuming

unitarity and the existence of three quark families, the best determination of the CKM matrix elements magnitudes is:

$$\begin{pmatrix} 0.97428 \pm 0.00015 & 0.2253 \pm 0.0007 & 0.00347^{+0.00016}_{-0.00012} \\ 0.2252 \pm 0.0007 & 0.97345^{+0.00015}_{-0.00016} & 0.0410^{+0.0011}_{-0.0007} \\ 0.00862^{+0.00026}_{-0.00020} & 0.0403^{+0.0011}_{-0.0007} & 0.999152^{+0.000030}_{-0.000045} \end{pmatrix}. \tag{2.57}$$

As the $t \to Wb$ vertex transition is, in first order, proportional to $|V_{tb}|^2$, and since $|V_{ts}|$ and $|V_{td}|$ are much smaller, the top quark decays mostly to a W boson and a bottom quark.

Even though the quark mixing violates CP and T symmetries to preserve the CPT invariance, neither CP nor T violations represent any arrow of time. Due to the unitarity of the Cabibbo-Kobayashi-Maskawa matrix, the quantum mixtures of quarks resulting from the weak interaction do not increase entropy and, therefore, the violation of CP and T symmetries cannot be related to the second law of thermodynamics [63].

2.3 Quantum Chromodynamics

Quantum Chromodynamics, a theory of the strong force that describes how the constituents of hadrons (quarks and gluons) interact, assumes the existence of a new quantum number, the color charge. Quarks can hold three different colors (red, green, blue), however, only appear in colorless bound states (hadrons), *i.e.* color singlets, an hypothesis known as *confinement* [21]. Since there are three color states, $SU(3)_c$ is the natural gauge symmetry group for QCD. The free Dirac Lagrangian for massive quarks,

$$\mathcal{L} = \sum_f \bar{q}_f \left(i\gamma^\mu \partial_\mu - m_f\right) q_f, \tag{2.58}$$

where $q_f^T = (q_f^1, q_f^2, q_f^3)$ is the quarks color vector of flavor f, is invariant under global $SU(3)_c$ transformations:

$$q_f^\alpha \to (q_f^\alpha)' = U_\beta^\alpha q_f^\beta, \tag{2.59}$$

where $U = e^{i\lambda^a \theta_a/2}$, satisfying $U^\dagger U = 1$ and $\det U = 1$. The matrices λ^a, for $a = 1, 2, ..., 8$, known as Gell-Mann matrices [18], represent the $SU(3)$ group generators, and θ_a are arbitrary parameters. The Gell-Mann matrices are traceless and satisfy the following commutation relation:

$$\left[\frac{\lambda^a}{2}, \frac{\lambda^b}{2}\right] = i f^{abc} \frac{\lambda^c}{2}, \tag{2.60}$$

where the structure constants f^{abc} are completely asymmetric. In order to preserve the local gauge symmetry, $\theta^a = \theta^a(x)$, the covariant derivative is defined as:

$$D^\mu q_f = \left(\partial^\mu + i g_s \frac{\lambda^a}{2} G_a^\mu(x)\right) q_f = \left(\partial^\mu + i g_s G^\mu(x)\right), \tag{2.61}$$

where $G^\mu(x) = \frac{1}{2}\lambda^a G_a^\mu(x)$, and transforms as,

$$G^\mu \to (G^\mu)' = U G^\mu U^\dagger + \frac{i}{g_s}\left(\partial^\mu U\right) U^\dagger. \tag{2.62}$$

Finally, the gauge-invariant kinetic term for the gluon fields is,

$$\mathcal{L}_K = -\frac{1}{4} G_a^{\mu\nu} G^a_{\mu\nu}, \tag{2.63}$$

where $G_a^{\mu\nu} = \partial^\mu G_a^\nu - \partial^\nu G_a^\mu - g_s f^{abc} G_b^\mu G_c^\nu$. Consequently, the final QCD Lagrangian can be written as,

$$\begin{aligned}
\mathcal{L} \;=\; & -\frac{1}{4}\left(\partial^\mu G_a^\nu - \partial^\nu G_a^\mu\right)\left(\partial_\mu G^a_\nu - \partial_\nu G^a_\mu\right) + \sum_f \bar{q}_f \left(i\gamma^\mu \partial_\mu - m_f\right) q_f \\
& - g_s G_a^\mu \sum_f \bar{q}_f^\alpha \gamma_\mu \left(\frac{\lambda^a}{2}\right)_{\alpha\beta} q_f^\beta \\
& + \frac{g_s}{2} f^{abc}\left(\partial^\mu G_a^\nu - \partial^\nu G_a^\mu\right) G_\mu^b G_\nu^c - \frac{g_s^2}{4} f^{abc} f_{ade} G_b^\mu G_c^\nu G_\mu^d G_\nu^e,
\end{aligned} \tag{2.64}$$

which contains the color interaction between quarks and gluons, and the cubic and quartic gluon self-interactions, corresponding to the Feynman diagrams shown in Figure 2.5.

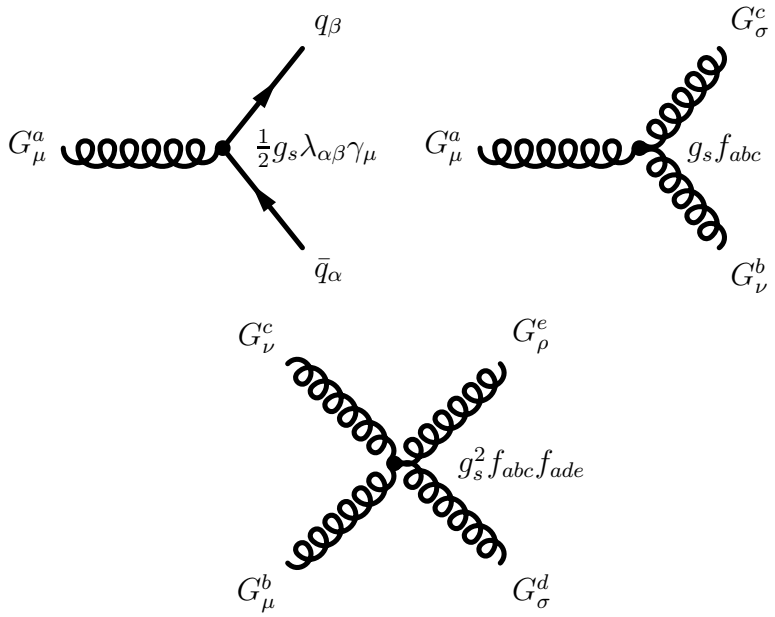

Figure 2.5: QCD interaction vertices.

2.4 Top Quark

The top quark, the third generation up-type quark of the SM, has spin 1/2, electric charge $+2/3$ e, and with a mass $m_t = 173.2 \pm 0.9$ GeV [1], is the most massive elementary particle observed to date. Discovered in 1995 by the DØ and CDF collaborations [58, 59], the top quark interacts through the electroweak and strong forces, and due to its large mass, the top quark may well play a fundamental role in the understanding of the electroweak symmetry breaking mechanism of the SM [64]. The top quark decays through the weak interaction, and in particular, decays mostly to a W boson and bottom quark with a mean lifetime estimated to be 10^{-25} seconds [64]. Due to its short lifetime, smaller than the typical hadronization time scale ($\sim 10^{-24}$ s), top quarks decay before hadronization can take place [65]. The top quark spin information is, therefore, preserved by the decay products before hadronization dilutes it. By measuring the angular distributions of the decay products, it is possible to access the spin information and hence probe the nature of the Wtb vertex.

The measurement of the top quark properties plays an important role in testing the SM and its possible extensions, which makes it one of the leading areas of research in the present days, within the high-energy physics community. The rich phenomenology available in the top quark includes the measurement of production cross-sections via the strong and the electroweak interactions, the top quark mass and electric charge, flavor changing neutral currents in top quark decays, spin correlations and top quark polarization, the Wtb vertex structure, same-sign top pair

production, among others. In this section, several top quark properties, in which the author was particularly involved during the course of this thesis, are presented on the light of the latest experimental results.

2.4.1 Top Quark Production

Since its discovery, the top quark has been produced in the main hadron colliders, the Tevatron and the Large Hadron Collider (LHC). At the LHC, the top quark can be produced by two main mechanisms, pair production ($t\bar{t}$) and single production (single top) via the strong and weak interactions, respectively. Some examples of leading-order Feynman diagrams for the top quark pair production and single top quark production are shown in Figure 2.6.

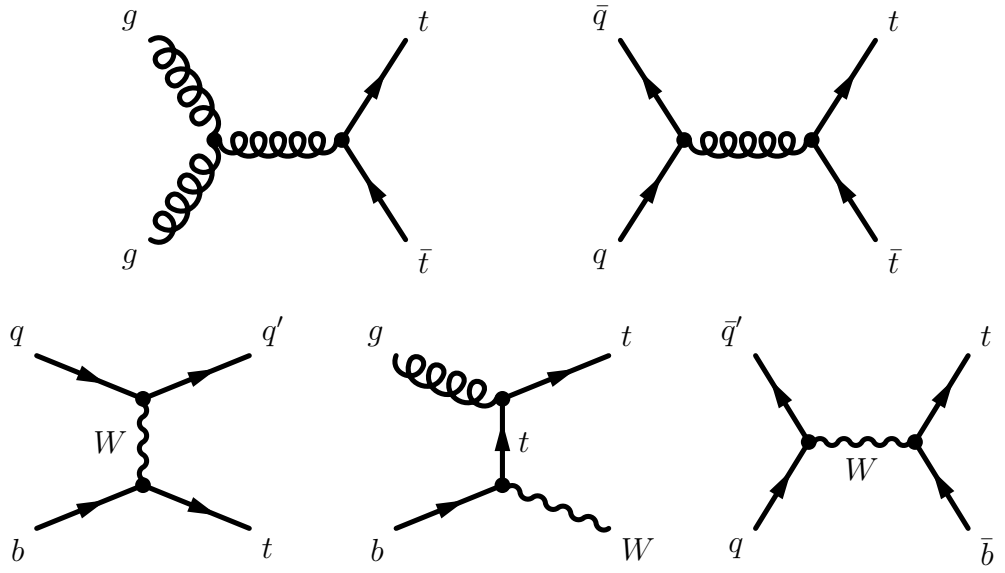

Figure 2.6: Examples of top quark pair production leading-order Feynman diagrams: gluon fusion (top left) and quark-antiquark annihilation (top right). Single top quark production Feynman diagrams: t-channel (bottom left), associate production (bottom center) and s-channel (bottom right).

The top quark pair production takes place through QCD interactions by gluon fusion and quark-antiquark annihilation. As the relative importance of each process depends on the center-of-mass energy, the gluon fusion is expected to dominate $t\bar{t}$ production with a fraction of 90%, in comparison to the 10% fraction of the quark-antiquark annihilation, given the range of center-of-mass energies at the LHC [65]. Events with a $t\bar{t}$ pair can be classified as 'single-lepton', 'dilepton', or 'all hadronic' by the decays of the two $W^{\pm}$ bosons: a pair of quarks ($W \to q\bar{q}$) or a lepton-neutrino pair ($W \to \ell\nu$), where ℓ refers to a charged lepton. The predicted SM $t\bar{t}$ cross section

for pp collisions at a centre-of-mass energy of $\sqrt{s} = 7$ TeV is $\sigma_{t\bar{t}} = 167^{+17}_{-18}$ pb for a top quark mass of 172.5 GeV/c^2 as obtained from approximate NNLO QCD calculations [66]. The most recent public results from the ATLAS and CMS collaborations on the top pair production cross-section measurement are summarized in Figure 2.7. The example of a $t\bar{t}$ dielectron event candidate observed at the ATLAS experiment is shown in Figure 2.8. At the Tevatron the dominant production mechanism was quark-antiquark annihilation, with a fraction of 85% [65].

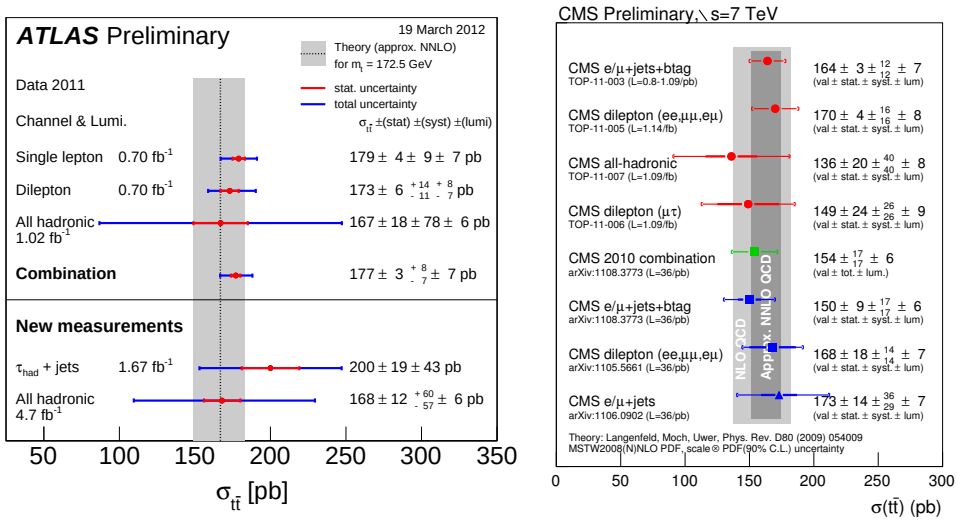

Figure 2.7: The two plots show the summary of measurements of the top pair production cross-section for the ATLAS (left) and CMS (right) experiments, compared to the corresponding theoretical expectation.

The single top quark production occurs, at the LHC, through the t-channel exchange of a virtual W boson, the s-channel decay of a virtual W boson, and the associate production of a top quark and a W boson. In pp collisions at a center-of-mass energy $\sqrt{s} = 7$ TeV, the predicted cross-sections are $64.6^{+3.3}_{-2.6}$ pb for the t-channel [67], 15.7 ± 1.4 pb for the associated production [68], and 4.6 ± 0.3 pb for the s-channel [69]. The single top quark production cross-section measurement is particularly relevant due to its sensitivity to the Cabibbo-Kobayashi-Maskawa quark mixing matrix element $|V_{tb}|^2$, which provides a direct determination of V_{tb} without assuming the number of quark generations. In addition, the single top quark production is sensitive to many models of new physics [70], such as anomalous couplings [71].

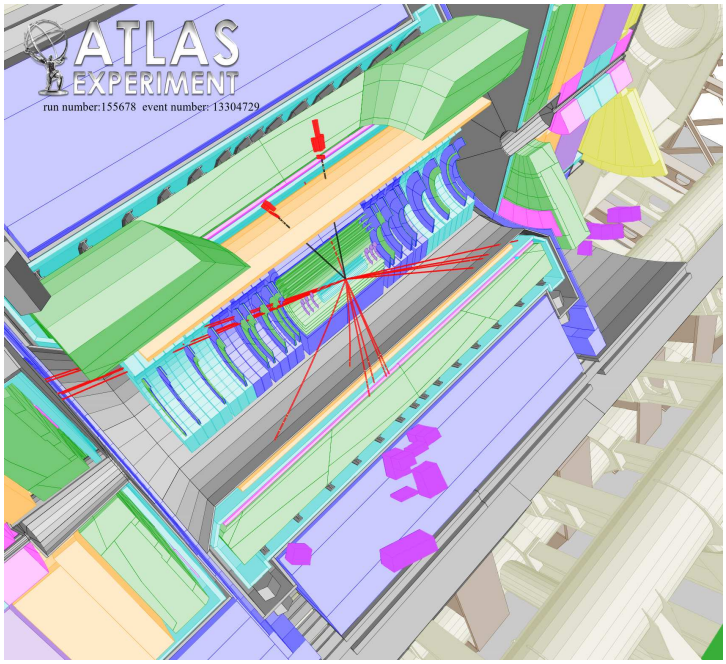

Figure 2.8: Event display of a $t\bar{t}$ dielectron candidate at the ATLAS experiment. The two electrons are picked out in black.

2.4.2 W Boson Polarization

In the SM the top quark has $V-A$ charged current weak interactions as the other fermions. Using the helicity basis to quantize spin, the $W^{\pm}$ bosons produced in the decay can be produced with helicity $0, +1, -1$, with corresponding partial widths Γ_0, Γ_{R}, Γ_{L}. If the b quark mass is neglected, the $W^{\pm}$ bosons from top quark decays cannot be produced with right-handed helicity, since massless left-handed particles can only have left-handed helicities. The polarization states of the $W^{\pm}$ bosons can be extracted from the angular distribution of its decay products. Considering the decay $t \to bW^{+} \to bl^{+}\nu_l$ and defining θ^* as, the angle between the charged lepton momentum from the W boson decay and the reversed b-quark momentum from top quark decay in the W boson rest frame, the normalized decay rate for top quarks is,

$$\frac{1}{\Gamma}\frac{d\Gamma}{d\cos\theta^*} = \frac{3}{8}(1+\cos\theta^*)^2 F_{\mathrm{R}} + \frac{3}{8}(1-\cos\theta^*)^2 F_{\mathrm{L}} + \frac{3}{4}\sin^2\theta^* F_0\,, \tag{2.65}$$

with $F_0 = \Gamma_0/\Gamma$, $F_{\mathrm{L}} = \Gamma_{\mathrm{L}}/\Gamma$ and $F_{\mathrm{R}} = \Gamma_{\mathrm{R}}/\Gamma$ representing the helicity fractions. The total decay width is defined as $\Gamma \equiv \Gamma(t \to W^{+}b) = \Gamma_{\mathrm{R}} + \Gamma_{\mathrm{L}} + \Gamma_0$. At tree level, F_{R}, F_{L} and F_0 are given by [72]:

$$F_{\mathrm{R}} = \frac{(1-y^2)^2 - x^2(1+y^2)}{(1-y^2)^2 + x^2(1-2x^2+y^2)} \tag{2.66}$$

$$F_{\mathrm{L}} = \frac{x^2(1-x^2+y^2+\sqrt{\lambda})}{(1-y^2)^2 + x^2(1-2x^2+y^2)} \tag{2.67}$$

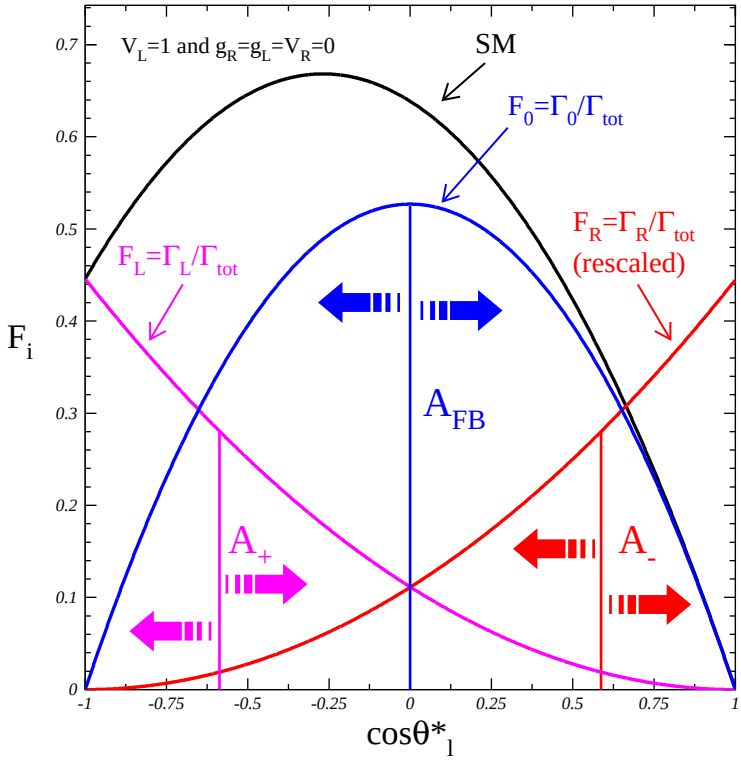

Figure 2.9: SM distribution of $\cos\theta^*$. The different contributions for each W boson polarization state in top quark decays are shown, as well as an illustration of how the angular asymmetries are defined. The right-handed component, which is highly suppressed in the SM, is scaled to the same size as the left-handed component in order to be visible.

$$F_0 = \frac{x^2(1-x^2+y^2-\sqrt{\lambda})}{(1-y^2)^2+x^2(1-2x^2+y^2)} \tag{2.68}$$

where $x = M_W/m_t$, $y = m_b/m_t$, and $\lambda = 1+x^4+y^4-2x^2y^2-2x^2-2y^2$. The helicity fractions are predicted in next-to-next-to-leading-order (NNLO) QCD calculations to be $F_0 = 0.687 \pm 0.005$, $F_\mathrm{L} = 0.311 \pm 0.005$, $F_\mathrm{R} = 0.0017 \pm 0.0001$ [73]. This angular distribution, represented in Figure 2.9, can be used to measure the W boson polarizations and hence probe physics beyond the SM.

A simple method to obtain information about the polarization states of the $W^\pm$ bosons is to perform a counting experiment by evaluating angular asymmetries in the distribution of $\cos\theta^*$ [74]. For any fixed value of z in the interval $[-1, 1]$, one can define an asymmetry

$$A_z = \frac{N(\cos\theta^* > z) - N(\cos\theta^* < z)}{N(\cos\theta^* > z) + N(\cos\theta^* < z)}\,. \tag{2.69}$$

The most obvious choice is $z = 0$, giving the forward-backward (FB) asymmetry

A_{FB}, which is related to the W boson helicity fractions by

$$A_{\mathrm{FB}} = \frac{3}{4}[F_{\mathrm{R}} - F_{\mathrm{L}}]\,. \tag{2.70}$$

The measurement of this asymmetry alone is not enough to fully specify the $\cos\theta^*$ distribution. Other asymmetries, for different values of z, have therefore to be considered. The determination of F_{i} is easier if asymmetries involving only F_{R} and F_0, or F_{L} and F_0 are chosen. This is achieved by choosing $z = \mp(2^{2/3} - 1)$:

$$\begin{aligned} z = -(2^{2/3} - 1) \;\; &\rightarrow \;\; A_z = A_+ = 3\beta[F_0 + (1+\beta)F_{\mathrm{R}}]\,, \\ z = (2^{2/3} - 1) \;\; &\rightarrow \;\; A_z = A_- = -3\beta[F_0 + (1+\beta)F_{\mathrm{L}}]\,, \end{aligned} \tag{2.71}$$

where $\beta = 2^{1/3} - 1$. The SM NNLO values for these angular asymmetries are $A_{\mathrm{FB}} = 0.232 \pm 0.004$, $A_+ = 0.537 \pm 0.004$ and $A_- = -0.841 \pm 0.006$ [73]. From the A_+ and A_- asymmetries and using $F_{\mathrm{R}} + F_{\mathrm{L}} + F_0 = 1$, the W boson helicity fractions can be obtained:

$$\begin{aligned} F_{\mathrm{R}} &= \frac{1}{1-\beta} + \frac{A_- - \beta A_+}{3\beta(1-\beta^2)}\,, \\ F_{\mathrm{L}} &= \frac{1}{1-\beta} - \frac{A_+ - \beta A_-}{3\beta(1-\beta^2)}\,, \\ F_0 &= -\frac{1+\beta}{1-\beta} + \frac{A_+ - A_-}{3\beta(1-\beta)}\,. \end{aligned} \tag{2.72}$$

It should be stressed that the angular asymmetries, as a consequence of their definition, *i.e.* ratios of number of events above and below a specific cut-off in the angular distribution, are expected to show lower systematic uncertainties when compared to the simple fit of the angular distribution itself.

2.4.3 Anomalous Couplings

The large top quark mass makes it more likely to be sensitive to physics beyond the SM. Above the electroweak symmetry breaking scale, new physics can be parameterized in terms of effective operators [75],

$$\mathcal{L}_{\mathrm{eff}} = \sum \frac{C_x}{\Lambda^2} O_x + \ldots\,, \tag{2.73}$$

where O_x are dimension-six effective operators invariant under the SM gauge symmetry $\mathrm{SU}(3)_c \times \mathrm{SU}(2)_L \times \mathrm{U}(1)_Y$, C_x are dimensionless constants and Λ is the new physics scale. Dimension-eight and higher-order operators are suppressed by highers powers of Λ, and are usually ignored. This parametrization is model-independent, based only on the gauge symmetry of the SM and the fact that the new physics is characterized by a new scale $\Lambda \gg v$.

Among all dimension-six operators, there are only four independent ones which contribute to the Wtb interaction [76, 77],

$$\begin{aligned}
O_{\phi q}^{(3,3+3)} &= \frac{i}{2}\left[\phi^\dagger(\tau^I D_\mu - \overleftarrow{D}_\mu \tau^I)\phi\right](\bar{q}_{L3}\gamma^\mu \tau^I q_{L3})\,, \\
O_{\phi\phi}^{33} &= i(\tilde{\phi}^\dagger D_\mu \phi)(\bar{t}_R \gamma^\mu b_R)\,, \\
O_{dW}^{33} &= (\bar{q}_{L3}\sigma^{\mu\nu}\tau^I b_R)\phi\, W_{\mu\nu}^I\,, \\
O_{uW}^{33} &= (\bar{q}_{L3}\sigma^{\mu\nu}\tau^I t_R)\tilde{\phi}\, W_{\mu\nu}^I\,,
\end{aligned} \tag{2.74}$$

using standard notation with q_{L3} representing the left-handed third generation quark doublet, t_R the right-handed top quark singlet, b_R the right-handed bottom quark singlet, ϕ the SM Higgs doublet, $\tilde{\phi} = i\tau^2\phi^*$, $W_{\mu\nu}^I$ the $\mathrm{SU}(2)_L$ field strength tensor, and D_μ ($\overleftarrow{D}_\mu$) the covariant derivative acting on the right (left). After electroweak symmetry breaking, these operators yield the Wtb Lagrangian

$$\begin{aligned}
\mathcal{L}_{Wtb} \;=\; & -\frac{g}{\sqrt{2}}\bar{b}\,\gamma^\mu\,(V_{\mathrm{L}}P_L + V_{\mathrm{R}}P_R)\,t\,W_\mu^- \\
& -\frac{g}{\sqrt{2}}\bar{b}\,\frac{i\sigma^{\mu\nu}q_\nu}{M_W}\,(g_{\mathrm{L}}P_L + g_{\mathrm{R}}P_R)\,t\,W_\mu^- + \mathrm{h.c.}\,,
\end{aligned} \tag{2.75}$$

where

$$\begin{aligned}
V_{\mathrm{L}} &= V_{tb} + C_{\phi q}^{(3,3+3)}\frac{v^2}{\Lambda^2}\,, & V_{\mathrm{R}} &= \frac{1}{2}C_{\phi\phi}^{33*}\frac{v^2}{\Lambda^2}\,, \\
g_{\mathrm{L}} &= \sqrt{2}C_{dW}^{33*}\frac{v^2}{\Lambda^2}\,, & g_{\mathrm{R}} &= \sqrt{2}C_{uW}^{33}\frac{v^2}{\Lambda^2}\,.
\end{aligned} \tag{2.76}$$

The anomalous couplings V_{R}, g_{L}, g_{R} generated by dimension-six operators are absent in the SM at the tree level, while the SM coupling V_{tb} receives a correction from the operator $O_{\phi q}^{(3,3+3)}$. In the presence of anomalous Wtb couplings the W helicity fractions studied here depart from their SM values [78], a fact that can be used to set constraints on the former. It is also worth noting that indirect, model-dependent limits on the anomalous couplings can be inferred from experimental measurements of radiative B meson decays and $B\bar{B}$ mixing [79]. They are expected to be in the range $V_{\mathrm{R}} \in [-0.0007, 0.0025]$, $g_{\mathrm{L}} \in [-0.0015, 0.0004]$ and $g_{\mathrm{R}} \in [-0.15, 0.57]$, barring possible cancellations among different contributions [80, 81]. The dependence of the partial widths corresponding to the three W-boson helicities on the Wtb anomalous

couplings was calculated in [74]:

$$\begin{aligned}
\Gamma_0 &= \frac{g^2|\vec{q}|}{32\pi}\left\{\frac{m_t^2}{m_W^2}\left[|V_{\rm L}|^2+|V_{\rm R}|^2\right]\left(1-x_W^2-2x_b^2-x_W^2x_b^2+x_b^4\right)-4x_b\,{\rm Re}\;V_{\rm L}V_{\rm R}^*\right.\\
&+\left[|g_{\rm L}|^2+|g_{\rm R}|^2\right]\left(1-x_W^2+x_b^2\right)-4x_b\,{\rm Re}\;g_{\rm L}g_{\rm R}^*\\
&-2\frac{m_t}{m_W}{\rm Re}\;\left[V_{\rm L}g_{\rm R}^*+V_{\rm R}g_{\rm L}^*\right]\left(1-x_W^2-x_b^2\right)\\
&\left.+2\frac{m_t}{m_W}x_b\,{\rm Re}\;\left[V_{\rm L}g_{\rm L}^*+V_{\rm R}g_{\rm R}^*\right]\left(1+x_W^2-x_b^2\right)\right\}\,,
\end{aligned}$$

$$\begin{aligned}
\Gamma_{\rm R,L} &= \frac{g^2|\vec{q}|}{32\pi}\left\{\left[|V_{\rm L}|^2+|V_{\rm R}|^2\right]\left(1-x_W^2+x_b^2\right)-4x_b\,{\rm Re}\;V_{\rm L}V_{\rm R}^*\right.\\
&+\frac{m_t^2}{m_W^2}\left[|g_{\rm L}|^2+|g_{\rm R}|^2\right]\left(1-x_W^2-2x_b^2-x_W^2x_b^2+x_b^4\right)-4x_b\,{\rm Re}\;g_{\rm L}g_{\rm R}^*\\
&-2\frac{m_t}{m_W}{\rm Re}\;\left[V_{\rm L}g_{\rm R}^*+V_{\rm R}g_{\rm L}^*\right]\left(1-x_W^2-x_b^2\right)\\
&\left.+2\frac{m_t}{m_W}x_b\,{\rm Re}\;\left[V_{\rm L}g_{\rm L}^*+V_{\rm R}g_{\rm R}^*\right]\left(1+x_W^2-x_b^2\right)\right\}\\
&\pm\frac{g^2}{64\pi}\frac{m_t^3}{m_W^2}\left\{-x_W^2\left[|V_{\rm L}|^2-|V_{\rm R}|^2\right]+\left[|g_{\rm L}|^2-|g_{\rm R}|^2\right]\left(1-x_b^2\right)\right.\\
&+2x_W\,{\rm Re}\;\left[V_{\rm L}g_{\rm R}^*-V_{\rm R}g_{\rm L}^*\right]+2x_Wx_b\,{\rm Re}\;\left[V_{\rm L}g_{\rm L}^*-V_{\rm R}g_{\rm R}^*\right]\}\\
&\times\left(1-2x_W^2-2x_b^2+x_W^4-2x_W^2x_b^2+x_b^4\right)\,,
\end{aligned}\tag{2.77}$$

with $x_W = m_W/m_t$, $x_b = m_b/m_t$ and,

$$|\vec{q}| = \frac{1}{2m_t}(m_t^4+m_W^4+m_b^4-2m_t^2m_W^2-2m_t^2m_b^2-2m_W^2m_b^2)^{1/2}\,,\tag{2.78}$$

being the modulus of the W-boson momentum in the top quark rest frame. This dependence can be seen in Figure 2.10 for the helicity fractions and in Figure 2.11 for the angular asymmetries, considering that only one coupling is different from zero at a time and assuming the CP-conserving case of real $V_{\rm R}$, $g_{\rm R}$ and $g_{\rm L}$. It can be seen that $F_{\rm L}$ and F_0 are more sensitive to $g_{\rm R}$ than to $g_{\rm L}$ and $V_{\rm R}$. This is due to the interference term $V_{\rm L}g_{\rm R}^*$, which is not suppressed by the bottom quark mass, as it happens for the $g_{\rm L}$ and $V_{\rm R}$ couplings. This linear term dominates over the quadratic one and makes $F_{\rm L}$ and F_0 (and related quantities) very sensitive to $g_{\rm R}$. It should also be noticed that the phases of the anomalous couplings influence the helicity fractions through the interference terms, which depend on the real part of $V_{\rm R}$, $g_{\rm L}$ and $g_{\rm R}$. $V_{\rm L}$ was assumed to be real, and normalized to unity. The quadratic terms were kept in the operator coefficients, which is consistent with the $1/\Lambda^2$ expansion of the effective operator framework [82].

In this thesis, the Wtb vertex structure is studied using data collected by the ATLAS experiment at a center-of-mass energy of $\sqrt{s} = 7$ TeV, corresponding to a

total integrated luminosity of 1.04 fb^{-1}. The W boson helicity fractions (F_0, F_L, F_R) and angular asymmetries (A_{FB}, A_+, A_-), are measured in the single lepton and dileptonic decay channels of $t\bar{t}$ events. These results, presented in Chapter 5, are in agreement with NNLO QCD predictions and are more precise than previous results obtained by the CDF and DØ experiments [83–85]. The limits obtained on the Wtb vertex anomalous couplings are consistent with the $(V - A)$ structure of the Wtb vertex and more precise than the previously obtained limits [86].

2.4.4 Flavor Changing Neutral Currents

According to the SM, the Flavor Changing Neutral Currents (FCNC) are absent at tree level and suppressed at one-loop level by the GIM mechanism, with a branching ratio of the order of 10^{-14} [49]. However, several models beyond the SM predict higher branching ratios for the top FCNC decays (shown in Table 2.3), such as quark-singlet model [87–89], the two-Higgs doublet model with (FC 2HDM) or without (2HDM) flavor-conservation [90–95], the minimal supersymmetric model (MSSM) [96–102], SUSY with R-parity violation ($\not{R}$ SUSY) [103], the Topcolor-assisted Technicolor model (TC2) [104] or models with warped extra dimensions (RS) [105,106]. The experimental limits on the branching fractions of the FCNC top quark

Process	SM	QS	2HDM	FC 2HDM	MSSM	$\not{R}$ SUSY	TC2	RS
$t \to u\gamma$	3.7×10^{-16}	7.5×10^{-9}	—	—	2×10^{-6}	1×10^{-6}	—	$\sim 10^{-11}$
$t \to uZ$	8×10^{-17}	1.1×10^{-4}	—	—	2×10^{-6}	3×10^{-5}	—	$\sim 10^{-9}$
$t \to ug$	3.7×10^{-14}	1.5×10^{-7}	—	—	8×10^{-5}	2×10^{-4}	—	$\sim 10^{-11}$
$t \to c\gamma$	4.6×10^{-14}	7.5×10^{-9}	$\sim 10^{-6}$	$\sim 10^{-9}$	2×10^{-6}	1×10^{-6}	$\sim 10^{-6}$	$\sim 10^{-9}$
$t \to cZ$	1×10^{-14}	1.1×10^{-4}	$\sim 10^{-7}$	$\sim 10^{-10}$	2×10^{-6}	3×10^{-5}	$\sim 10^{-4}$	$\sim 10^{-5}$
$t \to cg$	4.6×10^{-12}	1.5×10^{-7}	$\sim 10^{-4}$	$\sim 10^{-8}$	8×10^{-5}	2×10^{-4}	$\sim 10^{-4}$	$\sim 10^{-9}$

Table 2.3: The theoretical values for the branching fractions of FCNC top quark decays predicted by the SM and exotic extensions [107].

decay channels, shown in Table 2.4, have been established at LEP [64, 108–112], HERA [113–116] and Tevatron [117–119] colliders.

	LEP	HERA	Tevatron
BR($t \to q\gamma$)	2.4%	0.64% ($tu\gamma$)	3.2%
BR($t \to qZ$)	7.8%	49% (tuZ)	3.2%
BR($t \to qg$)	17%	13%	2.0×10^{-4} (tug), 3.9×10^{-3} (tcg)

Table 2.4: Several experimental 95% CL upper limits on the branching fractions of the FCNC top quark decay channels.

A search for FCNC decays of top quarks produced in pairs was performed using data collected by the ATLAS experiment at a center-of-mass energy of $\sqrt{s} = 7$ TeV and corresponding to an integrated luminosity of 2.1 fb^{-1}. The search for the $t \to qZ$ decay mode was performed by studying top-quark pair production with one top quark decaying according to the SM and the other according to the FCNC ($t\bar{t} \to bWqZ$). No evidence for such a signal was found. An observed limit at 95% CL on the $t \to qZ$ FCNC top-quark decay branching fraction was set at BR($t \to qZ$) $< 0.73\%$, assuming BR($t \to bW$)+BR($t \to qZ$) $= 1$. This result is compatible with the expected limit, assuming the data are described correctly by the SM, of BR($t \to qZ$) $< 0.93\%$ [10]. A BR($t \to qZ$) larger than 0.24% was excluded at the 95% CL by the CMS experiment [120].

2.4.5 Same-sign Top Quark Production

The search for events with two same charge leptons in hadron colliders is particularly useful, due to the low SM background contributions, to probe new theories such as flavor-changing Z bosons [121], proposed to explain the forward-backward $t\bar{t}$ production asymmetry measured at the Tevatron [122, 123], or new heavy quarks [124, 125]. The CMS and CDF Collaborations searched for fourth-generation down-type quarks with same-sign leptons using 34 pb^{-1} of pp collisions [126] and 2.7 fb^{-1} of $p\bar{p}$ collisions [127], respectively, setting the lower mass limits of 361 GeV and 338 GeV, at 95% CL. The ATLAS and CDF Collaborations searched for fourth-generation down-type quarks in single-lepton events with many jets using 1.1 fb^{-1} of pp collisions [128] and 4.8 fb^{-1} of $p\bar{p}$ collisions [129], respectively. The lower mass limits of 480 GeV and 372 GeV, respectively, were set at 95% CL. The CMS experiment also presented results of a search for same-sign dileptons with b-jets, using 4.98 fb^{-1} of pp collisions at $\sqrt{s} = 7$ TeV. A limit was set at $\sigma(pp \to tt) < 0.61$ pb at 95% CL, and used to set bounds on the parameter space of two models of same-sign top pair production [130].

The ATLAS experiment presented a search for events characterized by two isolated same-sign leptons in association with at least two jets and large $E_{\mathrm{T}}^{\mathrm{miss}}$ [11]. The same-sign top-quark production [131–133] and the pair production of down-type heavy quarks of charge $-1/3$ [134] processes, were considered as signal and the leading order Feynman diagrams are represented in Figures 2.12 and 2.13, respectively. The process shown in Figure 2.12 can be mediated at the tree level by the exchange of a s-channel resonance (left), or a t-channel resonance (right). In the case of new vector bosons exchanged in the s-channel, the new particle must be a colour-triplet or colour-sextet with charge 4/3, while for t-channel exchange it can be a colour-singlet or color-octet, both with zero charge. For resonance masses

much larger than the electroweak symmetry breaking scale, all these cases can be described by a gauge-invariant effective four-fermion interaction (middle). For the heavy quark search, a specific model was used, in which the heavy quark is fourth-generation chiral quark, represented by b', as shown in Figure 2.13.

The observed data was found to be consistent with SM expectations. Upper limits were set at 95% CL on the cross section of new sources of same-sign top-quark pair production via a heavy mediator at 1.7 pb for each chirality and, for light Z' mediators, limits were established from 1.4 to 2.0 pb depending on the Z' mass. These limits were also interpreted as constraints on coefficients of effective operators which mediate $uu \to tt$ [135, 136]. In addition, a lower limit of 450 GeV was set at 95% CL on the mass of fourth-generation down-type quarks. Recently, the ATLAS experiment also presented a search for pair production of down-type heavy quarks (b'), single and pair production of heavy top quark partners ($T_{5/3}$), and production of events containing four top quarks ($t\bar{t}t\bar{t}$) using 4.98 fb^{-1} of pp collisions at $\sqrt{s} = 7$ TeV [137]. The corresponding lower limit on both the b' and $T_{5/3}$ mass is 0.67 TeV at 95% CL, when produced in pairs. When including the single production mechanism, limits on $T_{5/3}$ production are 0.68 TeV and 0.70 TeV for a coupling constant of the $tWT_{5/3}$ vertex equal to 1 and 3, respectively. The upper limit on the four top quarks production cross section is 61 fb at 95% CL.

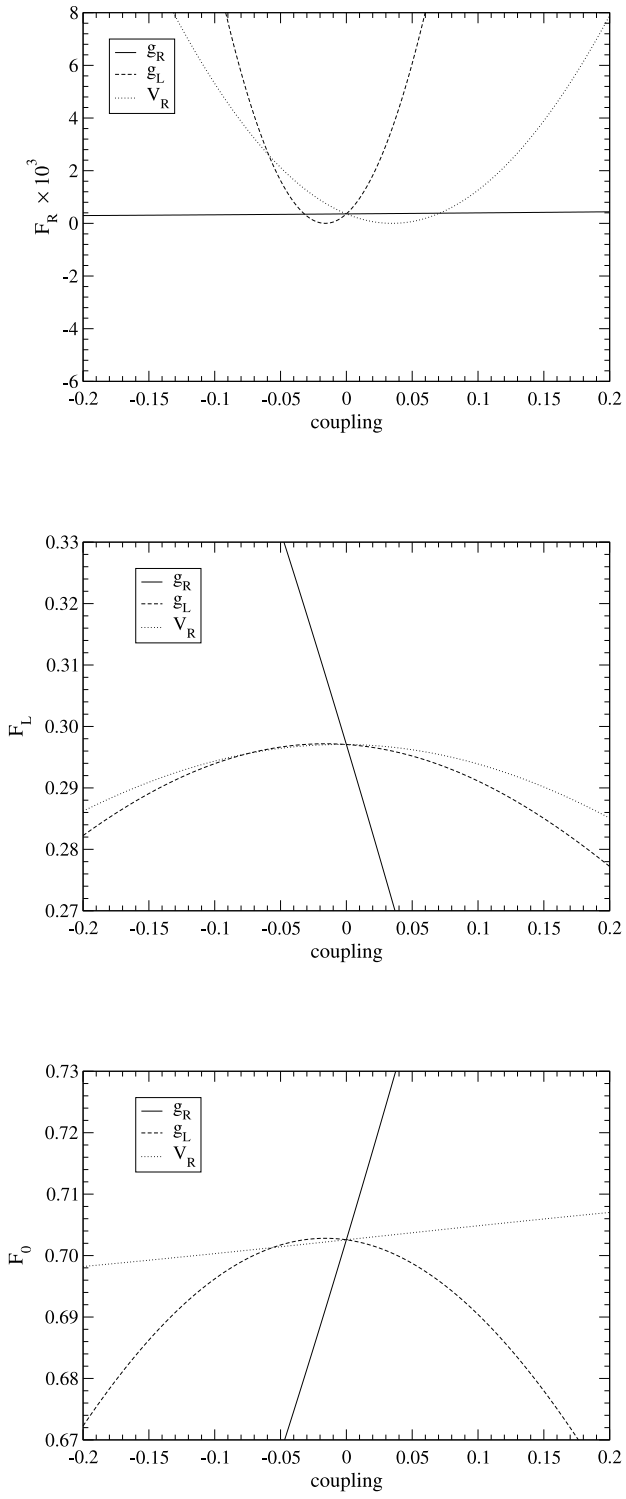

Figure 2.10: Dependence of the helicity fractions $F_{\rm i} = \Gamma_i/\Gamma$ on the anomalous couplings (see equation (2.75)), in the CP-conserving case.

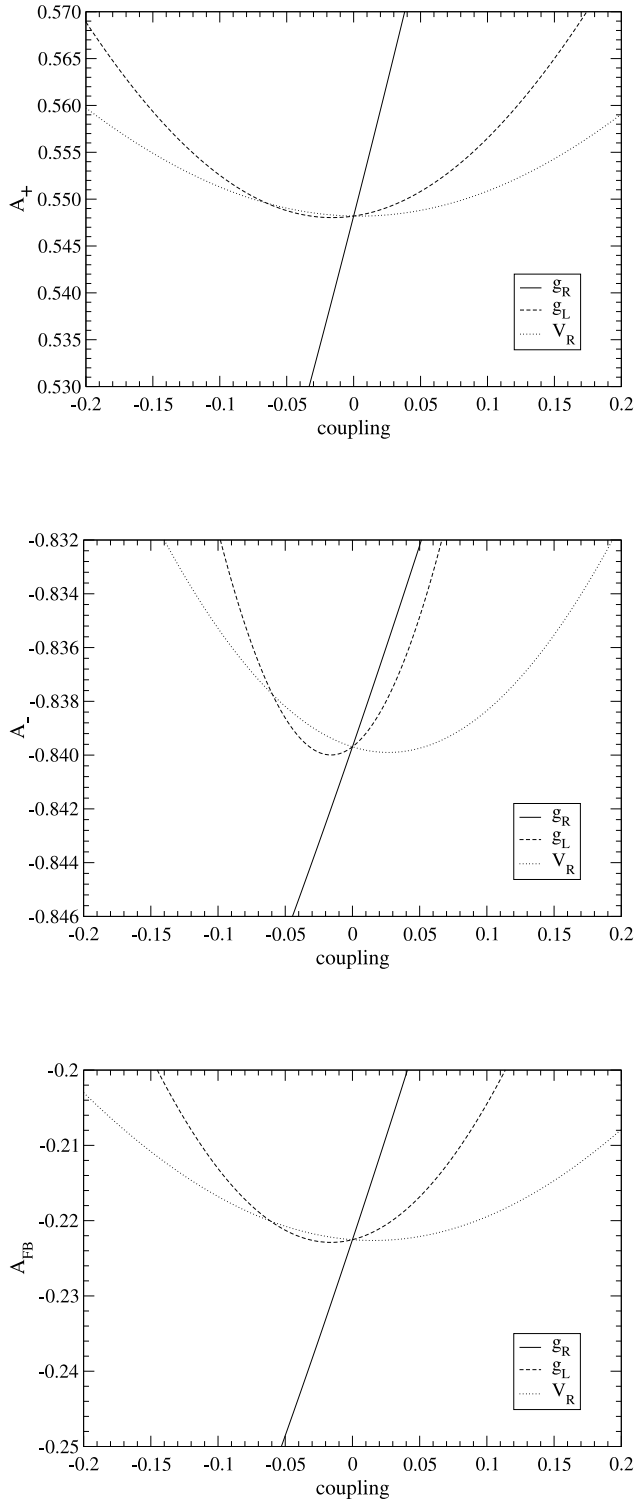

Figure 2.11: Dependence of the angular asymmetries A_{FB}, A_+ and A_- on the couplings g_{L}, g_{L} and V_{R}, for the CP-conserving case.

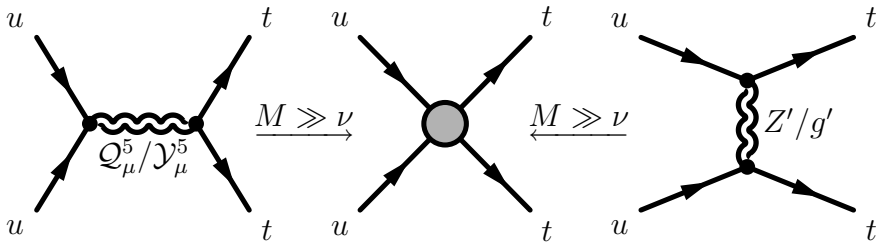

Figure 2.12: Production of same-sign top-quark pairs via the production of a heavy vector boson (such as color-triplet $\mathcal{Q}_\mu^5$ or color-sextet $\mathcal{Y}_\mu^5$) in the s-channel (left) or exchange of a heavy vector boson (such as Z' or g') in the t-channel (right). For large resonance masses, both cases can be described by a four-fermion interaction (middle).

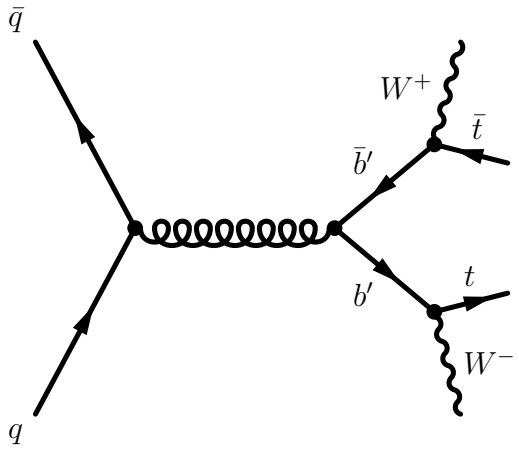

Figure 2.13: Pair production and decay of fourth generation heavy quarks.

Chapter 3

Experimental Apparatus

In this chapter, the CERN laboratory, the Large Hadron Collider, and the ATLAS detector are presented. The ATLAS subdetectors, trigger and data acquisition system are briefly described as well.

3.1 CERN

The European Organization for Nuclear Research (CERN) is the world largest particle physics research laboratory, covering six square kilometers scattered over twelve sites on the Franco-Swiss border, near Geneva. Established in 1954, CERN has currently twenty member-states and hosts about 10,000 visiting scientists and engineers working together in international collaborations, representing 608 academic institutions and 113 nationalities. The organization hosts facilities for experimental particle physics, such as the 34 kilometers of particle accelerators installed 100 meters underground, particle detectors placed in caverns of the size of cathedrals, and other infrastructures needed for high-energy physics research.

Several important particle physics advances have been achieved in experiments at CERN, such as the discovery of neutral currents in the Gargamelle bubble chamber [138], the discovery of $W^{\pm}$ and Z bosons in the UA1 and UA2 experiments [34, 35], the determination of the number of light neutrino families at the Large Electron-Positron Collider [50], the first creation of antihydrogen atoms in the PS210 experiment [139], the discovery of direct CP violation in the NA48 experiment [140], the isolation of 38 atoms of anti-hydrogen [141], and maintaining anti-hydrogen for over 15 minutes [142]. In addition to these scientific discoveries, several technological advances took place at CERN, such as the creation of the World Wide Web by Sir Tim Berners-Lee, and more recently, the computer network infrastructure Worldwide LHC Computing Grid.

3.2 Large Hadron Collider

The Large Hadron Collider (LHC) [143], located at CERN, is the largest and highest-energy particle accelerator of the world, with the goal of testing the predictions of several different theories of particle physics, in particular, if the recently observed signal in the 124-126 GeV mass region corresponds to the hypothesized SM Higgs boson or to any other mechanism of electroweak spontaneous symmetry breaking. The high luminosity and increased cross-sections at the LHC enable further high precision tests of QCD, electroweak interactions, and flavor physics. In addition, new heavy gauge bosons W' and Z' could be accessible for masses up to ~ 6 TeV, and the searches for flavor changing neutral currents and lepton flavor violation processes may also open a window into new physics. The decays of supersymmetric particles, such as squarks and gluinos, would involve cascades which, if R-parity is conserved, always contain a lightest stable supersymmetric particle (LSP). As the LSP would interact very weakly with the detector, the experiments would measure a significant $E_{\mathrm{T}}^{\mathrm{miss}}$ in the final state. Finally, several new models propose the existence of extra dimensions leading to a characteristic energy scale of quantum gravity in the TeV region.

The LHC lies in a 27 kilometers circular tunnel, at a depth ranging from 50 to 175 meters underground, built for the previous collider, the Large Electron-Positron Collider (LEP). The LHC started operations in September 2008, when the first proton beams successfully circulated in the main ring. The first collisions at 3.5 TeV per beam took place on 30 March 2010, and set a new world record for the highest-energy man-made particle collisions. The LHC proceeded with its physics program at $\sqrt{s} = 7$ TeV for the rest of 2010 and 2011, and is currently operating at 4 TeV per beam until the beginning of 2013. A shutdown is planned for the beginning of 2013 to upgrade the accelerator to its design center-of-mass energy, $\sqrt{s} = 14$ TeV, and resume operations in late 2014.

The LHC contains two parallel beam pipes that intersect at four points, each containing a proton beam traveling in opposite directions around the ring. Each of the four collision points, depicted in Figure 3.1, corresponds to one of the main LHC experiments: ATLAS (A Toroidal LHC ApparatuS), CMS (Compact Muon Solenoid), ALICE (A Large Ion Collider Experiment) and LHCb. The LHC comprises 1232 dipole magnets, each 14.3 meters long, to bend the beams around the circular path, while an additional 392 quadrupole magnets are used to keep the beams focused. These type-II superconducting magnets, made of copper-clad niobium-titanium (NbTi), operate at an average temperature of 1.9 K, kept by approximately 96 tones of superfluid liquid helium He-II. A transverse view of the pipe is shown in Figure 3.2, where the two pipes of the beam can be seen as well

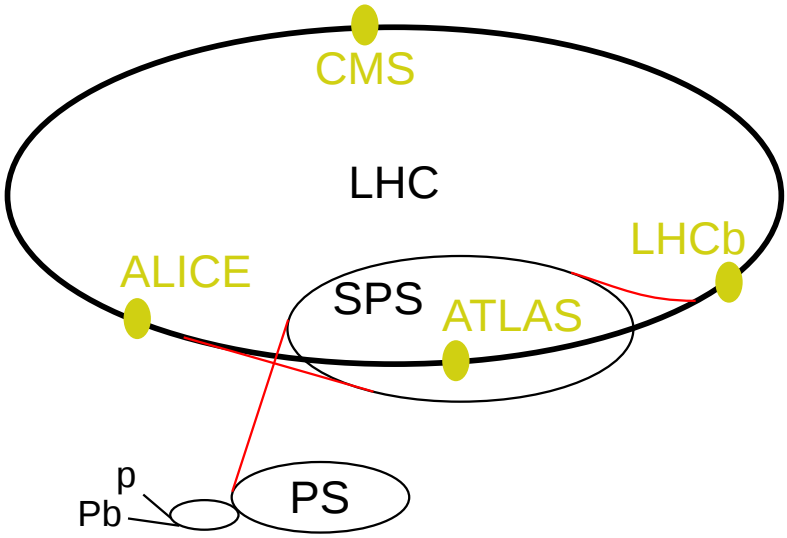

Figure 3.1: Scheme of the LHC experiments and the preaccelerators.

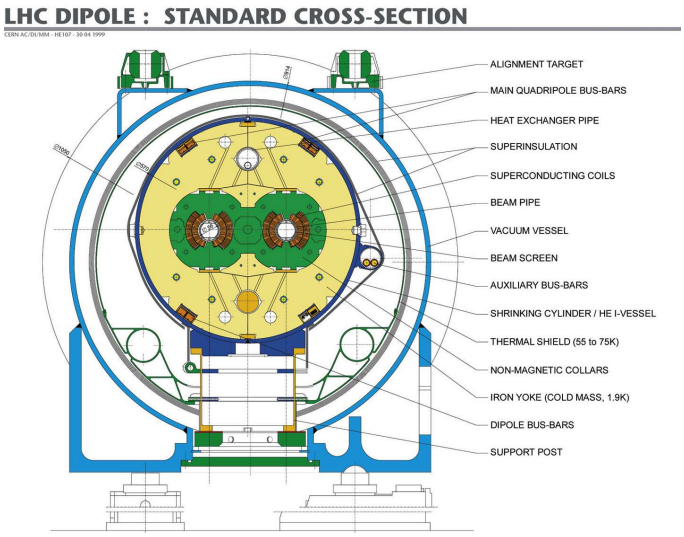

Figure 3.2: Diagram showing the cross-section of an LHC dipole magnet with cold mass and vacuum chamber.

as the superconducting coils around. At the design energy of 7 TeV per beam, the superconducting dipole magnets shall produce a magnetic field of 8.3 T with electric currents of 11700 A. Furthermore, the LHC is conceived to support proton beams composed by 2808 bunches, 25 nanoseconds apart, providing a collision rate of 40 MHz and a design luminosity of 10^{34} cm^{-2}s^{-1}.

3.3 ATLAS Detector

The ATLAS detector [144], shown in Figure 3.3, is a general-purpose detector, made of cylindrical layers around the beam pipe and two end-caps, in order to cover the maximum possible solid angle around the interaction point. The nature of proton-proton collisions imposes several experimental difficulties to the identification of interesting physics signatures. Some of these difficulties come, for example, from the presence of several piled-up events in every candidate event (pile-up), or the domination of QCD jet production cross-sections over rare physics processes, which requires the identification of experimental signatures characteristic of the physics processes in question, such as $E_{\mathrm{T}}^{\mathrm{miss}}$ or secondary vertices. In order to overcome such difficulties, the ATLAS detector was projected with the following requirements:

- Due to the experimental conditions at the LHC, the detectors require fast, radiation-hard electronics and sensor elements. In addition, high detector granularity is needed to handle the particle fluxes and to reduce the influence of overlapping events.

- Large acceptance in pseudorapidity[1] with almost full azimuthal angle coverage is required.

- Good charged-particle momentum resolution and reconstruction efficiency in the inner tracker are essential. For offline tagging of τ-leptons and b-jets, vertex detectors close to the interaction region are required to observe secondary vertices.

- Very good electromagnetic (EM) calorimetry for electron and photon identification and measurements, complemented by full-coverage hadronic calorimetry for accurate jet and missing transverse energy measurements, are important requirements, as these measurements form the basis of many of the studies mentioned above.

- Good muon identification and momentum resolution over a wide range of momenta and the ability to determine unambiguously the charge of high p_{T} muons are fundamental requirements.

- Highly efficient triggering on low transverse-momentum objects with sufficient background rejection, is a prerequisite to achieve an acceptable trigger rate for most physics processes of interest.

[1] The pseudorapidity is defined as $\eta = -\ln[\tan(\theta/2)]$, and the distance ΔR in the pseudorapidity-azimuthal angle space is defined as $\Delta R = \sqrt{\Delta\phi^2 + \Delta\eta^2}$. The ATLAS coordinate system is represented in Figure 3.4.

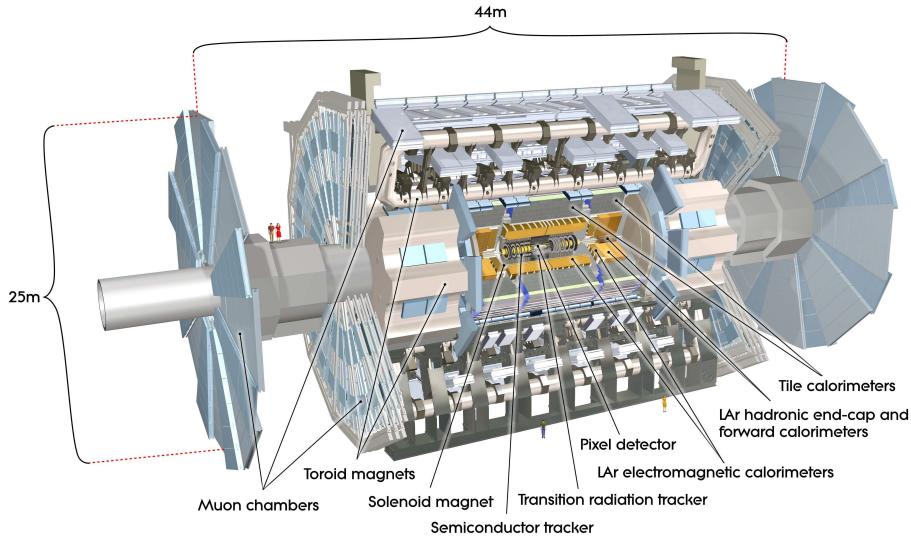

Figure 3.3: Scheme of the ATLAS detector. The different subdetectors and magnets are shown.

The detector is 44 metres long, 25 metres in diameter, weights about 7000 tones, and is composed by several layers, each with a specific purpose on the reconstruction of particles. The four main components are the Inner Detector, the calorimeters, the muon spectrometer and the magnetic systems. The Inner Detector is located near the beam pipe with the purpose of recording the first hits of charged particles that interact with the detector material. In addition, the solenoid around the Inner Detector creates a 2 T magnetic field, with the aim of curving very energetic particles in order to measure their momentum. The hadronic and electromagnetic calorimeters are in the layer surrounding the Inner Detector, both with the basic function of measuring the particles energies. The electromagnetic calorimeter was designed to measure the energy of charged particles and photons through the electromagnetic interaction, while the hadronic calorimeter measures the energy of hadrons that interact via the strong interaction. Finally, the muon spectrometer starts at a radius of 4.25 m around the calorimeters and extends to the end of the detector, at a radius of 11 m. The toroid magnets generate the magnetic field for the muon spectrometer, and allow the determination of the muons momenta from the deflection of their trajectories. All these components are described with more detail in the following subsections, and the general performance goals for the ATLAS detector are summarized in Table 3.1.

Since the start of operations, the ATLAS detector has recorded more than 26 fb^{-1} of data and each subsystem has been operating above 95% efficiency. In Figure 3.5, the cumulative luminosity versus day delivered to (green), and recorded by ATLAS

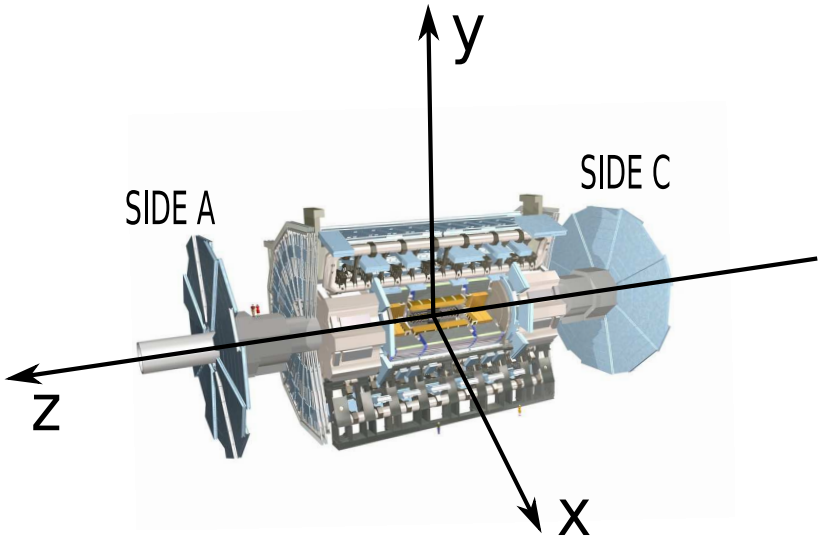

Figure 3.4: ATLAS coordinate system: the positive x-axis is defined as pointing from the interaction point to the centre of the LHC ring and the positive y-axis is defined as pointing upwards. The side-A of the detector is defined as that with positive z and side-C is that with negative z. The azimuthal angle ϕ is measured around the beam axis (with $\phi = 0$ corresponding to the x-axis), and the polar angle θ is the angle from the beam axis.

(yellow) during stable beams and for pp collisions are shown at 7 TeV center-of-mass energy in 2011 (left) and at 8 TeV center-of-mass energy in 2012 (right). The mean number of interactions per crossing for the 2011 and 2012 data is presented in Figure 3.6, and the example of a $Z \to \mu\mu$ event candidate is shown in Figure 3.7 in a high pileup environment, with 25 reconstructed vertices, where the two leptons are highlighted in yellow.

3.3.1 Inner Detector

The Inner Detector [145–147], shown in Figure 3.8, is dedicated to the tracking and identification of charged particles, and is the closest layer to the beam pipe, positioned only a few centimeters away from it. With an acceptance in pseudorapidity of $|\eta| < 2.5$, and full coverage in ϕ, the detector provides a transverse momentum resolution, in the plane perpendicular to the beam axis, of $\sigma_{p_{\mathrm{T}}}/p_{\mathrm{T}} = 0.05\% p_{\mathrm{T}}/\mathrm{GeV} \oplus 1\%$ and a transverse impact parameter resolution of 10 μm for high momentum particles in the central η region. The Inner Detector comprises three complementary sub-detectors: the Pixel Detector, the Semiconductor Tracker (SCT) and the Transition Radiation Tracker (TRT). The Pixel Detector is the innermost part of detector and consists of 3 cylindrical layers composed by pixel sensors and microstrips. Due

Component	Resolution	η	*Trigger* (η)
ID	$\frac{\sigma_{p_T}}{p_T} = 0.05\% p_T \oplus 1\%$	± 2.5	
EM Cal.	$\frac{\sigma_E}{E} = 10\%/\sqrt{E} \oplus 0.7\%$	± 3.2	± 2.5
Hadronic Cal.			
barrel and end-cap	$\frac{\sigma_E}{E} = 50\%/\sqrt{E} \oplus 3\%$	± 3.2	± 3.2
forward	$\frac{\sigma_E}{E} = 100\%/\sqrt{E} \oplus 10\%$	$3.1 < \lvert\eta\rvert < 4.9$	$3.1 < \lvert\eta\rvert < 4.9$
Muon detection	$\frac{\sigma_{p_T}}{p_T} = 10\%$ at p_T=1 TeV	± 2.7	± 2.4

Table 3.1: General performance goals of the ATLAS detector. For high-p_T muons, the muon spectrometer performance is independent of the inner-detector system. The unit for E and p_T is GeV.

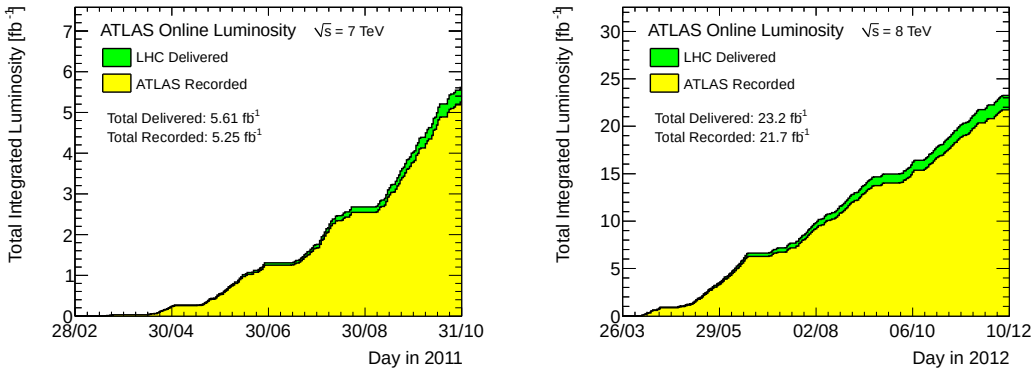

Figure 3.5: Cumulative luminosity versus day delivered to (green), and recorded by ATLAS (yellow) during stable beams and for pp collisions are shown at 7 TeV center-of-mass energy in 2011 (left) and at 8 TeV center-of-mass energy in 2012 (right).

to its location, the Pixel Detector must be very resistant to radiation. The detector consists of 1744 silicon pixel modules arranged in three concentric barrel layers and two endcaps of three disks each. It provides typically three measurement points for particles originating in the beam-interaction region. The Semiconductor Tracker is very similar to the Pixel Detector but tracks particles over a much larger area, therefore, it is useful for tracking in the plane perpendicular to the beam. The detector consists of 4088 modules of silicon-strip detectors arranged in four concentric barrels and two endcaps of nine disks each. It provides typically eight strip measurements (four space-points) for particles originating in the beam-interaction region. The Transition Radiation Tracker is a combination of a straw tracker formed by many small straws and a transition radiation detector providing about 36 points per track. The TRT also identifies electrons by the detection of transition-radiation photons in the xenon gas mixture of the straw tubes. The combination of the two techniques

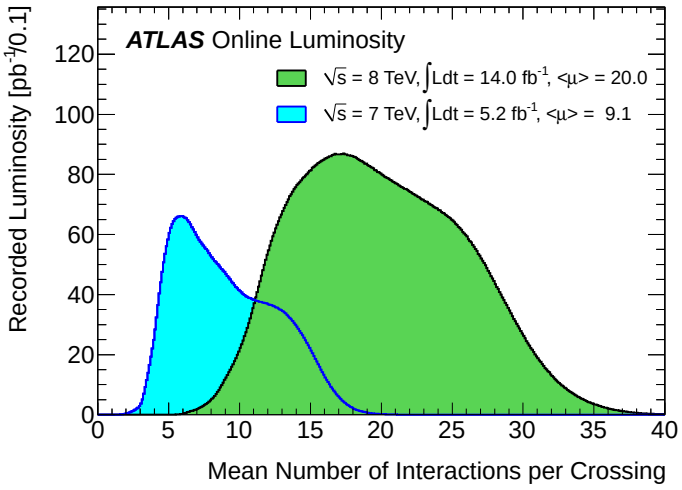

Figure 3.6: The luminosity-weighted distribution of the mean number of interactions per crossing is shown for the 2011 and 2012 data. This shows the full 2011 run and 2012 data taken between April 4th and September 17th. The integrated luminosities and the mean μ values are given in the figure.

provides a very robust pattern recognition and high precision in the azimuthal angle, ϕ, and in the z coordinate. The detector consists of 298 304 proportional drift tubes (straws), 4 mm in diameter, read out by 350 848 channels of electronics.

3.3.2 Calorimetry

There are two calorimeters in the ATLAS detector, the electromagnetic [148–150] and the hadronic [2, 148, 151], covering the regions $|\eta| < 3.2$ and $|\eta| < 4.9$, respectively. While the electromagnetic calorimeter was designed to identify and measure the energy of the particles that interact through the electromagnetic force, the hadronic calorimeter absorbs the energy of particles that interact through the strong force, after crossing the electromagnetic calorimeter, *i.e.* the particle shower resulting from the hadronization of the quarks, also known as jet. Calorimeters have a primary role in a general-purpose hadron collider detector, and the ATLAS calorimeter system provides accurate energy and position measurements of electrons, photons, isolated hadrons, taus and jets. The ATLAS calorimeter system can be seen in Figure 3.9.

The electromagnetic calorimeter (LAr), is a lead/liquid-argon sampling detector housed in one barrel and two end-cap cryostats, with accordion geometry that provides full azimuthal symmetry. The electromagnetic calorimeter contains a barrel part (EMB), and a end-cap part (EMEC), covering the regions $|\eta| < 1.475$ and

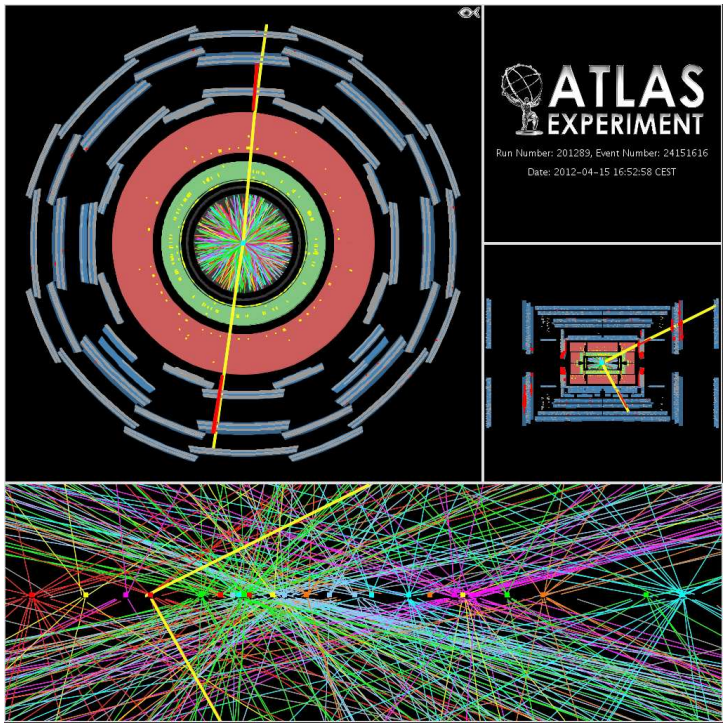

Figure 3.7: A candidate Z boson event in the dimuon decay with 25 reconstructed vertices. This event was recorded on April 15th 2012 and demonstrates the high pileup environment in 2012 running. For this display the track p_{T} threshold is 0.4 GeV and all tracks are required to have at least 3 Pixel and 6 SCT hits.

$1.375 < |\eta| < 3.2$, respectively. In addition, for $|\eta| < 1.8$, a pre-sampler consisting of an active LAr layer and installed directly in front of the EM calorimeters, recovers information of the energy lost along the way to the calorimeter. The copper-liquid argon hadronic endcap calorimeter (HEC) covers the region $1.5 < |\eta| < 3.2$, and a copper/tungsten-liquid argon forward calorimeter (FCal) covers the region closest to the beam $3.1 < |\eta| < 4.9$. All the LAr detectors are segmented transversally and divided in three or four layers in depth, comprising a total of 182 468 readout cells.

The hadronic calorimeter (TileCal) is a sampling calorimeter using plastic scintillator as the active material and lowcarbon steel (iron) as the absorber. The TileCal contains a Long-Barrel (divided in LBA and LBC) and two Extended-Barrels (EBA and EBC), each of cylindrical shape, built of 64 independent wegdes (modules) along the azimuthal direction. The Long-Barrel covers the $|\eta| < 1.0$ region while the Extended-Barrel covers the $0.8 < |\eta| < 1.7$ region. The four partitions are arranged along the beam axis from negative to positive as follows: EBC, LBC, LBA and EBA. TileCal is also divided along the radial direction in 3 sampling layers (A, BC and D). The light produced by particles when crossing the TileCal *tiles* is read out from

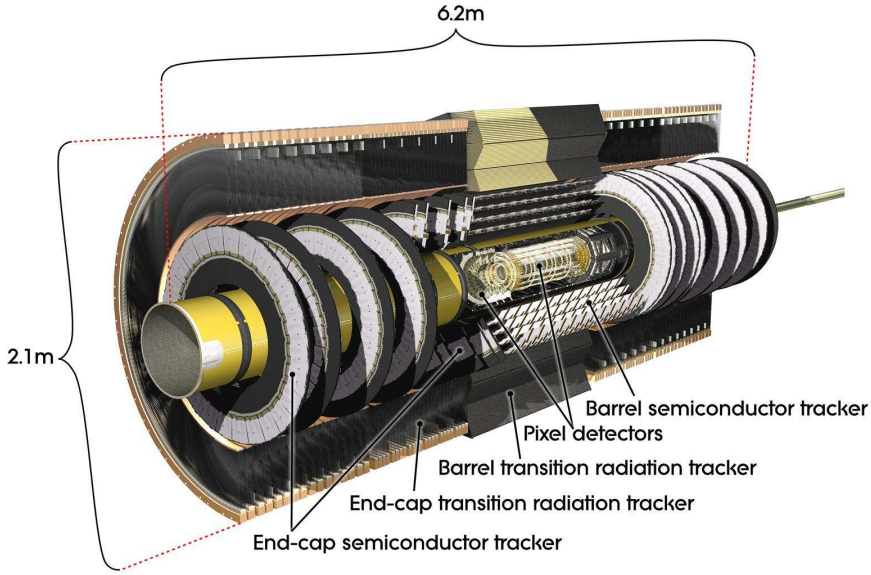

Figure 3.8: Cut-away image of the ATLAS Inner Detector.

two sides by wavelength shifting (WLS) fibers which are bundled together in groups to form readout cells with three different sampling depths. The fibres coupled to each edge of the scintillating tiles are read out by two separate channels to provide redundancy. With a total of 5184 read out cells, comprising 9856 channels, a typical granularity of $\Delta\eta \times \Delta\phi = 0.1 \times 0.1$ (0.1×0.2 for the last layer) is achieved, which allows good jet energy and missing transverse energy resolutions. A more detailed description of TileCal can be found in the section 4.

3.3.3 Muon Spectrometer

The ATLAS Muon Spectrometer [152,153] is designed to provide a standalone measurement of the muon momentum with an uncertainty in the transverse momentum varying from 3% at 100 GeV to about 10% at 1 TeV, and to provide a trigger for muons with varying transverse momentum thresholds down to a few GeV. The Muon Spectrometer is based on the magnetic deflection of muon tracks and extends from a radius of 4.25 m around the calorimeters to the outer radius of the detector. Despite the different magnetic field configuration and lower spatial precision, the muon spectrometer works under the same base of the Inner Detector, with muons curving in the magnetic field, allowing the measurement of their momentum. As the muon trajectory is always normal to the main component of the magnetic field, the transverse momentum resolution is roughly independent of η over the whole acceptance.

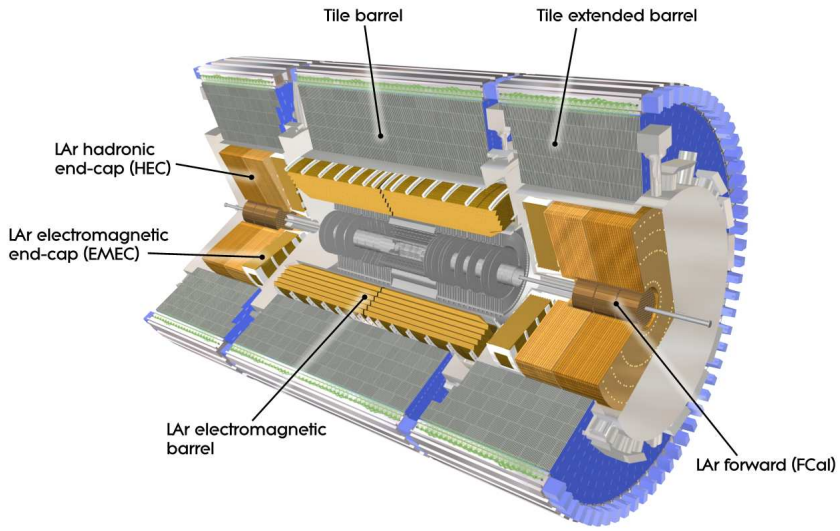

Figure 3.9: Cut-away view of the ATLAS calorimeter system.

The magnetic field is provided by three toroids, one in the "barrel" ($|\eta| < 1.1$) and one for each "end-cap" ($1.1 < |\eta| < 2.7$), and the muon curvature is measured by means of four different tracking detector technologies. For most of the acceptance Monitored Drift Tube (MDT) chambers are used, composed of two MultiLayers (ML) made of three or four layers of tubes. In the end-cap inner region, for $|\eta| < 2.0$, Cathode Strip Chambers (CSC) are used because of their capability to cope with higher background rates. Finally, Resistive Plate Chambers (RPC) and Thin Gap Chambers (TGC) provide fast trigger signals in the barrel and endcap regions. The ATLAS Muon Spectrometer components are shown in Figure 3.10.

3.3.4 Magnet System

The ATLAS magnetic system [154] has 22 metres in diameter and is 26 metres long with an overall stored energy of 1.6 GJ. This magnet system is formed by four superconducting magnets, the inner solenoid which provides a 2 T magnetic field parallel to the beam pipe for the Inner Detector, the barrel toroid and the two end-cap toroids that create a toroidal magnetic field between 0.5 T and 1 T for the muon spectrometer.

The solenoid has an inner radius of 2.46 m, an outer radius of 2.63 m and is 5.29 m long, with a stored energy of 39 MJ. The uniformity and strength of the magnetic field produced by this solenoid allows measurements to be made very precisely. Due to the strength of the magnetic field, the detector system is not able to measure the momentum of low energy particles (hundreds of MeV). The barrel toroid is formed

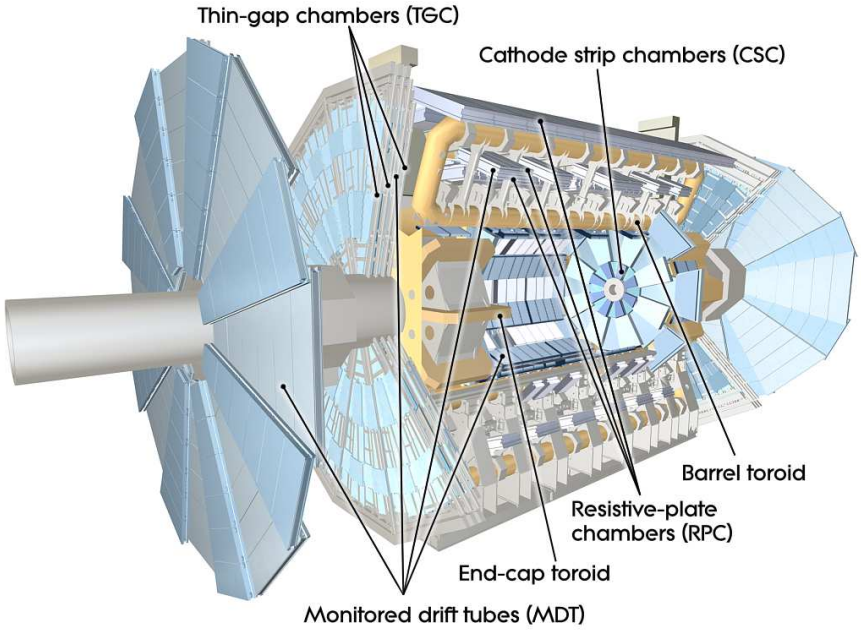

Figure 3.10: Overview of the ATLAS muon spectrometer components.

by eight air-core superconducting coils, shown in Figure 3.11, installed in a length of 25.3 m with an inner radius of 9.4 m and an outer radius of 20.1 m, involving the calorimeters. The two-end cap toroids weight 240 tones, and are necessary to increase the magnetic field in the end cap region. The end-cap toroids are subject to a Lorentz force of 280 tones pushing them into the barrel toroid and, unlike the solenoid, the barrel toroid and the two end-caps do not produce an uniform magnetic field in the Muon Spectrometer.

3.3.5 Trigger and Data Acquisition System

The ATLAS trigger system [155, 156] is composed by three distinct levels: L1, L2, and the event filter, to deal with the huge amount of data produced by the LHC ($\approx$ 1 Petabyte/second of raw data). The trigger system identifies, in real time, the most interesting events, and each trigger level refines the decisions made at the previous level and, where necessary, applies additional selection criteria. The first level uses a limited amount of the total detector information to make a decision in less than 2.5 ms, reducing the rate to about 75 kHz. The two higher levels access more detector information for a final rate of up to 200 Hz with an event size of approximately 1.3 Mbyte.

The L1 trigger searches for high transverse-momentum muons, electrons, photons, jets, and τ-leptons decaying into hadrons, as well as large missing and total

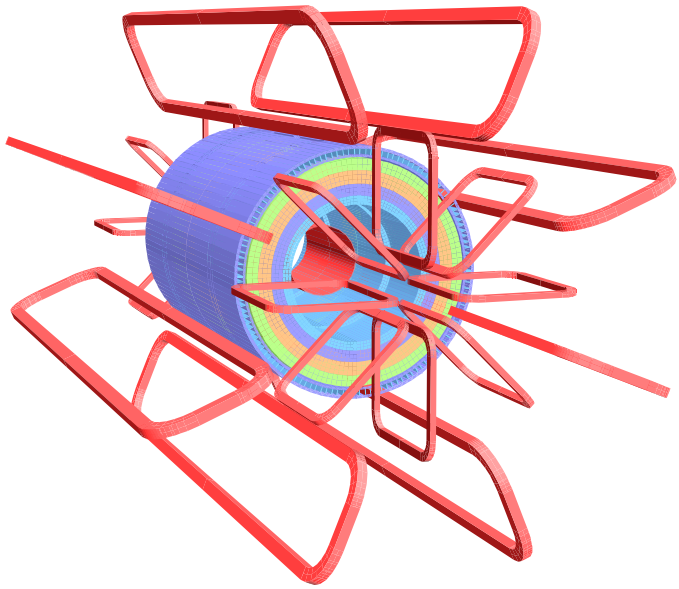

Figure 3.11: Geometry of the magnet system. The eight barrel toroid coils, with the end-cap coils interleaved are visible. The solenoid winding lies inside the calorimeter volume. The tile calorimeter is modelled by four layers with different magnetic properties, plus an outside return yoke.

transverse energy. Its selection is based on information from a subset of detectors. High transverse-momentum muons are identified using trigger chambers in the barrel and end-cap regions of the spectrometer, and calorimeter selections are based on reduced-granularity information from all the calorimeters. Events passing the L1 trigger selection are transferred to the next stages of the detector-specific electronics and subsequently to the data acquisition. The L1 trigger also uses Regions of Interest (RoI). The RoI's are regions in η and ϕ within the detector, where its selection process has identified interesting features, and also contains information of the criteria passed.

The L2 selection is seeded by the RoI information provided by the L1 trigger over a dedicated data path and uses, at full granularity and precision, all the available detector data within the RoI's (approximately 2% of the total event data). The L2 selection is designed to reduce the trigger rate to approximately 3.5 kHz, with an event processing time of about 40 ms, averaged over all events. Finally, the final stage of the event selection is carried out by the event filter, which reduces the event rate to roughly 200 Hz. Its selections are implemented using offline analysis procedures within an average event processing time of the order of four seconds.

The data acquisition system receives and buffers the event data at the L1 trigger accept rate moving the data within the RoI's to the L2 trigger. The events selected

by the L2 trigger are moved to the Event Filter and those that fulfill this last selection criteria are finally stored in the permanent event storage. The ATLAS trigger and data acquisition system scheme is presented in Figure 3.12.

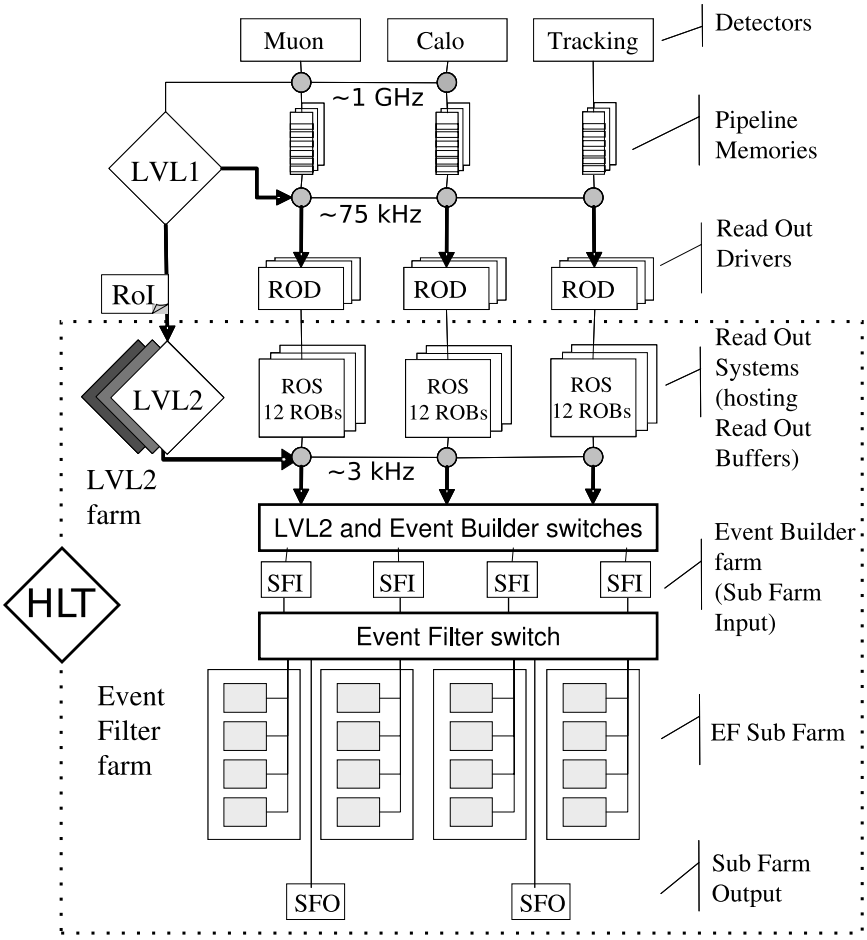

Figure 3.12: ATLAS trigger and data acquisition systems.

3.4 Worldwide LHC Computing Grid

The LHC Computing Grid is a distribution network, connecting 140 computing centers in 35 countries, and designed to analyze the 15 Petabytes of data annually produced at the LHC [157, 158].

The data from the LHC experiments is distributed around the globe, according to a four-tiered model. The CERN computer center, considered Tier-0 of the LHC Computing Grid, where a primary backup is recorded on tape, has a dedicated 10 Gb/s connection to the counting room. This data is distributed to eleven large computer centers with sufficient storage capacity, the Tier-1 centers in Europe, Asia,

and North America, via dedicated 10 Gb/s links. Subsequently, the Tier-1 centers make data available to more than 150 Tier-2 centers, each consisting of one or several collaborating computing facilities, which can store sufficient data and provide adequate computing power for specific analysis tasks. Individual scientists can access these facilities through Tier-3 computing resources, which consist of local clusters.

The infrastructure chain, which allowed the analysis of data presented in this thesis, involved the central production at CERN (Tier-0), the processing of LHC data at the PIC (Barcelona) Tier-1, and local facilities in Coimbra and Lisbon together with a local ATLAS computer farm [159–163].

Chapter 4

Correlated Noise Unfolding on TileCal

The correlated noise component of TileCal, the barrel hadronic calorimeter of the ATLAS experiment at the Large Hadron Collider, is studied and an algorithm is used to parameterize and unfold it from the response of the photomultipliers. It is shown that the correlated noise component can be significantly reduced and mostly removed not only for pedestal runs, but also in the presence of physics signals like minimum bias events in 900 GeV collisions and 7 TeV simulated top quark pair production events.

4.1 Introduction

The ATLAS hadronic calorimeter (TileCal) [2, 148, 151] is composed of iron as the absorber and scintillating tiles as the active material. The absorber structure is a laminate of steel plates of various dimensions, connected to a massive structural element referred to as a girder [151]. As discussed in section 3.3.2, the Tile Calorimeter is designed as one barrel and two extended barrels, each of cylindrical shape, built of 64 independent wegdes (modules) along the azimuthal direction, shown in Figure 4.1. The Long-Barrel (LBA and LBC) covers the $|\eta| < 1.0$ region while the Extended-Barrels cover (EBA and EBC) the $0.8 < |\eta| < 1.7$ region. The four partitions are arranged along the beam axis from negative to positive as follows: EBC, LBC, LBA and EBA. TileCal is also divided along the radial direction in 3 sampling layers (A, BC and D).

The light produced by particles when crossing the TileCal *tiles* is read out from two sides by wavelength shifting (WLS) fibers which are bundled together in groups to form readout cells with three different sampling depths. The fibres coupled to each edge of the scintillating tiles are read out by two separate channels to provide

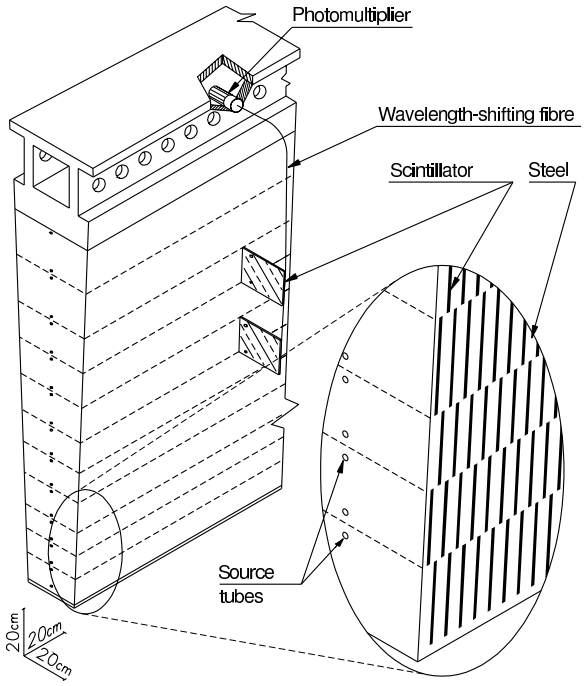

Figure 4.1: Mechanical structure of a TileCal module, showing the slots in the iron for scintillating tiles and the method of light collection by WLS fibers to PMTs. The holes for radioactive source tubes that traverse the module parallel to the colliding beams are also shown.

redundancy. With a total of 5184 read out cells, comprising 9856 channels, a typical granularity of $\Delta\eta \times \Delta\phi = 0.1 \times 0.1$ (0.1×0.2 for the last layer) is achieved, which allows good jet energy and missing transverse energy resolutions. The TileCal cell structure is shown in Figure 4.2.

The channels reading out a wedge are grouped in assemblies (drawers) of 48 readout units hosted inside the girder at the outer radius of the calorimeter. The signal pulse produced by each photomultiplier is shaped, amplified with two gain factors (low gain and high gain), whose nominal ratio is 1:64, by fast and low-noise front-end electronics. The amplified signals are sampled and digitized at 40 MHz by two 10-bit Analog to Digital Converters. During this process undesirable signal interference effects might occur as it has been reported in a previous study [164]. This results in a correlated noise pattern between different channels which may have a negative impact on the TileCal performance. Finally, digitized samples - high-gain or low-gain depending on the signal amplitude, are sent via optical links to off-detector back-end electronics. The correlated noise seems to manifest itself in regions of 6 or 12 channels, which is the extent of the digitizers and motherboards cards, respectively. There are "sensitive" areas in the drawer front-end (FE) assem-

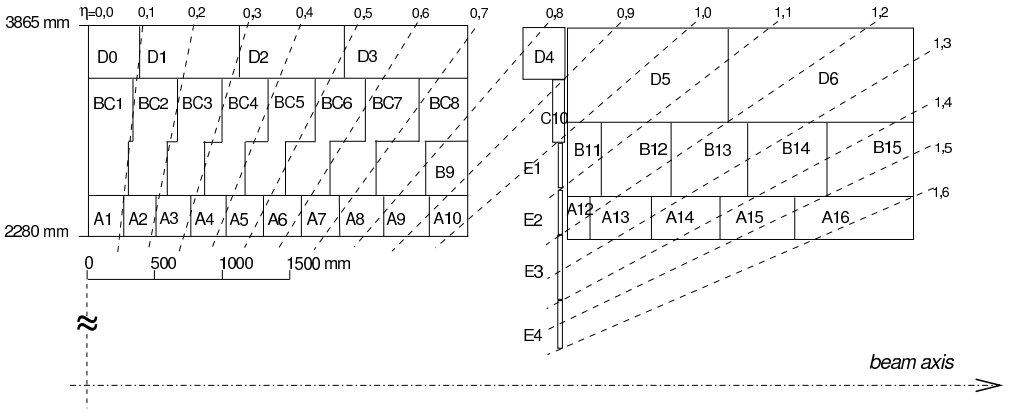

Figure 4.2: Segmentation in depth and η of the Tile Calorimeter modules in the barrel (left) and extended barrel (right). The bottom of the picture corresponds to the inner radius of the cylinder. The Tile Calorimeter is symmetric with respect to the interaction point. The cells between two consecutive dashed lines form the first level trigger calorimeter tower.

bly where the electromagnetic interference between the Low Voltage Power Supply (LVPS) and FE is pronounced, i.e. the area close to the LVPS (channels > 42) and the border between the two sub-assemblies (channels around 24). This effect is enhanced by the fact that switching DC-DC converters are used as LVPS.

The channel signal properties - pulse amplitude, time and pedestal - for all TileCal channels are reconstructed with the Optimal Filtering (OF) method [165], which makes use of weighted linear combinations of the digitized signal samples (spaced by 25 ns). The energy (given by the amplitude A) and time (τ) are computed using the following equations:

$$A = \sum_{i=1}^{n=7} w_i S_i \qquad \tau = \frac{1}{A} \sum_{i=1}^{n=7} b_i S_i, \tag{4.1}$$

where S_i is the sample taken at time $t_i\,(i = 1, ..., n)$. The coefficients of these combinations, w_i and b_i, known as the OF weights, are obtained from the knowledge of the pulse shape and noise autocorrelation matrix, and are chosen in such a way that the impact of the noise to the calorimeter resolution is minimized. The pulse shape, extracted from data taken at the testbeam, is shown in Figure 4.3. This pulse shape is the reference used in the estimation of the OF weights.

The reconstructed channel energy used by the High Level Trigger and offline is:

$$E_{\text{channel}} = A \cdot C_{\text{ADC}\to\text{pC}} \cdot C_{\text{pC}\to\text{GeV}} \cdot C_{\text{Cs}} \cdot C_{\text{Laser}}. \tag{4.2}$$

The signal amplitude A represents the measured energy in ADC counts, the factor $C_{\text{ADC}\to\text{pC}}$ is the conversion factor of ADC counts to charge and is determined for each

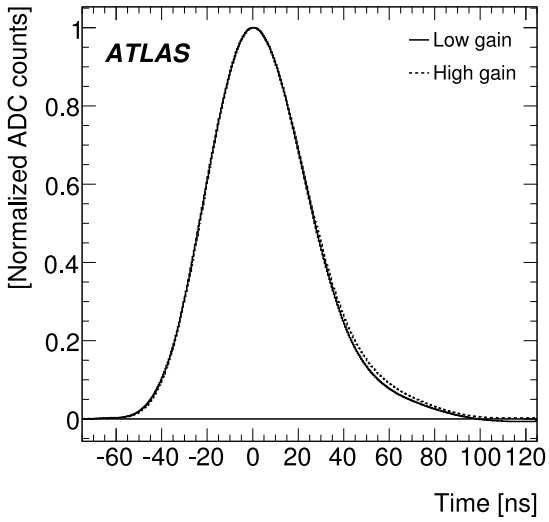

Figure 4.3: Pulse shape for high and low gain from testbeam data.

channel using a well defined injected charge with the CIS (Charge Injection System) calibration System. The factor $C_{\mathrm{pC}\rightarrow\mathrm{GeV}}$ is the conversion factor of charge to energy in GeV and is defined at testbeam for a subset of modules via the response to electron beams of known momentum in the first radial layer. This factor is globally applied to all cells after being adjusted for a dependence on the radial layer. The factor C_{Cs} corrects for residual non-uniformities after the gain equalization of all channels has been performed by the Cs radioactive source system. The factor C_{Laser}, corrects for non-linearities of the PMT response measured by the Laser calibration system. The derived time dependence of the last two factors is applied to preserve the energy scale of TileCal.

The cell energy is the sum, and the cell time the average, of the respective measurements by the two corresponding readout channels. In cases of single readout cells, or if one of the channels is masked out, the cell energy is twice the energy measured in the single available channel. The measurement of the cell's energy is thus robust to failures in a single readout channel.

4.2 Noise Treatment at Reconstruction

The features of the Tile Calorimeter noise described in this section have an impact on the energy reconstruction and affect the resolution of physical quantities like missing transverse energy and jets energies. The ATLAS reconstruction of the energy deposits in the calorimeters is based on the topological clustering algorithm [166]. The algorithm identifies energy depositions that are not likely to be noise fluctuations.

The default threshold corresponds to 4 σ for a normal probability distribution. Once seeded, the cluster is expanded to the neighboring cells that have 4.6% risk of being noise fluctuations (corresponding to 2 σ for a normal probability distribution). Finally, the cluster is further expanded to include the immediate neighboring cells.

The estimation of the compatibility of the energy deposition with a noise fluctuation hypothesis is important to reduce the impact of noise on the resolution of the $E_{\mathrm{T}}^{\mathrm{miss}}$ and jets energy resolution, and in the identification of proton-proton inelastic scattering events. The procedure was the same for the Tile Calorimeter and the LAr Calorimeter until spring 2009. It was based on the assumption that the shape of the reconstructed amplitudes of randomly triggered events for cells was gaussian and the RMS of the cell energy distribution was used to compute the significance of the energy deposit: energy deposits with $E > 4$ RMS were used to seed topoclusters.

Figure 4.4 shows the energy distribution of a typical TileCal cell for randomly triggered events. Deviations from the gaussian assumption are visible in the tails of the distribution. Figure 4.5 shows the accumulated distribution of the reconstructed energy for randomly triggered events divided by the RMS of the cell energy distributions (E_i/RMS_i), where i is the index of the cell. In the case where cells have gaussian noise distributions, the accumulated distribution would be a normal distribution with parameter $\sigma = 1$. In the case of TileCal cells, the deviation from the normal behavior is clearly visible starting from values above 2. In particular, the number of randomly triggered energy deposits above 4 is 2 orders of magnitude greater than the expected one for a normal distribution. This discrepancy creates a significant worsening of the performance of the calorimeter in the low energy regime.

For this reason, the estimation of the significance of the energy deposition has been updated by using a more realistic template of the energy shape [2]. A two gaussian template with 6 independent parameters has been used to fit the energy distribution. Of the 6 independent parameters, only σ_1, σ_2 and the relative normalization of the 2 gaussians, R, are free parameters. The absolute normalization is constrained by the probability density function (p.d.f.) total integral = 1. The mean of the distributions is constrained to $\mu_1 = \mu_2 = 0$. Figure 4.6 shows the fit of the template function of a typical cell and Figure 4.7 shows the improvement in the estimation of the significance of the energy deposition of the randomly triggered events. For the two gaussian p.d.f., the significance is defined as E/σ_{eq} and clusters are seeded cells with significance above 4. One σ_{eq} is defined as $\int_{-\sigma_{eq}}^{\sigma_{eq}} f_{p.d.f.} = 0.68$; two σ_{eq} is defined as $\int_{-2\sigma_{eq}}^{2\sigma_{eq}} f_{p.d.f.} = 0.954$, etc.

This template of the energy shape yields a correct estimation of the significance of the energy deposits and it improves the performance of the $E_{\mathrm{T}}^{\mathrm{miss}}$ and jets reconstruction objects, as shown in [2]. However, it does not take into account cell to cell

correlations, for which additional techniques like the ones described in this thesis are necessary.

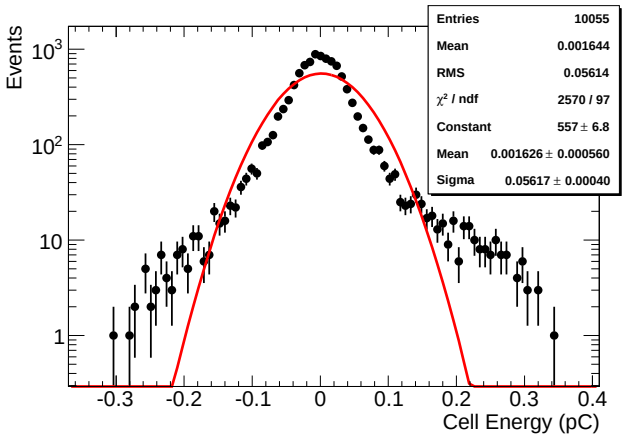

Figure 4.4: Shape of the reconstructed amplitude of a typical cell for randomly triggered events. The distribution is fitted with a gaussian function.

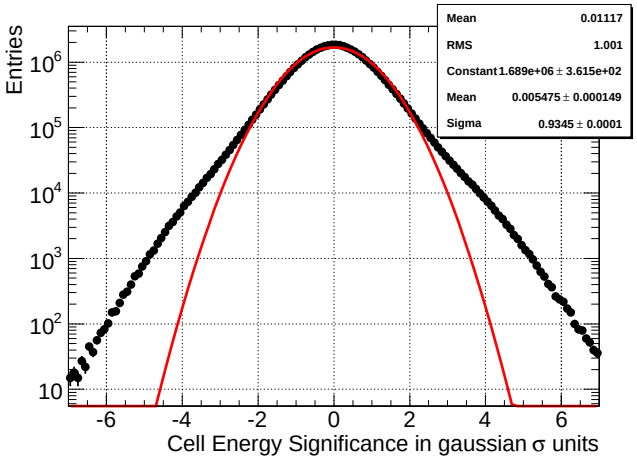

Figure 4.5: Significance of the reconstructed amplitude of TileCal cells for randomly triggered events evaluated with gaussian template functions. The significance distribution is fitted with a gaussian function.

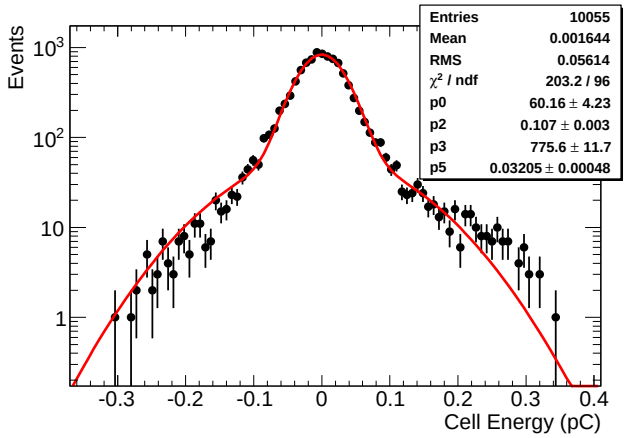

Figure 4.6: Shape of the reconstructed amplitude of a typical cell for randomly triggered events. The distribution is fitted with a two gaussian function.

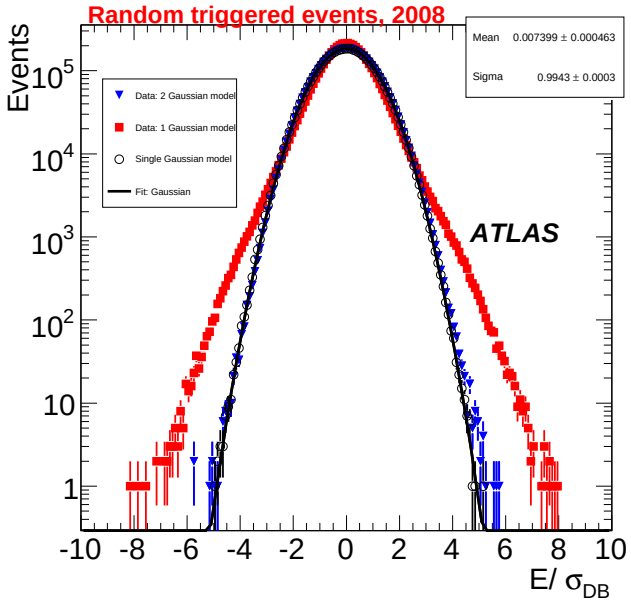

Figure 4.7: Significance of the reconstructed amplitude of TileCal cells for randomly triggered events evaluated with two gaussian template functions. The distribution is superimposed with the expected distribution for perfectly gaussian noise and the significance obtained with gaussian template functions. The significance distribution obtained with two gaussian template functions is fitted with a gaussian function.

4.3 TileCal Correlated Noise

The correlated noise in TileCal plays an important role in the pedestal degradation [3]. The correlation effect between channels within the same partition can be evaluated with the covariance matrix:

$$\mathbf{cov}(x_i, x_j) = E[(x_i - \mu_i)(x_j - \mu_j)] = E[x_i x_j] - \mu_i \mu_j, \tag{4.3}$$

or the correlation matrix,

$$\rho(x_i, x_j) = \frac{\mathbf{cov}(x_i, x_j)}{\sqrt{E[(x_i - \mu_i)^2]}\sqrt{E[(x_j - \mu_j)^2]}} = \frac{\mathbf{cov}(x_i, x_j)}{\sigma_i . \sigma_j}, \tag{4.4}$$

where x_i and x_j are the noise contributions from channels i and j, respectively, μ_i and μ_j are their corresponding mean values, and the operator E denotes the expectation value. The channel signals (x_i and x_j) refer to the signal reconstructed by the non-iterative Optimal Filter method [167]. The extension to the full set of channels within the specific TileCal module is straightforward. The resulting correlation matrix can then provide useful information about how the signal from a specific channel is related to the signal in any other channel. The correlated noise was studied using 10 000 events from a standalone bi-gain pedestal run taken in standard final front-end Tile electronics, final finger Low Voltage Power Supply (fLVPS), in 2009-08-16 during cosmics data taking (run 125204).

To address the problem, it is desirable to consider a general approach based on first principles which does not depend on the specific source of the problem. The approach presented assumes that the observed noise measurement (x_i) in a particular channel i of the TileCal module, is a combination of a genuine intrinsic noise component (β_i) plus a contribution which depends on the response of all readout channels in the module as a whole and it is probably dominated by the closest neighbors. The simplest approach to describe the noise measurement in channel i is then to consider x_i as being a linear combination between the intrinsic noise component (β_i) and a weighted sum of the signals of all the other readout channels (N) in the module i.e.,

$$x_i = \beta_i + \sum_{j \neq i}^{N} \alpha_{i,j} x_j, \tag{4.5}$$

where x_i and x_j are the noise signals for channels i and j respectively. These signals refer to the pulse amplitudes reconstructed by the non-iterative Optimal Filter method [167, 168] using the 7 digitized measurements of the pulse. The $\alpha_{i,j}$ unknown parameters ensure measurements from other readout channels are taken into account with different weights. Given the fact that pedestal subtracted signals

around zero are used, the β_i values are expected to be zero. For each channel, the measured noise can be compared with the model above using the usual χ^2 method,

$$\chi^2_i = \sum_{\text{Events}} \frac{\left[x_i - (\beta_i + \sum_{k\neq i}^{N} \alpha_{i,k} x_k)\right]^2}{\sigma_i^2}, \tag{4.6}$$

which can be minimized (individualy for each channel) with respect to each one of the $\alpha_{i,j}$ and β_i parameters of the model,

$$\frac{\partial \chi^2_i}{\partial \alpha_{i,1}} = \frac{\partial \chi^2_i}{\partial \alpha_{i,2}} = ... = \frac{\partial \chi^2_i}{\partial \alpha_{i,N}} = \frac{\partial \chi^2_i}{\partial \beta_i} = 0. \tag{4.7}$$

Assuming that the noise correlations are the same independently of the signal amplitude, the noise correlations information (embedded in the α matrix) can be extracted from the first out of seven digitized samples and the α matrix itself:

$$\begin{pmatrix} 0 & \alpha_{1,2} & ... & \alpha_{1,N} \\ \alpha_{2,1} & 0 & ... & \alpha_{2,N} \\ ... & ... & ... & ... \\ \alpha_{N,1} & \alpha_{N,2} & ... & 0 \end{pmatrix}.$$

The values of the α_{ij} and of the offset β_i are obtained with the minimization procedure. The reconstruction of the signal in channel i (s_i^{rec}) is performed by removing the offset evaluated during the minimization procedure β_i and by applying the α matrix to the measured values of all the other channels of the module according to,

$$s_i^{rec} = s_i - (\alpha_{i,1}x_1 + \alpha_{i,2}x_2 + ... + \beta_i + ... + \alpha_{i,N}x_N) \tag{4.8}$$

If the method provides a good description of the correlations in the noise pattern, one may expect that the noise distribution will be narrower after correcting any undesirable effects, closer to the intrinsic noise distribution.

In Figure 4.8 (left), correlations between channels are clearly visible in high-gain for the TileCal module LBA9. Regions of high and low correlation values are visible reflecting the configuration of the TileCal hardware with clear clusters of neighbor channels determining the signal responses, the behavior in magnitude and shape is typical for TileCal drawers. These correlations were significantly reduced after applying the correlated noise χ^2 unfolding, Figure 4.8 (right). In Figure 4.9, the reconstructed energy from channel 19 (left) and channel 47 (right) of the TileCal LBA23 module are shown in ADC counts before (red dots) and after (blue line) applying the χ^2 unfolding. Channel 19 is an example of a non-correlated channel and the signal remains uncorrelated after applying the method. Channel 47 is an example of a highly correlated to its neighbors channel and the tails are significantly

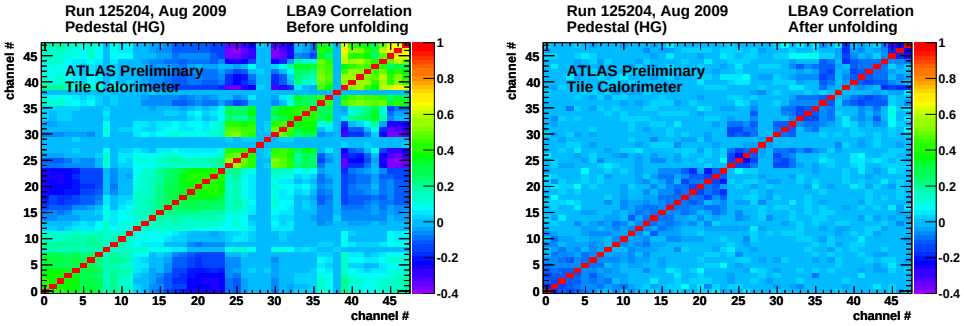

Figure 4.8: Correlation plot of the noise value (evaluated as explained in the text) for all the channels in module LBA9 before (left) and after (right) the unfolding of the noise correlation effect.

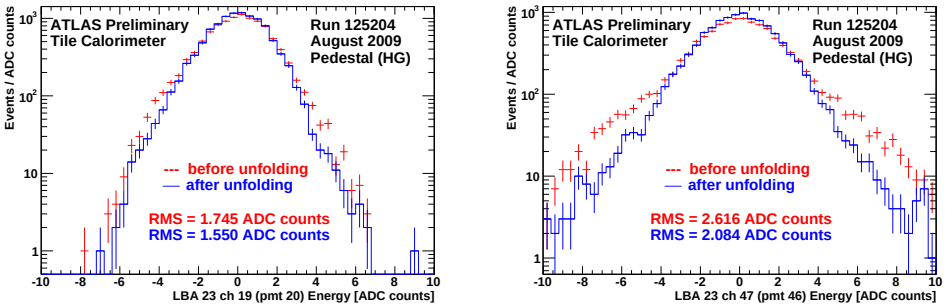

Figure 4.9: LBA23 channels 19 (left) and 47 (right) before and after applying the χ^2 unfolding.

reduced after applying the method. The reconstructed energy from LBA23 channel 46 is plotted against the one from channel 47, in Figure 4.10, before (left) and after (right) unfolding the correlated noise component with the χ^2 method. A clear improvement is observed, i.e. the correlation between both readout channels are very much reduced after applying the unfolding.

In order to study the possibility of using the χ^2 method in the presence of physics signals, a special calibration run was used to check the existence of cross-talk induced by the physics signals. A calibration run where a charge of 100 pC is injected, per event, by the Charge Injection System in each read-out channel of the drawer was used. A total of 1000 events per channel were analyzed when channel 3 of LBA48 was fired. The information from the first out of seven digitized samples (only sensitive to pedestal noise) is successfully used to unfold the noise correlations in the presence of physics signals. The correlated noise component is significantly reduced for the third sample. The unfolding was applied to all samples with similar results to validate the

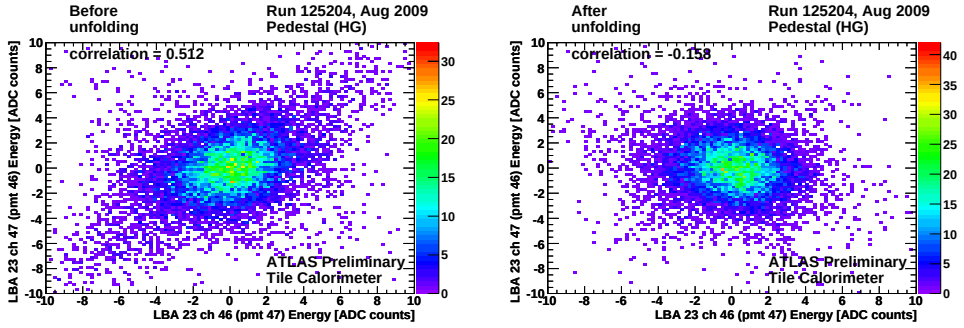

Figure 4.10: LBA23 channel 46 against channel 47 before (left) and after (right) applying the χ^2 unfolding.

performance of the unfolding method in the presence of a controlled injected signal. The correlation matrices calculated for the third [1] of the seven digitized samples of a channel signal pulse are shown in Figure 4.11 before (left) and after (right) applying the correlated noise χ^2 unfolding. The analysis of this special calibration run, where only one channel is fired at a time, excludes the presence of cross-talk allowing the method described herein to be applied in the presence of physics signals.

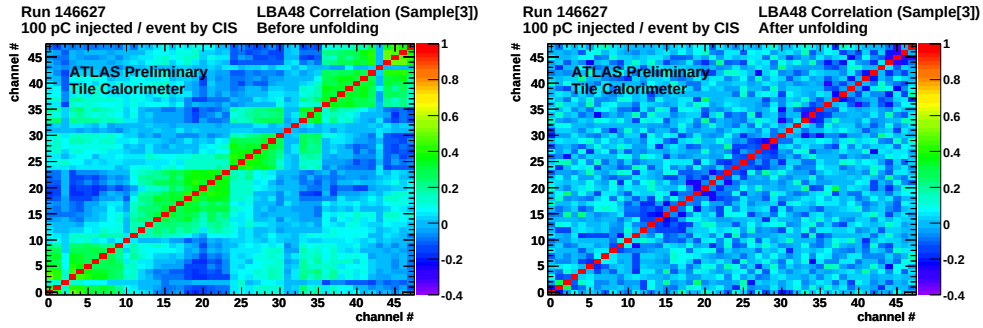

Figure 4.11: Correlation matrices for LBA48 using the third out of seven digitized samples before (left) and after (right) applying the χ^2 unfolding.

The survey of the standalone pedestal run correlation matrices, before and after the correction, of several TileCal modules is presented in Appendix A. Despite the evidence of a similar pattern, the use of a single matrix to describe the general behavior of the TileCal correlated noise effect is discarded. In modules LBA15 and LBC18, the power supply is physically separated from the modules. Since they present different noise correlations values, no relation can be established between the distance of the power supply to the module and the channels correlations. It

[1] The peak of the pulse is timed to be between the third and the fourth samples.

is also important to stress that LBC modules from 41 to 48, shown for some examples, correspond to one of the regions in TileCal where correlated noise is more important. The EBC12 module clearly shows how the correlations match with the hardware structure (Digitizers and Motherboards). The algorithm performance is also shown in Appendix A for LBA48 when channel 3 is being fired (1000 events). The correlation matrices are shown before and after applying the unfolding method for the seven digitized samples, using the information from the first digitized sample.

4.4 Method Performance on Physics Signals

The algorithm described before was applied to two different kinds of data events: Minimum Bias events from early collisions at 900 GeV and simulated $t\bar{t}$ events at 7 TeV. A detailed study for all channels of all modules is presented in this section in order to quantify the performance of the method.

4.4.1 900 GeV Minimum Bias Data

The validation of the method, in the presence of physics signals, is presented using a simulated sample with realistic correlations added and a collisions' data sample from Minimum Bias events. The information from the first out of seven digitized samples of a channel signal pulse (only sensitive to pedestal noise) is used to unfold the noise correlations in the presence of physics signals, only possible because no additional cross-talk was observed in the presence of controlled injected signals using special calibration runs. The reconstructed energy for Minimum Bias trigger data taken at a centre-of-mass energy of 900 GeV [169] (10 000 events collected in December 2009) is shown in the Figure 4.12. The red dashed line is before the noise correlations unfolding and the blue full line is after the unfolding. The figure includes the reconstructed energy of all channels (so that the total number of entries is the number of events $\times$ number of channels). No visible bias is introduced by the noise correlations unfolding method, the signal keeps the same shape, and no degradation is induced by the correction. The correlations seen in the pedestal region can be successfully unfolded with the χ^2 method without affecting the signal distribution.

4.4.2 7 TeV $t\bar{t}$ Simulated Data

In the ATLAS detector simulation, the output of each TileCal channel is the sum of pedestal, signal and random noise. The correlations between the noise of the different channels of each module were implemented in the simulation by generating independent Gaussian variables with mean equal to zero and standard deviation equal to

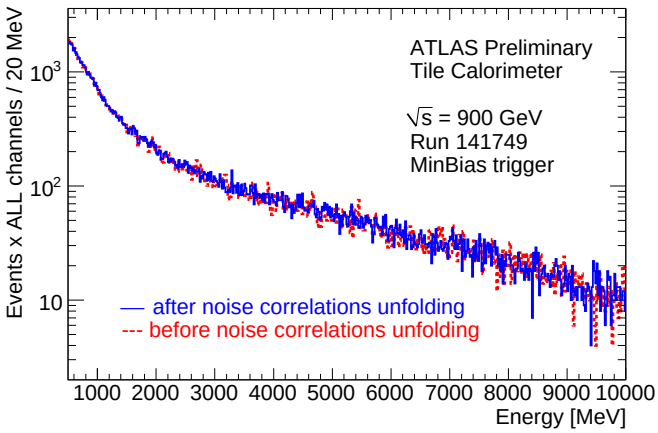

Figure 4.12: Reconstructed energy for real 900 GeV collisions data before and after applying the χ^2 unfolding.

one. The output is convoluted with the desired decomposed covariance matrix [24]. The decomposition of the covariance matrices was done using the Cholesky's algorithm [24]. The work described in [164] considered only four covariance matrices (low gain/high gain and barrel/extended barrel) whereas here, two matrices per module (for low and high gain) were used, giving a total of 512 matrices.

The implementation was tested with simulated samples of non-interacting particles (geantinos), i.e., only the pedestal noise component is present. This allows to compare directly the input covariance matrices taken from data with the output ones, since in the presence of signal, the output of each TileCal channel is no longer described by Gaussian distributions. Figure 4.13 shows the input covariance matrix for high gain of module LBA24 and the corresponding output covariance matrices for Samples 0 and 4. It can be seen that the output covariance matrices are compatible with the one used as input.

To see the effect of the correlated noise in the presence of signal, a $t\bar{t}$ sample generated at 7 TeV with MC@NLO [170] was used[2]. Figure 4.14 shows the obtained covariance matrices for Samples 0, 4 and 6 of module LBA24 (high gain), using as input covariance matrix the one that was used for the geantino samples.

The algorithm was also tested using these simulated (with 1 gaussian correlated noise) $t\bar{t}$ events at 7 TeV including the correlation patterns. The plot with the reconstructed energy of all channels (so that the total number of entries is the number of events $\times$ number of channels) was done for three different situations, without correlations (with 1 gaussian non-correlated noise), with correlations before the cor-

[2]Actually, centrally produced files of hits for sample number 105200 with tags e510 and s765, were used.

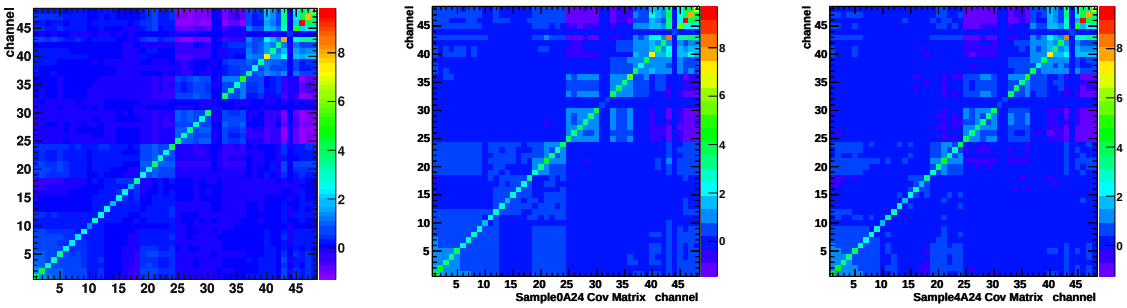

Figure 4.13: The input covariance matrix for high gain of module LBA24 (left) and corresponding output covariance matrices for Samples 0 (center) and 4 (right) obtained with the simulation of the geantinos sample.

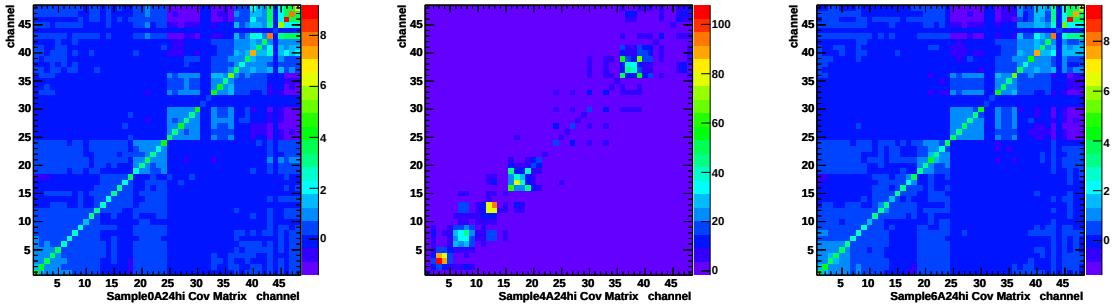

Figure 4.14: Output covariance matrices for Samples 0 (left), 4 (center) and 6 (right) obtained with the simulation of the $t\bar{t}$ sample.

rection and with correlations after correction. The reconstructed cell energy for 10 000 $t\bar{t}$ simulated events generated at 7 TeV with MC@NLO [170] is presented in the Figure 4.15 for the three different situations: without channel-to-channel correlations (black dotted line), with correlations before the noise correlations unfolding (red dashed line) and with correlations after noise correlations unfolding (blue full line). Once more, no visible bias is introduced by the noise correlations unfolding method.

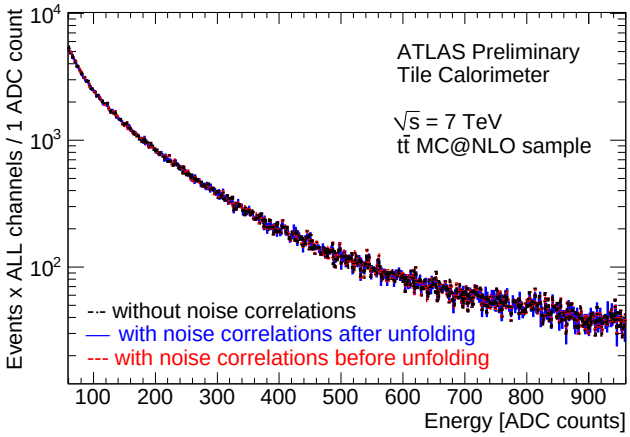

Figure 4.15: Reconstructed energy of all channels and all modules in different in the signal region is shown covering the highest amplitudes. Red is before the correction, blue is after the correction and black is uncorrelated.

4.5 Conclusions

The method proposed to remove the correlated noise component of the TileCal has been tested and approved through this systematic survey of the TileCal modules as a powerful solution to the coherent noise presence in pedestal runs. This approach shall be regarded as well as an effective diagnosis tool to the general behaviour of TileCal modules.

The analysis of special calibration runs, where only one channel is fired at a time, excluded the presence of cross-talk allowing the method described herein to be applied in the presence of physics signals. No degradation of the signal was observed. The results on Minimum Bias and simulated $t\bar{t}$ events show a clear improvement on the pedestal noise distribution and again the signal is not degraded as one would expect. In conclusion, the method proved to be very effective and reliable for different kinds of events, both real and simulated.

Chapter 5

Study of the Wtb Vertex Structure

A study of the polarization of $W^{\pm}$ bosons in top quark decays, which is sensitive to the Wtb vertex structure, is presented: W boson helicity fractions (F_0, F_{L}, F_{R}) and certain angular asymmetries (A_{FB}, A_+, A_-) are measured. The analysis uses the data collected by the ATLAS experiment at a center-of-mass energy of $\sqrt{s} = 7$ TeV, corresponding to an integrated luminosity of around 1.04 fb^{-1}. The $t\bar{t}$ events decaying through the single lepton ($t\bar{t} \to bW^+\bar{b}W^- \to bq\bar{q}\bar{b}\ell\nu_\ell$) and dilepton ($t\bar{t} \to bW^+\bar{b}W^- \to b\ell\nu_\ell\bar{b}\ell\nu_\ell$) topologies are considered. The measurements are used to establish the allowed regions for possible anomalous Wtb couplings and set limits on the contribution of physics beyond the Standard Model, within an effective field theory.

5.1 Introduction

As already mentioned in Chapter 2, and repeated here for the sake of easy reading, the Wtb vertex is defined by the electroweak interaction and has a $(V-A)$ structure where V and A are the vector and axial-vector contributions to the vertex. The $W^{\pm}$ bosons are produced as real particles in top quark decays, and their polarization in the helicity axis can be longitudinal, left-handed or right-handed. The fractions of events with a particular polarization, F_0, F_{L} and F_{R}, are referred to as helicity fractions, and can be extracted from measurements of the angular distribution of the decay products of the top quark. The angle θ^* is defined as the angle between the momentum direction of the charged lepton from the decay of the W boson and the reversed momentum direction of the b-quark from the decay of the top quark, both boosted into the W boson rest frame [78]. The angular distribution is:

$$\frac{1}{\sigma}\frac{\mathrm{d}\sigma}{\mathrm{d}\cos\theta^*} = \frac{3}{4}\left(1-\cos^2\theta^*\right) F_0 + \frac{3}{8}\left(1-\cos\theta^*\right)^2 F_{\mathrm{L}} + \frac{3}{8}\left(1+\cos\theta^*\right)^2 F_{\mathrm{R}}\,. \quad (5.1)$$

The helicity fractions are predicted in next-to-next-to-leading-order (NNLO) QCD calculations to be $F_0 = 0.687 \pm 0.005$, $F_{\mathrm{L}} = 0.311 \pm 0.005$, $F_{\mathrm{R}} = 0.0017 \pm 0.0001$ [73], and all previous measurements of the helicity fractions, performed by the CDF and DØ Collaborations [83–85] at the Tevatron, are in agreement with Standard Model predictions. Information about the polarization of the $W^{\pm}$ bosons can also be obtained through complementary observables, such as the angular asymmetries, A_+ and A_-, defined as:

$$A_{\pm} = \frac{N(\cos\theta^* > z) - N(\cos\theta^* < z)}{N(\cos\theta^* > z) + N(\cos\theta^* < z)}, \tag{5.2}$$

with $z = \pm(1 - 2^{2/3})$ for $A_{\pm}$, allowing the dependence on F_{L} and F_{R} to cancel, respectively. The asymmetries can be related to the helicity fractions by a simple system of equations [74, 171]. In the Standard Model, the NNLO values for these asymmetries are $A_+ = 0.537 \pm 0.004$ and $A_- = -0.841 \pm 0.006$ [73].

In the presence of anomalous Wtb couplings the helicity fractions and angular asymmetries depart from their Standard Model values [74, 78]. In the context of a dimension-six effective field theory for the Wtb vertex [75, 76, 172], the coefficients controlling the strength of the dimension-six operators can be constrained by measurements of the helicity fractions or the angular asymmetries.

In this chapter, the measurements of the W boson polarization in top quark decays and the constraints on the Wtb vertex structure are presented, based on a data set recorded with the ATLAS detector between March and June 2011 and corresponding to an integrated luminosity of 1.04 fb^{-1} [8]. The helicity fractions were measured using two different methods, the template method, which compares the observed $\cos\theta^*$ distribution with templates for different W boson helicity states obtained from simulation, and the asymmetry method. The work of this thesis is centered on the angular asymmetry method, which uses the unfolded $\cos\theta^*$ spectrum, corrected for background contributions, to extract the angular asymmetries, and thus, the helicity fractions. The single lepton and dilepton topologies, both considered in the analyses presented in this chapter, have one and two isolated charged leptons in the final state. Only electrons and muons, including those from τ decays, are considered here as signal. Limits on anomalous couplings, generated by the dimension-six operators, were set using the combined result from the two measurements.

5.2 Data and Monte Carlo Samples

The analyses presented in this chapter use the data from pp collisions at a center-of-mass energy of 7 TeV, collected using single lepton triggers with transverse mo-

mentum thresholds of 20 GeV for electrons and 18 GeV for muons, corresponding to an integrated luminosity of 1.04 ± 0.04 fb^{-1} [173, 174].

Signal and most background processes were modelled by Monte Carlo (MC) simulation. The signal process was simulated using two different generators. The leading order (LO) Monte Carlo generator PROTOS [71,74] was used with the CTEQ6L1 sets of parton distribution functions (PDFs) [175] to generate three samples assuming $F_0 = 1$, $F_L = 1$ and $F_R = 1$, respectively. This was achieved by choosing appropriate values for anomalous Wtb couplings, as described in [74, 171], and presented in Table 5.1. The output was interfaced to PYTHIA [176] to simulate parton showers and hadronization. The PROTOS generator was compared with NLO generators MC@NLO and POWHEG, as shown in Figure 5.1. In addition, the next-to-leading-order (NLO) generator MC@NLO [170,177,178] was used with the CTEQ6.6 PDF set [179] for studies of systematic differences in the top quark production and decay modelling.

	V_L	V_R	g_L	g_R
$F_0 = 1$	1.53205	0	−0.01989	0.714647
$F_L = 1$	0.504619	0.001919	0	1.08275
$F_R = 1$	0.001919	0.504619	1.08275	0

Table 5.1: Anomalous couplings values used in PROTOS to generate $t\bar{t}$ templates with longitudinal ($F_0 = 1$), left-handed ($F_L = 1$) and right-handed ($F_R = 1$) W boson polarizations. The masses $m_t = 172.5$ GeV, $m_W = 80.4$ GeV and $m_b = 4.8$ GeV were assumed.

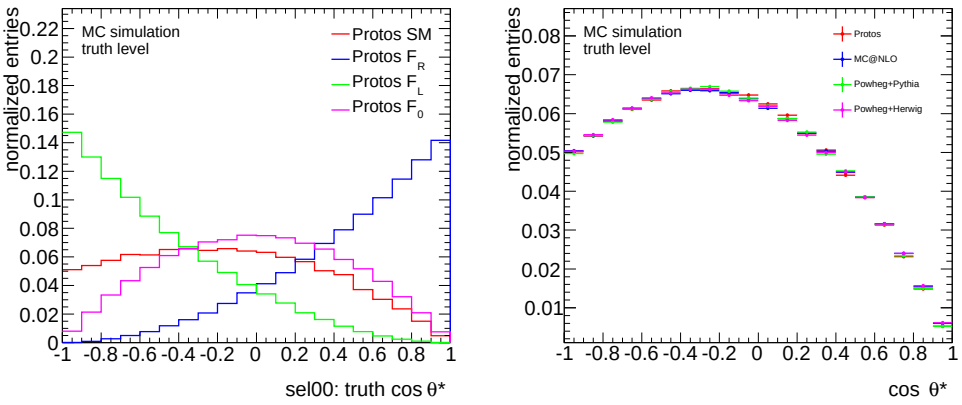

Figure 5.1: PROTOS templates for $\cos\theta^*$ distribution at truth level (left) and PROTOS/MC@NLO/POWHEG generators comparison for $\cos\theta^*$ distribution also at truth level (right).

The W and Z boson production in association with multiple jets was simulated using the ALPGEN generator [180] and the CTEQ6L1 PDF set. Tree-level matrix elements with up to five final-state partons were included. The MLM matching method was used to remove overlaps between the n and $n+1$ parton samples [181]. Heavy flavor samples containing $Wb\bar{b}$, $Wc\bar{c}$, Wc and $Zb\bar{b}$ events were simulated separately. The Z+jets samples were generated with dileptons in the invariant mass range $10 < m_{\ell\ell} < 2000$ GeV. Diboson processes were simulated using HERWIG [182]. Single top quark production was simulated using MC@NLO, invoking the 'diagram removal scheme' [183] to remove overlaps between the single top quark and $t\bar{t}$ final states. An additional sample of W+jets events was generated with SHERPA [184] and used to study systematic uncertainties. Apart from the PROTOS $t\bar{t}$ samples, all events were hadronized with HERWIG using JIMMY [185] for the underlying event model. Different underlying event tunes were used, depending on the hadronization program used (*i.e.* PYTHIA or HERWIG) [186].

Additional MC samples were used for the evaluation of systematic uncertainties. These were generated with the ACERMC [187] and POWHEG [188, 189] generators interfaced to PYTHIA for hadronization. A top quark mass of 172.5 GeV was assumed for all signal samples if not stated otherwise. Additional MC@NLO samples were generated assuming different top quark masses.

All simulated events contain multiple pp-interactions and contain pileup contributions corresponding to a bunch spacing of 50 ns. These simulated events were re-weighted such that the average number of interactions per proton-proton bunch crossing was the same in data and MC simulation. The average number of interactions per event was roughly six. All samples were processed by the detector and trigger simulation after event generation [190, 191], and subjected to the same reconstruction algorithms as the data.

The cross-section of simulated $t\bar{t}$ samples was normalized to 164.6 pb, the value obtained from approximate NNLO calculations [66, 192, 193], and consistent with recent measurements [194]. The diboson with jets production was rescaled to match NLO calculations of the inclusive cross-sections. While the Z+jets normalization was obtained from the NNLO QCD cross-section calculations in the single lepton channels, a data-driven estimate for the normalization was used for the dilepton channels [194]. The W+jets background contribution in the single lepton channels was obtained from simulation, except that its normalization was derived from data, from a study of the asymmetry in the production of $W^{\pm}$ bosons [195]. For the single lepton analysis, the multijet production background, where an electron or muon originates from hadron decay or instrumental background, was estimated from data using the data-driven Matrix Method, described in [195,196]. For the dilepton anal-

ysis, background contributions from W+jets, single lepton $t\bar{t}$ and single top quark production were also estimated using the data-driven Matrix Method, described in [194]. In both the single lepton and dilepton analyses this source of background is labelled as "misidentified leptons".

5.2.1 W+jets Background

The W+jets background normalization in the single lepton channels was derived from data using the W^++jets and W^-+jets production asymmetry. At the LHC the rate of W^++jets is larger than that of W^-+jets because there are more valence u quarks than d quarks in the proton. As the ratio of W^++jets and W^-+jets cross sections is predicted much more precisely than the total W+jets cross section [197, 198], this asymmetry was exploited to measure the total W+jets background from the data.

Since, to a good approximation, processes other than W+jets give equal numbers of positively and negatively charged leptons, the formula

$$N_{W^+} + N_{W^-} = \left(\frac{r_{MC}+1}{r_{MC}-1}\right)(D^+ - D^-), \tag{5.3}$$

can be used to estimate the total number of W events in the selected sample. Here $D^+(D^-)$ are the total numbers of events in data passing the selection cuts described in section 5.3.6 (apart from the b-tagging requirement) with positively (negatively) charged leptons, and $r_{MC} \equiv \frac{N(pp\to W^+)}{N(pp\to W^-)}$ is evaluated from Monte Carlo simulation, using the same event selection.

The ratio r_{MC} was found to be 1.56±0.06 in the electron channel and 1.65±0.08 in the muon channel. The dominant uncertainties on r_{MC} originated from those of the parton distribution functions, the jet energy scale, and the heavy flavor fractions in W+jets events (fractions of W+jets events containing $b\bar{b}$ pairs, $c\bar{c}$ pairs and c quarks).

5.2.2 Drell-Yan Estimation

To estimate the Z+jets background in the dilepton channels (excluding the decay to $\tau^+\tau^-$), the number of Drell-Yan events is measured in a control region orthogonal to the signal region. The contamination in the control region from background physics processes is subtracted from data relying on the Monte Carlo prediction, and a scale factor is derived using Drell-Yan simulations to extrapolate from the control region (CR) into the signal region (SR):

$$\text{Drell-Yan back. estimates} = \frac{\text{MC}_{\text{Drell-Yan}}(\text{SR})}{\text{MC}_{\text{Drell-Yan}}(\text{CR})} \times \left(\text{Data}(\text{CR}) - \text{MC}_{\text{other}}(\text{CR})\right), \tag{5.4}$$

where $\mathrm{MC}_{\text{Drell-Yan}}$(SR/CR) represent the number of events in the signal and control regions, respectively. $\mathrm{MC}_{\text{other}}$ is the number of events from physics backgrounds that contaminate the control region. Data(CR) is the observed number of events in the control region in data. The Drell-Yan background normalization prediction from the Monte Carlo is thus scaled by the ratio of data and Monte Carlo events in the control region. The signal and control regions are shown in Figure 5.2, and the observed and expected number of events in the signal and control regions are summarized in Table 5.2 for the dielectron and dimuon channels, together with the corresponding normalization scale factors. The uncertainties were estimated by taking into account the statistical fluctuation of the data in the CR, and by varying the $E_{\mathrm{T}}^{\mathrm{miss}}$ cut in the CR from 40 GeV to 30 GeV. The dielectron and dimuon invariant masses distributions are shown in Figure 5.3, where the detailed good agreement between the data and the signal+background model is visible.

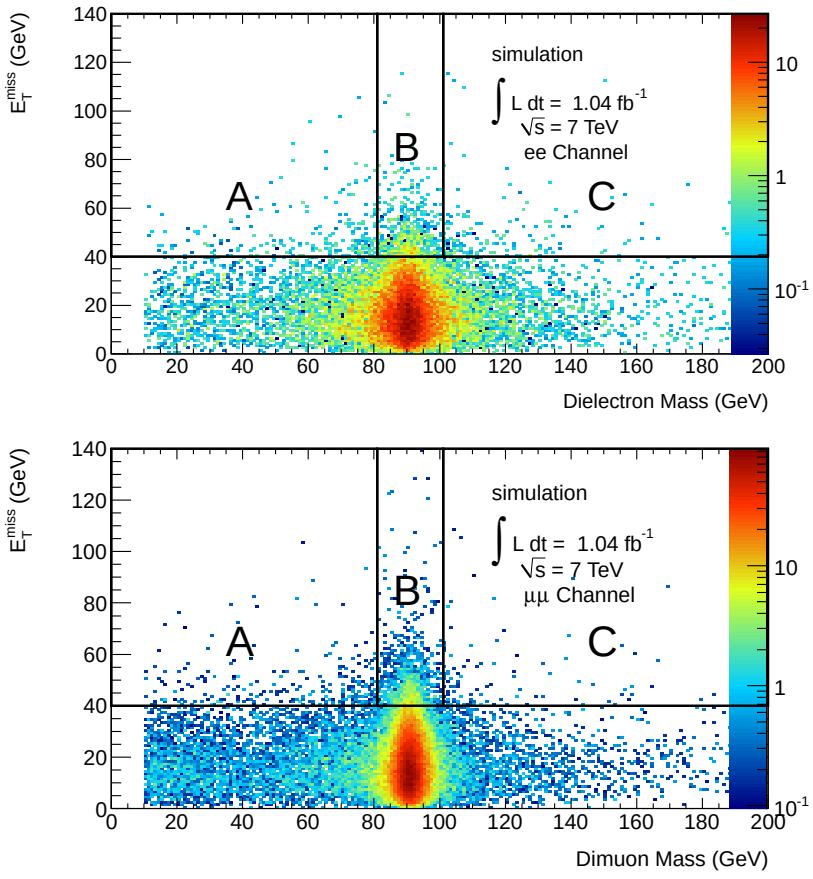

Figure 5.2: The dielectron (top) and dimuon (bottom) invariant masses versus $E_{\mathrm{T}}^{\mathrm{miss}}$ distributions for Z+jets Monte Carlo are shown. The distributions are used to normalize the Z+jets background using data. Regions A and C correspond to the signal regions, and B to the control region used in the calculation of the normalizations.

Channel	Data(CR)	DY MC(CR)	Physics Background Sources $t\bar{t}$	$Z \to \tau\tau$	S.T. + W	Diboson	Mis. Lep.	SF
ee	164	62	46	0.0	2.4	4.4	0	1.8 ± 0.2
$\mu\mu$	296	180	86	0.0	5.0	6.8	0	1.1 ± 0.1

Table 5.2: Number of observed events in data in the control region (Data(CR)), the number of Monte Carlo events in the signal (MC(SR)) and control (MC(CR)) regions and the number of events from other physics background sources contaminating the control region.

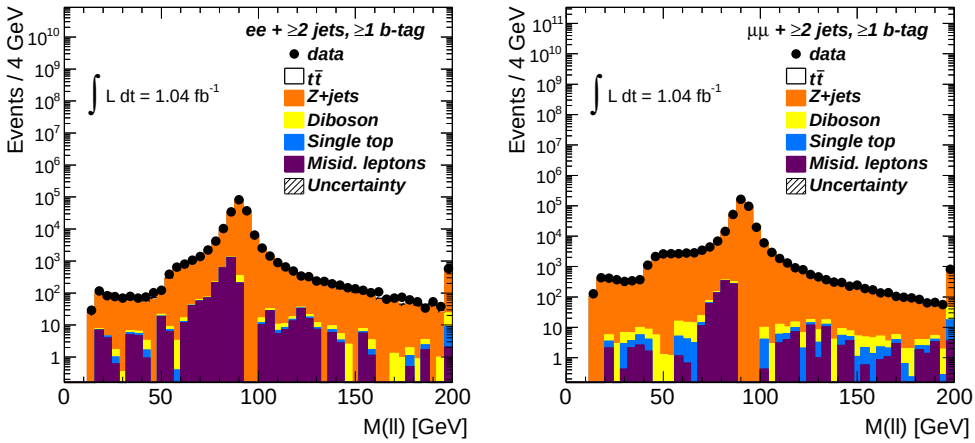

Figure 5.3: The dielectron (left) and dimuon (right) invariant mass distributions.

5.2.3 Misidentified Leptons

The Matrix Method [194], used to estimate the contribution of multijet background with fake leptons in both the single lepton and dilepton channels, accounts intrinsically for backgrounds with one and two misidentified leptons. A lepton selection based upon "loose" quality criteria was defined for both electrons and muons, by dropping some of the object selection requirements. The efficiencies for real and misidentified loose leptons to pass the default selection based on "tight" selection criteria, were then measured using control regions purified in real and misidentified leptons. Real efficiencies were determined from $Z \to ll$ samples in data, while misidentified leptons efficiencies were measured in data by using a control region defined separately for the different channels, where the contribution of misidentified leptons is dominant.

5.3 Object Reconstruction and Event Selection

The reconstruction and identification of electrons, muons, jets and the magnitude of the missing transverse momentum ($E_{\mathrm{T}}^{\mathrm{miss}}$) used in these analyses, followed the criteria employed for the measurement of the $t\bar{t}$ production cross-section [196]. The $t\bar{t}$ events with at least one isolated charged lepton (electron or muon) in the final state were considered as signal, including the events with τ leptons decaying into muons or electrons. The details on the description of the trigger and the vertex requirements can be found in [195]. All the events were required to have a well-defined primary vertex with at least five associated tracks and to fulfil the several objects selection criteria, described as follows.

5.3.1 Trigger Requirements

Each event must have at least one lepton matched to the appropriate trigger. Electrons selected according to the criteria presented in section 5.3.2 were required in data and MC to match to an electron passing the `EF_e20_medium` trigger path [199]. The efficiency of the trigger (ϵ_{trig}) and the data/MC efficiency ratio (SF_{trig}) were measured using $Z \rightarrow ee$ and $W \rightarrow e\nu$ events and found to be in the plateaux for $E_T > 25$ GeV, with $\epsilon_{trig} \simeq 98\%$ and $SF_{trig}(\eta)$ within 98% and 100% for all but the very forward ($|\eta| > 2$) regions. Events in the muon channel were selected at the trigger level requesting the `EF_mu18` trigger chain was fired [200]. The chain was seeded at Level-1 by a L1_MU10 item, selecting RoI's in the muon spectrometer with at least 10 GeV of estimated transverse momentum. The L2 and EF trigger ROIs were both matched to a combined `Muid` muon track by requesting that they be closer than $\Delta R = 0.15$. The trigger request was applied to both 2011 collision data and MC10b simulated events.

5.3.2 Electrons

Reconstructed electrons were required to have $E_{\mathrm{T}} > 25$ GeV and $|\eta| < 2.47$, excluding the $1.37 < |\eta| < 1.52$ regions, which corresponds to the gap between the barrel and end-cap parts of the electromagnetic calorimeter [150]. At large transverse energy (E_{T}), the calorimeter energy resolution is dominated by a constant term which is measured in data to be 1.2% in the barrel ($|\eta| < 1.37$) and 1.8% in the endcaps ($1.52 < |\eta| \leq 2.47$). The energy not associated to the electron cluster, but contained in a cone of $\Delta R = \sqrt{(\Delta\phi)^2 + (\Delta\eta)^2} = 0.2$ around it, was required not to exceed 3.5 GeV. The electrons must also pass an E_{T} isolation cut (calorimeter-based) in a cone of $\Delta R = 0.2$, along with a p_{T} isolation cut (tracking-based) in a cone of $\Delta R = 0.3$, derived for 90% efficiency. After the full event selection, an additional

cut is applied requiring the electron z_0, *i.e.* the z coordinate value of the track at the point of closest approach to the z-axis, with respect to the primary vertex to be less than 2 mm.

5.3.3 Muons

Muons were required to have $p_{\mathrm{T}} > 20$ GeV and $|\eta| < 2.5$. The sum of track transverse momenta and the total energy deposited in a cone of $\Delta R = 0.3$ around the muon were both required to be less than 4 GeV. Muons were also required to have at least one Pixel hit or have crossed one dead pixel sensor, and to have a B-layer hit (if expected). In addition, the sum of the number of SCT hits and number of crossed dead SCT sensors had to be greater than five, and the number of SCT holes plus the number of pixel holes could not be greater than three. After the full event selection a cut is applied requiring the muon z_0 with respect to the primary vertex to be less than 2 mm.

5.3.4 Jets

Jets were reconstructed with the anti-k_t algorithm [201] with a radius parameter equal to 0.4. They were required to have $p_{\mathrm{T}} > 25$ GeV and $|\eta| < 2.5$. Jets within $\Delta R = 0.2$ of an electron candidate were removed to avoid double counting, which can occur because electron clusters are also reconstructed as jets. Muons reconstructed within a $\Delta R = 0.4$ cone of a jet satisfying $p_{\mathrm{T}} > 20$ GeV were removed to reduce the contamination caused by muons from hadron decays within jets.

5.3.5 *b*-Jets

A combination of two algorithms was used for b-jet identification (b-tagging). They are based on reconstructed secondary vertices and the impact parameter significances of tracks within jets [202]. One b-tagger, JetFitter, exploits the topology of weak b- and c-hadron decays inside the jet. A Kalman filter is used to find a common line on which the primary vertex and the b- and c-hadron decay vertices lie, as well as their position on this line, giving an approximated flight path for the b-hadron. With this approach, the b- and c-hadron vertices are not necessarily merged, even when only a single track is attached to each of them. The discrimination between b-, c- and light jets is based on a likelihood using the masses, momenta, flight-length significances, and track multiplicities of the reconstructed vertices as inputs. To further increase the flavor discrimination power, a second b-tagger is run which does not attempt to directly reconstruct decay-vertices. Instead, this tagger (IP3D) uses the transverse and the longitudinal impact parameter significances of each track within the jet

to determine a likelihood that the jet originates from a b-quark. The IP3D and JetFitter tagger results are combined using an artificial neural network to determine a single discriminant variable which is used to make tagging decisions. The chosen working point resulted in a b-tagging efficiency of 70% for jets originating from b-quarks in a sample of simulated $t\bar{t}$ events and a light-quark jet rejection factor of about 100. The tagging rates for the inclusive jet sample and for the one enriched in heavy-flavor jets are shown in Figure 5.4.

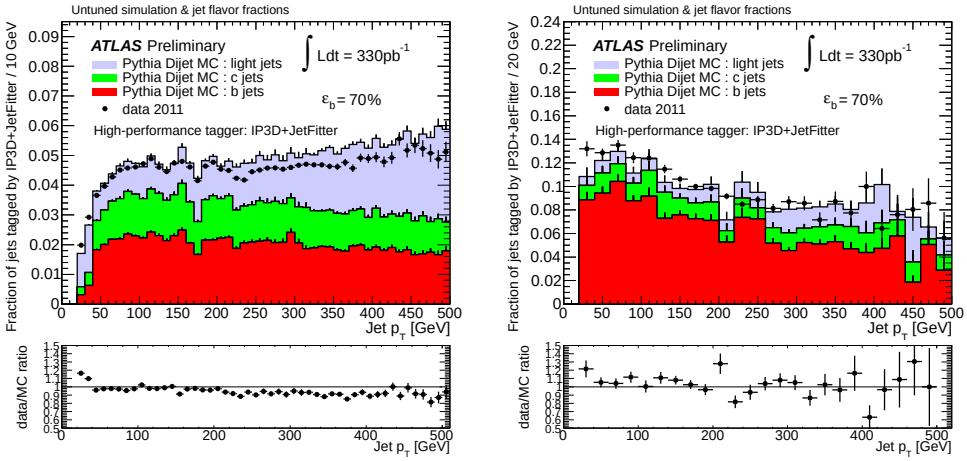

Figure 5.4: Distribution of the tagging rate for the IP3D+JetFitter tagging algorithm at an operating point leading to 70% b-jet efficiency for experimental data (solid black points) and for simulated data (filled histograms for the various flavors) versus the jet transverse momentum. Jets are from the inclusive leading jet sample (left) and Jets from the sample enriched in heavy-flavor jets (right). The ratio data/simulation is shown at the bottom of each plot.

5.3.6 Event Selection

The single lepton $t\bar{t}$ signal is characterized by an isolated charged lepton (electron or muon) with high p_{T} and missing transverse energy corresponding to the undetected neutrino from the W leptonic decay, two b quark jets and two light jets from the hadronic W decay. Events with τ leptons which decay leptonically are considered part of the signal. The selection of events for the single lepton analysis consists of a series of requirements on the reconstructed objects, designed to select events with the above topology. The two channels with either an electron or a muon in the final state are referred to as single-electron and single-muon channels, and the following event selection requirements are applied:

- the appropriate single-electron or single-muon trigger had fired;

- events were required to contain exactly one isolated electron or muon;
- in the single-electron channel, $E_{\mathrm{T}}^{\mathrm{miss}} > 35$ GeV and $m_{\mathrm{T}}(W) > 25$ GeV were required[1] while in the single-muon channel the criteria were $E_{\mathrm{T}}^{\mathrm{miss}} > 20$ GeV and $E_{\mathrm{T}}^{\mathrm{miss}} + m_{\mathrm{T}}(W) > 60$ GeV;
- events were required to have at least four jets, with at least one of them being tagged as a b-jet.

The dilepton $t\bar{t}$ signal is characterized by two high-p_{T} isolated charged leptons, missing transverse momentum corresponding to the undetected neutrinos from the two leptonically decaying $W^{\pm}$ bosons, and two b-quark jets. The three channels are referred to as ee, $\mu\mu$ and $e\mu$ channels. The following event selection requirements were applied:

- the single-electron trigger had fired for the $e^{-}e^{+}$ channel, the single-muon trigger had fired for the $\mu^{-}\mu^{+}$ channel and either of these triggers had fired for the $e^{\mp}\mu^{\pm}$ channel;
- events were required to contain exactly two oppositely charged and isolated leptons (ee, $\mu\mu$ or $e\mu$);
- at least two jets, with at least one of them being b-tagged, were required;
- in order to avoid the low-mass Drell-Yan background region, events were required to have $m_{\ell\ell} > 15$ GeV;
- in the ee and $\mu\mu$ channels, the missing transverse momentum had to satisfy $E_{\mathrm{T}}^{\mathrm{miss}} > 40$ GeV, and the invariant mass of the two leptons had to differ by at least 10 GeV from the Z boson mass, *i.e.* $|m_{\ell\ell} - m_Z| > 10$ GeV, with $m_Z = 91$ GeV, in order to suppress backgrounds from Z+jets events and events containing misidentified leptons;
- in the $e\mu$ channel, no $E_{\mathrm{T}}^{\mathrm{miss}}$ or Z boson mass veto cuts were applied; however, the variable H_{T}, defined as the scalar sum of the transverse energies of the two charged leptons and all selected jets, must satisfy $H_{\mathrm{T}} > 130$ GeV to suppress backgrounds from Z+jets production;
- events were required to pass the $t\bar{t}$ reconstruction criteria, described in the next section.

[1]Here $m_{\mathrm{T}}(W)$ is the W boson transverse mass, reconstructed as $\sqrt{2p_{\mathrm{T}}^{\ell}p_{\mathrm{T}}^{\nu}\left[1-\cos(\phi^{\ell}-\phi^{\nu})\right]}$ where the measured missing transverse momentum provides the neutrino information.

5.4 Event Reconstruction

The reconstruction of $t\bar{t}$ events in the single lepton channels uses a χ^2 minimization and, in the dilepton channels, the $t\bar{t}$ system is reconstructed by solving a set of six independent equations. As a result, the $\cos\theta^*$ distribution is obtained in order to measure the angular asymmetries and helicity fractions. The two methods are explained in detail in the following subsections.

5.4.1 Single Lepton Topology

The reconstruction of single lepton $t\bar{t}$ events requires the knowledge of the four momenta of all jets and leptons (charged and neutral) in the events. While for the jets and charged leptons these measurements are experimentally available, for the neutrinos only the transverse energy (momentum) is measured. To evaluate the p_z component of the neutrino momentum, full event reconstruction is performed. In this section the χ^2 method used to reconstruct $t\bar{t}$ single lepton events is described.

In the χ^2 method the event reconstruction is accomplished by minimizing the χ^2 defined according to

$$\chi^2 = \frac{(m_{\ell\nu \mathrm{j_a}} - m_\mathrm{t})^2}{\sigma_\mathrm{t}^2} + \frac{(m_{\mathrm{j_b j_c j_d}} - m_\mathrm{t})^2}{\sigma_\mathrm{t}^2} + \frac{(m_{\ell\nu} - m_\mathrm{W})^2}{\sigma_\mathrm{W}^2} + \frac{(m_{\mathrm{j_c j_d}} - m_\mathrm{W})^2}{\sigma_\mathrm{W}^2} \ , \qquad (5.5)$$

where $m_\mathrm{t} = 172.5$ GeV, $m_\mathrm{W} = 80.4$ GeV, $\sigma_\mathrm{t} = 14$ GeV and $\sigma_\mathrm{W} = 10$ GeV are the expected top quark and W boson mass resolutions, ℓ represents the selected electron or muon, $m_{\ell\nu}$ is the invariant mass of the electron (muon) and the neutrino, and $j_{\mathrm{a,b,c,d}}$ corresponds to all possible combinations of four jets among all selected jets in the event (with $m_{\ell\nu \mathrm{j_a}}$, $m_{\mathrm{j_b j_c j_d}}$ and $m_{\ell\nu \mathrm{j_a}}$ being the corresponding invariant masses). The neutrino was reconstructed using the missing transverse energy, with the p_z^ν component allowed to vary. The solution corresponding to the minimum χ^2 value is chosen to be the correct one. No b-tagging information was used at this level. The $\sqrt{\chi^2}$ distributions are shown in Figure 5.5. The invariant masses of the $W^\pm$ bosons and t-quarks reconstructed by the χ^2 method can be seen in Figure 5.6.

In this analysis, the $t\bar{t}$ events with a single lepton (an electron or a muon either from the W decay or from a leptonic tau decay, with the tau being originated in the $W \to \tau\nu$ decay) are considered as signal. After perfoming the $t\bar{t}$ system reconstruction, it is possible to reconstruct the $\cos\theta^*$ distribution shown in Figure 5.7, based on which the angular asymmetries are evaluated.

The difference between the reconstructed and generated (parton level) $\cos\theta^*$ was evaluated using Monte Carlo $t\bar{t}$ simulated signal events. These resolution distributions are shown in Figure 5.8.

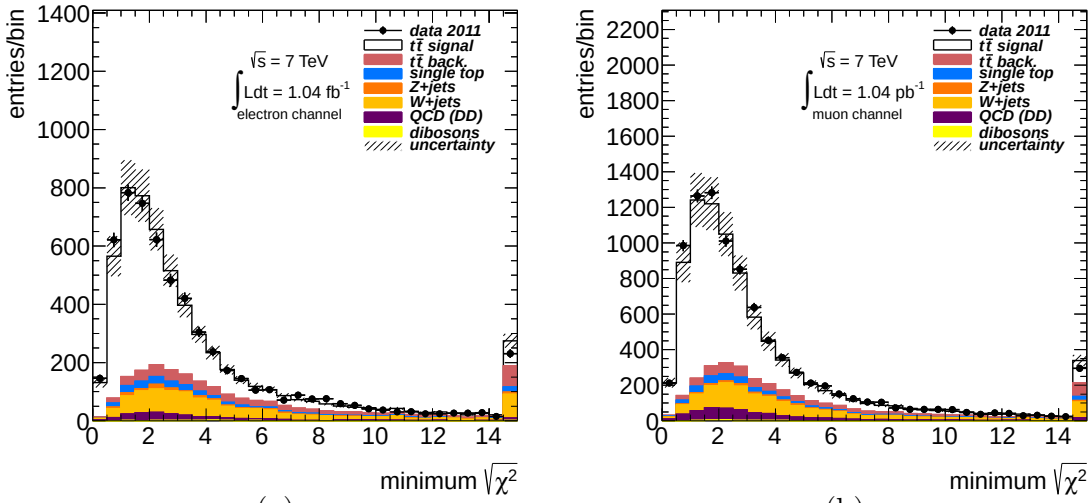

Figure 5.5: $\sqrt{\chi^2}$ distributions for the (a) e+jets and (b) μ+jets channels.

5.4.2 Dilepton Topology

The reconstruction of $t\bar{t}$ events requires a knowledge of the jet and lepton momenta together with the missing energy. If the masses of the $W^{\pm}$ bosons and top quarks are used as constraints, six unknown variables remain to fully reconstruct the dileptonic $t\bar{t}$ topology, i.e., the three momenta of the two neutrinos present in the events. To find a kinematic solution for the neutrino momenta, the following six independent equations are used,

$$\begin{aligned} p_x^{\nu 1} + p_x^{\nu 2} &= \not{E}_x, \\ p_y^{\nu 1} + p_y^{\nu 2} &= \not{E}_y, \\ (p_{\ell 1} + p_{\nu 1})^2 &= m_W^2, \\ (p_{\ell 2} + p_{\nu 2})^2 &= m_W^2, \\ (p_{W1} + p_{b1})^2 &= m_t^2, \\ (p_{W2} + p_{b2})^2 &= m_t^2. \end{aligned} \tag{5.6}$$

While $\not{E}_x$ and $\not{E}_y$ represent the components of the missing transverse energy, $p_{\ell 1}$ and $p_{\ell 2}$ (p_{b1} and p_{b2}) correspond to the two lepton (two b-jets) four momenta, respectively. The quantities m_W and m_t are the W boson and top quark masses, respectively.

If only one jet was tagged as a b-jet in the event selection, the b-jet and the highest p_{T} non-b-jet are used. In case at least two jets are tagged as b-jets, the two highest p_{T} b-jets are used. To obtain the correct kinematic solution, the $b(\bar{b})$

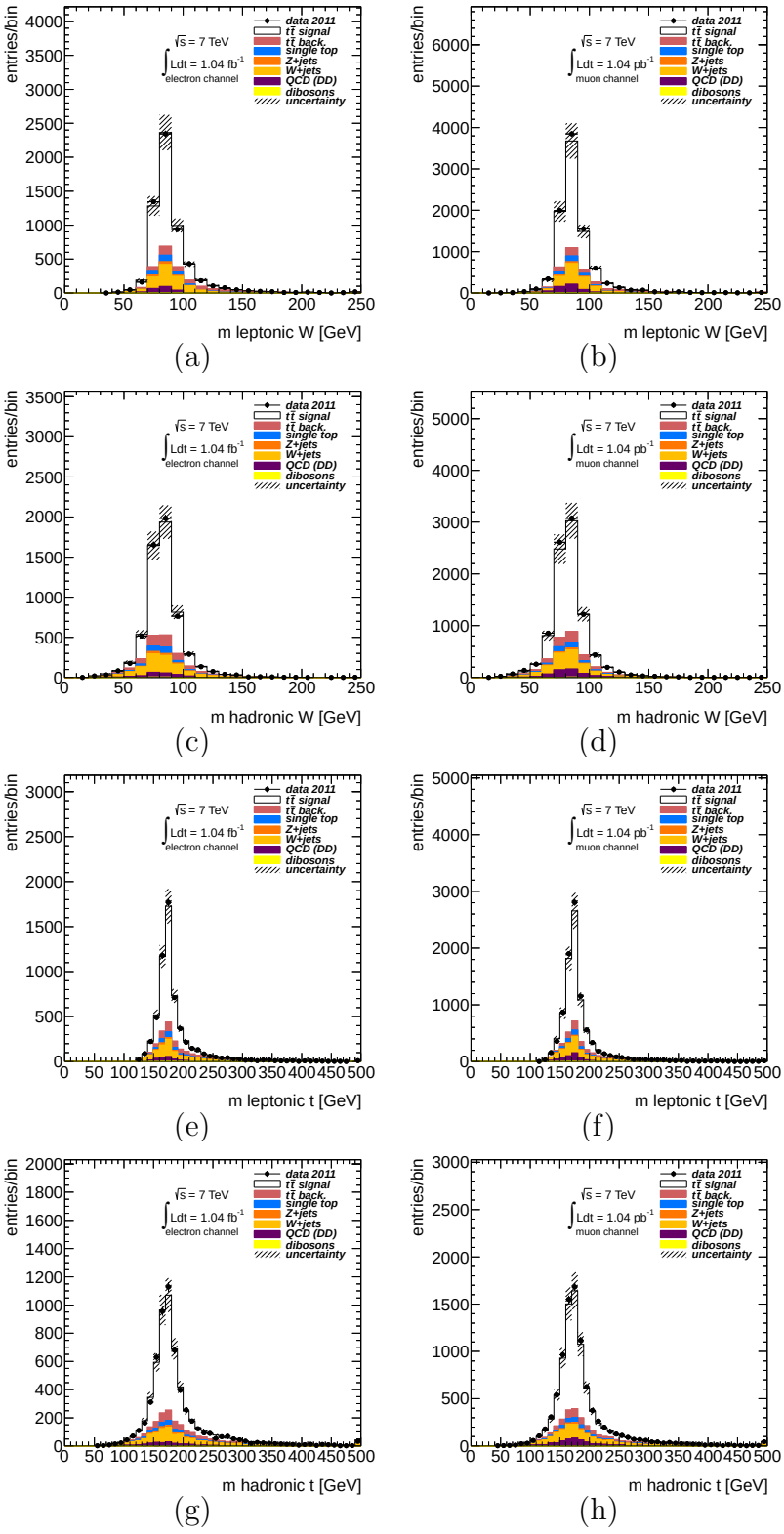

Figure 5.6: Distributions obtained with the χ^2 method of the (a) and (b) leptonic W mass; (c) and (d) hadronic W mass; (e) and (f) leptonic t mass and (g) and (h) hadronic t mass. The left (right) column correspond to the e (μ) channel.

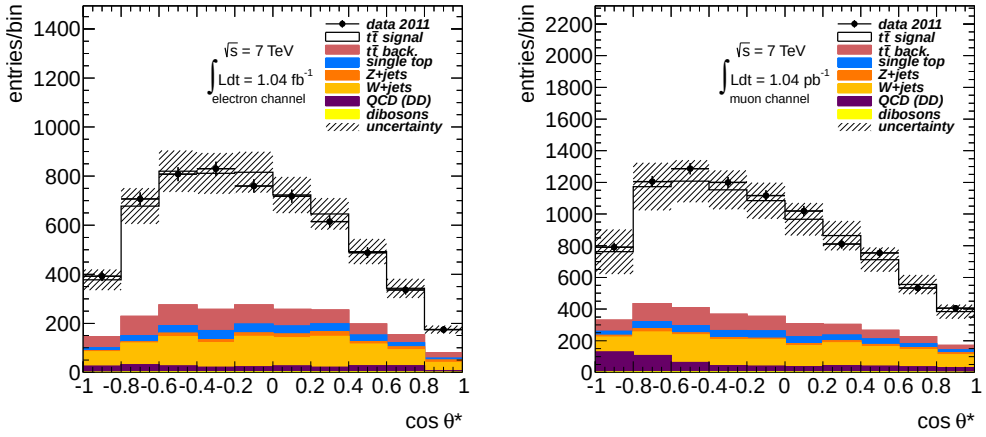

Figure 5.7: $\cos\theta^*$ distributions for the χ^2 method in the (a) e+jets and (b) μ+jets channels.

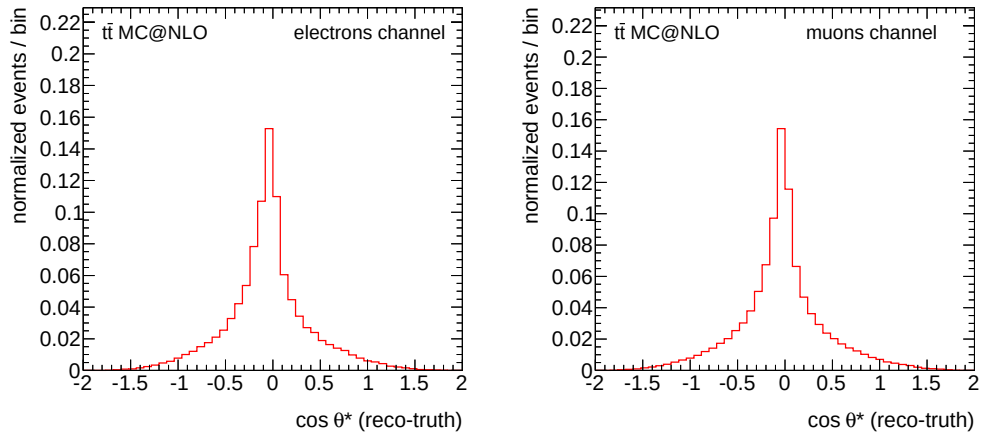

Figure 5.8: The difference between the reconstructed and generated (parton level) $\cos\theta^*$ distribution for the χ^2 method is shown for the (a) e+jets and (b) μ+jets channels.

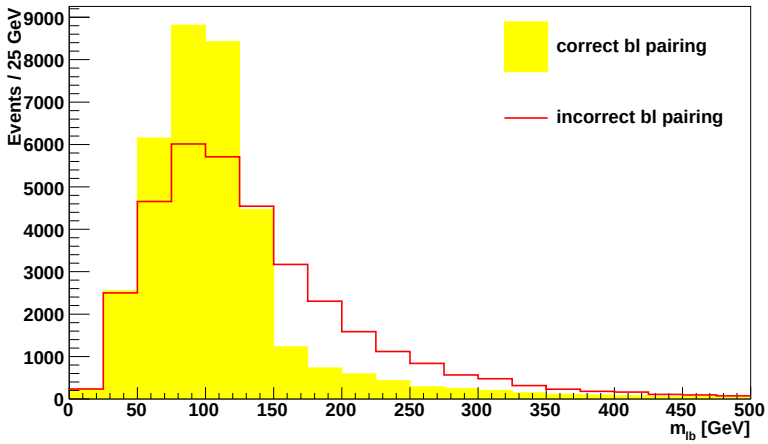

Figure 5.9: The $b\ell$ invariant mass distribution at the reconstruction level is shown for the correct (shaded region) and incorrect (full line) pairing. The distributions are shown at the reconstruction level.

quark jet must be paired with the charged lepton from the same $t(\bar{t})$ quark decay. The criteria used to perform the $b\ell$ pairing are defined as follows. For each event that passes the event selection, there are only two different $b\ell$ pairing possibilities, and these can be represented as $(b_a\ell_a, b_b\ell_b)$ (the correct combination) or $(b_a\ell_b, b_b\ell_a)$ (the incorrect combination). Each term $b_i\ell_j$ $(i, j = a, b)$, denotes the case where the b quark and lepton ℓ originates from the decay of top quark i and j, respectively. The invariant mass $m_{b\ell}$ for the correct and incorrect pairing (with the correct and incorrect assignment being evaluated using parton level information) is shown in Figure 5.9. As can be seen, the combination which gives the lowest value for the invariant mass, most likely corresponds to the correct solution. The mass difference $(m_{b_a\ell_a} + m_{b_b\ell_b}) - (m_{b_a\ell_b} + m_{b_b\ell_a})$ was estimated to be below zero in 67.5% of the cases, using truth information (Figure 5.10). This implies that, by choosing the $b\ell$ pairing combination with a mass difference below zero, a purity of 67.5% is obtained while keeping 100% efficiency for signal events. Here purity means the probability that the pairing has been correctly performed.

An iterative procedure is used to find solutions to the six equations in two steps, fixing the W boson mass to 80.4 GeV:

- *Step one*: the $b\ell$ pairing is chosen using the procedure described above and solutions are evaluated using a top quark mass set to 172.5 GeV. For events where no solution is found, the top mass is varied, in steps of $\pm$1.5 GeV, between 157.5 GeVand 187.5 GeV.

- *Step two*: if the previous step does not result in a solution, the other possible

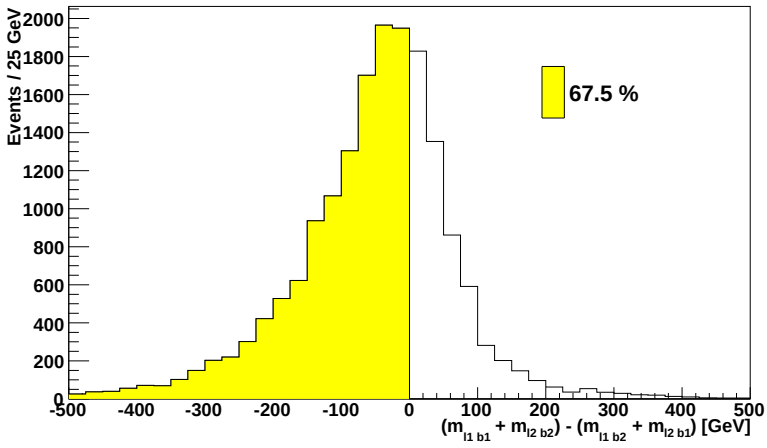

Figure 5.10: The mass difference is shown at the reconstruction level (see text for details). The b-jets and leptons are matched to the corresponding objects at the truth level by using a ΔR criteria. The shaded area corresponds to negative mass difference and constitutes 67.5% of the signal sample.

$b\ell$ pairing is tried and the procedures defined in the first step are repeated once again.

There can be up to four different solutions for the neutrino momenta, for each $t\bar{t}$ dileptonic event. The neutrino solution is chosen from the 2 or 4 possible solutions according to a minimal transverse momenta criteria which is based in the fact that the preferred solution minimizes the product of the reconstructed neutrino and anti-neutrino transverse momenta. This criteria is motivated by the typical low p_{T} spectra of the neutrinos. In 70% of the cases, the solution closest to the generated kinematics is found.

The mass distributions for the top and anti-top quarks, and the p_{T} distributions for the neutrino and anti-neutrino, can be seen in Figure 5.11. The reconstructed angular distributions ($\cos\theta^*$) are shown in Figure 5.12. The difference between the reconstructed and generated (parton level) $\cos\theta^*$ was evaluated using Monte Carlo $t\bar{t}$ simulated signal events. These resolution distributions are shown in Figure 5.13.

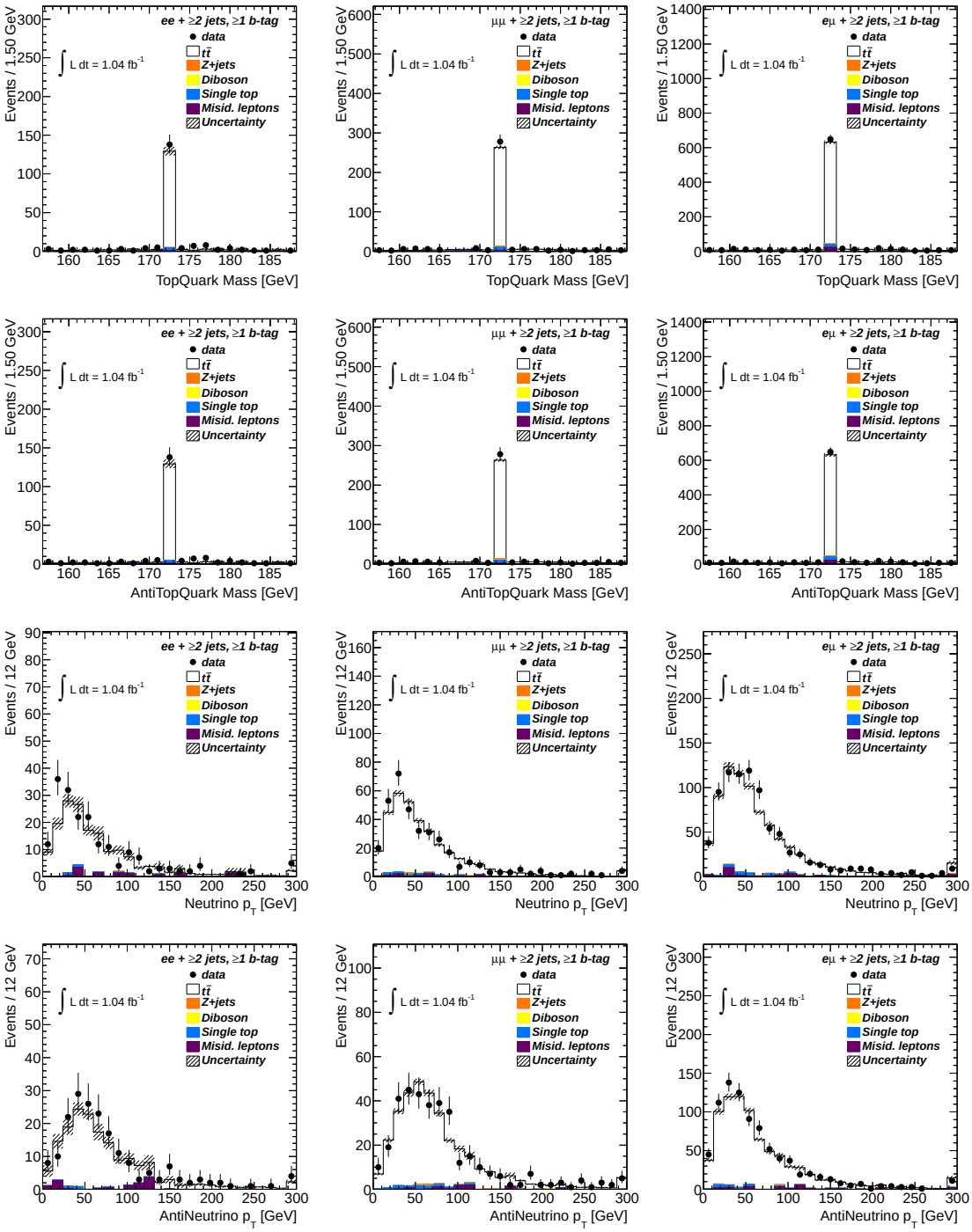

Figure 5.11: Top and anti-top quarks mass distributions, and neutrino and anti-neutrino p_{T} distributions the $e^{-}e^{+}$ (left), $\mu^{-}\mu^{+}$ (center) and $e^{\mp}\mu^{\pm}$ (right) channels.

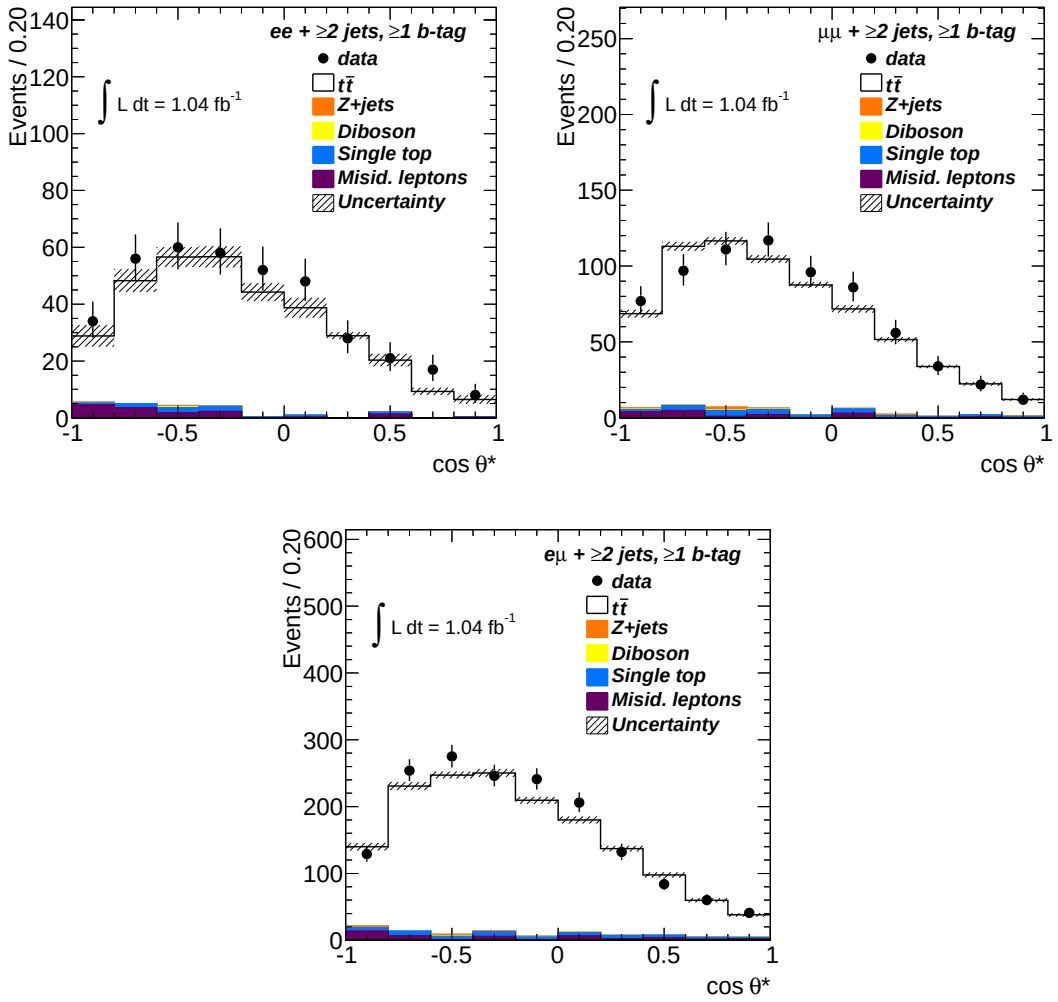

Figure 5.12: Comparison between data and signal+background model for the e^-e^+, $\mu^-\mu^+$ and $e^\mp\mu^\pm$ channels after event selection and full $t\bar{t}$ reconstruction. The figures show the angular distributions ($\cos\theta^*$).

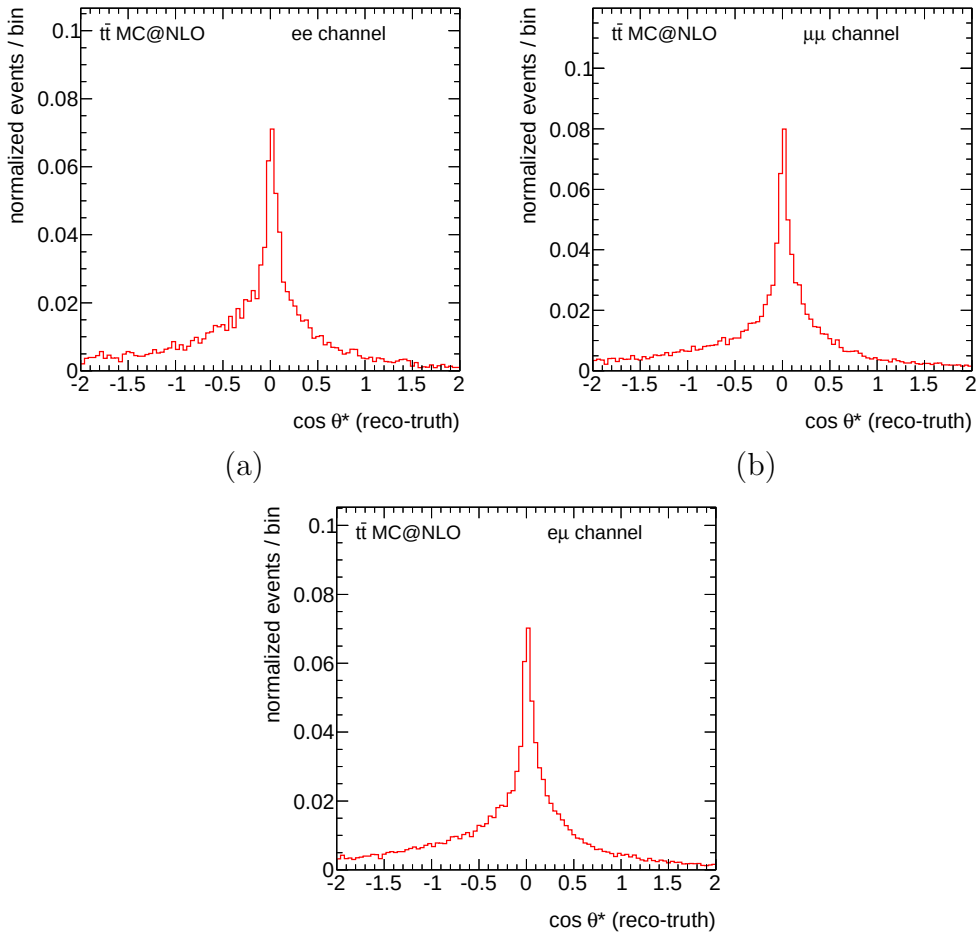

Figure 5.13: The difference between the reconstructed and generated (parton level) $\cos\theta^*$ distribution for the χ^2 method is shown for the (a) e^-e^+ channel, (b) $\mu^-\mu^+$ channel and (c) $e^\mp\mu^\pm$ channel.

5.5 Event Yields

The numbers of events expected after all selection requirements are shown in Table 5.3 for the single-electron and single-muon channels, together with the observed numbers of events in the data sample. The dominant backgrounds in the selected sample are W+jets production, which has the same signature as the $t\bar{t}$ signal, and multijet production. Both W+jets and multijet production are dominated by events with light quarks and gluons which makes tagging of jets produced by b quarks a powerful tool to enrich $t\bar{t}$ signal. The single-electron channel contains significantly fewer events than the single-muon channel due to the more stringent requirements on the lepton E_{T} (p_{T}), $E_{\mathrm{T}}^{\mathrm{miss}}$ and $m_{\mathrm{T}}(W)$. The observed numbers of events are in agreement with those expected, with purities of 75% and 72% for the single electron and single muon channels, where purity means the expected fraction of signal in the data. Example distributions in data are compared with the Standard Model predictions in Figures 5.14 and 5.15. The expected distributions are in good agreement with the data.

The numbers of events expected after all selection requirements are shown in Table 5.4 for the three dilepton channels, together with the observed numbers of events in the data sample. The observed numbers of events are in agreement with those expected, with a purity of 94% for all three channels. Control plots after the final selection and requiring full reconstruction of the $t\bar{t}$ system are shown in Figures 5.16, 5.17 and 5.18, for the $e^{-}e^{+}$, $\mu^{-}\mu^{+}$ and $e^{\pm}\mu^{\mp}$ channels, respectively.

Process	Single electron	Single muon
$t\bar{t}$	4400 ± 1100	6500 ± 1400
W+jets	900 ± 700	1400 ± 1000
Z+jets	120 ± 90	140 ± 90
Diboson	14 ± 12	22 ± 12
Single top	260 ± 90	360 ± 110
Misidentified leptons	220 ± 220	500 ± 500
Total predicted	5900 ± 1300	9000 ± 1800
Data	5830	9121

Table 5.3: Event yields in the single-electron and single-muon channels after the event selection. The table shows the expected number of events including their estimated total uncertainty as well as the number of events observed in the data sample.

Process	ee channel	$\mu\mu$ channel	$e\mu$ channel
$t\bar{t}$	159 ± 28	320 ± 40	750 ± 100
Z+jets (ee,$\mu\mu$)	0.7 ± 2.0	2 ± 4	—
Z+jets ($\tau\tau$)	0.0 ± 3.8	1.4 ± 1.3	4.7 ± 3.1
Diboson	0.2 ± 0.3	0.6 ± 0.3	1.3 ± 0.5
Single top	5.0 ± 1.3	10.8 ± 2.4	24 ± 5
Misidentified leptons	4 ± 2	7 ± 4	19 ± 9
Total predicted	170 ± 30	340 ± 40	800 ± 100
Data	191	354	836

Table 5.4: Event yields in the dilepton channels after the event selection and event reconstruction. The table shows the expected number of events including their estimated total uncertainty as well as the number of events observed in the data sample.

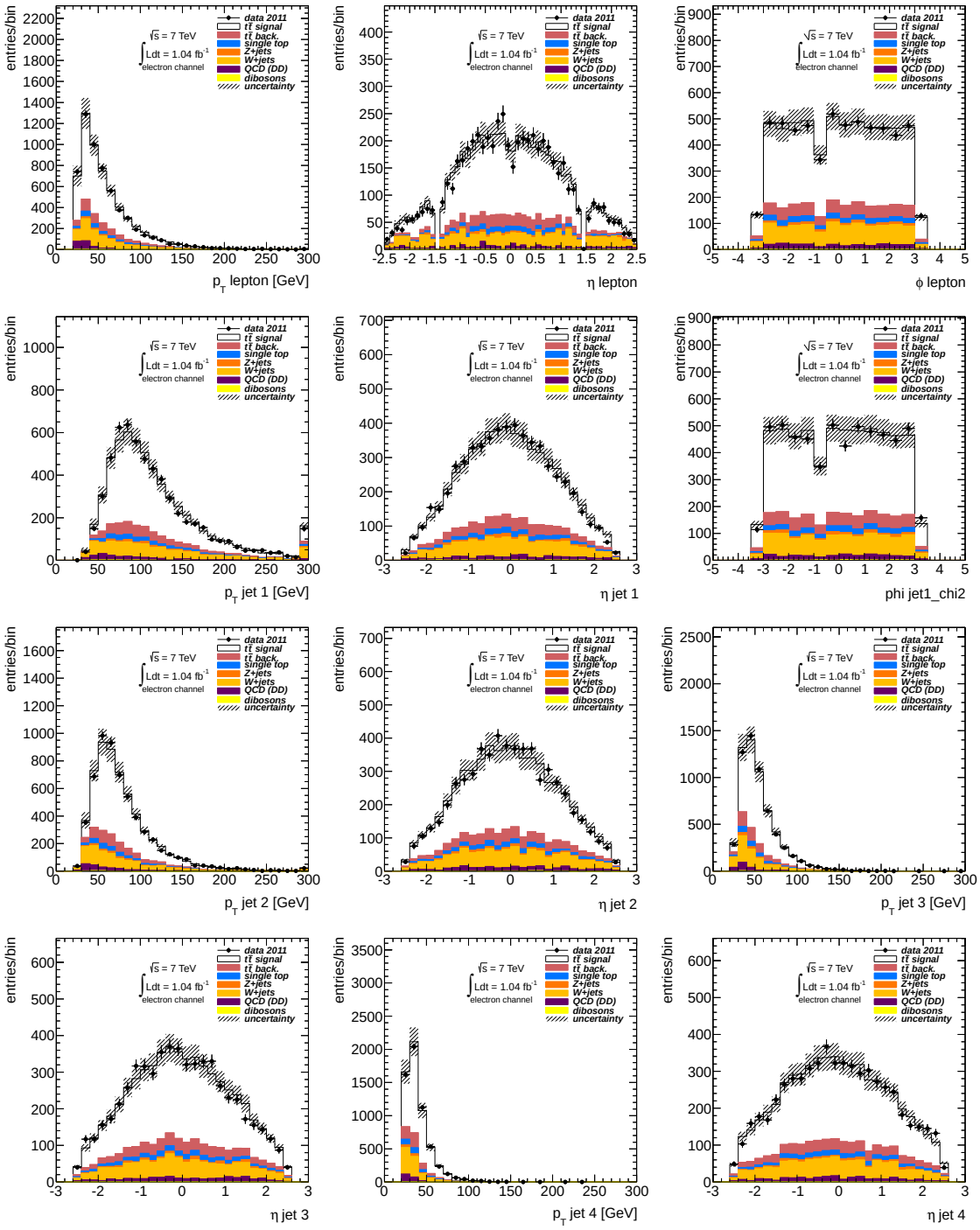

Figure 5.14: Comparison between data and signal+background model in the e+jets channel after event selection. The figures show the distributions of lepton and jet p_T and η.

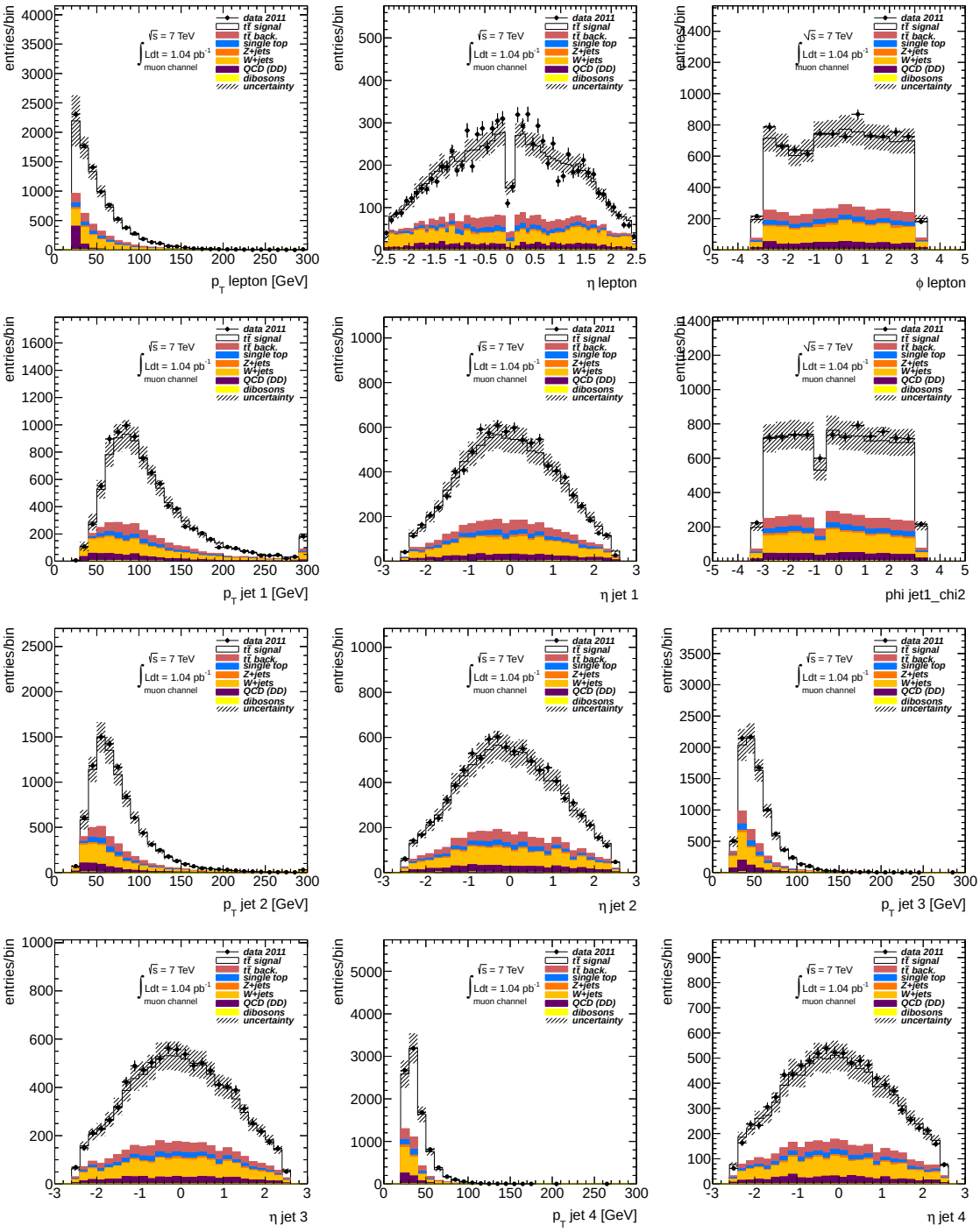

Figure 5.15: Comparison between data and signal+background model in the μ+jets channel after event selection. The figures show the distributions of lepton and jet p_T and η.

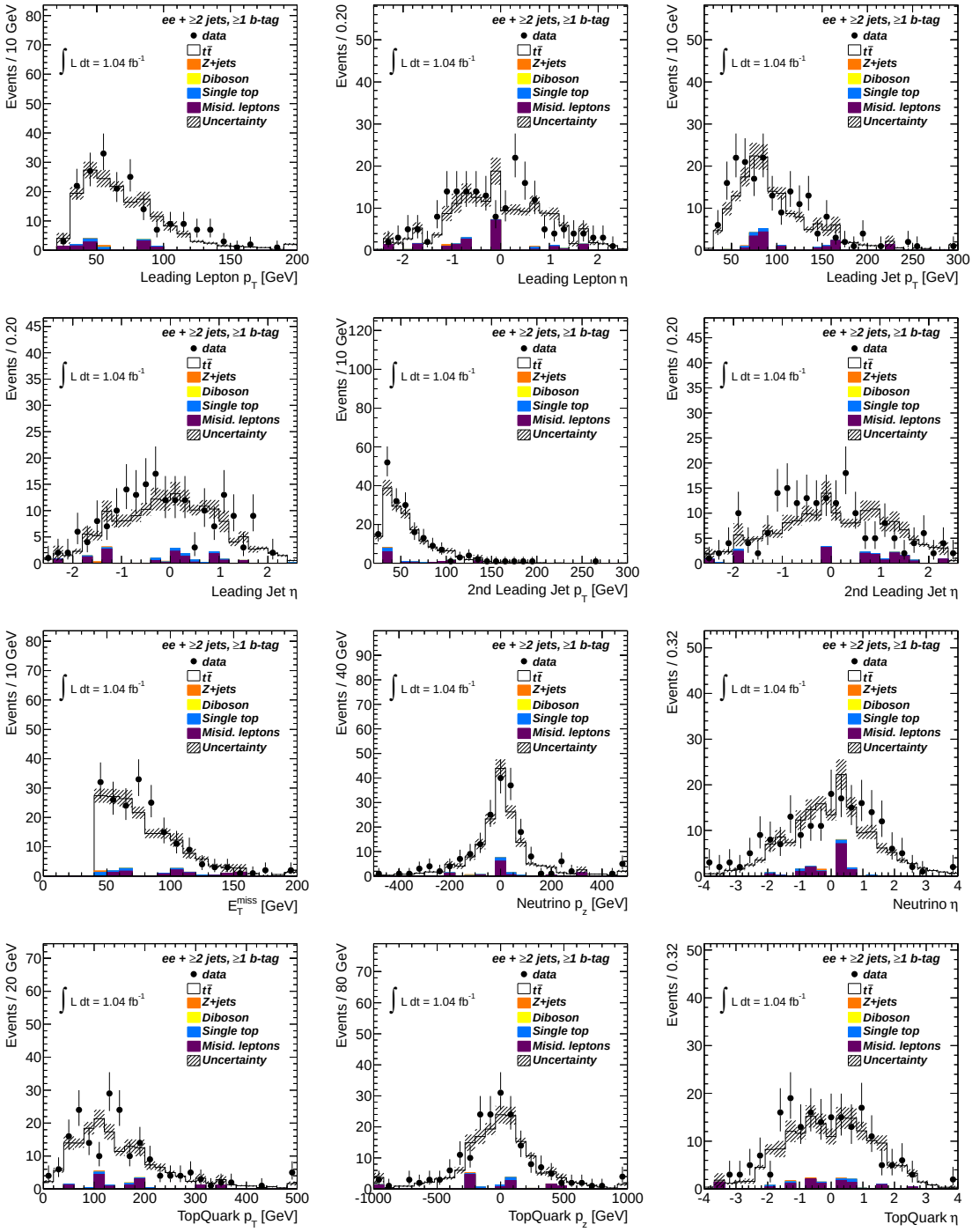

Figure 5.16: Comparison between data and signal+background model in the e^-e^+ channel after event selection and full $t\bar{t}$ reconstruction. The figures show the distributions of lepton and jet p_{T} and η as well as the missing transverse energy $E_{\mathrm{T}}^{\mathrm{miss}}$.

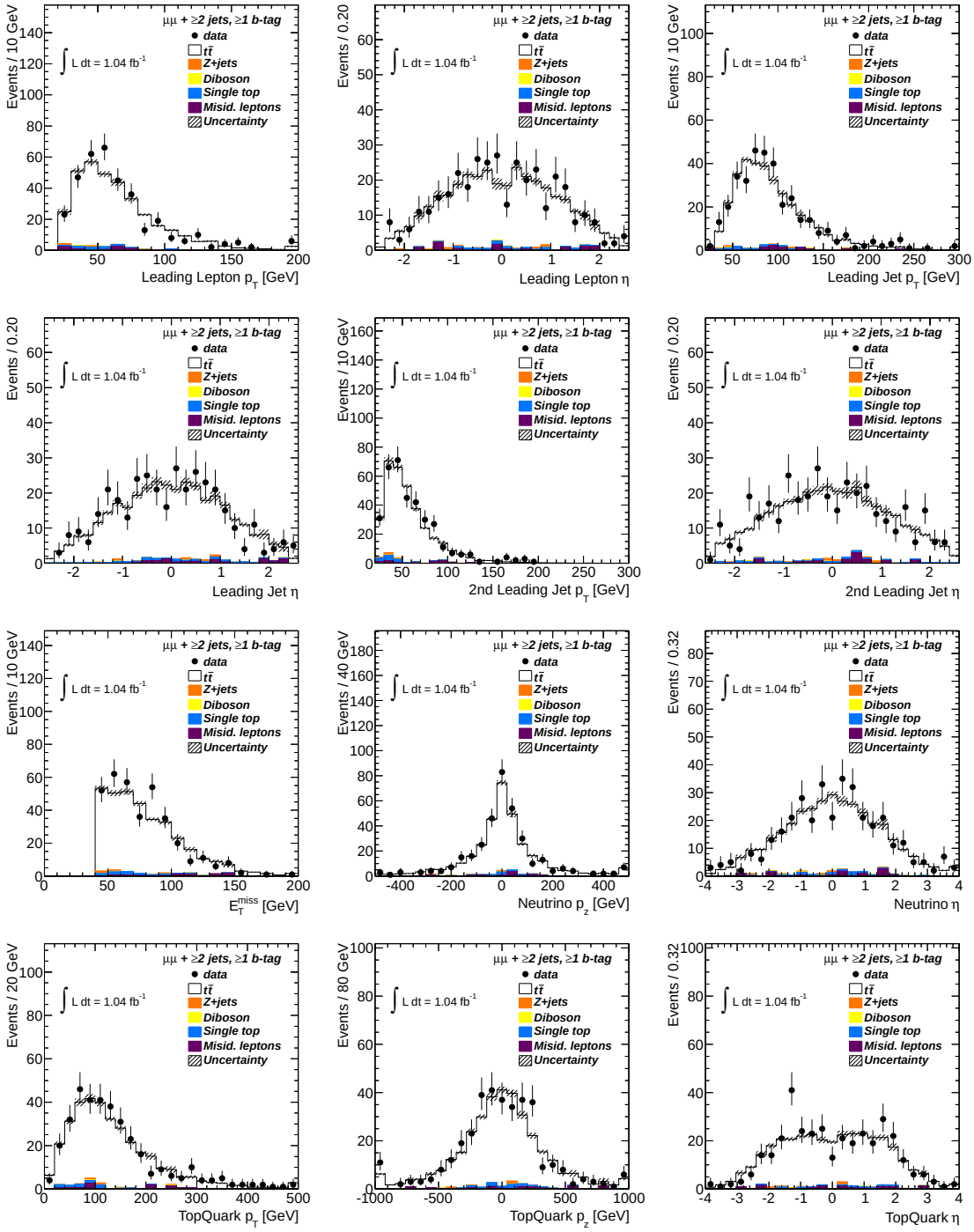

Figure 5.17: Comparison between data and signal+background model in the $\mu^-\mu^+$ channel after event selection and full $t\bar{t}$ reconstruction. The figures show the distributions of lepton and jet p_{T} and η as well as the missing transverse energy $E_{\mathrm{T}}^{\mathrm{miss}}$.

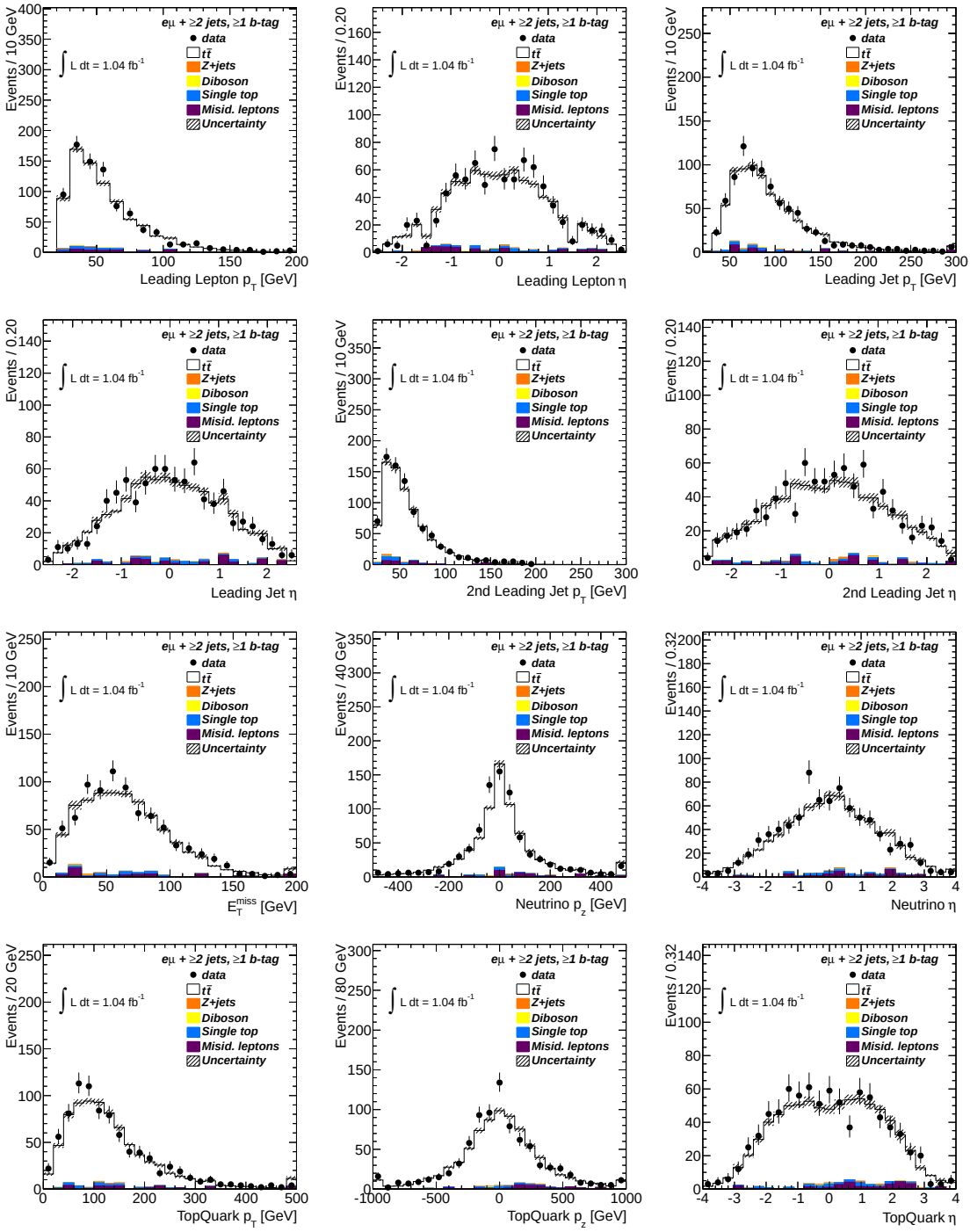

Figure 5.18: Comparison between data and signal+background model in the $e^{\mp}\mu^{\pm}$ channel after event selection and full $t\bar{t}$ reconstruction. The figures show the distributions of lepton and jet p_{T} and η as well as the missing transverse energy $E_{\mathrm{T}}^{\mathrm{miss}}$.

5.6 Results

The angular distributions are distorted by the detector response, the kinematic cuts applied in the trigger and the offline event reconstruction and selection. Following the usual methods used in ATLAS, two unfolding methods may be used to extract the helicity fractions from the reconstructed angular distributions: unfolding using bin-by-bin correction factors (labeled as "correction function method") or using a template method. In the first method, the parton level distribution is recovered by applying bin-by-bin correction factors to the reconstructed $\cos\theta^*$ distribution in order to obtain the corresponding parton level distribution. The template method uses Monte Carlo templates corresponding to different pure helicity states ($F_0 = 1$, $F_{\mathrm{L}} = 1$ and $F_{\mathrm{R}} = 1$) to extract the helicity fractions from the fit to the reconstructed $\cos\theta^*$ distribution. The work of this thesis is based on the correction function method.

For the measurement of the angular asymmetries, A_+ and A_-, the $\cos\theta^*$ distributions are divided into four non-uniform bins, which are used to count the number of events above and below $z = \pm(1 - 2^{2/3})$, as defined in equation (5.2). A background subtraction in the observed $\cos\theta^*$ distribution is performed. Subsequently, the following steps are applied iteratively: the number of reconstructed events above and below $\cos\theta^* = z$ are counted in data for each asymmetry and correction factors are evaluated by comparing the SM expectation with the reconstructed number of simulated $t\bar{t}$ events. These factors, shown in Figure 5.19, allow for corrections to be made for event selection and reconstruction effects. The obtained angular asymmetries are then converted into W boson helicity fractions and these values are used to re-derive the $\cos\theta^*$ distribution and evaluate new correction factors. The procedure is repeated until the method converges, *i.e.* until the differences between the output observables and the input hypothesis at the previous iteration step are below 0.5%. Figure 5.20 shows the distribution of $\cos\theta^*$ in the single lepton and dilepton channels after the background subtraction and the correction for detector and reconstruction effects as used by the asymmetry method as well as the Standard Model expectations. The final results on the angular asymmetries and helicity fractions for the individual single lepton and dilepton channels are summarized in Tables 5.5 and 5.6, respectively. The effects of the systematic uncertainties are discussed in the next section.

Consistency tests were performed using Monte Carlo samples with different helicity fractions and no bias was observed. The convergence of the method can be seen in Figure 5.21, for which pseudo-data with a particular choice of the parameters $(F_0, F_{\mathrm{L}}, F_{\mathrm{R}}) = (0.5, 0.1, 0.4)$ is assumed. As the number of iterations increase the convergence of the measured values to the true values is clearly visible. The calibra-

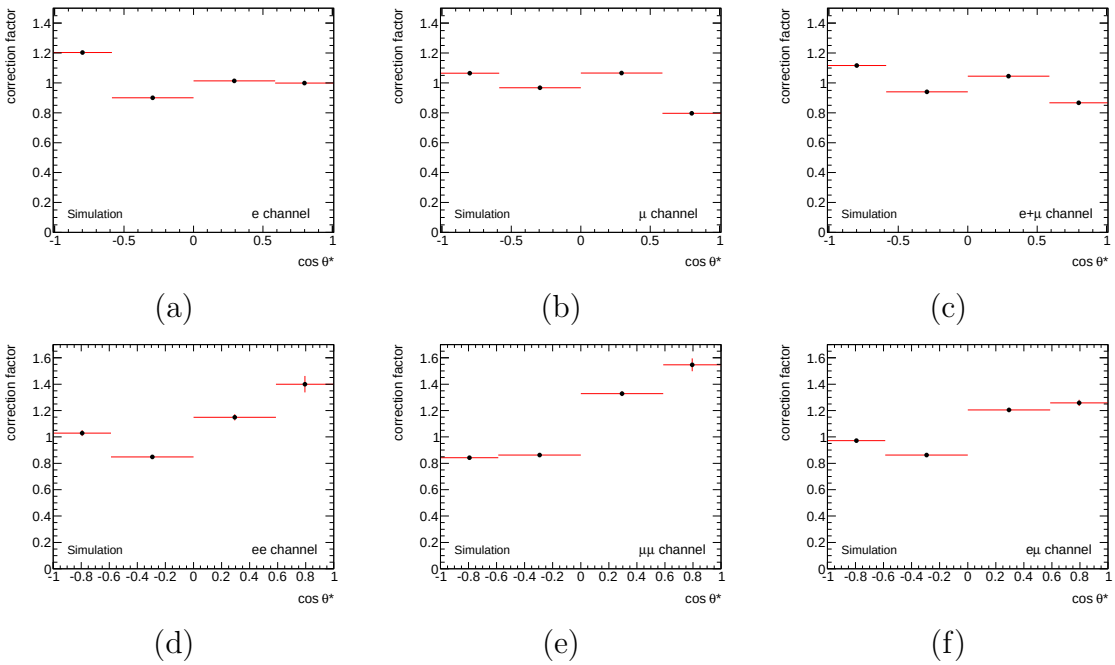

Figure 5.19: Correction functions for the Standard Model hypothesis. The correction functions for the (a) e channel; (b) μ channel; (c) combined $e+\mu$ channels; (d) e^-e^+ channel; (e) $\mu^-\mu^+$ channel and (f) $e^\mp\mu^\pm$ channel are shown.

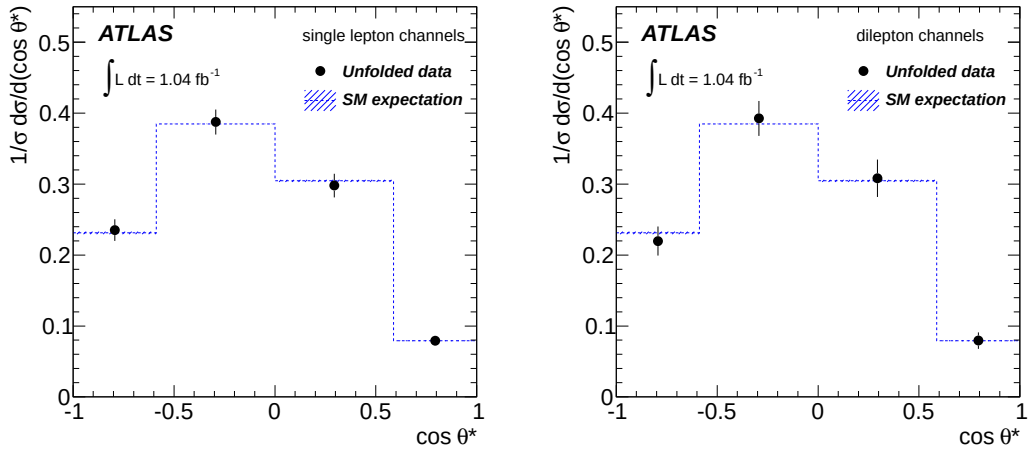

Figure 5.20: Unfolded distributions of $\cos\theta^*$ for the single lepton (left) and dilepton (right) channels. The error bars on unfolded data (markers) include both the statistical and systematic contributions. For comparison, the Standard Model NNLO QCD prediction (dashed line) and its uncertainty are also shown.

	e+jets			μ+jets			combined		
	A_{FB}	A_+	A_-	A_{FB}	A_+	A_-	A_{FB}	A_+	A_-
Central value	-0.244	0.511	-0.839	-0.247	0.541	-0.843	-0.246	0.530	-0.841
Statistical uncertainty	0.022	0.020	0.013	0.017	0.015	0.009	0.013	0.012	0.007
Total syst. uncertainty	0.051	0.035	0.038	0.038	0.061	0.022	0.037	0.046	0.024
Total uncertainty	0.056	0.040	0.040	0.042	0.062	0.024	0.039	0.048	0.025
	F_0	F_{L}	F_{R}	F_0	F_{L}	F_{R}	F_0	F_{L}	F_{R}
Central value	0.638	0.348	0.014	0.697	0.305	-0.002	0.673	0.322	0.005
Statistical uncertainty	0.044	0.028	0.020	0.032	0.021	0.014	0.025	0.017	0.011
Total syst. uncertainty	0.095	0.051	0.055	0.116	0.085	0.039	0.095	0.065	0.039
Total uncertainty	0.104	0.059	0.059	0.120	0.087	0.041	0.098	0.067	0.040

Table 5.5: Summary of the angular asymmetries and W helicity fractions for the single lepton channel.

	e^-e^+			$\mu^-\mu^+$			$e^{\mp}\mu^{\pm}$		
	A_{FB}	A_+	A_-	A_{FB}	A_+	A_-	A_{FB}	A_+	A_-
Central value	-0.198	0.543	-0.785	-0.192	0.595	-0.859	-0.245	0.547	-0.847
Statistical uncertainty	0.061	0.055	0.041	0.044	0.032	0.027	0.028	0.024	0.017
Total syst. uncertainty	0.091	0.072	0.055	0.069	0.050	0.060	0.059	0.038	0.037
Total uncertainty	0.109	0.091	0.068	0.082	0.059	0.066	0.065	0.045	0.040
	F_0	F_{L}	F_{R}	F_0	F_{L}	F_{R}	F_0	F_{L}	F_{R}
Central value	0.599	0.324	0.077	0.818	0.225	-0.043	0.726	0.280	-0.006
Statistical uncertainty	0.126	0.079	0.062	0.078	0.047	0.041	0.053	0.034	0.026
Total syst. uncertainty	0.166	0.104	0.083	0.142	0.074	0.086	0.097	0.055	0.054
Total uncertainty	0.208	0.130	0.103	0.162	0.088	0.095	0.111	0.065	0.060

Table 5.6: Summary of the angular asymmetries and W helicity fractions for the dilepton channel.

tion curves showing that the correction function method can measure the angular asymmetries in an unbiased way are shown in Figures 5.22 and 5.23, for the single lepton and dilepton channels, respectively.

The statistical error evaluation was validated by building 5000 ensembles, each one of them corresponding to a pseudo-data distribution of $\cos\theta^*$ for an integrated luminosity of around 1.04 fb^{-1}. These pseudo-data distributions were built by varying each $\cos\theta^*$ bin according to a Poisson distribution. For each pseudo-data distribution the correction function method was used, performing the background subtraction, applying the correction function and evaluating the angular asymmetries and corresponding errors. The pull distributions, defined as the difference of the measured and the expected SM value for each observable (A_{FB}, A_+ and A_-), normalized to the statistical uncertainty for each pseudo-data distribution, are shown in Figure 5.24 for the single lepton channels, and in Figure 5.25 for dilepton channels. The distribution of the expected errors for each observable are shown in Figures 5.26 and 5.27 for the single lepton and dilepton channels, respectively. The dependence of the

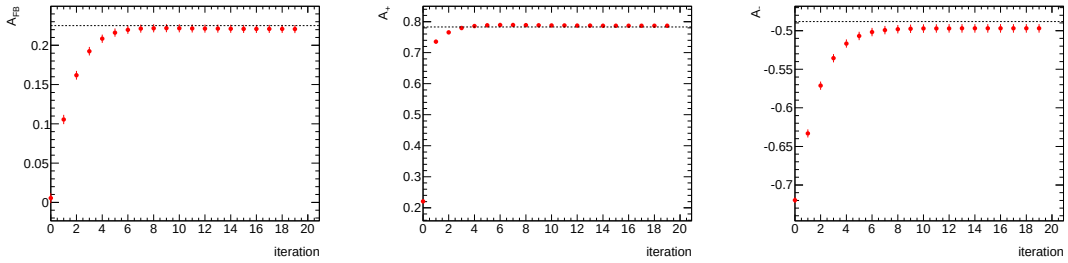

(a) (b) (c)

Figure 5.21: The convergence of the iterative procedure in the correction function method is shown for a pseudo-data with the W helicity fractions set to $(F_0, F_{\mathrm{L}}, F_{\mathrm{R}}) = (0.5, 0.1, 0.4)$. The output of the (a) A_{FB}, (b) A_+ and (c) A_- is represented as a function of the iteration number. The dashed horizontal line represents the generated value of the asymmetries in the pseudo-data.

corrected angular asymmetries with the number of reconstructed vertices in data is shown in Figure 5.28.

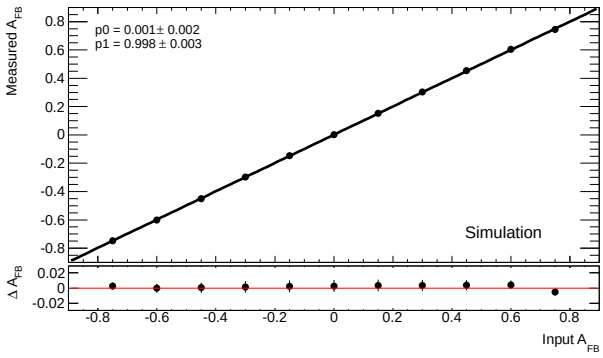

(a)

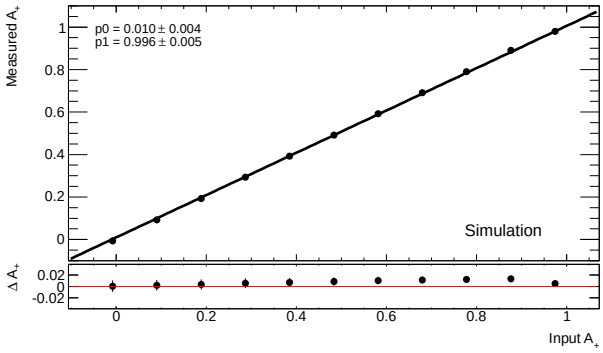

(b)

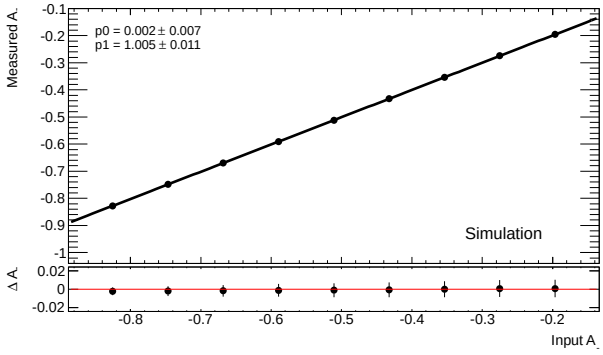

(c)

Figure 5.22: Calibration curves for the correction function method (single lepton topology): (a) A_{FB} asymmetry; (b) A_+ asymmetry and (c) A_- asymmetry.

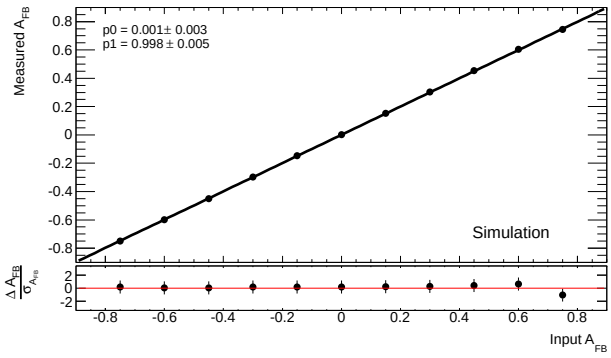

(a)

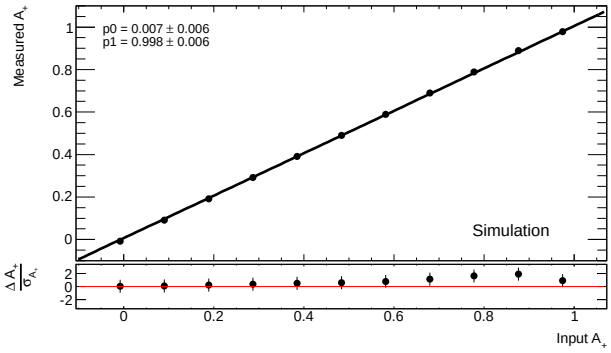

(b)

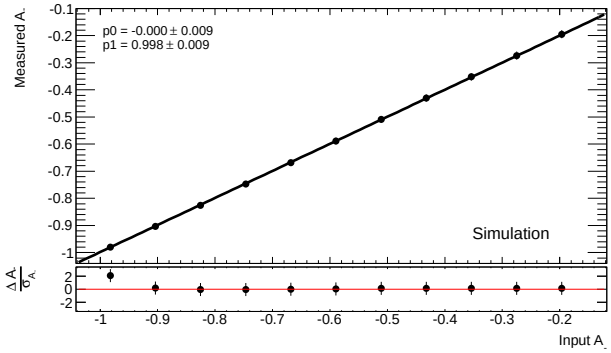

(c)

Figure 5.23: Calibration curves for the correction function method (dilepton topology): (a) A_{FB} asymmetry; (b) A_+ asymmetry and (c) A_- asymmetry.

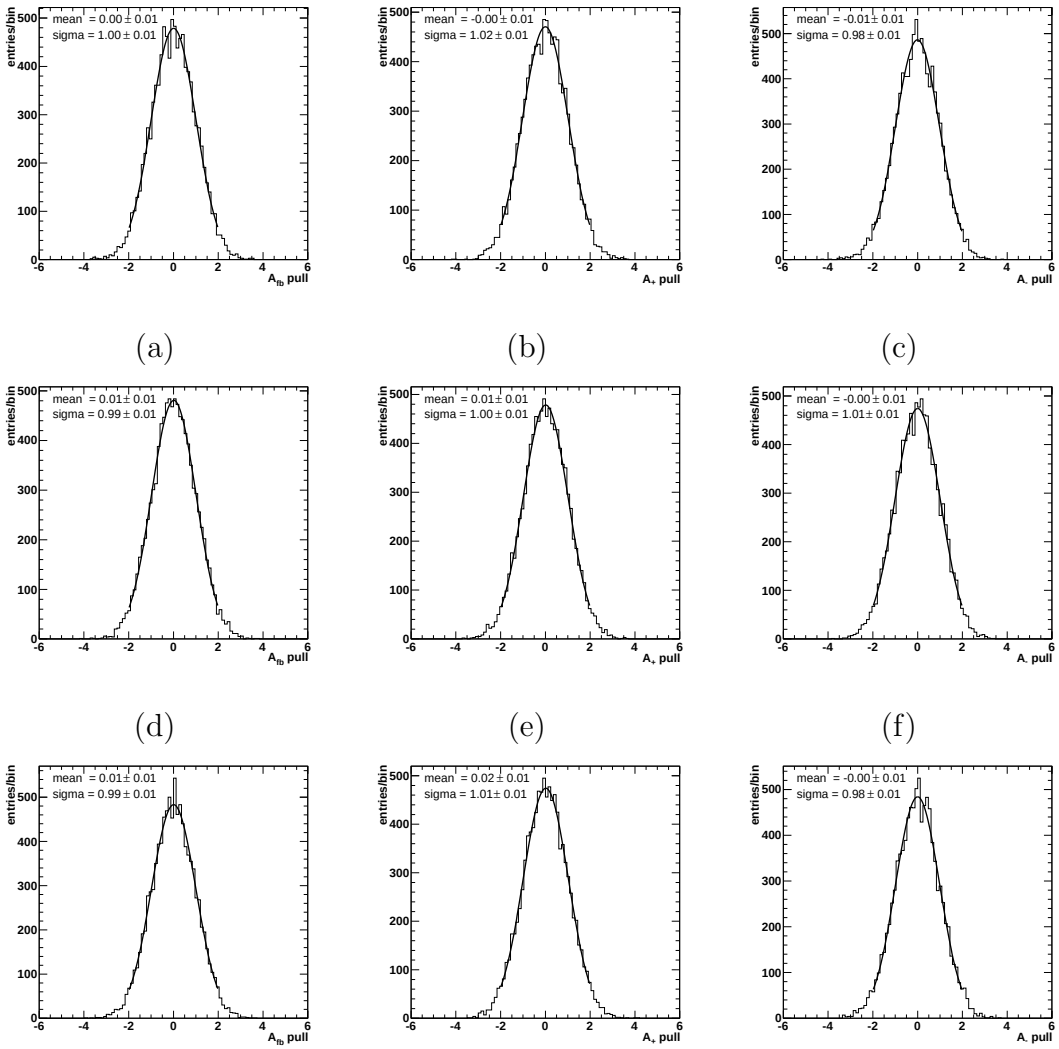

Figure 5.24: Pull values for angular asymmetries obtained for the e+jets channel (upper row), the μ+jets channel (middle row) and for the combined results (lower row) for the correction function analysis (single lepton topology). 5000 pseudo experiments based on the data distribution of $\cos\theta^*$ were used. Monte Carlo was normalized to a luminosity of 1.04 fb^{-1}.

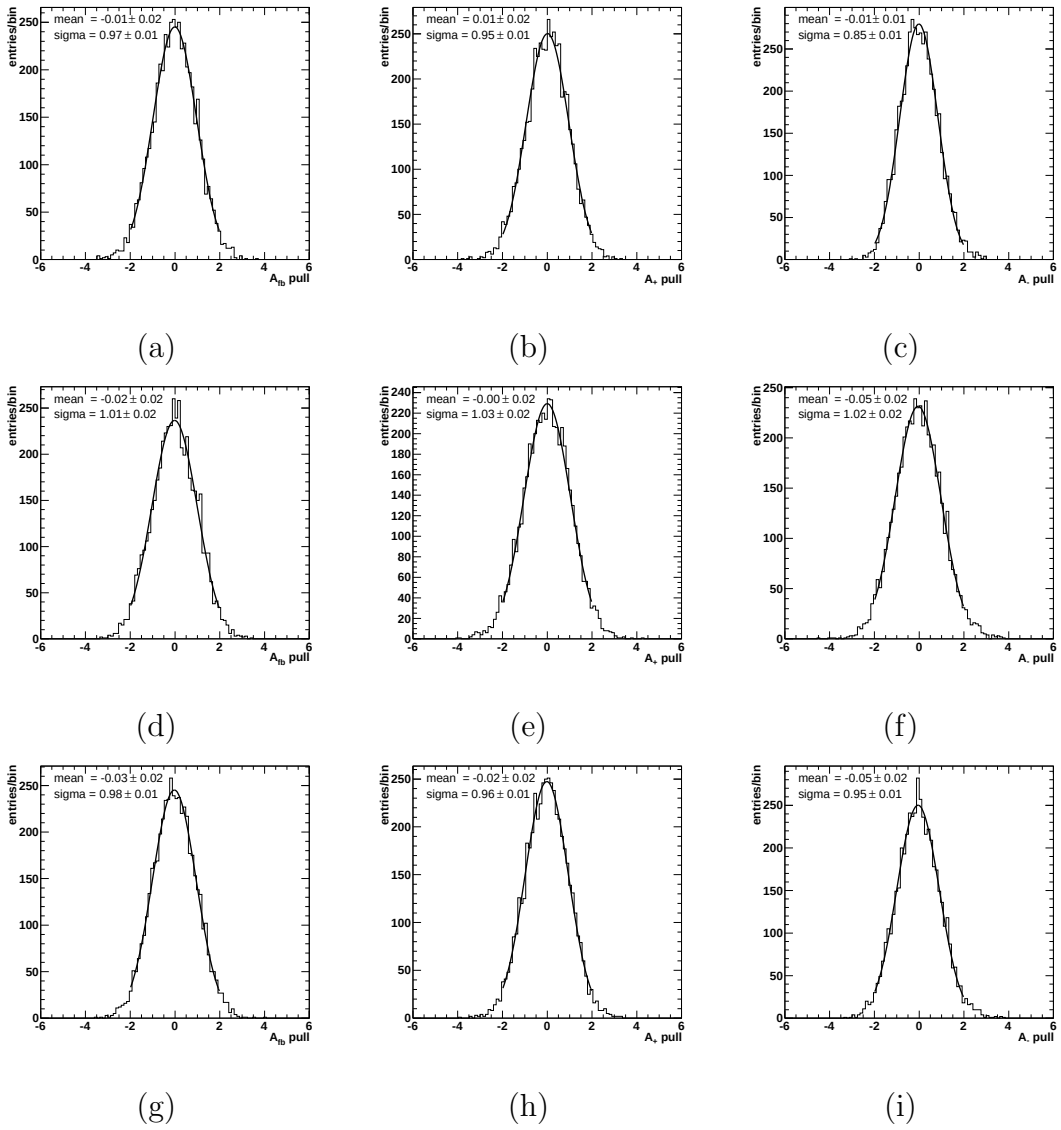

Figure 5.25: Pull values for angular asymmetries obtained for the e^-e^+ channel (upper row), the $\mu^-\mu^+$ (middle row) and the $e^\mp\mu^\pm$ results (lower row) for the correction function analysis (dilepton topology). 5000 pseudo experiments based on the data distribution of $\cos\theta^*$ were used. Monte Carlo was normalized to a luminosity of 1.04 fb^{-1}.

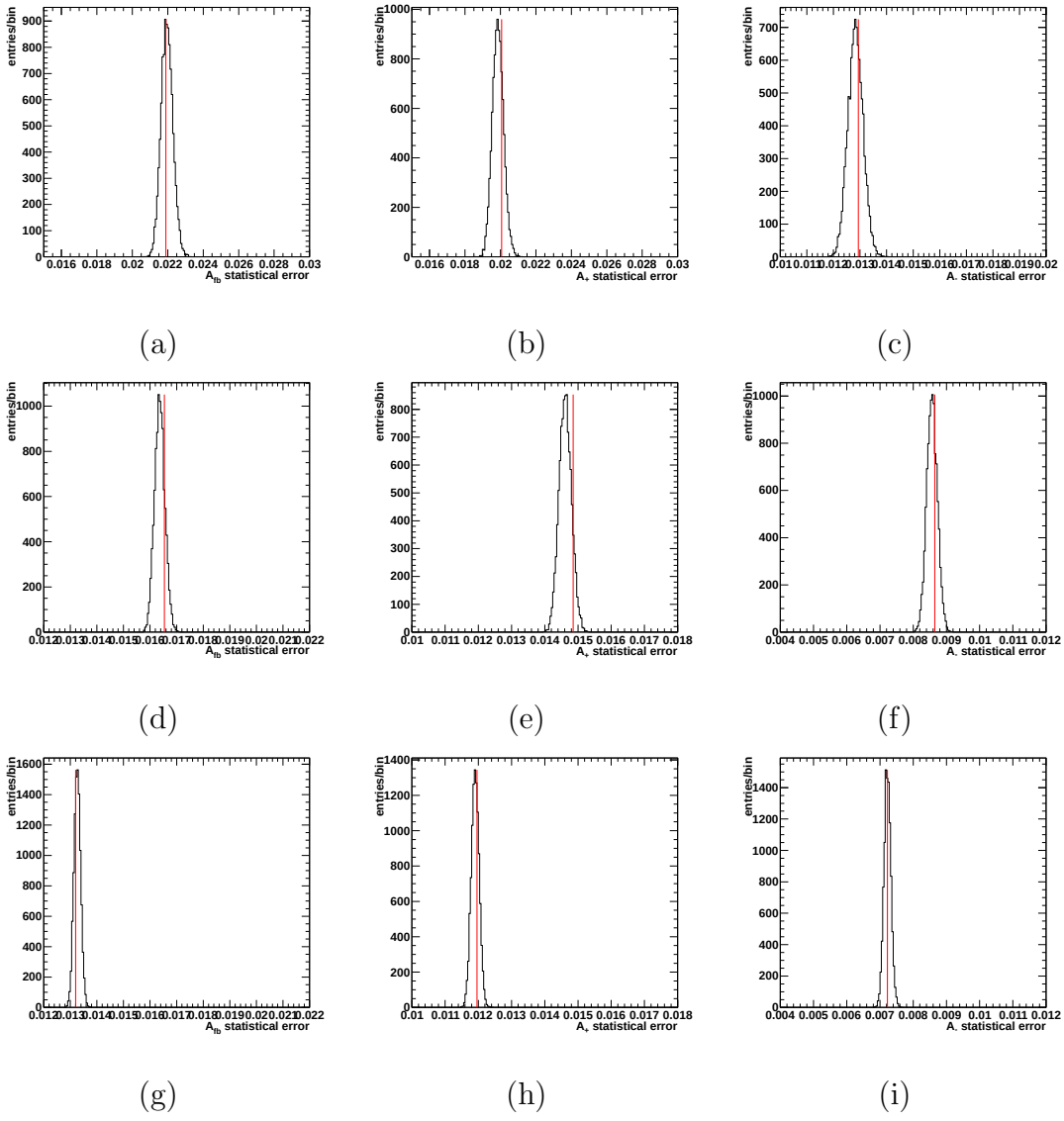

Figure 5.26: Distributions of the expected angular asymmetries statistical errors, obtained for the e+jets channel (upper row), the μ+jets channels (middle row) and the combined results (lower row) for the correction function analysis (single lepton topology). 5000 pseudo experiments based on the data distribution of $\cos\theta^*$ were used. The measured error for each observable is represented by the vertical line. Monte Carlo was normalized to a luminosity of 1.04 fb^{-1}.

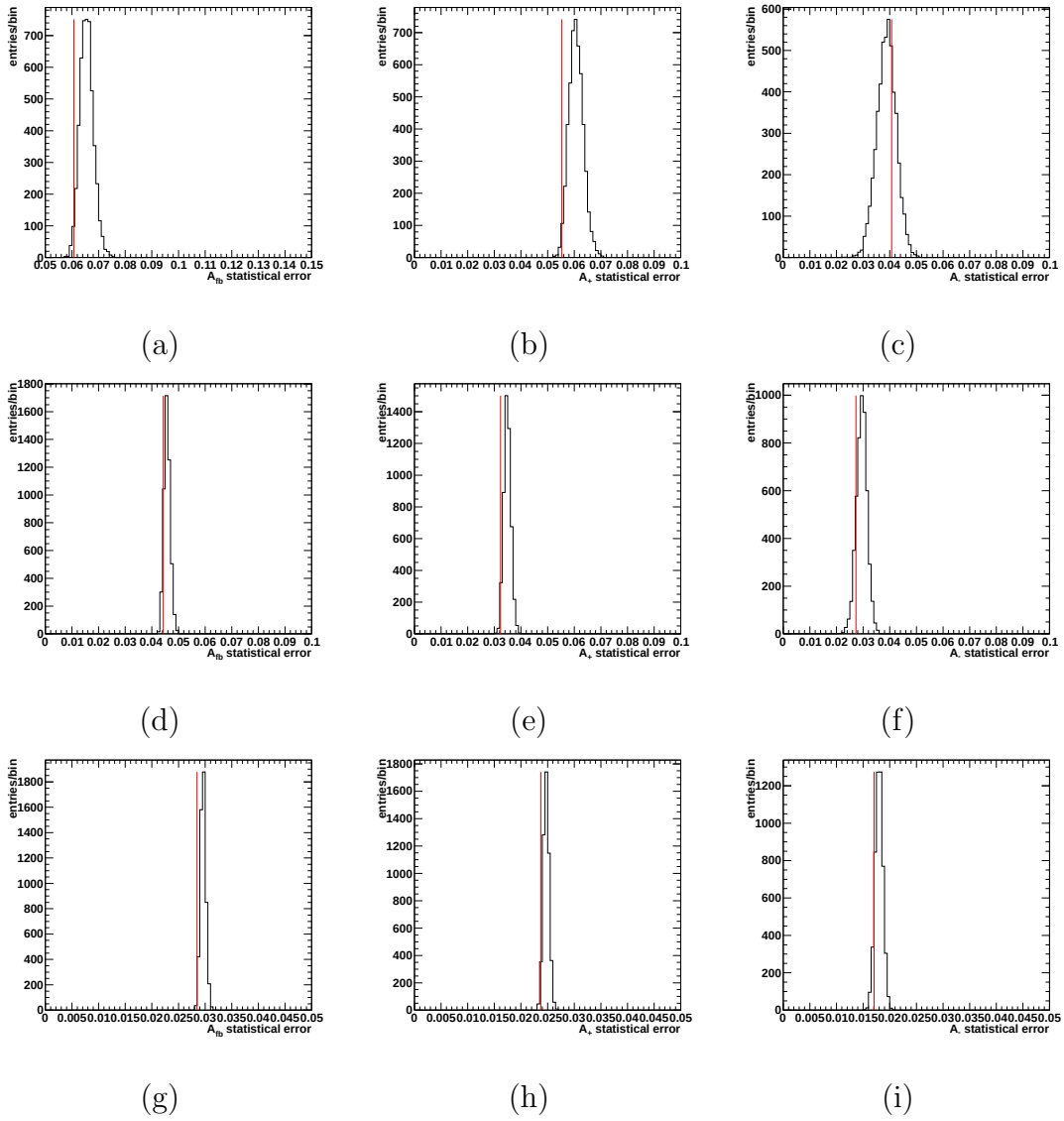

Figure 5.27: Distributions of the expected angular asymmetries statistical errors, obtained for the e^-e^+ channel (upper row), the $\mu^-\mu^+$ (middle row) and the $e^\mp\mu^\pm$ results (lower row) for the correction function analysis (dilepton topology). 5000 pseudo experiments based on the data distribution of $\cos\theta^*$ were used. The measured error for each observable is represented by the mean value of the distribution.

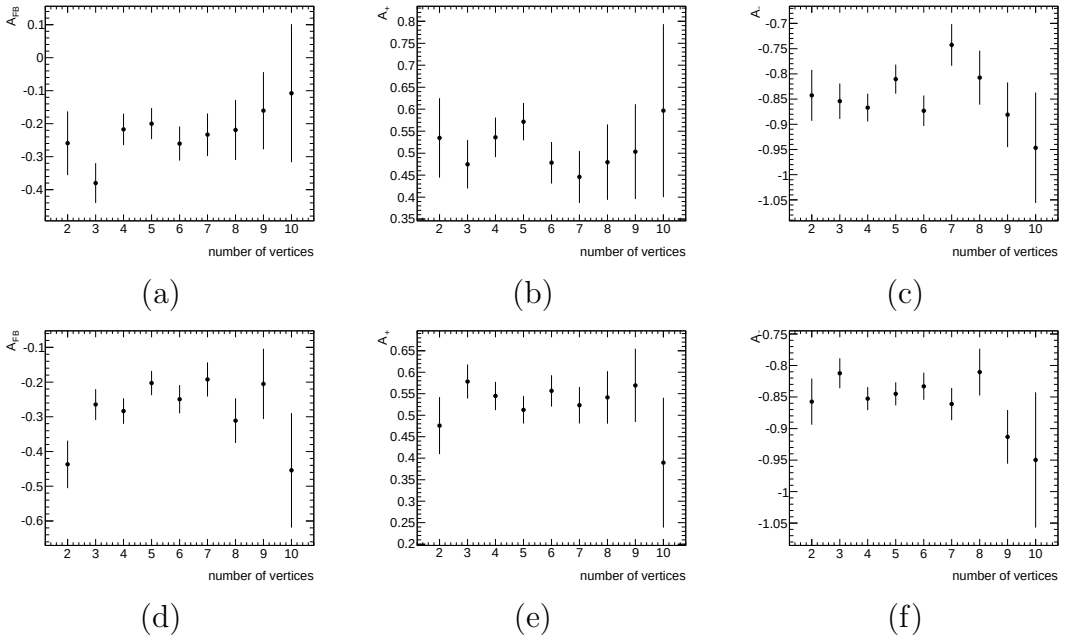

Figure 5.28: The dependence of the corrected angular asymmetries with the number of reconstructed vertices in data is shown: (a-c) single electron channel; (d-f) single muon channel.

5.6.1 Systematic Uncertainties

Several sources of systematic uncertainty were taken into account in the analyses presented here. These were categorized into the modelling of the signal and background processes, the detector modelling, and the reconstruction method. For each source of uncertainty, an ensemble of 5000 pseudoexperiments was created. The average of the observables in each ensemble is compared with the expected value of the observable (evaluated without the systematic change), and the difference is quoted as the systematical error.

Signal and background modelling

The signal process was modelled with different Monte Carlo generators. Sources of systematic uncertainty considered here were the choice of generator and parton shower model, the choice of parton distribution functions, the assumed top quark mass and the choice of parameters which control the amount of initial and final state radiation. Predictions from the MC@NLO and POWHEG generators were compared. The parton showering was tested by comparing two POWHEG samples interfaced to HERWIG and PYTHIA, respectively. The amount of initial and final state radiation was varied by modifying parameters in ACERMC interfaced to PYTHIA. The parameters were varied in a range comparable with those used in the

Perugia Soft/Hard tune variations [203]. The impact of the choice of parton distribution functions was studied using the reweighting procedure described in [204]. MC@NLO samples were generated assuming different top quark masses and their predictions were compared. The observed differences in the results were scaled to variations of 0.9 GeV in the top quark mass according to the uncertainty on its Tevatron average value [1]. The impact of different models of colour reconnection was studied by comparing samples simulated with AcerMC using the Perugia 2010 tune with and without colour reconnection [203] as well as the tune A-Pro and ACR-Pro [205, 206].

Background processes were either modelled by simulation or were estimated in auxiliary measurements. The number of events with misidentified leptons was estimated in data for each channel [195] and the uncertainty on the normalization was estimated to be 50% before and 100% after the b-tagging requirement. The normalization of W+jets processes was estimated from supplementary measurements using the asymmetric production of positively and negatively charged $W^{\pm}$ bosons. The uncertainty was estimated using Berends-Giele-scaling [207] which yielded 48% for events with four jets and increased with the jet multiplicity by 24% per additional jet [196]. Systematic uncertainties on the shapes of the W+jets distributions were assigned based on samples with different simulation parameters such as the minimum transverse momentum of the parton and the functional form of the factorization scale in Alpgen. Scaling factors correcting the fraction of heavy flavor contributions in simulated W+jets samples were estimated in auxiliary measurements described in [195]. The uncertainties were 76% for $Wb\bar{b}$+jets and $Wc\bar{c}$+jets contributions, and 35% for Wc+jets contributions. The uncertainty on the normalization of Z+jets events was estimated using Berends-Giele-scaling. The uncertainties in the normalization were 48% for events with four jets and increased with the jet multiplicity by 24% per additional jet. A systematic uncertainty in the shape was accounted for by comparing simulated samples generated with Alpgen and Sherpa. The uncertainty on the normalization of the small background contributions from single top quark and diboson production was estimated to be about 10% (depending on the channel) and 5%, respectively. The former estimate was based on the difference between the predictions from MC@NLO and MCFM [208], whereas the latter comes from scale and PDF uncertainties evaluated with MCFM.

Detector modelling

The mis-modelling of lepton trigger, reconstruction and selection efficiencies in simulation was corrected for by scale factors derived from auxiliary measurements of the processes $Z \to \mu\mu$ and $Z \to ee$ [199, 200]. The uncertainties were evaluated by

changing the event selection of the supplementary measurement and by testing the stability of the results against changing LHC and ATLAS run conditions. The same processes were used to measure the lepton momentum scale and resolution. Scale factors and their uncertainties were derived to match the simulation to observed distributions. Details are given in [196].

The jet energy scale was derived using information from test-beam data, LHC collision data and simulation. Its uncertainty varies between 2.5% and 7% in the central η region, depending on jet p_{T} and η [209]. This includes uncertainties in the flavor composition of the samples and mis-measurements from close-by jets. An additional p_{T}-dependent uncertainty of up to 2.5% was assigned to jets matched to b-quarks (using Monte Carlo generator-level information) due to differences between light-quark and gluon jets as opposed to jets containing b-hadrons. Additional uncertainties of up to 5% (8%) in the central (forward) region were added due to pileup. The energy resolution for jets in Monte Carlo simulation was adjusted to that observed in data. Uncertainties on the energy resolution of 4–45%, decreasing with jet p_{T}, were assigned. The reconstruction efficiency of jets was found to be in good agreement with the predictions from simulation and uncertainties of 1–2% were assigned.

The uncertainties on the momenta of electrons, muons and jets were propagated into the missing transverse momentum, and a 10% uncertainty from pileup was added.

The b-tagging efficiencies and mis-tag rates have been measured in data [210]. Jet p_{T}-dependent scale factors, applied to simulation to match the data, have uncertainties which range from 9% to 16% and 12% to 45%, respectively.

The uncertainty on the measured luminosity was estimated to be 3.7% [173].

Due to a hardware failure, a small, rectangular region of the ATLAS electromagnetic calorimeter could not be read out in a subset of the data (0.87 fb^{-1}). Data and Monte Carlo events in which a jet or an electron were close to the affected calorimeter region were rejected. The calorimeter readout systematic uncertainty was evaluated by varying the criteria to reject these events.

Reconstruction method

For the χ^2 method, the relative uncertainty between the top quark and W boson mass resolutions (σ_{t} and σ_{W} in equation (5.5)) was addressed by evaluating the effect of changing 25% the mass resolutions. The largest deviation was taken as the uncertainty associated with the reconstruction method. The systematic uncertainty for the dileptonic reconstruction method was estimated in a similar fashion.

Source	e+jets			μ+jets			combined		
	A_{FB}	A_+	A_-	A_{FB}	A_+	A_-	A_{FB}	A_+	A_-
Statistical uncertainty	0.022	0.020	0.013	0.017	0.015	0.009	0.013	0.012	0.007
Luminosity	0.004	0.001	0.002	0.002	0.000	0.002	0.003	0.001	0.002
MET pileup	0.003	0.001	0.002	0.002	0.002	0.005	0.000	0.001	0.003
MET LAr hole	0.003	0.002	0.001	0.002	0.001	0.001	0.002	0.001	0.001
MET cell-out	0.003	0.003	0.002	0.003	0.002	0.004	0.000	0.002	0.003
Lepton trigger	0.004	0.002	0.002	0.005	0.001	0.004	0.004	0.002	0.004
Lepton energy scale	0.008	0.003	0.004	0.002	0.001	0.002	0.004	0.001	0.002
Lepton energy resolution	0.011	0.004	0.019	0.007	0.017	0.002	0.002	0.012	0.008
Lepton reconstruction	0.005	0.004	0.002	0.002	0.001	0.002	0.003	0.001	0.002
Jet energy scale	0.009	0.013	0.019	0.016	0.006	0.009	0.008	0.006	0.013
Jet energy resolution	0.004	0.015	0.017	0.013	0.024	0.001	0.007	0.020	0.006
Jet reconstruction	0.003	0.002	0.000	0.000	0.001	0.000	0.001	0.000	0.000
b-tagging	0.010	0.004	0.005	0.004	0.002	0.003	0.007	0.003	0.004
PDF	0.002	0.003	0.003	0.002	0.003	0.003	0.002	0.003	0.003
ISR/FSR	0.025	0.013	0.010	0.013	0.011	0.008	0.018	0.008	0.008
Showering/hadronization	0.002	0.005	0.002	0.005	0.004	0.001	0.002	0.001	0.001
$t\bar{t}$ generator	0.011	0.009	0.001	0.008	0.007	0.001	0.010	0.007	0.001
Color reconnection	0.006	0.008	0.004	0.003	0.002	0.001	0.004	0.001	0.002
Top mass	0.019	0.001	0.001	0.004	0.003	0.008	0.011	0.002	0.005
W+jets bkg norm.	0.022	0.005	0.006	0.012	0.006	0.010	0.017	0.006	0.008
W+jets bkg shape	0.004	0.003	0.003	0.002	0.001	0.001	0.002	0.002	0.001
HF content of W+jets	0.013	0.004	0.005	0.007	0.002	0.005	0.010	0.003	0.005
Z+jets bkg norm.	0.009	0.005	0.004	0.003	0.001	0.002	0.005	0.002	0.003
QCD bkg norm.	0.007	0.010	0.009	0.018	0.049	0.003	0.008	0.035	0.005
QCD bkg shape	0.008	0.012	0.008	0.001	0.003	0.000	0.003	0.006	0.002
Diboson norm.	0.001	0.001	0.001	0.001	0.001	0.001	0.001	0.001	0.001
Single top norm.	0.003	0.002	0.002	0.003	0.002	0.002	0.003	0.001	0.002
Reconstruction method	0.011	0.008	0.003	0.009	0.009	0.005	0.010	0.009	0.004
Total syst. uncertainty	0.051	0.035	0.038	0.038	0.061	0.022	0.037	0.046	0.024
Total uncertainty	0.056	0.040	0.040	0.042	0.062	0.024	0.039	0.048	0.025

Table 5.7: Systematic sources of uncertainty on asymmetries for the single lepton topology (correction function method).

Results

The effect of each systematic uncertainty on the considered angular asymmetries and helicity fractions are shown in Tables 5.7 and 5.8 for the single lepton channels and, in Tables 5.9 and 5.10, for the dilepton channels. The discussed systematic uncertainty dominates the error on the measurements, with jet energy scale, and signal and background modelling being the dominant sources of uncertainty for the single lepton channels, and with jet energy scale, jet energy resolution, and signal and background modelling being the dominant sources of uncertainty for the dilepton channels.

Source	e+jets			μ+jets			combined		
	F_0	F_{L}	F_{R}	F_0	F_{L}	F_{R}	F_0	F_{L}	F_{R}
Statistical uncertainty	0.044	0.028	0.020	0.032	0.021	0.014	0.025	0.017	0.011
Luminosity	0.004	0.002	0.003	0.003	0.001	0.003	0.004	0.002	0.003
MET pileup	0.004	0.002	0.003	0.010	0.003	0.007	0.006	0.002	0.004
MET LAr hole	0.004	0.003	0.002	0.003	0.001	0.001	0.003	0.001	0.001
MET cell-out	0.007	0.004	0.003	0.008	0.003	0.006	0.007	0.003	0.004
Lepton trigger	0.005	0.003	0.003	0.007	0.002	0.006	0.008	0.003	0.006
Lepton energy scale	0.009	0.005	0.006	0.004	0.002	0.003	0.004	0.002	0.003
Lepton energy resolution	0.034	0.009	0.026	0.030	0.023	0.007	0.026	0.017	0.012
Lepton reconstruction	0.008	0.006	0.003	0.004	0.002	0.003	0.004	0.002	0.003
Jet energy scale	0.042	0.020	0.027	0.020	0.009	0.013	0.026	0.010	0.018
Jet energy resolution	0.042	0.022	0.025	0.042	0.033	0.009	0.037	0.028	0.012
Jet reconstruction	0.003	0.003	0.001	0.002	0.001	0.000	0.000	0.000	0.000
b-tagging	0.012	0.006	0.007	0.007	0.003	0.004	0.009	0.005	0.006
PDF	0.008	0.004	0.004	0.008	0.004	0.004	0.008	0.004	0.004
ISR/FSR	0.030	0.019	0.015	0.025	0.016	0.012	0.021	0.012	0.012
Showering/hadronization	0.010	0.007	0.003	0.007	0.006	0.002	0.003	0.001	0.001
$t\bar{t}$ generator	0.016	0.012	0.004	0.012	0.010	0.003	0.012	0.010	0.003
Color reconnection	0.016	0.011	0.006	0.004	0.003	0.002	0.004	0.002	0.003
Top mass	0.003	0.001	0.001	0.015	0.005	0.011	0.010	0.003	0.007
W+jets bkg norm.	0.014	0.007	0.009	0.021	0.009	0.014	0.018	0.009	0.011
W+jets bkg shape	0.008	0.004	0.004	0.003	0.001	0.001	0.004	0.003	0.002
HF content of W+jets	0.012	0.006	0.007	0.010	0.003	0.007	0.011	0.005	0.007
Z+jets bkg norm.	0.012	0.007	0.006	0.004	0.002	0.003	0.007	0.003	0.004
QCD bkg norm.	0.025	0.014	0.013	0.086	0.068	0.018	0.062	0.048	0.015
QCD bkg shape	0.026	0.017	0.012	0.005	0.004	0.001	0.011	0.008	0.004
Diboson norm.	0.003	0.001	0.001	0.003	0.001	0.001	0.003	0.001	0.001
Single top norm.	0.005	0.003	0.003	0.005	0.003	0.003	0.004	0.002	0.003
Reconstruction method	0.015	0.011	0.005	0.019	0.013	0.008	0.018	0.013	0.007
Total syst. uncertainty	0.095	0.051	0.055	0.116	0.085	0.039	0.095	0.065	0.039
Total uncertainty	0.104	0.059	0.059	0.120	0.087	0.041	0.098	0.067	0.040

Table 5.8: Systematic sources of uncertainty on W helicity fractions obtained from the angular asymmetries for the single lepton topology (correction function method).

Source	ee			$\mu\mu$			$e\mu$		
	A_{FB}	A_+	A_-	A_{FB}	A_+	A_-	A_{FB}	A_+	A_-
Statistical uncertainty	0.061	0.055	0.041	0.044	0.032	0.027	0.028	0.024	0.017
Luminosity	0.002	0.001	0.002	0.002	0.000	0.001	0.001	0.001	0.001
MET pileup	0.005	0.002	0.003	0.005	0.002	0.001	0.000	0.000	0.001
MET LAr hole	0.004	0.002	0.002	0.002	0.001	0.001	0.001	0.001	0.000
MET cell-out	0.003	0.002	0.003	0.003	0.001	0.001	0.000	0.000	0.001
Lepton trigger	0.004	0.002	0.002	0.003	0.002	0.002	0.001	0.001	0.001
Lepton energy scale	0.007	0.004	0.006	0.003	0.002	0.001	0.002	0.002	0.002
Lepton energy resolution	0.004	0.001	0.001	0.001	0.001	0.001	0.001	0.001	0.001
Lepton reconstruction	0.004	0.002	0.002	0.003	0.003	0.002	0.001	0.002	0.001
Jet energy scale	0.055	0.029	0.023	0.039	0.027	0.019	0.041	0.023	0.024
Jet energy resolution	0.016	0.007	0.001	0.012	0.000	0.010	0.005	0.005	0.004
Jet reconstruction	0.004	0.000	0.002	0.001	0.000	0.001	0.001	0.000	0.000
b-tagging	0.004	0.003	0.003	0.001	0.001	0.001	0.001	0.002	0.001
PDF	0.005	0.005	0.008	0.009	0.009	0.015	0.008	0.007	0.013
ISR/FSR	0.028	0.040	0.027	0.035	0.031	0.027	0.031	0.015	0.015
Showering/hadronization	0.019	0.013	0.010	0.005	0.003	0.015	0.004	0.015	0.006
$t\bar{t}$ generator	0.002	0.040	0.006	0.009	0.004	0.026	0.004	0.006	0.004
Color reconnection	0.023	0.010	0.011	0.010	0.023	0.004	0.022	0.011	0.007
Top mass	0.040	0.006	0.033	0.027	0.008	0.025	0.003	0.010	0.001
Z+jets bkg norm.	0.001	0.008	0.000	0.002	0.006	0.001	0.001	0.001	0.001
Misidentified leptons	0.008	0.002	0.002	0.002	0.001	0.002	0.002	0.010	0.002
Diboson norm.	0.002	0.002	0.001	0.002	0.001	0.001	0.001	0.001	0.000
Single top norm.	0.001	0.001	0.001	0.002	0.001	0.001	0.001	0.001	0.001
Reconstruction method	0.038	0.027	0.015	0.028	0.009	0.025	0.013	0.000	0.016
Total syst. uncertainty	0.091	0.072	0.055	0.069	0.050	0.060	0.059	0.038	0.037
Total uncertainty	0.109	0.091	0.068	0.082	0.059	0.066	0.065	0.045	0.040

Table 5.9: Systematic sources of uncertainty on asymmetries for the dilepton topology (correction function method).

Source	ee			$\mu\mu$			$e\mu$		
	F_0	F_{L}	F_{R}	F_0	F_{L}	F_{R}	F_0	F_{L}	F_{R}
Statistical uncertainty	0.126	0.079	0.062	0.078	0.047	0.041	0.053	0.034	0.026
Luminosity	0.003	0.002	0.002	0.002	0.001	0.001	0.002	0.001	0.001
MET pileup	0.007	0.003	0.004	0.004	0.003	0.001	0.002	0.001	0.001
MET LAr hole	0.005	0.003	0.003	0.004	0.002	0.002	0.003	0.002	0.001
MET cell-out	0.007	0.004	0.004	0.002	0.001	0.001	0.002	0.000	0.001
Lepton trigger	0.005	0.003	0.003	0.005	0.003	0.003	0.003	0.002	0.001
Lepton energy scale	0.013	0.006	0.009	0.004	0.003	0.002	0.005	0.003	0.003
Lepton energy resolution	0.003	0.002	0.002	0.003	0.002	0.002	0.002	0.001	0.001
Lepton reconstruction	0.005	0.003	0.003	0.006	0.004	0.003	0.003	0.002	0.001
Jet energy scale	0.068	0.042	0.035	0.061	0.039	0.030	0.061	0.034	0.034
Jet energy resolution	0.012	0.009	0.003	0.017	0.003	0.013	0.012	0.008	0.006
Jet reconstruction	0.004	0.001	0.003	0.002	0.000	0.001	0.001	0.001	0.001
b-tagging	0.008	0.005	0.004	0.002	0.001	0.002	0.005	0.003	0.002
PDF	0.017	0.008	0.011	0.032	0.014	0.021	0.027	0.011	0.018
ISR/FSR	0.088	0.057	0.041	0.075	0.044	0.040	0.038	0.021	0.022
Showering/hadronization	0.029	0.018	0.014	0.027	0.007	0.020	0.030	0.022	0.011
$t\bar{t}$ generator	0.071	0.055	0.017	0.046	0.012	0.035	0.013	0.008	0.007
Color reconnection	0.027	0.014	0.016	0.040	0.031	0.010	0.024	0.016	0.011
Top mass	0.060	0.016	0.046	0.046	0.015	0.034	0.017	0.014	0.004
Z+jets bkg norm.	0.014	0.011	0.003	0.011	0.008	0.003	0.003	0.002	0.001
Misidentified leptons	0.005	0.003	0.002	0.003	0.001	0.002	0.018	0.014	0.005
Diboson norm.	0.004	0.002	0.002	0.003	0.002	0.001	0.001	0.001	0.001
Single top norm.	0.003	0.002	0.002	0.003	0.002	0.002	0.002	0.001	0.001
Reconstruction method	0.056	0.038	0.024	0.047	0.016	0.034	0.028	0.006	0.022
Total syst. uncertainty	0.166	0.104	0.083	0.142	0.074	0.086	0.097	0.055	0.054
Total uncertainty	0.208	0.130	0.103	0.162	0.088	0.095	0.111	0.065	0.060

Table 5.10: Systematic sources of uncertainty on W helicity fractions obtained from the angular asymmetries for the dilepton topology (correction function method).

5.7 Combination of Results

The combination of the individual measurements of the W boson helicity fractions (F_0 and F_{L}) and asymmetries (A_+ and A_-) in the single lepton and dilepton channels was done using the best linear unbiased estimator (BLUE) method [211, 212]. The BLUE method has been widely used in high energy physics, and corresponds to the analytical solution to the problem of minimizing the χ^2 for the combination of measurements. As such, it provides a better means of understanding the results of the combination than a numerical approach, and a simpler means of correctly estimating the individual contributions to the errors on the combined results. Any correlations between the measurements of different observables, whether positive or negative, always result in decreasing the combined errors on each observable, with respect to the case where these are not taken into account. The impact of the systematic uncertainties was studied and the results are summarized in Table 5.11, which also gives the combination of all channels. The results are compatible with each other and with the final combination. The statistical correlation coefficient between A_+ and A_- was estimated to be 0.16 using Monte-Carlo simulation, while the measured correlation coefficient (considering statistical and systematic effects in the all channels) is 0.11.

The combined results for the angular asymmetries and W helicity fractions obtained from the angular asymmetries from the single lepton channels are:

$$\begin{aligned} A_+ &= 0.517 \pm 0.016\ (\text{stat.}) \pm 0.034\ (\text{syst.})\ , \\ A_- &= -0.843 \pm 0.008\ (\text{stat.}) \pm 0.022\ (\text{syst.})\ . \end{aligned} \tag{5.7}$$

The corresponding W helicity fractions obtained from the angular asymmetries are $F_0 = 0.654 \pm 0.080$ (stat. + syst.), $F_{\mathrm{L}} = 0.339 \pm 0.054$ (stat. + syst.) and $F_{\mathrm{R}} = 0.007 \pm 0.036$ (stat. + syst.). The combined results for the dilepton channels are:

$$\begin{aligned} A_+ &= 0.558 \pm 0.023\ (\text{stat.}) \pm 0.038\ (\text{syst.})\ , \\ A_- &= -0.841 \pm 0.016\ (\text{stat.}) \pm 0.037\ (\text{syst.})\ . \end{aligned} \tag{5.8}$$

The corresponding W helicity fractions obtained from the angular asymmetries are $F_0 = 0.722 \pm 0.110$ (stat. + syst.), $F_{\mathrm{L}} = 0.283 \pm 0.064$ (stat. + syst.) and $F_{\mathrm{R}} = -0.005 \pm 0.059$ (stat. + syst.). A combination of all five channels yields:

$$\begin{aligned} A_+ &= 0.530 \pm 0.015\ (\text{stat.}) \pm 0.031\ (\text{syst.})\ , \\ A_- &= -0.846 \pm 0.010\ (\text{stat.}) \pm 0.020\ (\text{syst.})\ . \end{aligned} \tag{5.9}$$

The corresponding W helicity fractions obtained from the angular asymmetries are $F_0 = 0.682 \pm 0.073$ (stat. + syst.), $F_{\mathrm{L}} = 0.320 \pm 0.048$ (stat. + syst.) and $F_{\mathrm{R}} =$

Source	Single lepton		Dilepton		All channels	
	A_+	A_-	A_+	A_-	A_+	A_-
Signal and background modelling						
Signal modelling	0.013	0.005	0.019	0.011	0.013	0.003
ISR/FSR	0.013	0.008	0.016	0.016	0.011	0.006
PDF	0.003	0.003	0.008	0.013	0.005	0.003
Top mass	0.002	0.008	0.010	0.004	0.005	0.004
QCD	0.016	0.003	0.009	0.002	0.012	0.003
W+jets	0.006	0.010	—	—	0.004	0.010
Background modelling	0.004	0.003	0.002	0.001	0.003	0.003
Detector modelling						
Lepton reconstruction	0.006	0.006	0.002	0.001	0.005	0.003
Jet energy scale	0.011	0.010	0.023	0.024	0.015	0.010
Jet reconstruction	0.017	0.002	0.004	0.004	0.013	0.002
b-tagging uncertainty	0.004	0.003	0.002	0.001	0.003	0.003
Calorimeter readout	0.004	0.004	0.001	0.001	0.003	0.004
Luminosity and pileup	0.001	0.005	0.001	0.001	0.001	0.005
Method	0.007	0.005	0.003	0.014	0.005	0.006
Systematic uncertainty	0.034	0.022	0.038	0.037	0.031	0.020

Table 5.11: Sources of systematic uncertainties and their impact on the measured A_+ and A_- angular asymmetries for the combined single lepton channels, the combined dilepton channels and the overall combination.

-0.002 ± 0.034 (stat. + syst.). In the combined fit of all five channels the total correlation coefficient between A_+ and A_- is 0.11. In the measurement of both asymmetries and helicity fractions, the systematic error dominates.

These results were also combined with the results obtained with the template fit method. Both the statistical correlations between analyses, and the correlations of systematic uncertainties, were taken into account. The statistical correlations were estimated to be between 40% and 49% for the single lepton channels and between 83% and 89% for the dilepton channels using pseudo-experiments obtained from simulated samples. The background-related systematic uncertainties were assumed to be fully correlated within single lepton channels and within dilepton channels, but uncorrelated between single lepton and dilepton measurements. The only exception is the uncertainty due to misidentified lepton background which depends on the lepton flavor and thus belongs to the group of lepton-related uncertainties, which were assumed to be fully correlated between the channels with same flavor leptons. The

method systematic uncertainties were assumed to be uncorrelated between channels and the remaining sources of systematic uncertainty were assumed to be fully correlated between channels. Various tests were performed in which the correlations among the sources of systematic uncertainty were varied. It was found that the values assumed for the correlations were conservative. The four measurements of the helicity fractions and the combined values are shown in Table 5.12 and Figure 5.29, and the impact of the systematic uncertainties is presented in Table 5.13. Most of the measurements and the combined result are limited by systematic uncertainties. The largest sources of uncertainty are the signal and background modelling, as well as the jet energy scale and jet reconstruction. The template fits are more sensitive to shape-related uncertainties, such as ISR/FSR and jet reconstruction, while the angular asymmetries are more sensitive to background normalization uncertainties, due to the background subtraction which needs to be performed.

The individual measurements agree reasonably well within their total uncertainties. The χ^2/dof for the global combination of the template fit and asymmetries measurements was 0.8 with a χ^2-probability of 75%, where dof is the number of degrees of freedom. The largest difference between two measurements is that between the single lepton and dilepton channels obtained with the template method. Since the measurements were performed in five independent channels (single electron, single muon, ee, $e\mu$ and $\mu\mu$), the combination was performed based on the five individual measurements taking into account all correlations. The χ^2/dof calculated using the BLUE method for this combination was 1.3 with a χ^2-probability of 23%.

The combined W boson helicity fractions are:

$$\begin{aligned} F_0 &= 0.67 \pm 0.03\ (\text{stat.}) \pm 0.06\ (\text{syst.})\,, \\ F_\text{L} &= 0.32 \pm 0.02\ (\text{stat.}) \pm 0.03\ (\text{syst.})\,, \\ F_\text{R} &= 0.01 \pm 0.01\ (\text{stat.}) \pm 0.04\ (\text{syst.})\,. \end{aligned} \tag{5.10}$$

The correlation coefficient between F_0 and F_L was estimated to be -0.96. For completeness, these results can be translated into angular asymmetries, yielding $A_+ = 0.53 \pm 0.02$ and $A_- = -0.84 \pm 0.02$.

Channel	F_0	F_{L}	F_{R}
W boson helicity fractions from the template fit			
Single leptons	$0.57 \pm 0.06 \pm 0.09$	$0.37 \pm 0.03 \pm 0.04$	$0.07 \pm 0.03 \pm 0.06$
Dileptons	$0.92 \pm 0.10 \pm 0.10$	$0.17 \pm 0.06 \pm 0.07$	$-0.09 \pm 0.05 \pm 0.06$
Combination	$0.66 \pm 0.06 \pm 0.07$	$0.33 \pm 0.03 \pm 0.03$	$0.01 \pm 0.03 \pm 0.06$
F_{R} fixed	$0.66 \pm 0.03 \pm 0.04$	$0.34 \pm 0.03 \pm 0.04$	0 (fixed)
W boson helicity fractions from the angular asymmetries			
Single leptons	$0.66 \pm 0.03 \pm 0.08$	$0.33 \pm 0.02 \pm 0.05$	$0.01 \pm 0.01 \pm 0.04$
Dileptons	$0.74 \pm 0.06 \pm 0.10$	$0.27 \pm 0.03 \pm 0.05$	$-0.01 \pm 0.03 \pm 0.05$
Combination	$0.67 \pm 0.04 \pm 0.07$	$0.32 \pm 0.02 \pm 0.04$	$0.01 \pm 0.02 \pm 0.04$
Overall combination	$0.67 \pm 0.03 \pm 0.06$	$0.32 \pm 0.02 \pm 0.03$	$0.01 \pm 0.01 \pm 0.04$

Table 5.12: Summary of the W boson helicity fractions measured using the two different techniques described and the combination. The quoted uncertainties are the statistical (first) and the systematic (second) uncertainties.

Source	Uncertainties		
	F_0	F_{L}	F_{R}
Signal and background modelling			
Generator choice	0.012	0.009	0.004
ISR/FSR	0.015	0.008	0.007
PDF	0.011	0.006	0.006
Top quark mass	0.016	0.009	0.008
Misidentified leptons	0.020	0.013	0.007
W+jets	0.016	0.008	0.008
Other backgrounds	0.006	0.003	0.003
Method-specific uncertainties	0.031	0.016	0.035
Detector modelling			
Lepton reconstruction	0.013	0.006	0.007
Jet energy scale	0.026	0.014	0.012
Jet reconstruction	0.012	0.005	0.007
b-tagging	0.007	0.003	0.004
Calorimeter readout	0.009	0.005	0.004
Luminosity and pileup	0.009	0.004	0.005
Total systematic uncertainty	0.06	0.03	0.04

Table 5.13: Sources of systematic uncertainty and their impact on the measured W boson helicity fractions for the combined single lepton and dilepton channels. The systematic uncertainties were symmetrized by using the larger uncertainty.

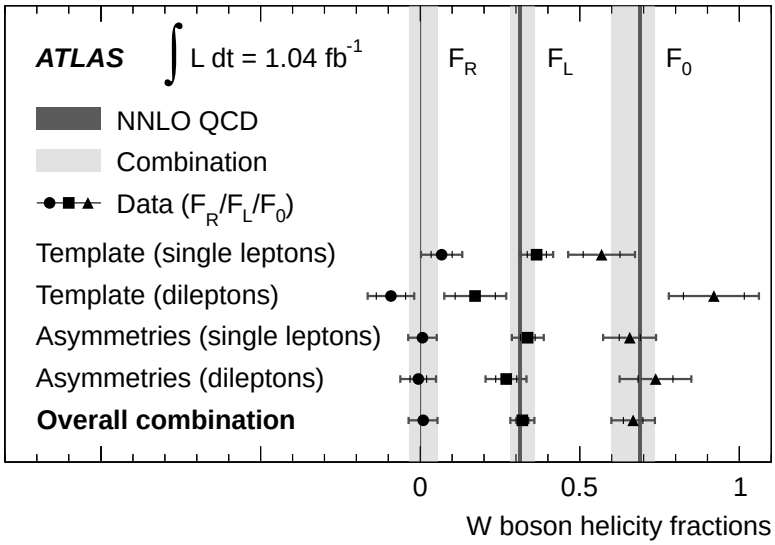

Figure 5.29: Overview of the four measurements of the W boson helicity fractions and the combined values. The error bars correspond to the statistical and total uncertainties.

5.8 Limits on Anomalous Couplings

Any deviation of F_0, $F_{\rm L}$, $F_{\rm R}$ or, A_+ and A_-, from the Standard Model prediction could be caused by new physics contributing to the Wtb vertex. From the measurement of helicity fractions or, alternatively, the asymmetries $A_\pm$, the limits on anomalous contributions to the Wtb vertex can be obtained, which can be easily translated into limits on effective operator coefficients C_x/Λ^2 by using equations 2.76.

It is important to note here the differences betwen the two b chirality-flipping operators involving right-handed b quarks, $O^{33}_{\phi\phi}$ and O^{33}_{dW} (they give the Wtb anomalous couplings $V_{\rm R}$ and $g_{\rm L}$) and the b chirality-conserving operator O^{33}_{uW} (giving $g_{\rm R}$). The former are the only two operators contributing to a non-zero F_R (which is negligible in the SM, $F_R \sim 10^{-4}$). Therefore, they are probed with good precision despite the fact that their effects are suppressed by m_b/m_t or $(v/\Lambda)^2$ with respect to O^{33}_{uW} which gives the leading corrections. Furthermore, it is necessary to stress that when obtaining limits on $O^{33}_{\phi\phi}$ and O^{33}_{dW}, namely anomalous couplings $V_{\rm R}$ and $g_{\rm L}$, it is crucial to keep the b quark mass in the calculations, because the b chirality flip is proportional to m_b. Eventually, interferences with the SM contribution involving b_L may be of the same order as the quadratic contributions of the new operators.

Limits on anomalous couplings ($V_{\rm R}$, $g_{\rm L}$ and $g_{\rm R}$) were obtained from the combined measurement of the W boson helicity fractions by exploiting their dependence on these couplings, as implemented in the TopFit program [74, 213] and normalizing to

$V_{\mathrm{L}} = 1$. The 68% and 95% confidence level (CL) regions on $(g_{\mathrm{L}}, g_{\mathrm{R}})$ are shown in Figure 5.30, assuming $V_{\mathrm{R}} = 0$. The upper disconnected region in the plot shows a large-g_{R} second solution to the quadratic equation relating the observables to the anomalous couplings. However, this region is disfavored by the measured cross-section for single top production at the Tevatron [71, 86, 214] and CMS [215].

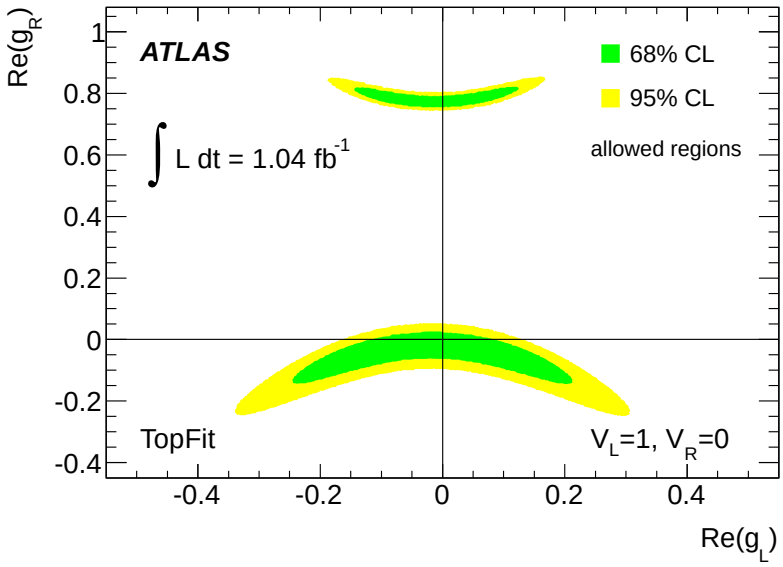

Figure 5.30: Allowed regions at 68% and 95% confidence level (CL) for the Wtb anomalous couplings g_{L} and g_{R}. In the Standard Model, the anomalous couplings vanish at tree level.

In addition to this two-dimensional limit it is useful to set limits on single anomalous couplings, taking only one of them non-zero at a time. These are, at 95% confidence level,

$$\begin{aligned}
\mathrm{Re}\,(V_{\mathrm{R}}) \in [-0.20, 0.23] \quad &\rightarrow \quad \frac{\mathrm{Re}\,(C^{33}_{\phi\phi})}{\Lambda^2} \in [-6.7, 7.8] \ \ \mathrm{TeV}^{-2}\,, \\
\mathrm{Re}\,(g_{\mathrm{L}}) \in [-0.14, 0.11] \quad &\rightarrow \quad \frac{\mathrm{Re}\,(C^{33}_{dW})}{\Lambda^2} \in [-1.6, 1.2] \ \ \mathrm{TeV}^{-2}\,, \\
\mathrm{Re}\,(g_{\mathrm{R}}) \in [-0.08, 0.04] \quad &\rightarrow \quad \frac{\mathrm{Re}\,(C^{33}_{uW})}{\Lambda^2} \in [-1.0, 0.5] \ \ \mathrm{TeV}^{-2}\,,
\end{aligned} \tag{5.11}$$

where $C^{33}_{\phi\phi}$, C^{33}_{dW}, C^{33}_{uW}, are the dimension-six operator coefficients, defined in equation (2.74). Alternatively, using a Bayesian approach [216], the measurement of the W boson helicity fractions with F_{R} fixed at zero, was translated into a 95% probability interval on $\mathrm{Re}\,(C^{33}_{uW})/\Lambda^2$, as proposed in [172]. This interval was found to be $[-0.9, 2.3]$ TeV^{-2}.

It can be seen that the limits on C_{dW}^{33} (mediating the production of right-handed b-quarks in the top decay) are of the same order of magnitude as the limits on C_{uW}^{33} (involving left-handed quarks). This reflects a good sensitivity to the effective operator corresponding to C_{dW}^{33}, even if its contribution is suppressed by $1/\Lambda^2$ instead of $1/\Lambda$ [82].

These limits are more stringent than those obtained by the DØ Collaboration [86, 217][2]. Indirect, model-dependent limits on the anomalous couplings have been inferred from measurements of radiative B-meson decays, measurements of $B\bar{B}$-mixing and electroweak precision data [80,81,218–220], but these limits include assumptions on the absence of additional new physics effects that are not needed in this analysis.

5.9 Conclusions

A measurement of the polarization of the $W^{\pm}$ bosons in top quark decays was presented, based on 1.04 fb^{-1} of data collected with the ATLAS detector in 2011. The single lepton and dilepton decay topologies of top quark pairs were considered in the analysis.

The helicity fractions obtained from a combination of template fits to the reconstructed $\cos\theta^*$ distributions and angular asymmetries calculated from the unfolded $\cos\theta^*$ distributions are $F_0 = 0.67 \pm 0.07$, $F_{\mathrm{L}} = 0.32 \pm 0.04$ and $F_{\mathrm{R}} = 0.01 \pm 0.05$, which can be translated into angular asymmetries yielding $A_+ = 0.53 \pm 0.02$ and $A_- = -0.84 \pm 0.02$. These results are in agreement with NNLO QCD predictions and are more precise than previous results obtained by the CDF and DØ Collaborations [83–85].

Limits on the Wtb vertex anomalous couplings were obtained from the combined results on the W boson helicity fractions. These results are consistent with the $(V-A)$ structure of the Wtb vertex and improve on the previously obtained limits [86].

[2]The limits from the DØ Collaboration were derived assuming a massless b-quark.

Chapter 6

Top Effective Operators at the ILC

In this chapter, the effect of top trilinear operators in $t\bar{t}$ production is explored in order to understand how possible future colliders, such as the International Linear Collider, may help improving the current limits obtained at the LHC. The sensitivity to these operators may largely surpass the one achievable by the LHC either in neutral or charged current processes, allowing to probe new physics scales up to 4.5 TeV for a center-of-mass energy of 500 GeV. It is shown how the use of beam polarization and an eventual energy upgrade to 1 TeV allow to disentangle all effective operator contributions to the $Zt\bar{t}$ and $\gamma t\bar{t}$ vertices.

6.1 Introduction

Precision measurements are an essential complement of direct searches for new physics beyond the Standard Model. The most important successes of the precision measurements are the prediction of the existence of the charm quark due to the absence of flavor-changing neutral currents, and the prediction of the top quark mass before its actual discovery. Therefore, the construction of a high-energy e^+e^- International Linear Collider has been proposed to complement direct searches carried at the Large Hadron Collider. In the case of the top quark, precision measurements of its properties, in particular of its couplings, are specially interesting because it is the heaviest elementary particle yet discovered, and thus, it is expected to be more sensitive to new physics at higher scales.

In this study, the effective operator approach was used, as for the study of the Wtb vertex structure in top quark decays with the ATLAS experiment, presented in the previous chapter. Unlike the previous approaches for the study of $e^+e^- \to t\bar{t}$ at the ILC with anomalous top couplings [221–226], the effective operator framework makes use of the full $\mathrm{SU}(3)_c \times \mathrm{SU}(2)_L \times \mathrm{U}(1)_Y$ gauge symmetry of the SM, not only the unbroken $\mathrm{SU}(3)_c \times \mathrm{U}(1)_{\mathrm{em}}$, which leads to several interesting implications. First

of all, the effective operator framework allows to reduce the number of independent parameters entering fermion trilinear interactions to four at most [76], one half of the total number of parameters involved in a general off-shell form factor. Second, it allows to set relations between new physics contributions to the top quark interactions, for example between left-handed contributions to the Wtb and $Zt\bar{t}$ vertices. Such relations not only reduce further the number of arbitrary parameters, but also introduce an useful synergy between measurements of different top quark vertices: the Wtb vertex studied in the previous chapter, and the $Zt\bar{t}$ involved in $t\bar{t}$ production at the ILC.

The effect of top trilinear effective operators in $e^+e^- \to t\bar{t}$ at the ILC is analyzed. The estimates show that the ILC sensitivity may largely surpass the one achievable at the LHC, either in top quark decays (current one [8] or envisaged [227]) or in $t\bar{t}Z$ and $t\bar{t}\gamma$ production [228, 229]. Moreover, the different ILC beam polarization options and CM energies could allow to disentangle the various effective operator contributions to the $Zt\bar{t}$ and $\gamma t\bar{t}$ vertices. Even though the effective operators also affect the top quark decay, their effect was not considered in this study.

6.2 Top Quark Pair Production with Effective Operators

From the minimal non-redundant set of dimension-six operators contributing to top quark vertices, presented in [76], only five contribute to $Zt\bar{t}$ and $\gamma t\bar{t}$ interactions,

$$\begin{aligned}
&O_{\phi q}^{(3,3+3)} = i\left[\phi^\dagger(\tau^I D_\mu - \overleftarrow{D}_\mu\tau^I)\phi\right](\bar{q}_{L3}\gamma_\mu\tau^I q_{L3})\,, && O_{uW}^{33} = (\bar{q}_{L3}\sigma^{\mu\nu}\tau^I t_R)\tilde{\phi}\,W^I_{\mu\nu}\,,\\
&O_{\phi q}^{(1,3+3)} = i(\phi^\dagger\overleftrightarrow{D}_\mu\phi)(\bar{q}_{L3}\gamma_\mu q_{L3})\,, && O_{uB\phi}^{33} = (\bar{q}_{L3}\sigma^{\mu\nu}t_R)\tilde{\phi}\,B_{\mu\nu}\,,\\
&O_{\phi u}^{3+3} = i(\phi^\dagger\overleftrightarrow{D}_\mu\phi)(\bar{t}_R\gamma_\mu t_R)\,, &&
\end{aligned} \tag{6.1}$$

where $B_{\mu\nu}$ represents the $\mathrm{U}(1)_Y$ field strength tensor, and $\overleftrightarrow{D}_\mu = D_\mu - \overleftarrow{D}_\mu$. The three operators in the left column of equations (6.1) are Hermitian, hence their coefficients are real. Including the SM and dimension-six operator contributions, the $Zt\bar{t}$ vertex reads

$$\mathcal{L}_{Zt\bar{t}} = -\frac{g}{2c_W}\bar{t}\,\gamma_\mu\left(c_L^t P_L + c_R^t P_R\right)t\;Z_\mu - \frac{g}{2c_W}\bar{t}\,\frac{i\sigma^{\mu\nu}q_\nu}{M_Z}\left(d_V^Z + id_A^Z\gamma_5\right)t\;Z_\mu\,, \tag{6.2}$$

with $c_L^t = X_{t\bar{t}}^L - 2s_W^2 Q_t$, $c_R^t = X_{t\bar{t}}^R - 2s_W^2 Q_t$ ($Q_t = 2/3$ is the top quark electric charge) and

$$\begin{aligned}
&X_{t\bar{t}}^L = 1 + \left[C_{\phi q}^{(3,3+3)} - C_{\phi q}^{(1,3+3)}\right]\frac{v^2}{\Lambda^2}\,, && d_V^Z = \sqrt{2}\,\mathrm{Re}\left[c_W C_{uW}^{33} - s_W C_{uB\phi}^{33}\right]\frac{v^2}{\Lambda^2}\,,\\
&X_{t\bar{t}}^R = -C_{\phi u}^{3+3}\frac{v^2}{\Lambda^2}\,, && d_A^Z = \sqrt{2}\,\mathrm{Im}\left[c_W C_{uW}^{33} - s_W C_{uB\phi}^{33}\right]\frac{v^2}{\Lambda^2}\,,
\end{aligned} \tag{6.3}$$

where the C constants are the coefficients of the operators in Eqs. (6.1) and Λ is the new physics scale. The $\gamma t\bar{t}$ vertex reads

$$\mathcal{L}_{\gamma t\bar{t}} = -eQ_t \bar{t}\,\gamma_\mu t\; A_\mu - e\bar{t}\,\frac{i\sigma^{\mu\nu}q_\nu}{m_t}\left(d_V^\gamma + id_A^\gamma\gamma_5\right) t\; A_\mu\,. \tag{6.4}$$

with

$$\begin{aligned} d_V^\gamma &= \frac{\sqrt{2}}{e}\,\mathrm{Re}\,\left[s_W C_{uW}^{33} + c_W C_{uB\phi}^{33}\right]\frac{vm_t}{\Lambda^2}\,, \\ d_A^\gamma &= \frac{\sqrt{2}}{e}\,\mathrm{Im}\,\left[s_W C_{uW}^{33} + c_W C_{uB\phi}^{33}\right]\frac{vm_t}{\Lambda^2}\,. \end{aligned} \tag{6.5}$$

Thus, the total number of real parameters necessary to describe non-SM contributions to the $Zt\bar{t}$ and $\gamma t\bar{t}$ vertices is six, corresponding to five dimension-six operators, three of them Hermitian. The two complex coefficients appear in two linearly independent combinations in the tensorial Z boson and photon interactions. The real parts of these combinations, d_V^Z and d_V^γ, correspond to magnetic dipole moments, whereas the imaginary parts d_A^Z, d_A^γ are CP-violating electric dipole moments.

One can perform an additional simplification by noticing that the contribution from dimension-six operators to the Zb_Lb_L vertex [76],

$$c_L^b = -1 - 2s_W^2 Q_b + \left[C_{\phi q}^{(3,3+3)} + C_{\phi q}^{(1,3+3)}\right]\frac{v^2}{\Lambda^2}\,, \tag{6.6}$$

involves precisely the same operators as in the Zt_Lt_L vertex. (For c_L^b the same normalization as in equation (6.2) is used.) The bottom quark couplings have been probed with great precision at PETRA, LEP and SLD. Thus, given the precision that is expected for top couplings at the LHC and ILC, it is a good approximation to assume

$$C_{\phi q}^{(1,3+3)} \simeq -C_{\phi q}^{(3,3+3)}\,, \tag{6.7}$$

since non-zero contributions from these operators must be balanced in order to keep the Zb_Lb_L vertex close to its SM value. Besides, the exact equality between these coefficients automatically holds for some SM extensions, for example with new charge 2/3 singlets [88, 89, 230, 231], so no fine-tuning is implied here.

The cross section of the $t\bar{t}$ production at the ILC, shown in Figure 6.1, was computed including top trilinear operators. Since the electron interactions have been probed with an excellent precision without noticing departures from the SM prediction, it was reasonable to assume:

$$\mathcal{L}_e = -eQ_e\bar{e}\,\gamma_\mu e\; A_\mu - \frac{g}{2c_W}\bar{e}\,\gamma_\mu\left(c_L^e P_L + c_R^e P_R\right) e\; Z_\mu\,, \tag{6.8}$$

with $c_L^e = -1 - 2s_W^2 Q_e$, $c_R^e = -2s_W^2 Q_e$ ($Q_e = -1$). In terms of the top quark and electron vertices, the polarized forward (F) and backward (B) cross sections for

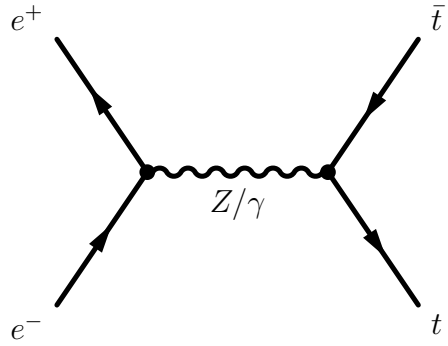

Figure 6.1: Feynman diagram of the top quark pair production at the ILC through the s-channel.

$e^+e^- \to t\bar{t}$ are[1]

$$\begin{aligned}
\sigma_{F,B}(e^+_R e^-_L) &= \frac{\beta}{32\pi}\left\{s(3+\beta^2)\left[|\mathcal{V}_{LL}|^2+|\mathcal{V}_{LR}|^2\right] \mp 3s\beta\left[|\mathcal{V}_{LL}|^2-|\mathcal{V}_{LR}|^2\right]\right. \\
&\quad +24m_t^2\,\mathrm{Re}\;\mathcal{V}_{LL}\mathcal{V}^*_{LR}+2s^2(3-\beta^2)\left[|\mathcal{T}_{LV}|^2+|\mathcal{T}_{LA}|^2\right] \\
&\quad +24m_t^2 s\left[|\mathcal{T}_{LV}|^2-|\mathcal{T}_{LA}|^2\right]-24sm_t\,\mathrm{Re}\left[(\mathcal{V}_{LL}+\mathcal{V}_{LR})\mathcal{T}^*_{LV}\right] \\
&\quad \left.\pm 12sm_t\beta\,\mathrm{Re}\left[(\mathcal{V}_{LL}-\mathcal{V}_{LR})\mathcal{T}^*_{LV}\right]\right\}\,, \\
\sigma_{F,B}(e^+_L e^-_R) &= \frac{\beta}{32\pi}\left\{s(3+\beta^2)\left[|\mathcal{V}_{RL}|^2+|\mathcal{V}_{RR}|^2\right] \pm 3s\beta\left[|\mathcal{V}_{RL}|^2-|\mathcal{V}_{RR}|^2\right]\right. \\
&\quad +24m_t^2\,\mathrm{Re}\;\mathcal{V}_{RL}\mathcal{V}^*_{RR}+2s^2(3-\beta^2)\left[|\mathcal{T}_{RV}|^2+|\mathcal{T}_{RA}|^2\right] \\
&\quad +24m_t^2 s\left[|\mathcal{T}_{RV}|^2-|\mathcal{T}_{RA}|^2\right]-24sm_t\,\mathrm{Re}\left[(\mathcal{V}_{RL}+\mathcal{V}_{RR})\mathcal{T}^*_{RV}\right] \\
&\quad \left.\mp 12sm_t\beta\,\mathrm{Re}\left[(\mathcal{V}_{RL}-\mathcal{V}_{RR})\mathcal{T}^*_{RV}\right]\right\}\,, \\
\sigma_{F,B}(e^+_L e^-_L) &= \sigma_{F,B}(e^+_R e^-_R)=0\,,
\end{aligned} \tag{6.9}$$

with $\mathcal{V}_{ij}$, $\mathcal{T}_{ij}$ defined as

$$\begin{aligned}
\mathcal{V}_{ij} &= e^2\left[\frac{c^e_i c^t_j}{4s^2_W c^2_W(s-M^2_Z)}+\frac{Q_e Q_t}{s}\right]\,, i,j=L,R\,, \\
\mathcal{T}_{ij} &= e^2\left[\frac{c^e_i d^Z_j}{4s^2_W c^2_W M_Z(s-M^2_Z)}+\frac{Q_e d^\gamma_j}{sm_t}\right]\,, i=L,R\,,\ j=V,A\,.
\end{aligned} \tag{6.10}$$

The detailed calculations that lead to these final equations can be found in Appendix B. The cross sections and asymmetries for arbitrary electron (positron) polarizations P_{e^-} (P_{e^+}) can be straightforwardly obtained,

$$\sigma_{F,B}=\frac{1}{4}\left[(1+P_{e^-})(1-P_{e^+})\sigma_{F,B}(e^+_L e^-_R)+(1-P_{e^-})(1+P_{e^+})\sigma_{F,B}(e^+_R e^-_L)\right]\,. \tag{6.11}$$

[1]The events in which the top quark moves along the positron direction are defined as 'forward', as shown in Figure 6.2. The subindices in e^+, e^- indicate the helicity.

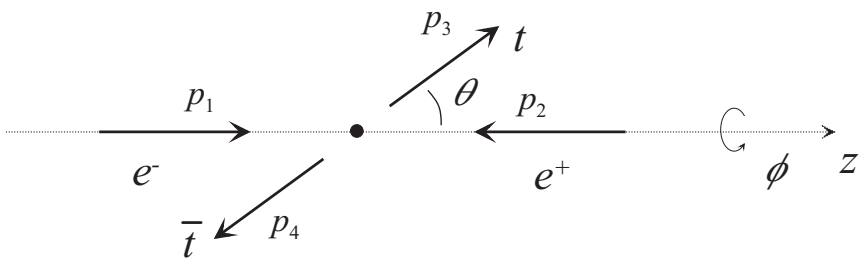

Figure 6.2: Electron-positron annihilation producing a pair of top quarks at the ILC in the laboratory rest frame.

Before the detailed analysis in the next section, it is clear how the different terms $\mathcal{V}_{ij}$, $\mathcal{T}_{ij}$ can be disentangled:

1. Both total cross sections and asymmetries have different dependence on $\mathcal{T}_{LV}$ and $\mathcal{T}_{RV}$ (which interfere with the vector terms) and their axial counterparts (which do not).

2. Forward-backward (FB) asymmetries distinguish $\mathcal{V}_{LL}$ from $\mathcal{V}_{LR}$ and $\mathcal{V}_{RL}$ from $\mathcal{V}_{RR}$, and thus c_L^t from c_R^t, for either beam polarization, and hence also for unpolarized beams.

3. Beam polarization distinguishes $\mathcal{T}_{LV}$ from $\mathcal{T}_{RV}$ and $\mathcal{T}_{LA}$ from $\mathcal{T}_{RA}$. (Also $\mathcal{V}_{LL}$ from $\mathcal{V}_{RL}$, and $\mathcal{V}_{LR}$ from $\mathcal{V}_{RR}$, but this is uninteresting in this study because the differences between these arise from the left- and right-handed electron couplings, assumed here as in the SM.) This allows to separate d_j^Z from d_j^γ, because the former is multiplied by a parity-violating coupling and the later by the electron charge.

4. Measurements at different CM energies can help resolve the vector ($\mathcal{V}_{ij}$) and tensor ($\mathcal{T}_{ij}$) contributions because the CM energy dependence is different. Note also that in the expressions of $\mathcal{V}_{ij}$ and $\mathcal{T}_{ij}$ the propagators are quite similar at ILC energies, $s - M_Z^2 \approx s$, so measurements at different CM energies cannot be used to distinguish off-shell Z boson and photon contributions.

6.3 ILC versus LHC Sensitivity

There are two effective operators involved in the $Zt\bar{t}$ vertex which have already been probed at the LHC: $O_{\phi q}^{(3,3+3)}$ and O_{uW}^{33}. As already shown in section 2.4.3, both these operators also modify the Wtb vertex. The limits on $C_{\phi q}^{(3,3+3)}$ can be extracted from

single top cross section measurements. For example, from the ATLAS t-channel measurement [232] one can get the limit

$$\frac{C_{\phi q}^{(3,3+3)}}{\Lambda^2} \in [-2.1, 6.7] \text{ TeV}^{-2} \tag{6.12}$$

with a 95% confidence level (CL), assuming no other non-SM contribution to single top production. The variation of the unpolarized cross section and FB asymmetry at ILC for $C_{\phi q}^{(3,3+3)}$ ranging in this interval is presented in Figure 6.3. The CM energy is taken as $\sqrt{s} = 500$ GeV. The bands represent a 1σ (inner, green) and 2σ (outer, yellow) variation around the SM value, assuming total uncertainties of 5% in the cross section and 2% in the asymmetry [233].[2] Here the rest of the operator coefficients are assumed to be zero, except for the relation in equation (6.7). The improvement of the ILC with respect to the LHC is evident, and comes not only from the smaller cross section uncertainties at the ILC but also because the contribution of this operator is enhanced via equation (6.7).

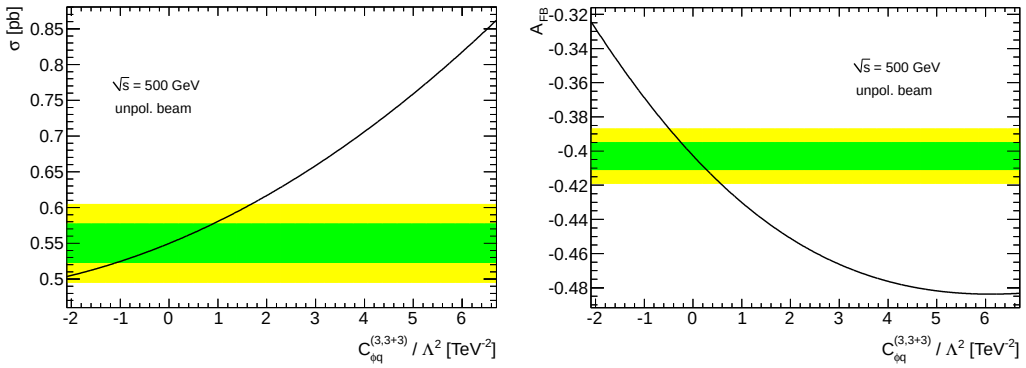

Figure 6.3: Dependence of the unpolarized cross section and FB asymmetry on $C_{\phi q}^{(3,3+3)}$.

Limits on C_{uW}^{33} have already been obtained from the measurement of helicity fractions in top decays by the ATLAS Collaboration [8], as shown in equation (5.11). In Figure 6.4, the variation of the unpolarized cross section and FB asymmetry at ILC is plotted, for Re C_{uW}^{33} within these limits. For this operator, the excellent sensitivity mainly stems from the $\sqrt{s}/m_t$ enhancement of its contribution to $e^+e^- \to$

[2] To our knowledge there are not yet complete studies of experimental systematics in the $t\bar{t}$ cross section and asymmetry measurements, and these values seem a reasonable estimate, given the expected improvement over LHC systematics for an e^+e^- machine. (Statistical uncertainties for cross sections and asymmetries are below 1% already for a luminosity of 100 fb^{-1}.) The main results of this study, that is, the improvement with respect to the LHC sensitivity and the possibility of disentangling effective operator contributions, are largely independent of the precise numbers assumed.

$t\bar{t}$ with respect to W helicity observables. Assuming that the operator coefficient equals unity, the sensitivity to the new physics scale Λ extends up to 4.5 TeV for this CM energy.

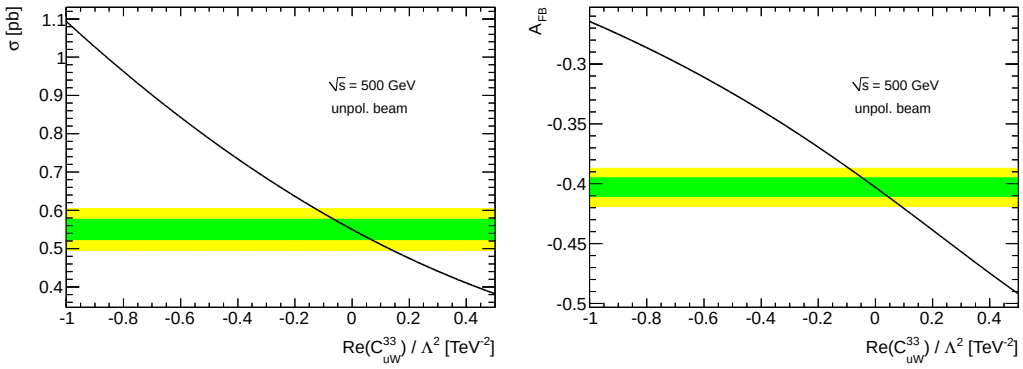

Figure 6.4: Dependence of the unpolarized cross section and FB asymmetry on Re C_{uW}^{33}.

The anti-Hermitian part of this operator can also be probed with a CP-violating asymmetry $A_{\rm FB}^{N}$ defined for polarized top decays [213], being the estimated sensitivity

$$\frac{\text{Im } C_{uW}^{33}}{\Lambda^2} \in [-0.9, 0.9] \text{ TeV}^{-2} \,. \tag{6.13}$$

The corresponding variation of the $t\bar{t}$ cross section and asymmetry are shown in Figure 6.5. The sensitivity is moderate in this case and comparable to the one at the LHC, in spite of the fact that the anti-Hermitian part of this operator does not interfere with the SM in CP-conserving quantities such as total cross sections and asymmetries, and their dependence on Im O_{uW}^{33} is quadratic (as it can be readily observed in the plots).

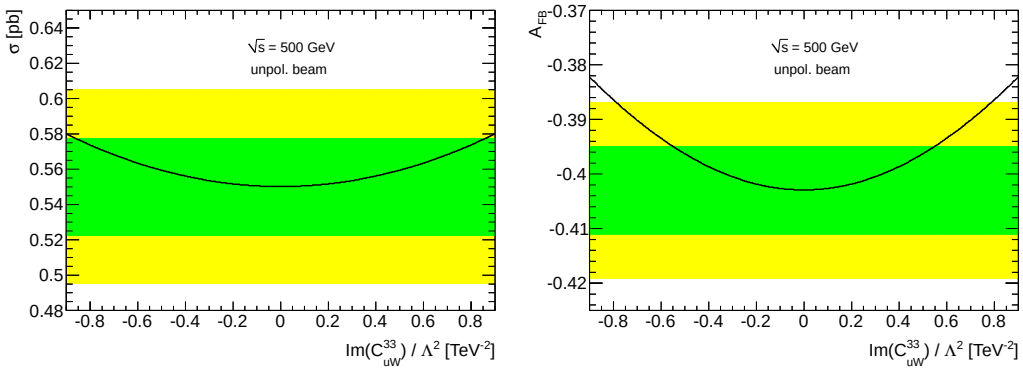

Figure 6.5: Dependence of the unpolarized cross section and FB asymmetry on Im C_{uW}^{33}.

Future LHC limits have also been estimated for $t\bar{t}Z$ and $t\bar{t}\gamma$ production [228]. The best ones are for the later process, and translated into our framework give

$$\begin{aligned} \frac{\text{Re } C_{uW}^{33}}{\Lambda^2}, \frac{\text{Im } C_{uW}^{33}}{\Lambda^2} &\in [-2.1, 2.1] \text{ TeV}^{-2}, \\ \frac{\text{Re } C_{uB\phi}^{33}}{\Lambda^2}, \frac{\text{Im } C_{uB\phi}^{33}}{\Lambda^2} &\in [-1.2, 1.2] \text{ TeV}^{-2}. \end{aligned} \tag{6.14}$$

The potential limit on Re C_{uW}^{33} has already been surpassed by the ATLAS W helicity measurement [8] and the limit on Im C_{uW}^{33} from CP violation in top decays is expected to be better. On the other hand, potential LHC limits on $O_{uB\phi}^{33}$ are relevant but would be surpassed at the ILC, as it can be seen in Figure 6.6.

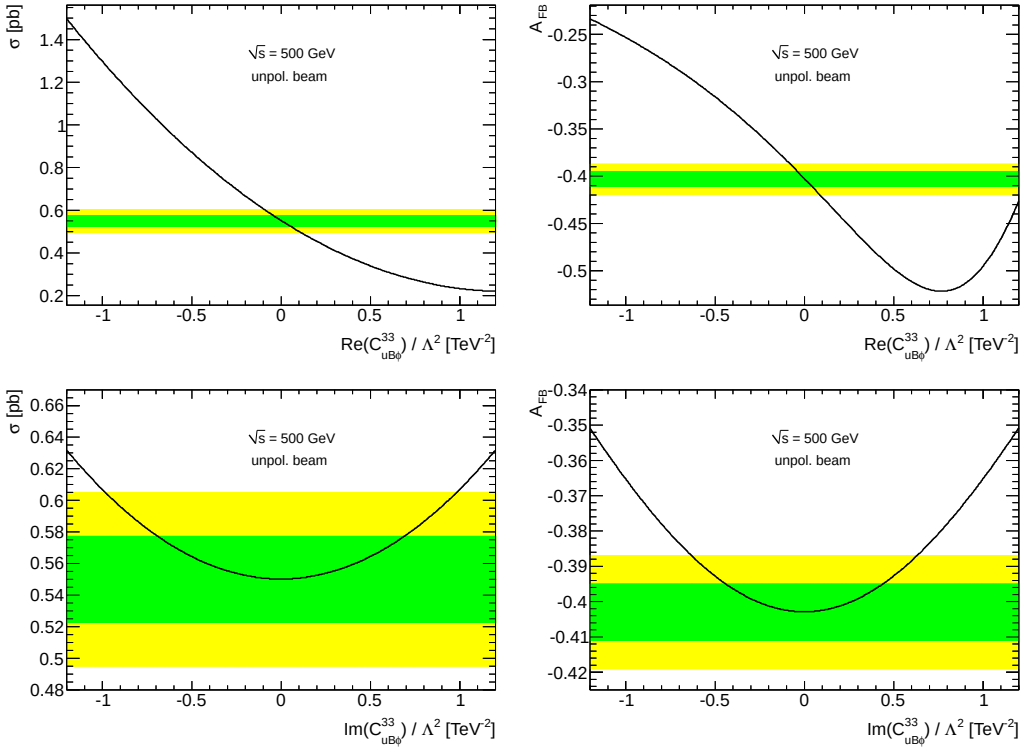

Figure 6.6: Dependence of the unpolarized cross section and FB asymmetry on Re $C_{uB\phi}^{33}$ (up) and Im $C_{uB\phi}^{33}$ (down).

6.4 Disentangling Operator Contributions

At the LHC, the $Zt\bar{t}$ and $\gamma t\bar{t}$ couplings can be independently measured in $t\bar{t}Z$ and $t\bar{t}\gamma$ associated production, respectively. However, the ILC sensitivity to anomalous contributions is probably much better, posing the question of whether the different contributions can also be disentangled at this collider, given the fact that both Z, γ

exchange in the s-channel contribute to $e^+e^- \to t\bar{t}$.[3] This is possible by using the different options proposed for the ILC, like beam polarization and a CM energy upgrade to 1 TeV. The electron longitudinal polarization is assumed to be $P_e = \pm 0.8$. Additional positron polarization improves the results, but, since this possibility is still under debate, no positron polarization is assumed. Since the left-right asymmetry A_{LR} is not independent from the polarized cross sections already considered, it was not used as a constraint. Nonetheless, since experimental systematics may be smaller for this observable, it may be useful to include it too. The limits presented here do not result from a global fit but they are obtained requiring 1σ agreement of the different cross sections and FB asymmetries considered in each case.

Measurements performed with different electron polarizations allow to distinguish d_i^Z from d_i^γ, $i = V, A$, which in turn allows to disentangle C_{uW}^{33} and $C_{uB\phi}^{33}$. To illustrate this, a simplified scenario where the rest of operator coefficients are set to zero is taken, while these two are assumed complex. In Figure 6.7 (left) the combined limits on Re C_{uW}^{33} and Re $C_{uB\phi}^{33}$ are shown without and with beam polarization. In the unpolarized case (yellow region) the measurements of both coefficients are largely anti-correlated, while the use of electron polarization (green region) allows to determine the both quantities with a far smaller uncertainty. This great improvement results from the complementarity of limits for left- and right-handed beams, whose corresponding allowed regions are nearly orthogonal (right panel).

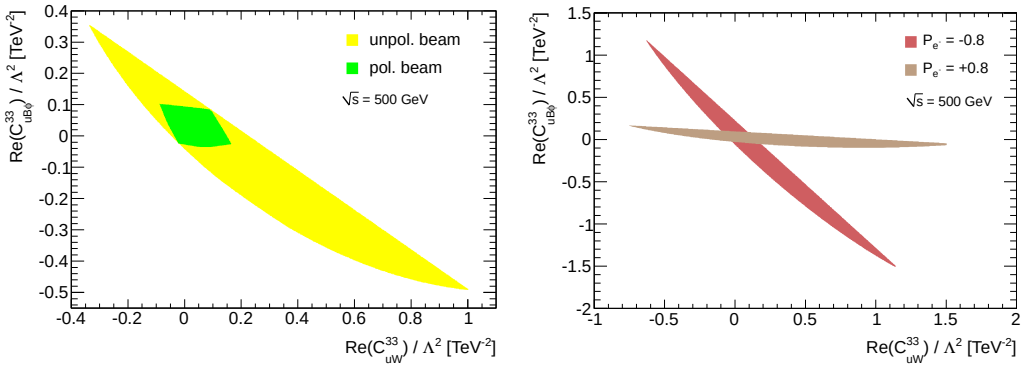

Figure 6.7: Left: combined limits on C_{uW}^{33} and $C_{uB\phi}^{33}$ for the cases of no beam polarization and electron beam polarization (only the real parts of these coefficients are shown). Right: complementarity of the measurements for $P_{e^-} = 0.8$ and $P_{e^-} = -0.8$.

As previously pointed out, measurements taken at different CM energies allow to

[3]Properly speaking, for tensor couplings the issue is not to measure separately the photon and Z boson couplings, but to disentangle possible contributions from the two operators O_{uW}^{33} and $O_{uB\phi}^{33}$, which simultaneously contribute to the $Zt\bar{t}$ and $\gamma t\bar{t}$ vertices with different weights, see equations (6.5). In this sense, the usual assumption of setting either the photon or Z boson contribution to zero to obtain limits on the other, is not useful in this effective operator framework.

distinguish γ^μ and $\sigma^{\mu\nu}$ couplings. At a given CM energy, it is often possible to fine-tune a cancellation between their contributions to cross sections and asymmetries so that the overall effects are small. This is not possible, however, at different CM energies, such as 500 GeV and 1 TeV, because the energy dependence of these contributions is different. An example of this interplay is shown in Figure 6.8, where a simplified scenario is considered where only $C_{\phi q}^{(3,3+3)}$ and C_{uW}^{33} are non-zero. The yellow region corresponds to limits with polarized beams at 500 GeV only, whereas the green region also includes limits at 1 TeV. The blue lines around the green region correspond to the constraints caused by each observable.

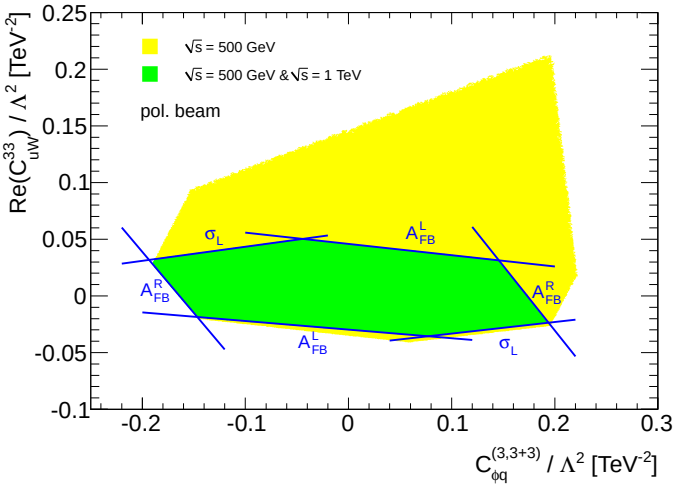

Figure 6.8: Combined limits on $C_{\phi q}^{(3,3+3)}$ and C_{uW}^{33} for a CM energy of 500 GeV and also with 1 TeV (only the real part of the later coefficient is shown).

Having shown the complementarity of the different beam polarization and CM energy options, Figure 6.9 shows the general limits for arbitrary $C_{\phi q}^{(3,3+3)}$, $C_{\phi u}^{3+3}$, C_{uW}^{33} and $C_{uB\phi}^{33}$, the later two complex (six real parameters in total), using polarized cross section and asymmetry measurements at 500 GeV and 1 TeV (eight constraints in total). These limits are excellent for C_{uW}^{33} and $C_{uB\phi}^{33}$, even if there is a large anti-correlation between the limits on their real parts. For $C_{\phi q}^{(3,3+3)}$ and $C_{\phi u}^{3+3}$ the limits are also interesting and better than the ones expected at the LHC through measurements of the single top cross section. These combined limits are numerically worse than the sensitivities shown in the previous section because here all possible cancellations between operator contributions are allowed. For example, if $C_{\phi u}^{3+3}$ is set to zero, the resulting limit on $C_{\phi q}^{(3,3+3)}$ improves by more than a factor of two.

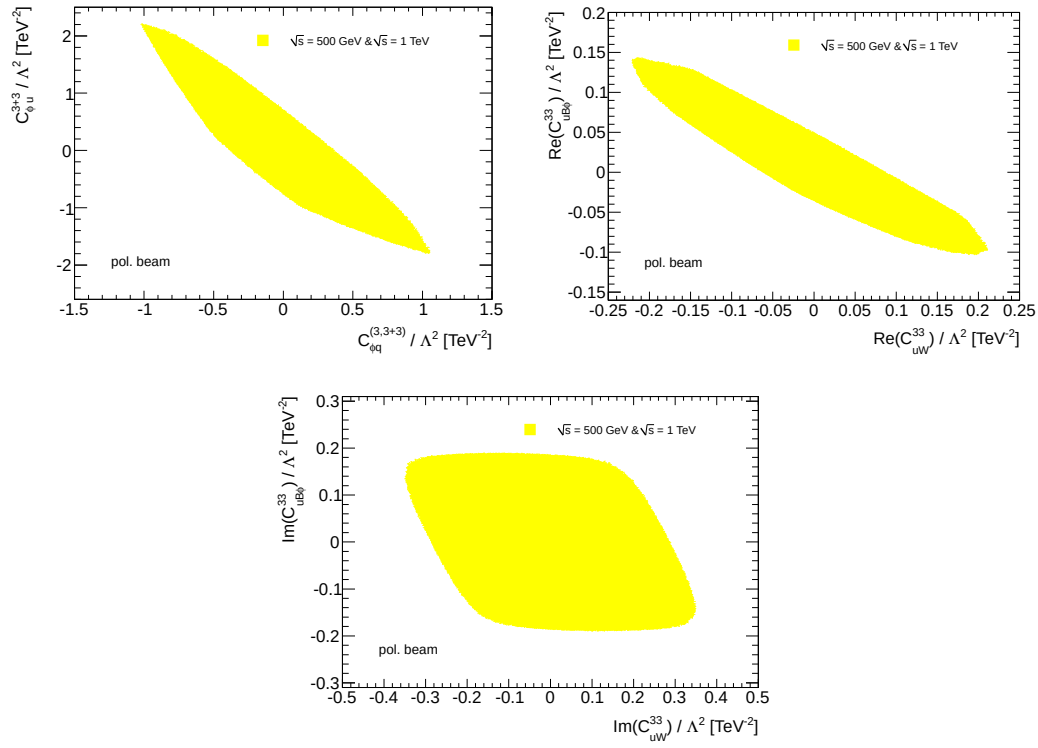

Figure 6.9: Combined limits on $Zt\bar{t}$ and $\gamma t\bar{t}$ trilinear effective operator coefficients.

6.5 Conclusions

The effect of top trilinear effective operators in $e^+e^- \to t\bar{t}$ at ILC energies was studied. The first purpose was to investigate the ILC sensitivity to these operators, comparing with the LHC. As already known, the sensitivity to $Zt\bar{t}$ and $\gamma t\bar{t}$ couplings is better at the ILC than in $t\bar{t}Z$ and $t\bar{t}\gamma$ at the LHC [228]. But, on the contrary of previous approaches, the effective operator framework adopted also allows for a direct comparison with charged current processes at the LHC, like single top production and decays $t \to Wb$. Despite the fact that the LHC prospects are already good due to its excellent statistics, the ILC sensitivity is even better for those operators. Assuming operator coefficients equal to unity, the new physics scales probed extend up to 4.5 TeV, for a CM energy of 500 GeV.

A second issue investigated in detail is how to set simultaneous bounds on all the operators involved, which contribute to the $Zt\bar{t}$ and $\gamma t\bar{t}$ vertices. The use of electron beam polarization is essential to disentangle contributions, as is the combination of measurements at 500 GeV and 1 TeV. The results presented here make manifest that the determination of top interactions constitute a physics case for the use of electron beam polarization, as well as for a possible CM energy upgrade to 1 TeV.

Chapter 7

Conclusions

In the first phase of the doctoral work, a χ^2 method was proposed to remove the correlated noise component of the TileCal. The method was tested and approved through a systematic survey of the TileCal modules as a powerful solution to the coherent noise presence in pedestal runs. This approach shall be regarded as well as an effective diagnosis tool to the general behavior of TileCal modules [2, 3]. The analysis of special calibration runs, where only one channel is fired at a time, excluded the presence of cross-talk allowing the χ^2 method to be applied in the presence of physics signals. No degradation of the signal was observed. The results on Minimum Bias and simulated $t\bar{t}$ events showed a clear improvement on the pedestal noise distribution and, once more, the signal was not degraded. In conclusion, the method proved to be very effective and reliable for different kinds of events, both real and simulated.

In the second phase of the studies, the measurement of the polarization of the W boson in top quark decays was performed, using 1.04 fb^{-1} of data collected from pp collisions with the ATLAS detector in 2011. The single lepton and dilepton decay topologies of top quark pairs were considered in the analysis. The helicity fractions obtained from a combination of template fits to the reconstructed $\cos\theta^*$ distributions and angular asymmetries calculated from the unfolded $\cos\theta^*$ distributions are $F_0 = 0.67 \pm 0.07$, $F_{\mathrm{L}} = 0.32 \pm 0.04$ and $F_{\mathrm{R}} = 0.01 \pm 0.05$, and can be translated into angular asymmetries yielding $A_+ = 0.53 \pm 0.02$ and $A_- = -0.84 \pm 0.02$ [8]. These results are in agreement with NNLO QCD predictions and are more precise than previous results obtained by the CDF and DØ Collaborations [83–85]. In addition, the limits on the Wtb vertex anomalous couplings were obtained from the combined results on the W boson helicity fractions. These results are consistent with the $(V - A)$ structure of the Wtb vertex and improve on the previous results [86].

The effect of top trilinear effective operators in $e^+e^- \rightarrow t\bar{t}$ at ILC energies was studied and compared with the LHC [9]. Despite the fact that the LHC prospects

are already good due to its excellent statistics, the sensitivity to these operators may largely surpass the one achievable by the LHC either in neutral or charged current processes. For a center-of-mass energy of 500 GeV, and assuming operator coefficients equal to unity, the new physics scales probed extend up to 4.5 TeV. In addition, the combination of measurements at 500 GeV and 1 TeV allow to disentangle contributions, as well as the use of electron beam polarization. These results make clear that the study of top interactions constitute a physics case for a possible CM energy upgrade to 1 TeV, and the use of electron beam polarization at the ILC.

Appendix A

Survey of the TileCal Correlated Noise

A.1 Introduction

A systematic survey of the TileCal correlated noise is presented in this appendix. The pedestal run correlation matrices are shown for several TileCal of the four partitions, before and after applying the χ^2 correction algorithm. A similar correlations pattern exists among the different TileCal modules within the same partition, visible in section A.2. However, the use of a single matrix to describe the general behavior of the TileCal correlated noise effect is discarded. Moreover, modules LBA15 and LBC18, in which the power supply is physically separated from the modules, present different noise correlations values. Therefore, no relation can be established between the distance of the power supply to the module and the channels correlations. It is also important to stress that LBC modules from 41 to 48, shown for some examples, correspond to one of the regions in TileCal where correlated noise is more important. Finally, the EBC12 module clearly shows how the correlations match with the hardware structure (Digitizers and Motherboards).

The algorithm performance is also shown in section A.4 for LBA48 when channel 3 is being fired (1000 events). The correlation matrices are shown before and after applying the unfolding method for the seven digitized samples, using the information from the first digitized sample.

A.2 Correlation matrices before applying the method

The correlation matrices before applying the method are shown for several modules, using the reconstructed energy with the optimal filter without iterations.

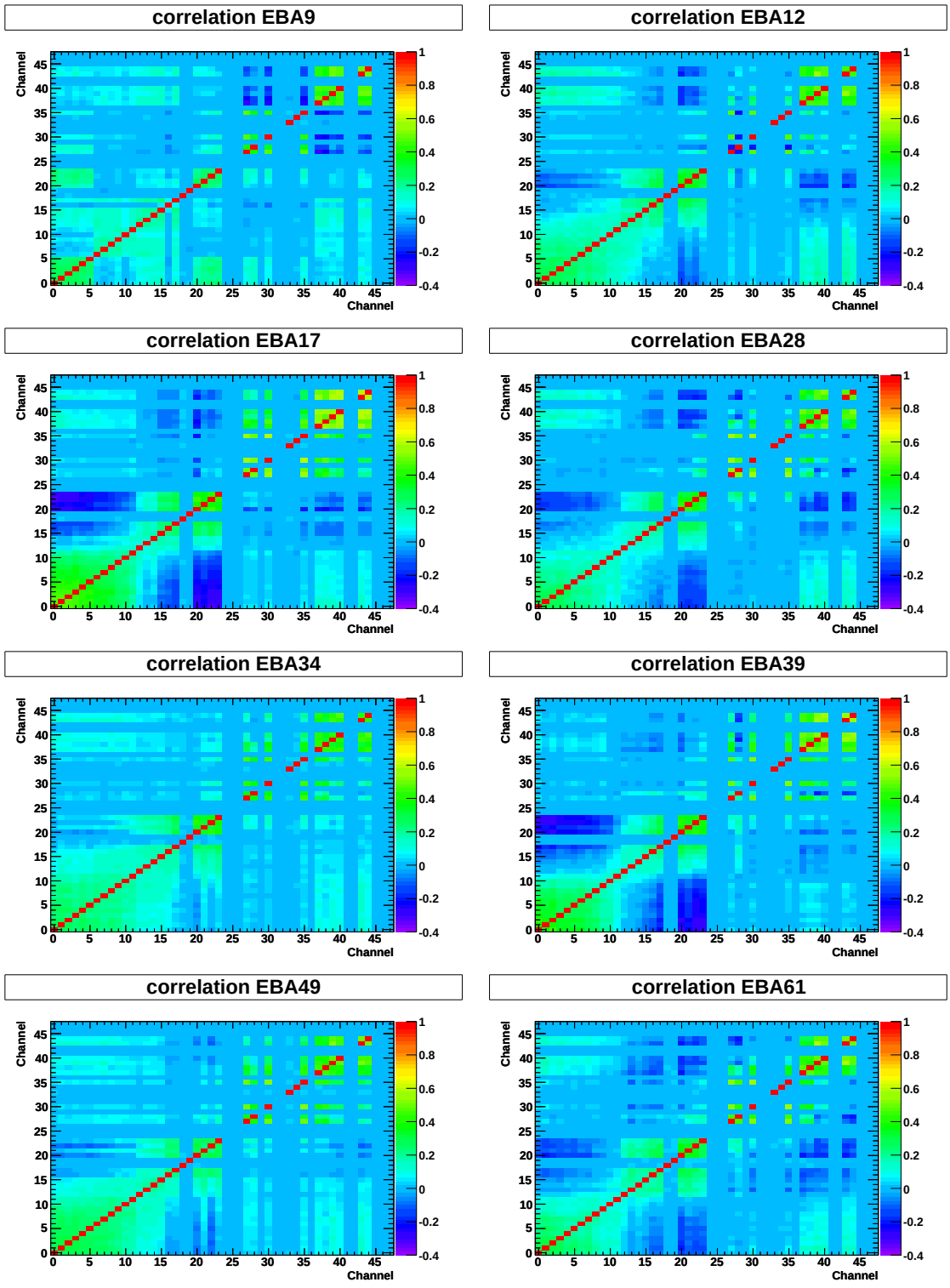

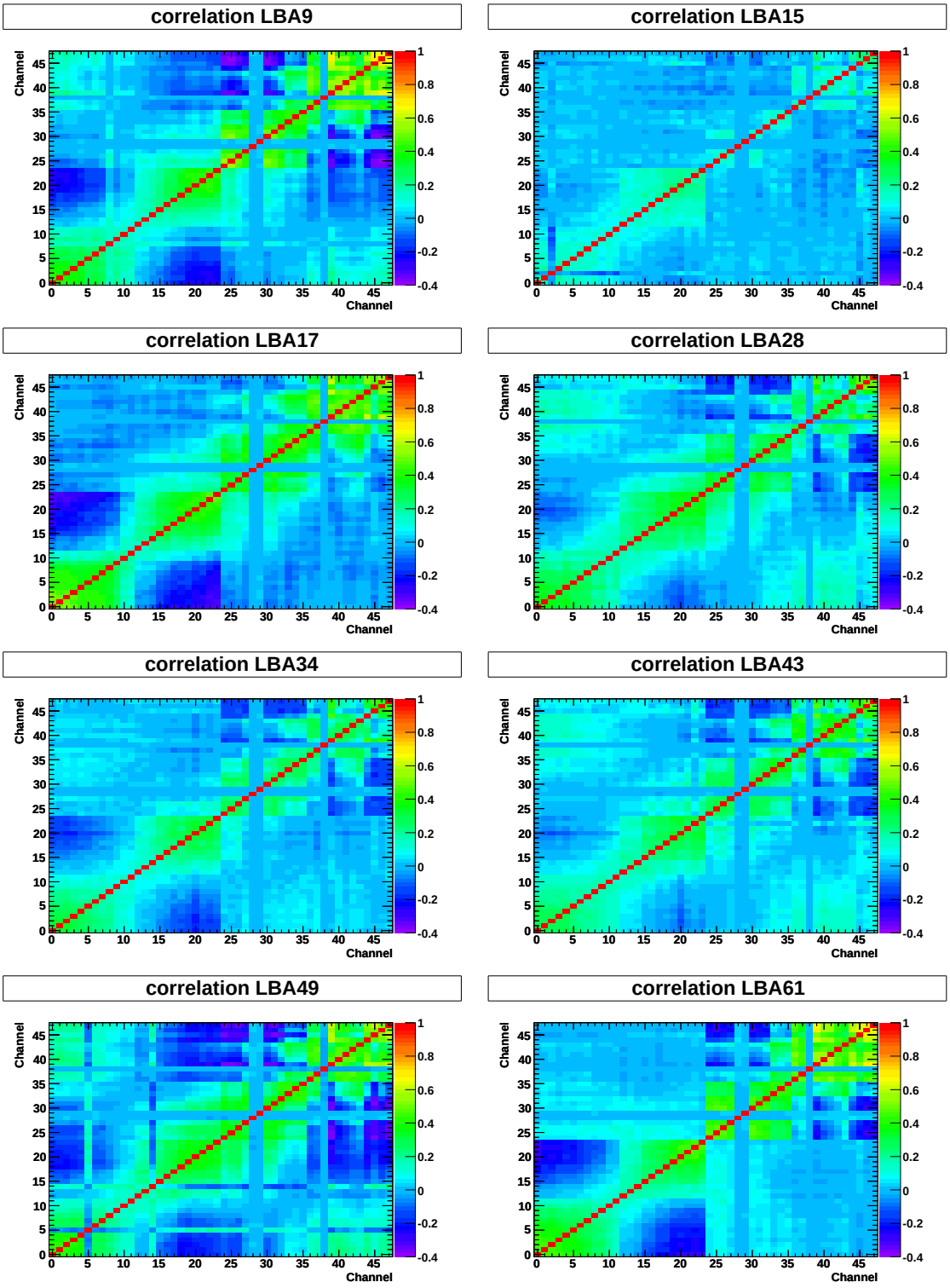
correlation LBA9
correlation LBA15
correlation LBA17
correlation LBA28
correlation LBA34
correlation LBA43
correlation LBA49
correlation LBA61
Channel
Channel

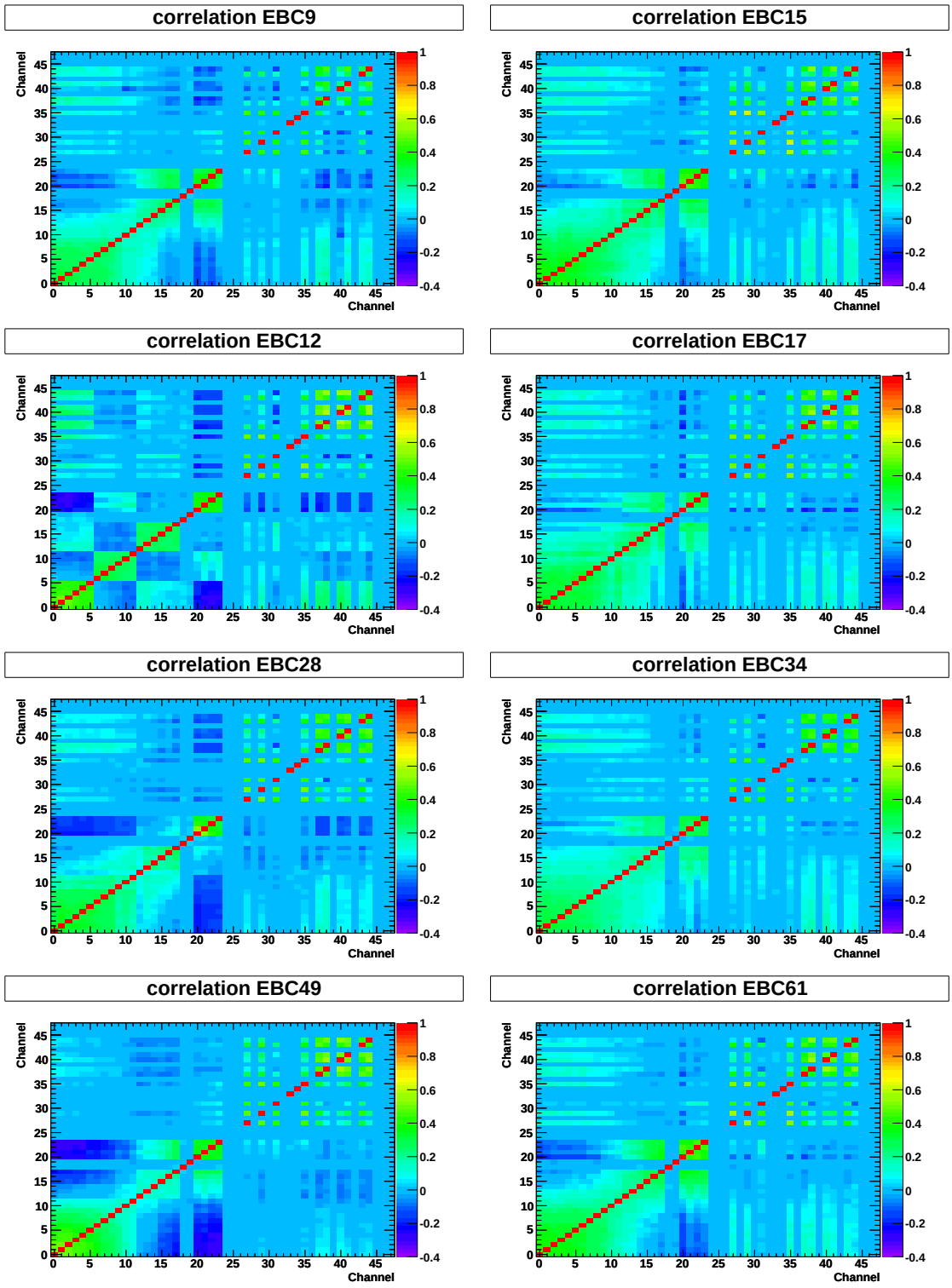
correlation EBC9
correlation EBC15
correlation EBC12
correlation EBC17
correlation EBC28
correlation EBC34
correlation EBC49
correlation EBC61
Channel
Channel

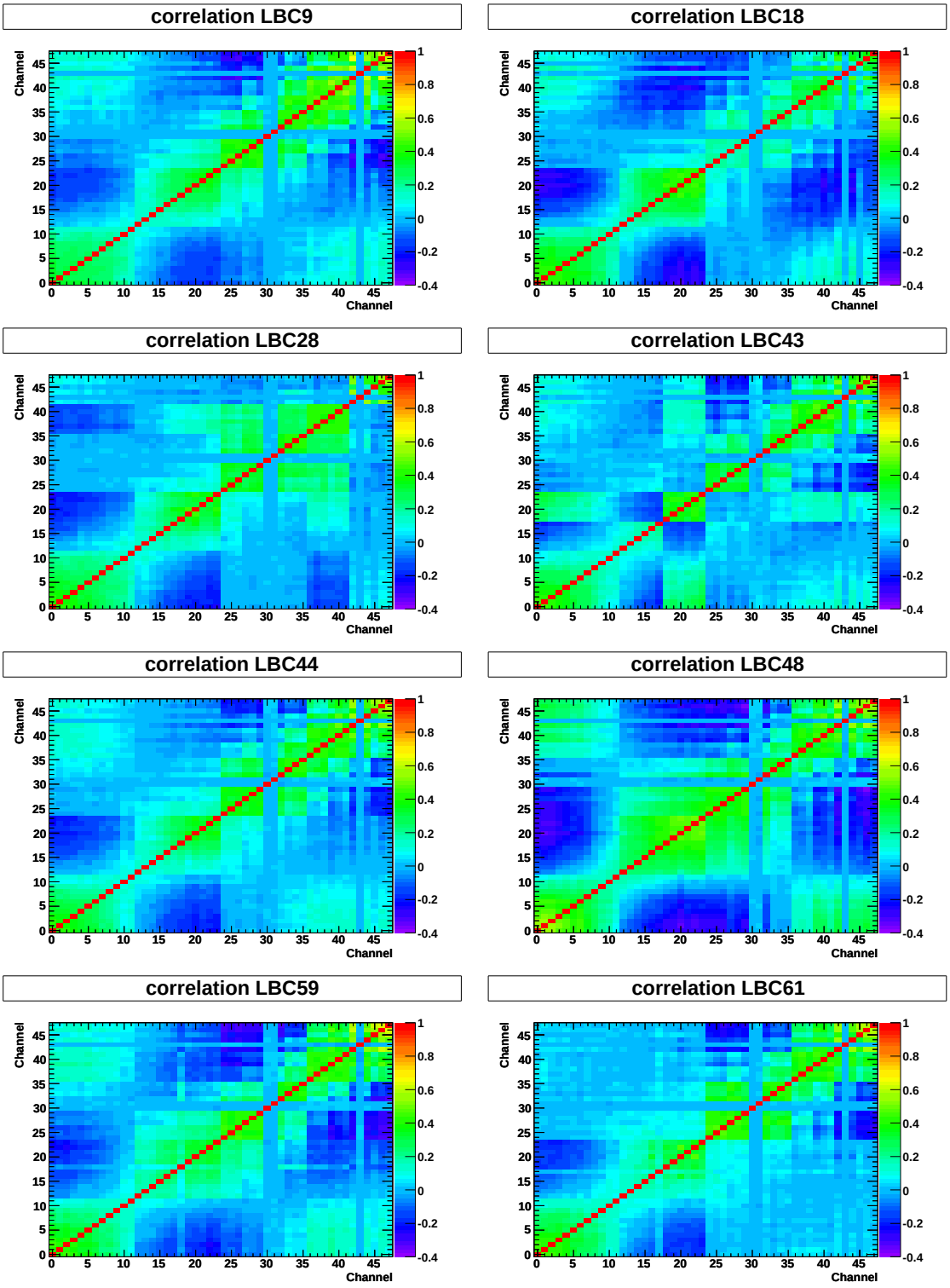
correlation LBC9
correlation LBC18
correlation LBC28
correlation LBC43
correlation LBC44
correlation LBC48
correlation LBC59
correlation LBC61
Channel
Channel

A.3 Correlation matrices after applying the method

The correlation matrices after applying the method are shown for several modules, using the reconstructed energy with the optimal filter without iterations.

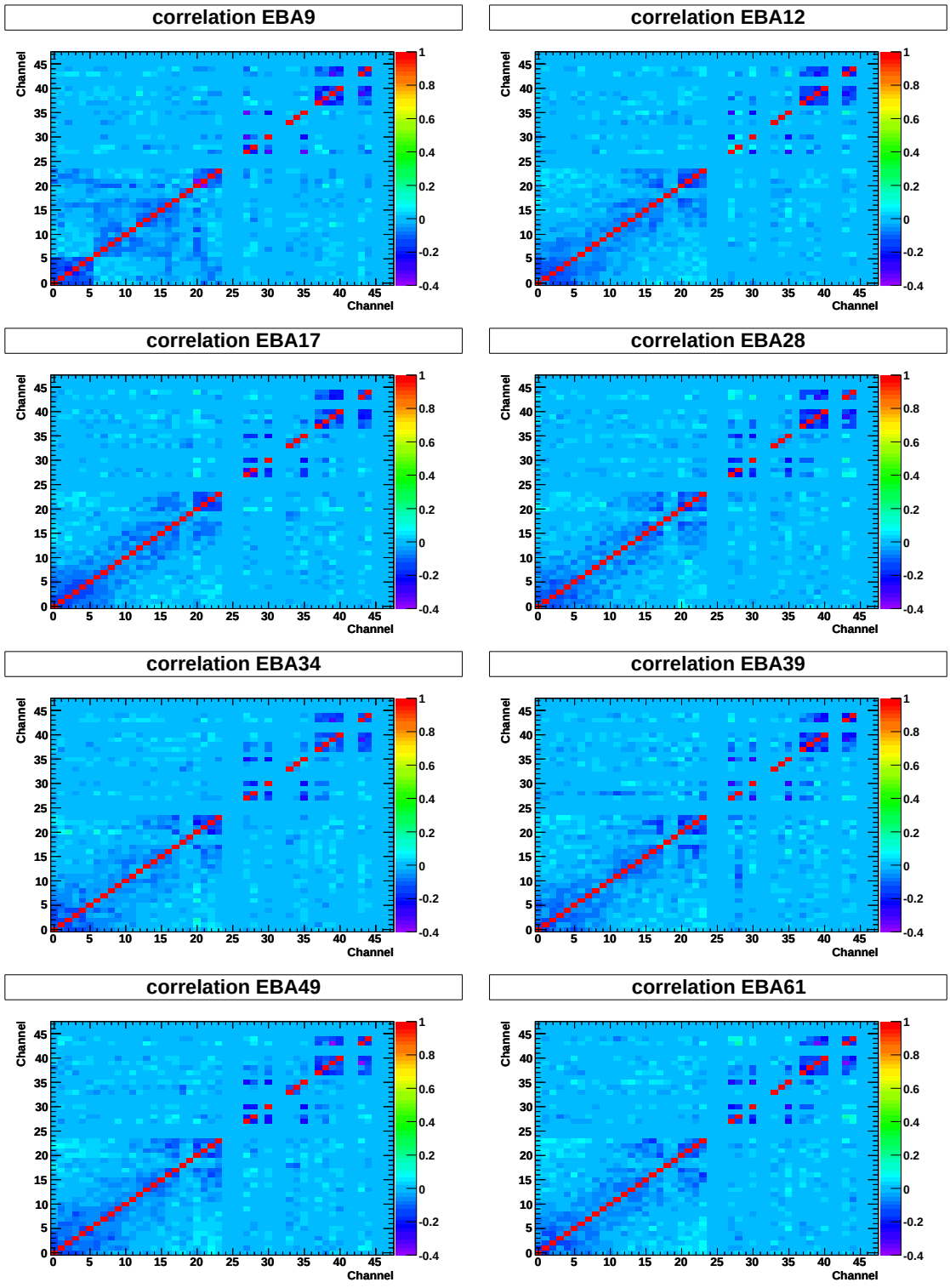

correlation LBA9

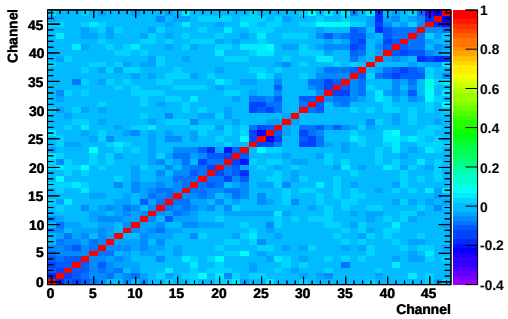

correlation LBA15

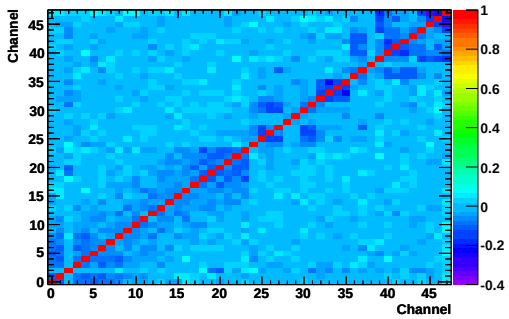

correlation LBA17

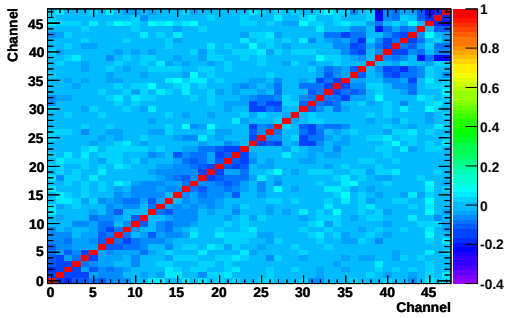

correlation LBA28

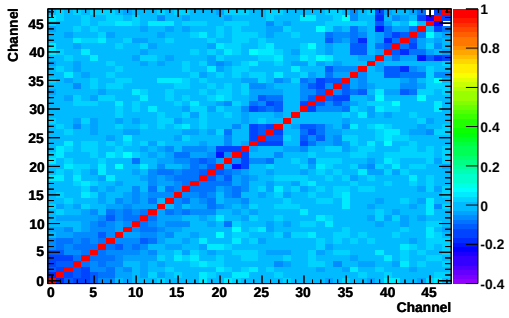

correlation LBA34

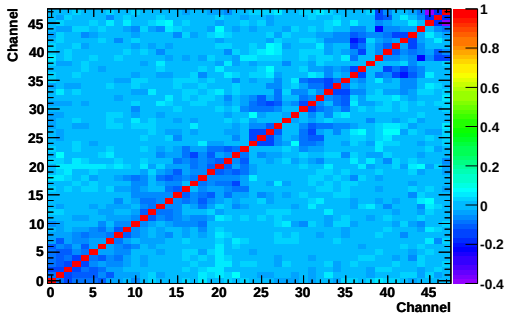

correlation LBA43

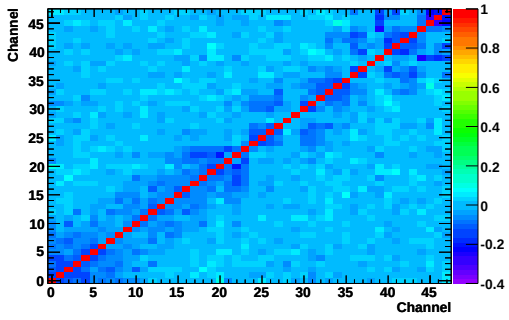

correlation LBA49

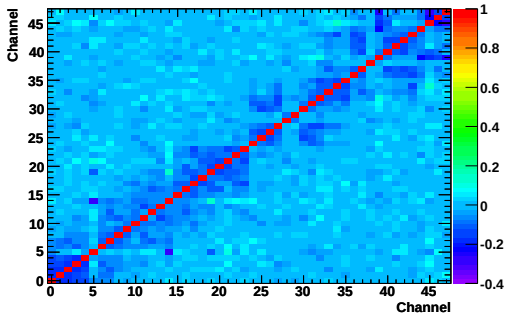

correlation LBA61

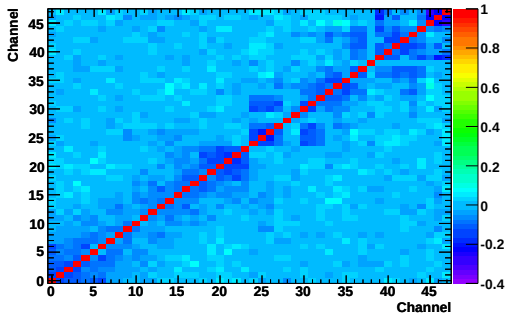

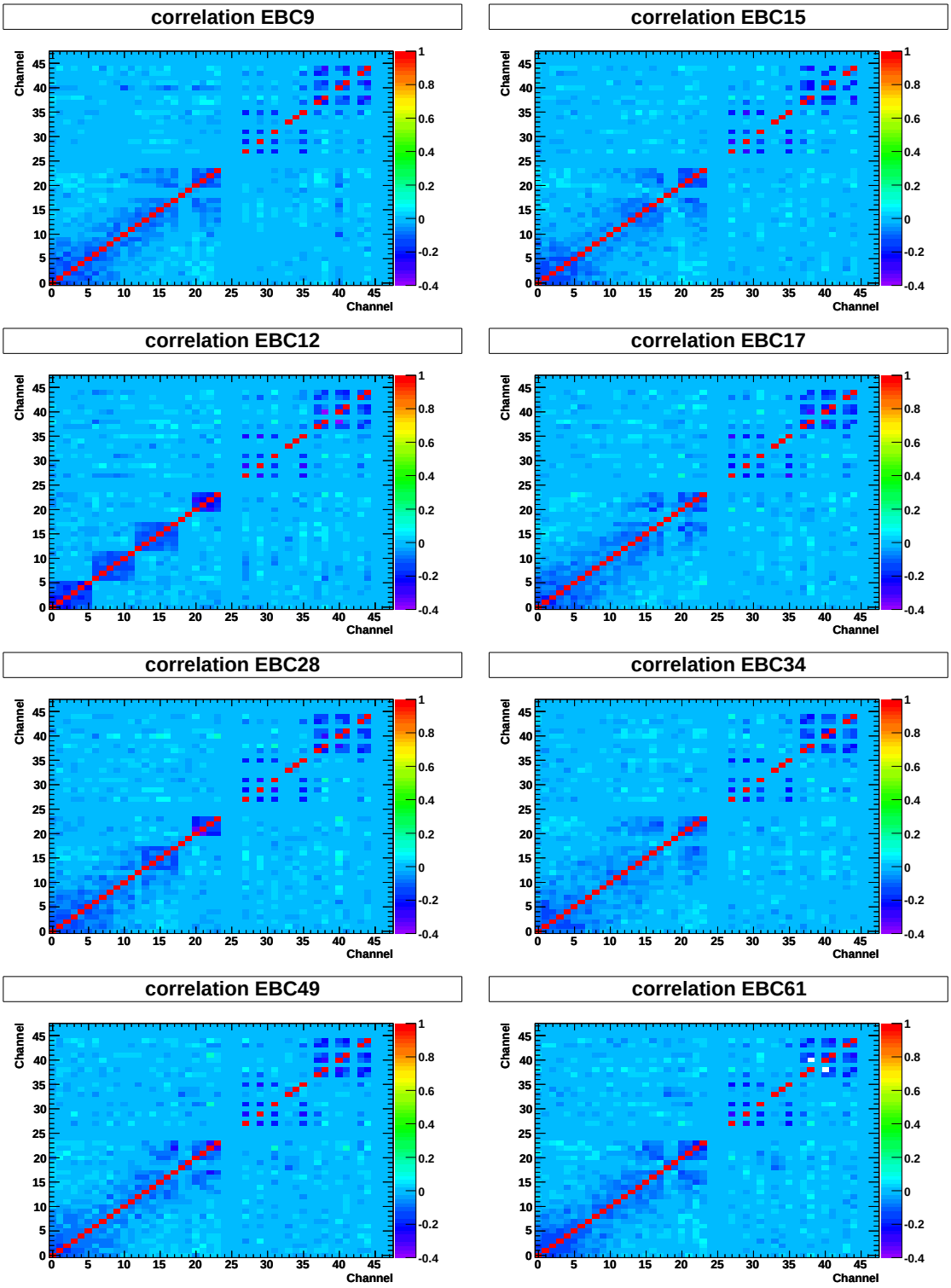
correlation EBC9
correlation EBC15
correlation EBC12
correlation EBC17
correlation EBC28
correlation EBC34
correlation EBC49
correlation EBC61
Channel
Channel

correlation LBC9

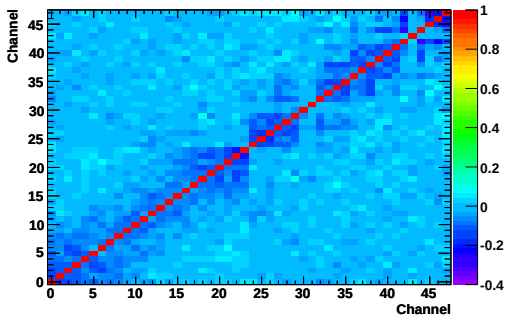

correlation LBC18

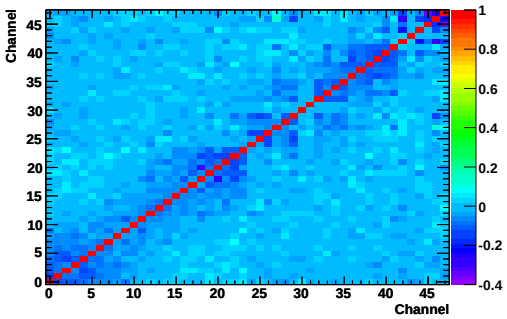

correlation LBC28

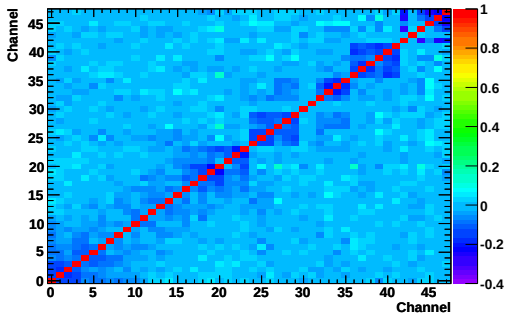

correlation LBC43

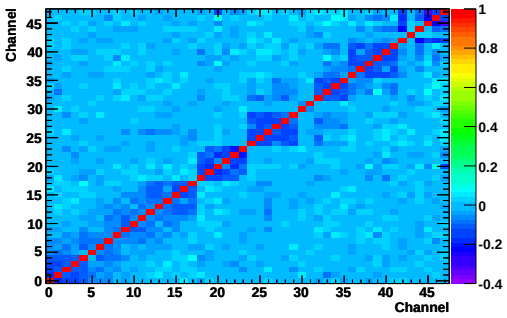

correlation LBC46

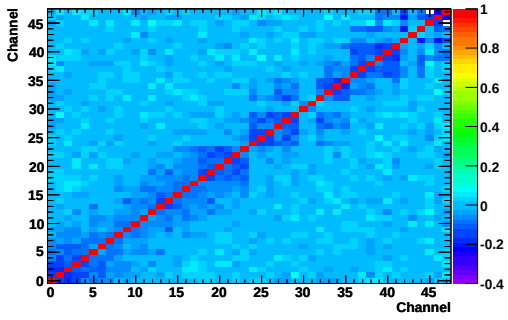

correlation LBC48

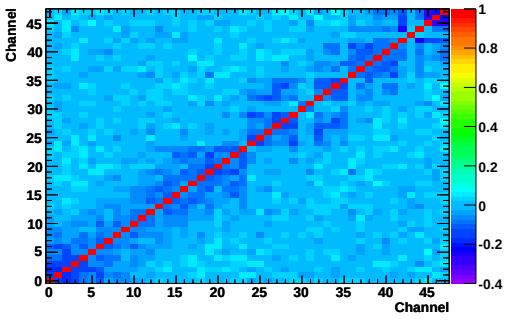

correlation LBC59

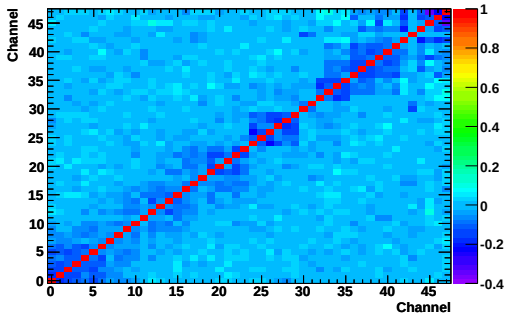

correlation LBC61

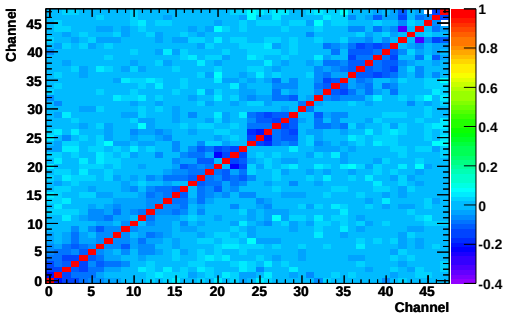

A.4 TileCIS correlation matrices before applying the method

The correlation matrices before applying the method are shown for LBA48 for all samples when channel 3 is being fired (1000 events), using the correlation pattern from Sample 0.

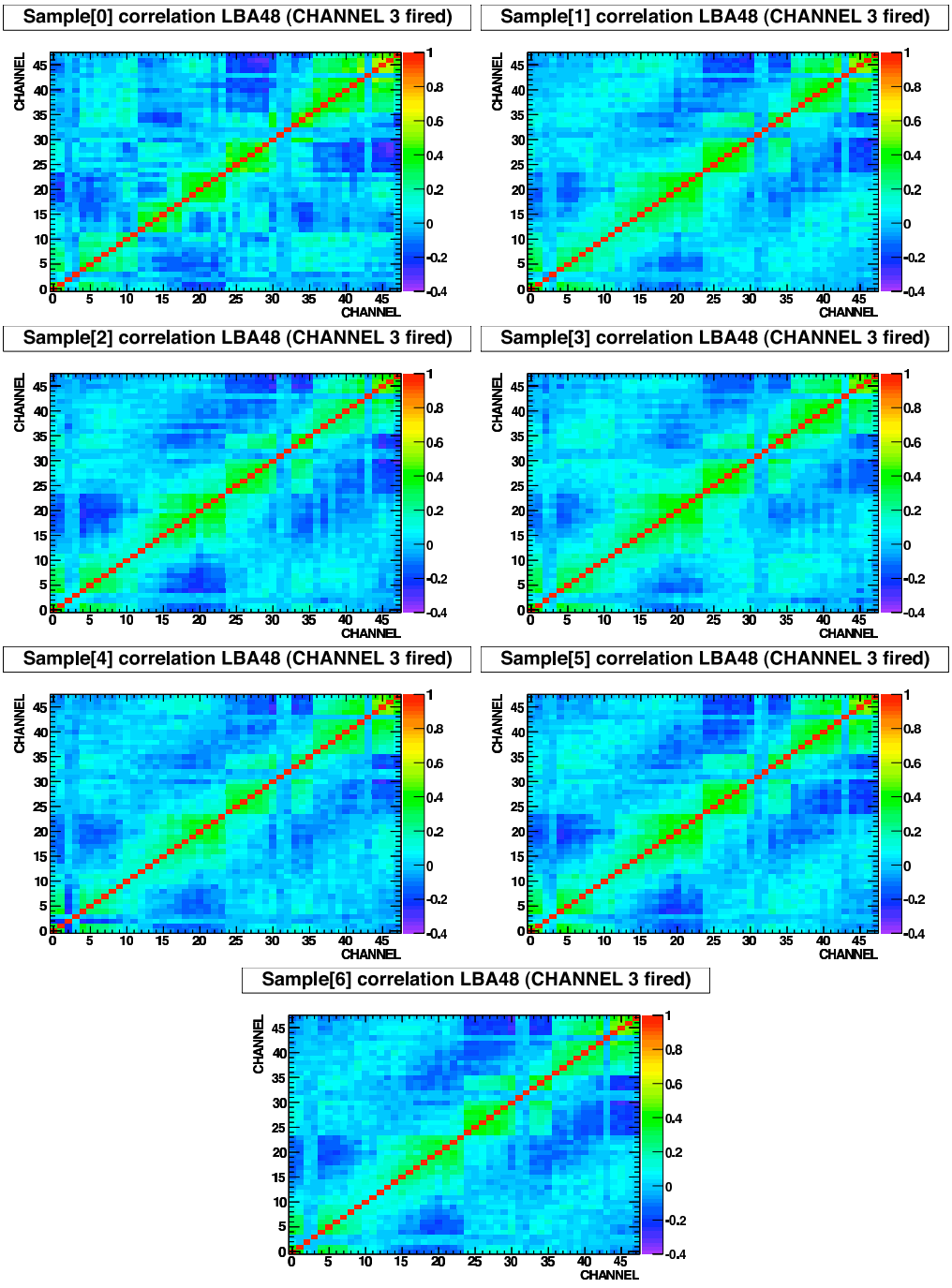

A.5 TileCIS correlation matrices after applying the method

The correlation matrices after applying the method are shown for LBA48 for all samples when channel 3 is being fired (1000 events), using the correlation pattern from Sample 0.

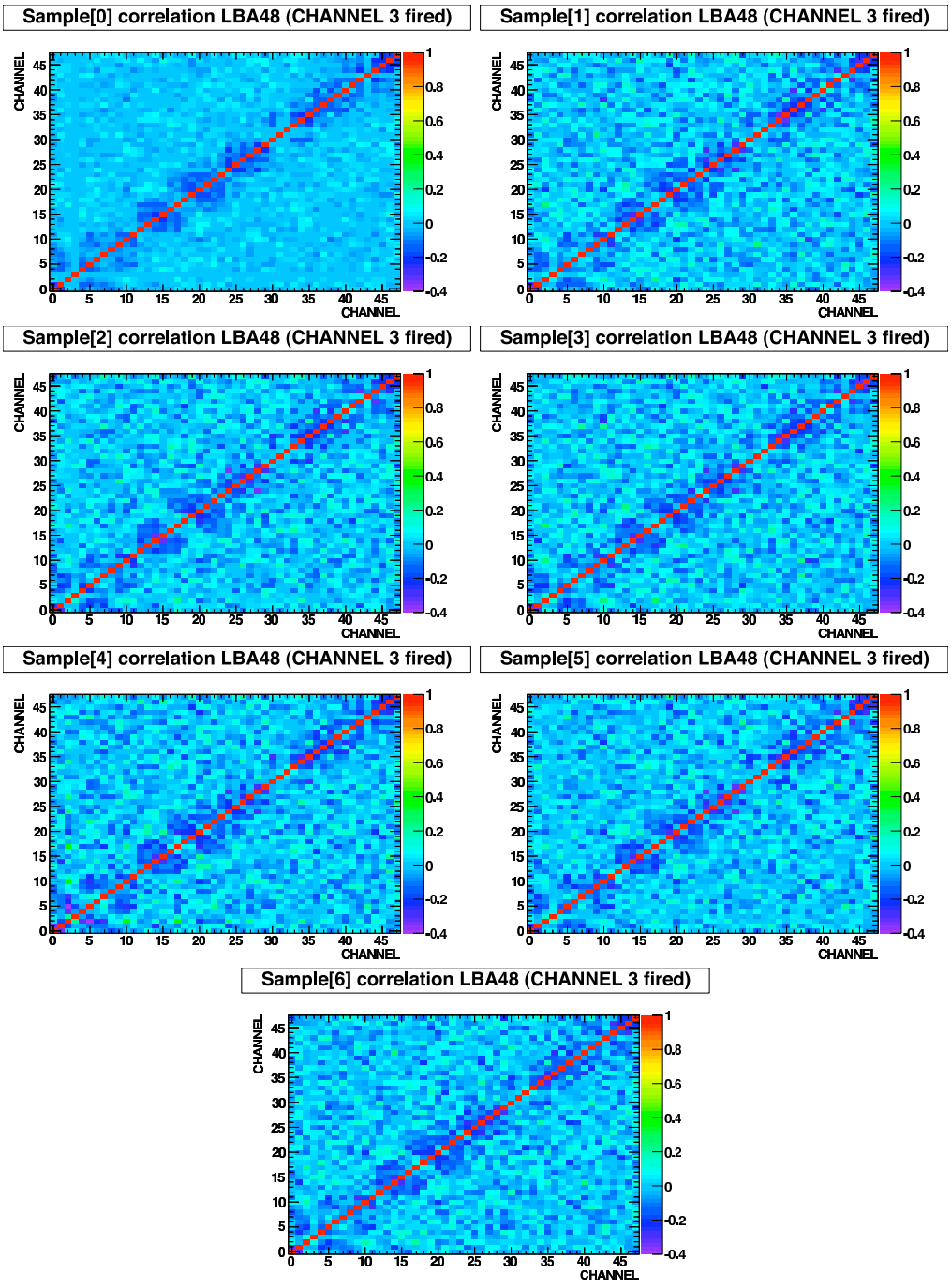

Appendix B

Top Quark Production at the ILC

B.1 Introduction

The top quark production at the ILC is dominated by the top quark pair production through the s-channel, shown in Figure B.1. As already mentioned, the $Zt\bar{t}$ vertex including the SM and dimension-six operator contributions, reads as

$$\mathcal{L}_{Zt\bar{t}} = -\frac{g}{2c_W}\bar{t}\,\gamma_\mu\left(c_L^t P_L + c_R^t P_R\right) t\; Z_\mu - \frac{g}{2c_W}\bar{t}\,\frac{i\sigma^{\mu\nu}q_\nu}{M_Z}\left(d_V^Z + id_A^Z\gamma_5\right) t\; Z_\mu\,, \tag{B.1}$$

with $c_L^t = X_{t\bar{t}}^L - 2s_W^2 Q_t$, $c_R^t = X_{t\bar{t}}^R - 2s_W^2 Q_t$ ($Q_t = 2/3$ is the top quark electric charge) and

$$\begin{aligned} X_{t\bar{t}}^L &= 1 + \left[C_{\phi q}^{(3,3+3)} - C_{\phi q}^{(1,3+3)}\right]\frac{v^2}{\Lambda^2}\,, & d_V^Z &= \sqrt{2}\,\mathrm{Re}\,\left[c_W C_{uW}^{33} - s_W C_{uB\phi}^{33}\right]\frac{v^2}{\Lambda^2}\,, \\ X_{t\bar{t}}^R &= -C_{\phi u}^{3+3}\frac{v^2}{\Lambda^2}\,, & d_A^Z &= \sqrt{2}\,\mathrm{Im}\,\left[c_W C_{uW}^{33} - s_W C_{uB\phi}^{33}\right]\frac{v^2}{\Lambda^2}\,, \end{aligned} \tag{B.2}$$

where the C constants are the coefficients of the operators and Λ is the new physics scale. The $\gamma t\bar{t}$ vertex reads

$$\mathcal{L}_{\gamma t\bar{t}} = -eQ_t\bar{t}\,\gamma_\mu t\; A_\mu - e\bar{t}\,\frac{i\sigma^{\mu\nu}q_\nu}{m_t}\left(d_V^\gamma + id_A^\gamma\gamma_5\right) t\; A_\mu\,. \tag{B.3}$$

with

$$\begin{aligned} d_V^\gamma &= \frac{\sqrt{2}}{e}\,\mathrm{Re}\,\left[s_W C_{uW}^{33} + c_W C_{uB\phi}^{33}\right]\frac{vm_t}{\Lambda^2}\,, \\ d_A^\gamma &= \frac{\sqrt{2}}{e}\,\mathrm{Im}\,\left[s_W C_{uW}^{33} + c_W C_{uB\phi}^{33}\right]\frac{vm_t}{\Lambda^2}\,. \end{aligned} \tag{B.4}$$

The electron vertex is assumed to be the SM one:

$$\mathcal{L}_e = -eQ_e\bar{e}\,\gamma_\mu e\; A_\mu - \frac{g}{2c_W}\bar{e}\,\gamma_\mu\left(c_L^e P_L + c_R^e P_R\right) e\; Z_\mu\,, \tag{B.5}$$

with $c_L^e = -1 - 2s_W^2 Q_e$, $c_R^e = -2s_W^2 Q_e$ ($Q_e = -1$).

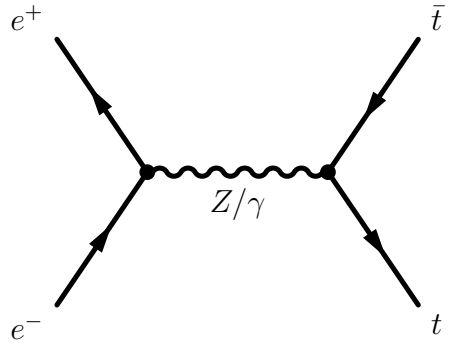

Figure B.1: Top quark production at the ILC through the s-channel.

B.2 Calculations

In the laboratory rest frame, shown in Figure B.2 (repeated here for convenience), the 4-vectors are defined as,

$$\begin{aligned} p_1 &= \left(\frac{\sqrt{s}}{2}, 0, 0, \frac{\sqrt{s}}{2}\right) , \\ p_2 &= \left(\frac{\sqrt{s}}{2}, 0, 0, -\frac{\sqrt{s}}{2}\right) , \\ p_3 &= \left(\frac{\sqrt{s}}{2}, \mathbf{q}\right) , \\ p_4 &= \left(\frac{\sqrt{s}}{2}, -\mathbf{q}\right) , \end{aligned} \tag{B.6}$$

which implies:

$$\begin{aligned} p_1 \cdot p_2 &= \frac{s}{2} \\ p_3 \cdot p_4 &= \frac{s}{2} - m_t^2 \\ p_1 \cdot p_3 &= \frac{s}{4} - \frac{\sqrt{s}}{2}|\mathbf{q}|\cos\theta = \frac{s}{4}\left(1 - \beta\cos\theta\right) , \\ p_1 \cdot p_4 &= \frac{s}{4} + \frac{\sqrt{s}}{2}|\mathbf{q}|\cos\theta = \frac{s}{4}\left(1 + \beta\cos\theta\right) , \\ p_2 \cdot p_3 &= \frac{s}{4} + \frac{\sqrt{s}}{2}|\mathbf{q}|\cos\theta = \frac{s}{4}\left(1 + \beta\cos\theta\right) , \\ p_2 \cdot p_4 &= \frac{s}{4} - \frac{\sqrt{s}}{2}|\mathbf{q}|\cos\theta = \frac{s}{4}\left(1 - \beta\cos\theta\right) , \end{aligned} \tag{B.7}$$

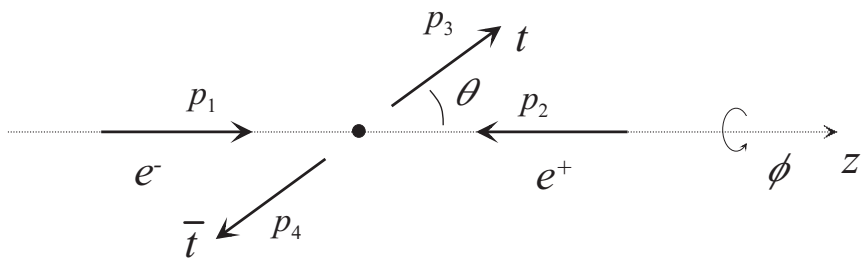

Figure B.2: Electron-positron annihilation producing a pair of top quarks at the ILC in the laboratory rest frame.

where $\sqrt{s}$ is the CM energy and $|\mathbf{q}| = \sqrt{\frac{s}{4} - m_t^2} = \frac{\sqrt{s}}{2}\sqrt{1 - \frac{4m_t^2}{s}} = \frac{\sqrt{s}}{2}\beta$, with $\beta = \sqrt{1 - \frac{4m_t^2}{s}}$. The desired products are then:

$$\begin{aligned}
(p_1 \cdot p_2)m_t^2 &= \frac{s}{2}m_t^2 \\
(p_1 \cdot p_2)(p_3 \cdot p_4) &= \frac{s}{2}\left(\frac{s}{2} - m_t^2\right) = \frac{s^2}{8}\left(1 + \beta^2\right) , \\
(p_1 \cdot p_3)(p_2 \cdot p_4) &= \frac{s^2}{16}\left(1 + \beta^2\cos^2\theta - 2\beta\cos\theta\right) , \\
(p_2 \cdot p_3)(p_1 \cdot p_4) &= \frac{s^2}{16}\left(1 + \beta^2\cos^2\theta + 2\beta\cos\theta\right) , \\
(p_2 \cdot p_3)(p_2 \cdot p_4) &= \frac{s^2}{16}\left(1 - \beta^2\cos^2\theta\right) .
\end{aligned} \tag{B.8}$$

The integration in the solid angle $\mathrm{d}\Omega = 2\pi\sin\theta\mathrm{d}\theta$, for the forward region, gives:

$$\begin{aligned}
\int_0^{\pi/2}(p_1 \cdot p_2)m_t^2 2\pi\sin\theta\mathrm{d}\theta &= \pi s m_t^2 \\
\int_0^{\pi/2}(p_1 \cdot p_2)(p_3 \cdot p_4)2\pi\sin\theta\mathrm{d}\theta &= \frac{\pi s^2}{4}\left(1 + \beta^2\right) , \\
\int_0^{\pi/2}(p_1 \cdot p_3)(p_2 \cdot p_4)2\pi\sin\theta\mathrm{d}\theta &= \frac{\pi s^2}{8}\left(1 + \frac{1}{3}\beta^2 - \beta\right) , \\
\int_0^{\pi/2}(p_2 \cdot p_3)(p_1 \cdot p_4)2\pi\sin\theta\mathrm{d}\theta &= \frac{\pi s^2}{8}\left(1 + \frac{1}{3}\beta^2 + \beta\right) , \\
\int_0^{\pi/2}(p_1 \cdot p_2)(p_2 \cdot p_3)(p_2 \cdot p_4)2\pi\sin\theta\mathrm{d}\theta &= \frac{\pi s^3}{16}\left(1 - \frac{1}{3}\beta^2\right) ,
\end{aligned}$$

and for the backward region:

$$\begin{aligned}
\int_{\pi/2}^{\pi}(p_1\cdot p_2)m_t^2 2\pi\sin\theta\mathrm{d}\theta &= \pi s m_t^2 \\
\int_{\pi/2}^{\pi}(p_1\cdot p_2)(p_3\cdot p_4)2\pi\sin\theta\mathrm{d}\theta &= \frac{\pi s^2}{4}\left(1+\beta^2\right), \\
\int_{\pi/2}^{\pi}(p_1\cdot p_3)(p_2\cdot p_4)2\pi\sin\theta\mathrm{d}\theta &= \frac{\pi s^2}{8}\left(1+\frac{1}{3}\beta^2+\beta\right), \\
\int_{\pi/2}^{\pi}(p_2\cdot p_3)(p_1\cdot p_4)2\pi\sin\theta\mathrm{d}\theta &= \frac{\pi s^2}{8}\left(1+\frac{1}{3}\beta^2-\beta\right), \\
\int_{\pi/2}^{\pi}(p_1\cdot p_2)(p_2\cdot p_3)(p_2\cdot p_4)2\pi\sin\theta\mathrm{d}\theta &= \frac{\pi s^3}{16}\left(1-\frac{1}{3}\beta^2\right).
\end{aligned}$$

The cross-section is given by:

$$\sigma = N_c\times\frac{|\mathbf{q}|}{\frac{\sqrt{s}}{2}}\frac{1}{64\pi^2 s}\int\sum_{\text{spins}}|\mathcal{M}|^2\mathrm{d}\Omega = 3\frac{\beta}{64\pi^2 s}\int\sum_{\text{spins}}|\mathcal{M}|^2\mathrm{d}\Omega\,, \tag{B.9}$$

where $N_c = 3$ is the number of colors, and $\mathcal{M}$ is the matrix element. In order to calculate the matrix elements, the following relations are particularly useful,

$$\sum_s u_\alpha(p,s)\bar{u}_\beta(p,s) = (\not{p}+m)_{\alpha\beta}\,, \tag{B.10}$$

$$\sum_s v_\alpha(p,s)\bar{v}_\beta(p,s) = (\not{p}-m)_{\alpha\beta}\,, \tag{B.11}$$

where $u(p,s)$ and $v(p,s)$ are Dirac spinors, and the sum is over all spins.

The matrix elements were computed for different polarization configurations in order to obtain the desired polarized cross-sections. The different configurations considered were a left-handed electron with a left-handed top quark ($\mathcal{M}^{LL}$), a left-handed electron with a right-handed top quark ($\mathcal{M}^{LR}$), a right-handed electron with a left-handed top quark ($\mathcal{M}^{RL}$), a right-handed electron with a right-handed top quark ($\mathcal{M}^{RR}$), and also the contributions from the axial and vectorial components, a left-handed electron with an axial top quark ($\mathcal{M}^{LA}$), a right-handed electron with an axial top quark ($\mathcal{M}^{RA}$), a left-handed electron with an vectorial top quark ($\mathcal{M}^{LV}$), and finally, a right-handed electron with an vectorial top quark ($\mathcal{M}^{RV}$). The interference terms, $\mathcal{M}^{LL}\mathcal{M}^{LR*}$, $\mathcal{M}^{RR}\mathcal{M}^{RL*}$, $\mathcal{M}^{LL}\mathcal{M}^{LA*}$, $\mathcal{M}^{RR}\mathcal{M}^{RV*}$, were also considered. The interference terms with the axial component have real part equal to zero. The calculation of these matrix elements is presented as follows.

B.2.1 Left-Left

$$
\begin{aligned}
-i\mathcal{M}^{LL} &= -i\mathcal{M}_Z^{LL} - i\mathcal{M}_\gamma^{LL} \\
&= \bar{v}(p_1)\left(-\frac{ie}{2s_W c_W}\gamma^\alpha c_L^e P_L\right)u(p_2)\frac{-ig_{\alpha\beta}}{s-M_Z^2}\bar{u}(p_3)\left(-\frac{ie}{2s_W c_W}\gamma^\beta c_L^t P_L\right)v(p_4) \\
&+ \bar{v}(p_1)(-ieQ_e\gamma^{\bar{\alpha}})P_L u(p_2)\frac{-ig_{\bar{\alpha}\bar{\beta}}}{s}\bar{u}(p_3)(-ieQ_t\gamma^{\bar{\beta}})P_L v(p_4) \\
&= ie^2\left(\frac{1}{4s_W^2c_W^2}\frac{c_L^e c_L^t}{s-M_Z^2}+\frac{Q_eQ_t}{s}\right)(\bar{v}(p_1)\gamma^\alpha P_L u(p_2))\,(\bar{u}(p_3)\gamma_\alpha P_L v(p_4)) \\
&= i\mathcal{V}_{LL}\,(\bar{v}(p_1)\gamma^\alpha P_L u(p_2))\,(\bar{u}(p_3)\gamma_\alpha P_L v(p_4)) \\
|\mathcal{M}^{LL}|^2 &= \mathcal{V}_{LL}^2 \\
&\times [\bar{v}(p_1)\gamma^\alpha P_L u(p_2)][\bar{u}(p_2)\gamma^{\bar{\alpha}} P_L v(p_1)] \\
&\times [\bar{u}(p_3)\gamma_\alpha P_L v(p_4)][\bar{v}(p_4)\gamma_{\bar{\alpha}} P_L u(p_3)] \\
\sum_{\text{spins}}|\mathcal{M}^{LL}|^2 &= \mathcal{V}_{LL}^2 \mathrm{Tr}\{\not{p}_1\gamma^\alpha P_L\ \not{p}_2\gamma^{\bar{\alpha}}P_L\}Tr\{(\not{p}_3+m_t)\gamma_\alpha P_L(\not{p}_4-m_t)\gamma_{\bar{\alpha}}P_L\} \\
&= 16\mathcal{V}_{LL}^2(p_1\cdot p_3)(p_2\cdot p_4)
\end{aligned}
$$

B.2.2 Right-Right

$$
\begin{aligned}
-i\mathcal{M}^{RR} &= -i\mathcal{M}_Z^{RR} - i\mathcal{M}_\gamma^{RR} \\
&= \bar{v}(p_1)\left(-\frac{ie}{2s_W c_W}\gamma^\alpha c_R^e P_R\right)u(p_2)\frac{-ig_{\alpha\beta}}{s-M_Z^2}\bar{u}(p_3)\left(-\frac{ie}{2s_W c_W}\gamma^\beta c_R^t P_R\right)v(p_4) \\
&+ \bar{v}(p_1)(-ieQ_e\gamma^{\bar{\alpha}})P_R u(p_2)\frac{-ig_{\bar{\alpha}\bar{\beta}}}{s}\bar{u}(p_3)(-ieQ_t\gamma^{\bar{\beta}})P_R v(p_4) \\
&= ie^2\left(\frac{1}{4s_W^2c_W^2}\frac{c_R^e c_R^t}{s-M_Z^2}+\frac{Q_eQ_t}{s}\right)(\bar{v}(p_1)\gamma^\alpha P_R u(p_2))\,(\bar{u}(p_3)\gamma_\alpha P_R v(p_4)) \\
&= i\mathcal{V}_{RR}\,(\bar{v}(p_1)\gamma^\alpha P_R u(p_2))\,(\bar{u}(p_3)\gamma_\alpha P_R v(p_4)) \\
|\mathcal{M}^{RR}|^2 &= \mathcal{V}_{RR}^2 \\
&\times [\bar{v}(p_1)\gamma^\alpha P_R u(p_2)][\bar{u}(p_2)\gamma^{\bar{\alpha}} P_R v(p_1)] \\
&\times [\bar{u}(p_3)\gamma_\alpha P_R v(p_4)][\bar{v}(p_4)\gamma_{\bar{\alpha}} P_R u(p_3)] \\
\sum_{\text{spins}}|\mathcal{M}^{RR}|^2 &= \mathcal{V}_{RR}^2 \mathrm{Tr}\{\not{p}_1\gamma^\alpha P_R\ \not{p}_2\gamma^{\bar{\alpha}}P_R\}Tr\{(\not{p}_3+m_t)\gamma_\alpha P_R(\not{p}_4-m_t)\gamma_{\bar{\alpha}}P_R\} \\
&= 16\mathcal{V}_{RR}^2(p_1\cdot p_3)(p_2\cdot p_4)
\end{aligned}
$$

B.2.3 Left-Right

$$
\begin{aligned}
-i\mathcal{M}^{LR} &= -i\mathcal{M}_Z^{LR} - i\mathcal{M}_\gamma^{LR} \\
&= \bar{v}(p_1)\left(-\frac{ie}{2s_W c_W}\gamma^\alpha c_L^e P_L\right)u(p_2)\frac{-ig_{\alpha\beta}}{s-M_Z^2}\bar{u}(p_3)\left(-\frac{ie}{2s_W c_W}\gamma^\beta c_R^t P_R\right)v(p_4) \\
&+ \bar{v}(p_1)(-ieQ_e\gamma^{\bar{\alpha}})P_L u(p_2)\frac{-ig_{\bar{\alpha}\bar{\beta}}}{s}\bar{u}(p_3)(-ieQ_t\gamma^{\bar{\beta}})P_R v(p_4) \\
&= ie^2\left(\frac{1}{4s_W^2c_W^2}\frac{c_L^e c_R^t}{s-M_Z^2}+\frac{Q_eQ_t}{s}\right)(\bar{v}(p_1)\gamma^\alpha P_L u(p_2))\,(\bar{u}(p_3)\gamma_\alpha P_R v(p_4)) \\
&= i\mathcal{V}_{LR}\,(\bar{v}(p_1)\gamma^\alpha P_L u(p_2))\,(\bar{u}(p_3)\gamma_\alpha P_R v(p_4)) \\
|\mathcal{M}^{LR}|^2 &= \mathcal{V}_{LR}^2 \\
&\times [\bar{v}(p_1)\gamma^\alpha P_L u(p_2)][\bar{u}(p_2)\gamma^{\bar{\alpha}} P_L v(p_1)] \\
&\times [\bar{u}(p_3)\gamma_\alpha P_R v(p_4)][\bar{v}(p_4)\gamma_{\bar{\alpha}} P_R u(p_3)] \\
\sum_{\text{spins}}|\mathcal{M}^{LR}|^2 &= \mathcal{V}_{LR}^2 \\
&\times Tr\{\not{p}_1\gamma^\alpha P_L\ \not{p}_2\gamma^{\bar{\alpha}}P_L\}Tr\{(\not{p}_3+m_t)\gamma_\alpha P_R(\not{p}_4-m_t)\gamma_{\bar{\alpha}}P_R\} \\
&= 16\mathcal{V}_{LR}^2(p_1\cdot p_4)(p_2\cdot p_3)
\end{aligned}
$$

B.2.4 Right-Left

$$
\begin{aligned}
-i\mathcal{M}^{RL} &= -i\mathcal{M}_Z^{RL} - i\mathcal{M}_\gamma^{RL} \\
&= \bar{v}(p_1)\left(-\frac{ie}{2s_W c_W}\gamma^\alpha c_R^e P_R\right)u(p_2)\frac{-ig_{\alpha\beta}}{s-M_Z^2}\bar{u}(p_3)\left(-\frac{ie}{2s_W c_W}\gamma^\beta c_L^t P_L\right)v(p_4) \\
&+ \bar{v}(p_1)(-ieQ_e\gamma^{\bar{\alpha}})P_R u(p_2)\frac{-ig_{\bar{\alpha}\bar{\beta}}}{s}\bar{u}(p_3)(-ieQ_t\gamma^{\bar{\beta}})P_L v(p_4) \\
&= ie^2\left(\frac{1}{4s_W^2c_W^2}\frac{c_R^e c_L^t}{s-M_Z^2}+\frac{Q_eQ_t}{s}\right)(\bar{v}(p_1)\gamma^\alpha P_R u(p_2))\,(\bar{u}(p_3)\gamma_\alpha P_L v(p_4)) \\
&= i\mathcal{V}_{RL}\,(\bar{v}(p_1)\gamma^\alpha P_R u(p_2))\,(\bar{u}(p_3)\gamma_\alpha P_L v(p_4)) \\
|\mathcal{M}^{RL}|^2 &= \mathcal{V}_{RL}^2 \\
&\times [\bar{v}(p_1)\gamma^\alpha P_R u(p_2)][\bar{u}(p_2)\gamma^{\bar{\alpha}} P_R v(p_1)] \\
&\times [\bar{u}(p_3)\gamma_\alpha P_L v(p_4)][\bar{v}(p_4)\gamma_{\bar{\alpha}} P_L u(p_3)] \\
\sum_{\text{spins}}|\mathcal{M}^{RL}|^2 &= \mathcal{V}_{RL}^2 \\
&\times Tr\{\not{p}_1\gamma^\alpha P_R\ \not{p}_2\gamma^{\bar{\alpha}}P_R\}Tr\{(\not{p}_3+m_t)\gamma_\alpha P_L(\not{p}_4-m_t)\gamma_{\bar{\alpha}}P_L\} \\
&= 16\mathcal{V}_{RL}^2(p_1\cdot p_4)(p_2\cdot p_3)
\end{aligned}
$$

B.2.5 Left-Axial

$$
\begin{aligned}
-i\mathcal{M}^{LA} &= -i\mathcal{M}_Z^{LA} - i\mathcal{M}_\gamma^{LA} \\
&= \bar{v}(p_1)\left(-\frac{ie}{2s_W c_W}\gamma^\alpha c_L^e P_L\right) \\
&\times\ u(p_2)\frac{-ig_{\alpha\beta}}{s-M_Z^2}\bar{u}(p_3)\left(-\frac{ie}{2s_W c_W}\frac{1}{M_Z}(\not{q}\gamma^\beta - \gamma^\beta\ \not{q})id_A^Z\gamma_5\right)v(p_4) \\
&+\ \bar{v}(p_1)\left(-ieQ_e\gamma^{\bar{\alpha}}\right)P_L u(p_2)\frac{-ig_{\bar{\alpha}\bar{\beta}}}{s}\bar{u}(p_3)\left(-i\frac{e}{m_t}(\not{q}\gamma^{\bar{\beta}} - \gamma^{\bar{\beta}}\ \not{q})id_A^\gamma\gamma_5\right)v(p_4) \\
&= -e^2\left(\frac{c_L^e d_A^Z}{4s_W^2 c_W^2 M_Z(s-M_Z^2)} + \frac{Q_e d_A^\gamma}{m_t s}\right) \\
&\times\ (\bar{v}(p_1)\gamma^\alpha P_L u(p_2))\,(\bar{u}(p_3)(\not{q}\gamma_\alpha - \gamma_\alpha\ \not{q})\gamma_5 v(p_4)) \\
&= -\mathcal{T}_{LA}\,(\bar{v}(p_1)\gamma^\alpha P_L u(p_2))\,(\bar{u}(p_3)(\not{q}\gamma_\alpha - \gamma_\alpha\ \not{q})\gamma_5 v(p_4)) \\
|\mathcal{M}^{LA}|^2 &= \mathcal{T}_{LA}^2 \\
&\times\ [\bar{v}(p_1)\gamma^\alpha P_L u(p_2)][\bar{u}(p_2)\gamma^{\bar{\alpha}} P_L v(p_1)] \\
&\times\ [\bar{u}(p_3)(\not{q}\gamma_\alpha - \gamma_\alpha\ \not{q})\gamma_5 v(p_4)][\bar{v}(p_4)(\not{q}\gamma_\alpha - \gamma_\alpha\ \not{q})\gamma_5 u(p_3)] \\
\sum_{\text{spins}}|\mathcal{M}^{LA}|^2 &= \mathcal{T}_{LA}^2 \mathrm{Tr}\{\not{p}_1\gamma^\alpha P_L\ \not{p}_2\gamma^{\bar{\alpha}}P_L\} \\
&\times\ Tr\{(\not{p}_3 + m_t)(\not{q}\gamma_\alpha - \gamma_\alpha\ \not{q})\gamma_5(\not{p}_4 - m_t)(\not{q}\gamma_\alpha - \gamma_\alpha\ \not{q})\gamma_5\} \\
&= 128\mathcal{T}_{LA}^2\left((p_1\cdot p_2)(p_1\cdot p_3)(p_1\cdot p_4) + (p_1\cdot p_2)(p_2\cdot p_3)(p_2\cdot p_4) - (p_1\cdot p_2)^2 m_t^2\right)
\end{aligned}
$$

B.2.6 Right-Axial

$$
\begin{aligned}
-i\mathcal{M}^{RA} &= -i\mathcal{M}_Z^{RA} - i\mathcal{M}_\gamma^{RA} \\
&= \bar{v}(p_1)\left(-\frac{ie}{2s_W c_W}\gamma^\alpha c_R^e P_R\right) \\
&\times\ u(p_2)\frac{-ig_{\alpha\beta}}{s-M_Z^2}\bar{u}(p_3)\left(-\frac{ie}{2s_W c_W}\frac{1}{M_Z}(\not{q}\gamma^\beta - \gamma^\beta\ \not{q})id_A^Z\gamma_5\right)v(p_4) \\
&+\ \bar{v}(p_1)\left(-ieQ_e\gamma^{\bar{\alpha}}\right)P_R u(p_2)\frac{-ig_{\bar{\alpha}\bar{\beta}}}{s}\bar{u}(p_3)\left(-i\frac{e}{m_t}(\not{q}\gamma^{\bar{\beta}} - \gamma^{\bar{\beta}}\ \not{q})id_A^\gamma\gamma_5\right)v(p_4) \\
&= -e^2\left(\frac{c_R^e d_A^Z}{4s_W^2 c_W^2 4M_Z(s-M_Z^2)} + \frac{Q_e d_A^\gamma}{m_t s}\right) \\
&\times\ (\bar{v}(p_1)\gamma^\alpha P_R u(p_2))\,(\bar{u}(p_3)(\not{q}\gamma_\alpha - \gamma_\alpha\ \not{q})\gamma_5 v(p_4)) \\
&= -\mathcal{T}_{RA}\,(\bar{v}(p_1)\gamma^\alpha P_R u(p_2))\,(\bar{u}(p_3)(\not{q}\gamma_\alpha - \gamma_\alpha\ \not{q})\gamma_5 v(p_4)) \\
|\mathcal{M}^{RA}|^2 &= \mathcal{T}_{RA}^2 \\
&\times\ [\bar{v}(p_1)\gamma^\alpha P_R u(p_2)][\bar{u}(p_2)\gamma^{\bar{\alpha}} P_R v(p_1)] \\
&\times\ [\bar{u}(p_3)(\not{q}\gamma_\alpha - \gamma_\alpha\ \not{q})\gamma_5 v(p_4)][\bar{v}(p_4)(\not{q}\gamma_\alpha - \gamma_\alpha\ \not{q})\gamma_5 u(p_3)] \\
\sum_{\text{spins}}|\mathcal{M}^{RA}|^2 &= \mathcal{T}_{RA}^2 \mathrm{Tr}\{\not{p}_1\gamma^\alpha P_R\ \not{p}_2\gamma^{\bar{\alpha}}P_R\} \\
&\times\ Tr\{(\not{p}_3 + m_t)(\not{q}\gamma_\alpha - \gamma_\alpha\ \not{q})\gamma_5(\not{p}_4 - m_t)(\not{q}\gamma_\alpha - \gamma_\alpha\ \not{q})\gamma_5\} \\
&= 128\mathcal{T}_{RA}^2\left((p_1\cdot p_2)(p_1\cdot p_3)(p_1\cdot p_4) + (p_1\cdot p_2)(p_2\cdot p_3)(p_2\cdot p_4) - (p_1\cdot p_2)^2 m_t^2\right)
\end{aligned}
$$

B.2.7 Left-Vectorial

$$
\begin{aligned}
-i\mathcal{M}^{LV} &= -i\mathcal{M}_Z^{LV} - i\mathcal{M}_\gamma^{LV} \\
&= \bar{v}(p_1)\left(-\frac{ie}{2s_W c_W}\gamma^\alpha c_L^e P_L\right) \\
&\times\ u(p_2)\frac{-ig_{\alpha\beta}}{s-M_Z^2}\bar{u}(p_3)\left(-\frac{ie}{2s_W c_W}\frac{1}{M_Z}(\not{q}\gamma^\beta - \gamma^\beta\ \not{q})d_V^Z\right)v(p_4) \\
&+\ \bar{v}(p_1)\left(-ieQ_e\gamma^{\bar{\alpha}}\right)P_L u(p_2)\frac{-ig_{\bar{\alpha}\bar{\beta}}}{s}\bar{u}(p_3)\left(-i\frac{e}{m_t}(\not{q}\gamma^{\bar{\beta}} - \gamma^{\bar{\beta}}\ \not{q})d_V^\gamma\right)v(p_4) \\
&= ie^2\left(\frac{c_L^e d_V^Z}{4s_W^2 c_W^2 M_Z(s-M_Z^2)} + \frac{Q_e d_V^\gamma}{m_t s}\right) \\
&\times\ (\bar{v}(p_1)\gamma^\alpha P_L u(p_2))\,(\bar{u}(p_3)(\not{q}\gamma_\alpha - \gamma_\alpha\ \not{q})v(p_4)) \\
&= i\mathcal{T}_{LV}\,(\bar{v}(p_1)\gamma^\alpha P_L u(p_2))\,(\bar{u}(p_3)(\not{q}\gamma_\alpha - \gamma_\alpha\ \not{q})v(p_4)) \\
|\mathcal{M}^{LV}|^2 &= \mathcal{T}_{LV}^2 \\
&\times\ [\bar{v}(p_1)\gamma^\alpha P_L u(p_2)][\bar{u}(p_2)\gamma^{\bar{\alpha}} P_L v(p_1)] \\
&\times\ [\bar{u}(p_3)(\not{q}\gamma_\alpha - \gamma_\alpha\ \not{q})v(p_4)][\bar{v}(p_4)(\gamma_{\bar{\alpha}}\ \not{q} - \not{q}\gamma_{\bar{\alpha}})u(p_3)] \\
\sum_{\text{spins}}|\mathcal{M}^{LV}|^2 &= \mathcal{T}_{LV}^2\mathrm{Tr}\{\not{p}_1\gamma^\alpha P_L\ \not{p}_2\gamma^{\bar{\alpha}}P_L\} \\
&\times\ Tr\{(\not{p}_3 + m_t)(\not{q}\gamma_\alpha - \gamma_\alpha\ \not{q})(\not{p}_4 - m_t)(\gamma_{\bar{\alpha}}\ \not{q} - \not{q}\gamma_{\bar{\alpha}})\} \\
&= 128\mathcal{T}_{LV}^2\left((p_1\cdot p_2)(p_1\cdot p_3)(p_1\cdot p_4) + (p_1\cdot p_2)(p_2\cdot p_3)(p_2\cdot p_4) + (p_1\cdot p_2)^2 m_t^2\right)
\end{aligned}
$$

B.2.8 Right-Vectorial

$$
\begin{aligned}
-i\mathcal{M}^{RV} &= -i\mathcal{M}_Z^{RV} - i\mathcal{M}_\gamma^{RV} \\
&= \bar{v}(p_1)\left(-\frac{ie}{2s_W c_W}\gamma^\alpha c_R^e P_R\right) \\
&\times\ u(p_2)\frac{-ig_{\alpha\beta}}{s-M_Z^2}\bar{u}(p_3)\left(-\frac{ie}{2s_W c_W}\frac{1}{M_Z}(\not{q}\gamma^\beta - \gamma^\beta\ \not{q})d_V^Z\right)v(p_4) \\
&+\ \bar{v}(p_1)\left(-ieQ_e\gamma^{\bar{\alpha}}\right)P_R u(p_2)\frac{-ig_{\bar{\alpha}\bar{\beta}}}{s}\bar{u}(p_3)\left(-i\frac{e}{m_t}(\not{q}\gamma^{\bar{\beta}} - \gamma^{\bar{\beta}}\ \not{q})d_V^\gamma\right)v(p_4) \\
&= ie^2\left(\frac{c_R^e d_V^Z}{4s_W^2 c_W^2 M_Z(s-M_Z^2)} + \frac{Q_e d_V^\gamma}{m_t s}\right) \\
&\times\ (\bar{v}(p_1)\gamma^\alpha P_R u(p_2))\,(\bar{u}(p_3)(\not{q}\gamma_\alpha - \gamma_\alpha\ \not{q})v(p_4)) \\
&= i\mathcal{T}_{RV}\,(\bar{v}(p_1)\gamma^\alpha P_R u(p_2))\,(\bar{u}(p_3)(\not{q}\gamma_\alpha - \gamma_\alpha\ \not{q})v(p_4)) \\
|\mathcal{M}^{RV}|^2 &= \mathcal{T}_{RV}^2 \\
&\times\ [\bar{v}(p_1)\gamma^\alpha P_R u(p_2)][\bar{u}(p_2)\gamma^{\bar{\alpha}} P_R v(p_1)] \\
&\times\ [\bar{u}(p_3)(\not{q}\gamma_\alpha - \gamma_\alpha\ \not{q})v(p_4)][\bar{v}(p_4)(\gamma_{\bar{\alpha}}\ \not{q} - \not{q}\gamma_{\bar{\alpha}})u(p_3)] \\
\sum_{\text{spins}}|\mathcal{M}^{RV}|^2 &= \mathcal{T}_{RV}^2\mathrm{Tr}\{\not{p}_1\gamma^\alpha P_R\ \not{p}_2\gamma^{\bar{\alpha}}P_R\} \\
&\times\ Tr\{(\not{p}_3 + m_t)(\not{q}\gamma_\alpha - \gamma_\alpha\ \not{q})(\not{p}_4 - m_t)(\gamma_{\bar{\alpha}}\ \not{q} - \not{q}\gamma_{\bar{\alpha}})\} \\
&= 128\mathcal{T}_{RV}^2\left((p_1\cdot p_2)(p_1\cdot p_3)(p_1\cdot p_4) + (p_1\cdot p_2)(p_2\cdot p_3)(p_2\cdot p_4) + (p_1\cdot p_2)^2 m_t^2\right)
\end{aligned}
$$

B.2.9 Interference

$$\begin{aligned}
\mathcal{M}^{LL}\mathcal{M}^{LR*} &= \mathcal{V}_{LL}\mathcal{V}_{LR} \\
&\times [\bar{v}(p_1)\gamma^{\alpha}P_L u(p_2)][\bar{u}(p_2)\gamma^{\bar{\alpha}}P_L v(p_1)] \\
&\times [\bar{u}(p_3)\gamma_{\alpha}P_L v(p_4)][\bar{v}(p_4)\gamma_{\bar{\alpha}}P_R u(p_3)]
\end{aligned}$$

$$\begin{aligned}
\sum_{\text{spins}} \mathcal{M}^{LL}\mathcal{M}^{LR*} &= \mathcal{V}_{LL}\mathcal{V}_{LR} \\
&\times \mathrm{Tr}\{\not{p}_1\gamma^{\alpha}P_L\ \not{p}_2\gamma^{\bar{\alpha}}P_L\} \\
&\times \mathrm{Tr}\{(\not{p}_3 + m_t)\gamma_{\alpha}P_L(\not{p}_4 - m_t)\gamma_{\bar{\alpha}}P_R\} \\
&= 8V_{LL}V_{LR}(p_1\cdot p_2)m_t^2
\end{aligned}$$

$$\begin{aligned}
\mathcal{M}^{RR}\mathcal{M}^{RL*} &= \mathcal{V}_{RR}\mathcal{V}_{RL} \\
&\times [\bar{v}(p_1)\gamma^{\alpha}P_R u(p_2)][\bar{u}(p_2)\gamma^{\bar{\alpha}}P_R v(p_1)] \\
&\times [\bar{u}(p_3)\gamma_{\alpha}P_R v(p_4)][\bar{v}(p_4)\gamma_{\bar{\alpha}}P_L u(p_3)]
\end{aligned}$$

$$\begin{aligned}
\sum_{\text{spins}} \mathcal{M}^{RR}\mathcal{M}^{RL*} &= \mathcal{V}_{RR}\mathcal{V}_{RL} \\
&\times \mathrm{Tr}\{\not{p}_1\gamma^{\alpha}P_R\ \not{p}_2\gamma^{\bar{\alpha}}P_R\} \\
&\times \mathrm{Tr}\{(\not{p}_3 + m_t)\gamma_{\alpha}P_R(\not{p}_4 - m_t)\gamma_{\bar{\alpha}}P_L\} \\
&= 8V_{RR}V_{RL}(p_1\cdot p_2)m_t^2
\end{aligned}$$

$$\begin{aligned}
\mathcal{M}^{LL}\mathcal{M}^{LV*} &= \mathcal{V}_{LL}\mathcal{V}_{LV} \\
&\times [\bar{v}(p_1)\gamma^{\alpha}P_L u(p_2)][\bar{u}(p_2)\gamma^{\bar{\alpha}}P_L v(p_1)] \\
&\times [\bar{u}(p_3)\gamma_{\alpha}P_L v(p_4)][\bar{v}(p_4)(\gamma_{\bar{\alpha}}\ \not{q} - \not{q}\gamma_{\bar{\alpha}})u(p_3)]
\end{aligned}$$

$$\begin{aligned}
\sum_{\text{spins}} \mathcal{M}^{LL}\mathcal{M}^{LV*} &= \mathcal{V}_{LL}\mathcal{V}_{LV} \\
&\times \mathrm{Tr}\{\not{p}_1\gamma^{\alpha}P_L\ \not{p}_2\gamma^{\bar{\alpha}}P_L\} \\
&\times \mathrm{Tr}\{(\not{p}_3 + m_t)\gamma_{\alpha}P_L(\not{p}_4 - m_t)(\gamma_{\bar{\alpha}}\ \not{q} - \not{q}\gamma_{\bar{\alpha}})\} \\
&= -32\mathcal{V}_{LL}\mathcal{V}_{LV}m_t(p_1\cdot p_2)\left((p_1\cdot p_3) + (p_2\cdot p_4)\right)
\end{aligned}$$

$$\begin{aligned}\mathcal{M}^{LR}\mathcal{M}^{LV*} &= \mathcal{V}_{LR}\mathcal{V}_{LV} \\ &\times [\bar{v}(p_1)\gamma^{\alpha}P_L u(p_2)][\bar{u}(p_2)\gamma^{\bar{\alpha}}P_L v(p_1)] \\ &\times [\bar{u}(p_3)\gamma_{\alpha}P_R v(p_4)][\bar{v}(p_4)(\gamma_{\bar{\alpha}}\ \not{q} - \not{q}\gamma_{\bar{\alpha}})u(p_3)]\end{aligned}$$

$$\begin{aligned}\sum_{\text{spins}}\mathcal{M}^{LR}\mathcal{M}^{LV*} &= \mathcal{V}_{LR}\mathcal{V}_{LV} \\ &\times \mathrm{Tr}\{\not{p}_1\gamma^{\alpha}P_L\ \not{p}_2\gamma^{\bar{\alpha}}P_L\} \\ &\times \mathrm{Tr}\{(\not{p}_3 + m_t)\gamma_{\alpha}P_R(\not{p}_4 - m_t)(\gamma_{\bar{\alpha}}\ \not{q} - \not{q}\gamma_{\bar{\alpha}})\} \\ &= -32\mathcal{V}_{LR}\mathcal{V}_{LV}m_t(p_1\cdot p_2)\left((p_1\cdot p_4) + (p_2\cdot p_3)\right)\end{aligned}$$

B.3 Cross-sections

Using equation B.9, the polarized forward (F) and backward (B) cross sections for $e^+e^- \to t\bar{t}$ are:

$$\begin{aligned}\sigma_{F,B}(e_R^+e_L^-) &= \frac{\beta}{32\pi}\left\{s(3+\beta^2)\left[|\mathcal{V}_{LL}|^2 + |\mathcal{V}_{LR}|^2\right] \mp 3s\beta\left[|\mathcal{V}_{LL}|^2 - |\mathcal{V}_{LR}|^2\right]\right. \\ &\quad +24m_t^2\,\mathrm{Re}\ \mathcal{V}_{LL}\mathcal{V}_{LR}^* + 2s^2(3-\beta^2)\left[|\mathcal{T}_{LV}|^2 + |\mathcal{T}_{LA}|^2\right] \\ &\quad +24m_t^2 s\left[|\mathcal{T}_{LV}|^2 - |\mathcal{T}_{LA}|^2\right] - 24sm_t\,\mathrm{Re}\left[(\mathcal{V}_{LL}+\mathcal{V}_{LR})\mathcal{T}_{LV}^*\right] \\ &\quad \left.\pm 12sm_t\beta\,\mathrm{Re}\left[(\mathcal{V}_{LL}-\mathcal{V}_{LR})\mathcal{T}_{LV}^*\right]\right\}, \\ \sigma_{F,B}(e_L^+e_R^-) &= \frac{\beta}{32\pi}\left\{s(3+\beta^2)\left[|\mathcal{V}_{RL}|^2 + |\mathcal{V}_{RR}|^2\right] \pm 3s\beta\left[|\mathcal{V}_{RL}|^2 - |\mathcal{V}_{RR}|^2\right]\right. \\ &\quad +24m_t^2\,\mathrm{Re}\ \mathcal{V}_{RL}\mathcal{V}_{RR}^* + 2s^2(3-\beta^2)\left[|\mathcal{T}_{RV}|^2 + |\mathcal{T}_{RA}|^2\right] \\ &\quad +24m_t^2 s\left[|\mathcal{T}_{RV}|^2 - |\mathcal{T}_{RA}|^2\right] - 24sm_t\,\mathrm{Re}\left[(\mathcal{V}_{RL}+\mathcal{V}_{RR})\mathcal{T}_{RV}^*\right] \\ &\quad \left.\mp 12sm_t\beta\,\mathrm{Re}\left[(\mathcal{V}_{RL}-\mathcal{V}_{RR})\mathcal{T}_{RV}^*\right]\right\}, \\ \sigma_{F,B}(e_L^+e_L^-) &= \sigma_{F,B}(e_R^+e_R^-) = 0\,, \end{aligned} \tag{B.12}$$

with $\mathcal{V}_{ij}$, $\mathcal{T}_{ij}$ defined as

$$\begin{aligned}\mathcal{V}_{ij} &= e^2\left[\frac{c_i^e c_j^t}{4s_W^2c_W^2(s-M_Z^2)} + \frac{Q_eQ_t}{s}\right], i,j = L,R\,, \\ \mathcal{T}_{ij} &= e^2\left[\frac{c_i^e d_j^Z}{4s_W^2c_W^2M_Z(s-M_Z^2)} + \frac{Q_e d_j^{\gamma}}{sm_t}\right], i = L,R,\ j = V,A\,. \end{aligned} \tag{B.13}$$

Bibliography

[1] Tevatron Electroweak Working Group, CDF, and D0 Collaborations. Combination of CDF and D0 results on the mass of the top quark using up to 5.8 fb^{-1} of data. Technical Report FERMILAB-TM-2504-E, CDF-NOTE-10549, D0-NOTE-6222, Fermilab, USA, 2011.

[2] ATLAS Collaboration. Readiness of the ATLAS Tile Calorimeter for LHC collisions. *Eur. Phys. J. C*, 70:1193–1236, Dec 2010.

[3] M.C.N. Fiolhais. Correlated noise unfolding on a Hadronic Calorimeter. Technical Report ATL-TILECAL-PROC-2011-003, CERN, Geneva, Feb 2011.

[4] M.C.N. Fiolhais. Correlated noise unfolding on a Hadronic Calorimeter. IEEE Catalog Number: CFP-11IMT, 892-895, ISBN: 978-1-4244-7934-4, May 2011.

[5] ATLAS Collaboration. Measurement of the W-boson polarisation in top quark decays in pp collision data at $\sqrt{s} = 7$ TeV using the ATLAS detector. Technical Report ATLAS-CONF-2011-037, CERN, Geneva, Mar 2011.

[6] ATLAS Collaboration. Measurement of the W boson polarisation in top quark decays in 0.70 fb^{-1} of pp collisions at $\sqrt{s} = 7$ TeV with the ATLAS detector. Technical Report ATLAS-CONF-2011-122, CERN, Geneva, Aug 2011.

[7] M.C.N. Fiolhais. Top quark mass and properties at ATLAS. Technical Report ATL-PHYS-PROC-2011-083, CERN, Geneva, Jul 2011. To appear in the proceedings of the XIX International Workshop on Deep-Inelastic Scattering and Related Subjects (DIS 2011), 11-15 April 2011, Newport News, VA, USA.

[8] ATLAS Collaboration. Measurement of the W boson polarization in top quark decays with the ATLAS detector. *JHEP*, 1206:088, 2012.

[9] J.A. Aguilar-Saavedra, M.C.N. Fiolhais, and A. Onofre. Top effective operators at the ILC. *JHEP*, 1207:180, 2012.

[10] ATLAS Collaboration. A search for flavour changing neutral currents in top-quark decays in pp collision data collected with the ATLAS detector at $\sqrt{s} = 7$ TeV. *JHEP*, 1209:139, 2012.

[11] ATLAS Collaboration. Search for same-sign top-quark production and fourth-generation down-type quarks in pp collisions at $\sqrt{s} = 7$ TeV with the ATLAS detector. *JHEP*, 1204:069, 2012.

[12] S. Glashow. Partial-symmetries of weak interactions. *Nuclear Physics*, 22:579–588, Feb 1961.

[13] Steven Weinberg. A model of leptons. *Phys. Rev. Lett.*, 19:1264–1266, Nov 1967.

[14] N. Svartholm. *Elementary particle theory: relativistic groups and analyticity.* Nobel symposium. John Wiley & Sons, 1968.

[15] F. Englert and R. Brout. Broken Symmetry and the Mass of Gauge Vector Mesons. *Phys. Rev. Lett.*, 13:321–323, Aug 1964.

[16] Peter W. Higgs. Broken Symmetries and the Masses of Gauge Bosons. *Phys. Rev. Lett.*, 13:508–509, Oct 1964.

[17] G. S. Guralnik, C. R. Hagen, and T. W. B. Kibble. Global Conservation Laws and Massless Particles. *Phys. Rev. Lett.*, 13:585–587, Nov 1964.

[18] G. Zweig. An SU(3) model for strong interaction symmetry and its breaking. Technical Report CERN-TH-401, CERN, Geneva, Jan 1964.

[19] M. Y. Han and Y. Nambu. Three-triplet model with double SU(3) symmetry. *Phys. Rev.*, 139:B1006–B1010, Aug 1965.

[20] O. W. Greenberg. Spin and Unitary Spin Independence in a Paraquark Model of Baryons and Mesons. *Phys. Rev. Lett.*, 13:598–602, Oct 1964.

[21] H. David Politzer. Reliable Perturbative Results for Strong Interactions? *Phys. Rev. Lett.*, 30:1346–1349, Jun 1973.

[22] H. David Politzer. Asymptotic Freedom: An Approach to Strong Interactions. *Phys.Rept.*, 14:129–180, Jul 1974.

[23] David J. Gross and Frank Wilczek. Ultraviolet Behavior of Non-Abelian Gauge Theories. *Phys. Rev. Lett.*, 30:1343–1346, Jun 1973.

[24] K. Nakamura *et al.* (Particle Data Group). Review of particle physics. *J. Phys. G: Nucl. Part. Phys.*, 37:075021, 2010.

[25] E. Stueckelberg. Die Wechselwirkungckracfte in der Electrodynamic und der Feldtheorie der Kernkraefle. *Helvetica Physica Acta*, 11:225–236, 1938.

[26] J. Schwinger. On Quantum-Electrodynamics and the Magnetic Moment of the Electron. *Phys. Rev.*, 73:416–417, Feb 1948.

[27] J. Schwinger. Quantum Electrodynamics. I. A Covariant Formulation. *Phys. Rev.*, 74:1439–1461, Nov 1948.

[28] R. P. Feynman. Space-Time Approach to Quantum Electrodynamics. *Phys. Rev.*, 76:769–789, Sep 1949.

[29] R. P. Feynman. The Theory of Positrons. *Phys. Rev.*, 76:749–759, Sep 1949.

[30] R. P. Feynman. Mathematical formulation of the quantum theory of electromagnetic interaction. *Phys. Rev.*, 80:440–457, Nov 1950.

[31] S. Tomonaga. On a Relativistically Invariant Formulation of the Quantum Theory of Wave Fields. *Progress of Theoretical Physics*, 1(2):27–42, 1946.

[32] F. J. Dyson. The Radiation Theories of Tomonaga, Schwinger, and Feynman. *Phys. Rev.*, 75:486–502, Feb 1949.

[33] F. J. Dyson. The S Matrix in Quantum Electrodynamics. *Phys. Rev.*, 75:1736–1755, Jun 1949.

[34] UA1 Collaboration. Further evidence for charged intermediate vector bosons at the SPS collider. *Phys. Lett. B*, 129:273–282, Sep 1983.

[35] UA1 Collaboration. Experimental observation of lepton pairs of invariant mass around 95 GeV/c^2 at the CERN SPS collider. *Phys. Lett. B*, 126:398–410, Jul 1983.

[36] Antonio Pich. The Standard Model of electroweak interactions. Technical Report CERN-2012-001, CERN, Geneva, Feb 2012.

[37] E. Fermi. Versuch einer Theorie der β-Strahlen. I. *Zeitschrift für Physik A Hadrons and Nuclei*, 88:161–177, 1934.

[38] D. Hanneke, S. Fogwell, and G. Gabrielse. New Measurement of the Electron Magnetic Moment and the Fine Structure Constant. *Phys. Rev. Lett.*, 100:120801, Mar 2008.

[39] T. D. Lee and C. N. Yang. Question of Parity Conservation in Weak Interactions. *Phys. Rev.*, 104:254–258, Oct 1956.

[40] C. S. Wu, E. Ambler, R. W. Hayward, D. D. Hoppes, and R. P. Hudson. Experimental Test of Parity Conservation in Beta Decay. *Phys. Rev.*, 105:1413–1415, Feb 1957.

[41] Nicola Cabibbo. Unitary Symmetry and Leptonic Decays. *Phys. Rev. Lett.*, 10:531–533, Jun 1963.

[42] Makoto Kobayashi and Toshihide Maskawa. CP-Violation in the Renormalizable Theory of Weak Interaction. *Progress of Theoretical Physics*, 49(2):652–657, 1973.

[43] B. Pontecorvo. Neutrino Experiments and the Problem of Conservation of Leptonic Charge. *Soviet Journal of Experimental and Theoretical Physics*, 26:984, May 1968.

[44] S. Fukuda *et al.* Determination of solar neutrino oscillation parameters using 1496 days of Super-Kamiokande-I data. *Phys. Lett. B*, 539(3-4):179 – 187, 2002.

[45] M. H. Ahn *et al.* Indications of Neutrino Oscillation in a 250 km Long-Baseline Experiment. *Phys. Rev. Lett.*, 90:041801, Jan 2003.

[46] S. N. Ahmed *et al.* Measurement of the Total Active ^{8}B Solar Neutrino Flux at the Sudbury Neutrino Observatory with Enhanced Neutral Current Sensitivity. *Phys. Rev. Lett.*, 92:181301, May 2004.

[47] K. Eguchi *et al.* First Results from KamLAND: Evidence for Reactor Antineutrino Disappearance. *Phys. Rev. Lett.*, 90:021802, Jan 2003.

[48] Ziro Maki, Masami Nakagawa, and Shoichi Sakata. Remarks on the Unified Model of Elementary Particles. *Progress of Theoretical Physics*, 28(5):870–880, 1962.

[49] S. L. Glashow, J. Iliopoulos, and L. Maiani. Weak Interactions with Lepton-Hadron Symmetry. *Phys. Rev. D*, 2:1285–1292, Oct 1970.

[50] ALEPH Collaboration, DELPHI Collaboration, L3 Collaboration, OPAL Collaboration, SLD Collaboration, LEP Electroweak Working Group, SLD Electroweak, and Heavy Flavour Groups. Precision electroweak measurements on the Z resonance. *Physics Reports*, 427(5-6):257 – 454, 2006.

[51] Yoichiro Nambu. Quasi-Particles and Gauge Invariance in the Theory of Superconductivity. *Phys. Rev.*, 117:648–663, Feb 1960.

[52] J. Goldstone. Field theories with "Superconductor" solutions. *Il Nuovo Cimento (1955-1965)*, 19:154–164, 1961. 10.1007/BF02812722.

[53] CMS Collaboration. Observation of a new boson at a mass of 125 GeV with the CMS experiment at the LHC. *Phys.Lett.B*, 2012.

[54] ATLAS Collaboration. Observation of a new particle in the search for the Standard Model Higgs boson with the ATLAS detector at the LHC. *Phys.Lett.B*, 2012.

[55] ATLAS Collaboration. Coupling properties of the new Higgs-like boson observed with the ATLAS detector at the LHC. Technical Report ATLAS-CONF-2012-127, CERN, Geneva, Sep 2012.

[56] J. H. Christenson, J. W. Cronin, V. L. Fitch, and R. Turlay. Evidence for the 2π Decay of the K_2^0 Meson. *Phys. Rev. Lett.*, 13:138–140, Jul 1964.

[57] S. W. Herb *et al.* Observation of a Dimuon Resonance at 9.5-GeV in 400-GeV Proton-Nucleus Collisions. *Phys. Rev. Lett.*, 39:252–255, 1977.

[58] D0 Collaboration. Search for high mass top quark production in $p\bar{p}$ collisions at $\sqrt{s} = 1.8$ TeV. *Phys. Rev. Lett.*, 74:2422–2426, 1995.

[59] CDF Collaboration. Observation of top quark production in $\bar{p}p$ collisions. *Phys. Rev. Lett.*, 74:2626–2631, 1995.

[60] Ling-Lie Chau and Wai-Yee Keung. Comments on the Parametrization of the Kobayashi-Maskawa Matrix. *Phys. Rev. Lett.*, 53:1802–1805, Nov 1984.

[61] Lincoln Wolfenstein. Parametrization of the Kobayashi-Maskawa Matrix. *Phys. Rev. Lett.*, 51:1945–1947, Nov 1983.

[62] C. Jarlskog. Commutator of the Quark Mass Matrices in the Standard Electroweak Model and a Measure of Maximal CP Nonconservation. *Phys. Rev. Lett.*, 55:1039–1042, Sep 1985.

[63] Miguel C.N. Fiolhais. The Cabibbo-Kobayashi-Maskawa density matrices. *Europhys. Lett.*, 98:51001, 2012.

[64] M. Beneke *et al.* Top quark physics. Technical Report CERN-TH-2000-100, CERN, Geneva, Mar 2000.

[65] Arnulf Quadt. Top quark physics at hadron colliders. *Eur. Phys. J. C*, 48:835–1000, 2006.

[66] M. Aliev *et al.* HATHOR: HAdronic Top and Heavy quarks crOss section calculatoR. *Comput. Phys. Commun.*, 182:1034–1046, 2011.

[67] Nikolaos Kidonakis. Next-to-next-to-leading-order collinear and soft gluon corrections for t-channel single top quark production. *Phys. Rev. D*, 83:091503, May 2011.

[68] Nikolaos Kidonakis. Two-loop soft anomalous dimensions for single top quark associated production with a W^- or H^-. *Phys. Rev. D*, 82:054018, Sep 2010.

[69] Nikolaos Kidonakis. Next-to-next-to-leading logarithm resummation for s-channel single top quark production. *Phys. Rev. D*, 81:054028, Mar 2010.

[70] Tim M. P. Tait and C.-P. Yuan. Single top quark production as a window to physics beyond the standard model. *Phys. Rev. D*, 63:014018, Dec 2000.

[71] J.A. Aguilar-Saavedra. Single top quark production at LHC with anomalous Wtb couplings. *Nucl. Phys. B*, 804:160–192, 2008.

[72] M. Fischer, S. Groote, J.G. Korner, and M.C. Mauser. Longitudinal, transverse-plus and transverse-minus W bosons in unpolarized top quark decays at $O(\alpha_s)$. *Phys. Rev. D*, 63:031501, 2001.

[73] Andrzej Czarnecki, Jurgen G. Korner, and Jan H. Piclum. Helicity fractions of W bosons from top quark decays at NNLO in QCD. *Phys. Rev.*, D81:111503, 2010.

[74] J.A. Aguilar-Saavedra, J. Carvalho, N. Castro, F. Veloso, and A. Onofre. Probing anomalous Wtb couplings in top pair decays. *Eur. Phys. J. C*, 50:519–533, 2007.

[75] W. Buchmuller and D. Wyler. Effective Lagrangian Analysis Of New Interactions And Flavor Conservation. *Nucl. Phys.*, B268:621, 1986.

[76] J.A. Aguilar-Saavedra. A minimal set of top anomalous couplings. *Nucl. Phys. B*, 812:181, 2009.

[77] J.A. Aguilar-Saavedra. A minimal set of top-Higgs anomalous couplings. *Nucl. Phys. B*, 821:215–227, 2009.

[78] G.L. Kane, G.A. Ladinsky, and C.P. Yuan. Using the top quark for testing standard model polarization and CP predictions. *Phys. Rev.*, D45:124, 1992.

[79] E. Barberio *et al.* Averages of $b-$hadron properties at the end of 2006. Technical Report FERMILAB-FN-0815-E, Fermilab, USA, 2007.

[80] Bohdan Grzadkowski and Mikolaj Misiak. Anomalous Wtb coupling effects in the weak radiative B-meson decay. *Phys. Rev. D*, 78:077501, 2008.

[81] F. del Aguila *et al.* Collider aspects of flavour physics at high Q. *Eur. Phys. J. C*, 57:183–308, 2008.

[82] Juan Antonio Aguilar-Saavedra. Effective operators in top physics. *PoS*, ICHEP2010:378, 2010.

[83] CDF and D0 Collaborations. Combination of CDF and D0 measurements of the W boson helicity in top quark decays. Technical Report FERMILAB-PUB-12-043-E, Fermilab, USA, 2012.

[84] CDF Collaboration. Measurement of W-Boson Polarization in Top-quark Decay in $p\bar{p}$ Collisions at sqrt(s) = 1.96 TeV. *Phys. Rev. Lett.*, 105:042002, Jul 2010.

[85] D0 Collaboration. Measurement of the W boson helicity in top quark decays using 5.4 fb^{-1} of $p\bar{p}$ collision data. *Phys. Rev. D*, 83:032009, 2011.

[86] D0 Collaboration. Search for anomalous Wtb couplings in single top quark production in $p\bar{p}$ collisions at $\sqrt{s} = 1.96$ TeV. *Phys. Lett. B*, 708:21–26, 2012.

[87] J.A. Aguilar-Saavedra and B.M. Nobre. Rare top decays t → gt; c gamma, t → gt; cg and CKM unitarity. *Phys. Lett. B*, 553:251–260, 2003.

[88] F. del Aguila, J.A. Aguilar-Saavedra, and R. Miquel. Constraints on top couplings in models with exotic quarks. *Phys. Rev. Lett.*, 82:1628–1631, 1999.

[89] J.A. Aguilar-Saavedra. Effects of mixing with quark singlets. *Phys. Rev. D*, 67:035003, 2003.

[90] T. P. Cheng and Marc Sher. Mass-matrix ansatz and flavor nonconservation in models with multiple Higgs doublets. *Phys. Rev. D*, 35:3484–3491, Jun 1987.

[91] B. Grzadkowski, J.F. Gunion, and P. Krawczyk. Neutral current flavor changing decays for the Z boson and the top quark in two-Higgs doublet models. *Phys. Lett. B*, 268(1):106–111, 1991.

[92] Michael E. Luke and Martin J. Savage. Flavor changing neutral currents in the Higgs sector and rare top decays. *Phys. Lett. B*, 307:387–393, 1993.

[93] David Atwood, Laura Reina, and Amarjit Soni. Probing flavor changing top - charm - scalar interactions in e^+e^- collisions. *Phys. Rev. D*, 53:1199–1201, 1996.

[94] David Atwood, Laura Reina, and Amarjit Soni. Phenomenology of two Higgs doublet models with flavor changing neutral currents. *Phys. Rev. D*, 55:3156–3176, 1997.

[95] Santi Bejar, Jaume Guasch, and Joan Sola. Loop induced flavor changing neutral decays of the top quark in a general two Higgs doublet model. *Nucl. Phys. B*, 600:21–38, 2001.

[96] Chong Sheng Li, R. J. Oakes, and Jin Min Yang. Rare decays of the top quark in the minimal supersymmetric model. *Phys. Rev. D*, 49:293–298, Jan 1994.

[97] G.M. de Divitiis, R. Petronzio, and L. Silvestrini. Flavor changing top decays in supersymmetric extensions of the standard model. *Nucl. Phys. B*, 504:45–60, 1997.

[98] Jorge L. Lopez, Dimitri V. Nanopoulos, and Raghavan Rangarajan. New supersymmetric contributions to $t \to c$V. *Phys. Rev. D*, 56:3100–3106, 1997.

[99] Jaume Guasch and Joan Sola. FCNC top quark decays: A Door to SUSY physics in high luminosity colliders? *Nucl. Phys. B*, 562:3–28, 1999.

[100] D. Delepine and S. Khalil. Top flavor violating decays in general supersymmetric models. *Phys. Lett. B*, 599:62–74, 2004.

[101] Jian Jun Liu, Chong Sheng Li, Li Lin Yang, and Li Gang Jin. $t \to c$V via SUSY FCNC couplings in the unconstrained MSSM. *Phys. Lett. B*, 599:92–101, 2004.

[102] J.J. Cao, G. Eilam, M. Frank, K. Hikasa, G.L. Liu, et al. SUSY-induced FCNC top-quark processes at the large hadron collider. *Phys. Rev. D*, 75:075021, 2007.

[103] Jin Min Yang, Bing-Lin Young, and X. Zhang. Flavor changing top quark decays in r parity violating SUSY. *Phys. Rev. D*, 58:055001, 1998.

[104] Gong-ru Lu, Fu-rong Yin, Xue-lei Wang, and Ling-de Wan. The Rare top quark decays $t \to c$V in the topcolor assisted technicolor model. *Phys. Rev. D*, 68:015002, 2003.

[105] Kaustubh Agashe, Gilad Perez, and Amarjit Soni. Flavor structure of warped extra dimension models. *Phys. Rev. D*, 71:016002, 2005.

[106] Kaustubh Agashe, Gilad Perez, and Amarjit Soni. Collider Signals of Top Quark Flavor Violation from a Warped Extra Dimension. *Phys. Rev. D*, 75:015002, 2007.

[107] J.A. Aguilar-Saavedra. Top flavor-changing neutral interactions: Theoretical expectations and experimental detection. *Acta Phys. Polon. B*, 35:2695–2710, 2004.

[108] ALEPH Collaboration. Search for Single Top Production in e+ e- collisions at $\sqrt{s}$ up to 209 GeV. *Phys. Lett. B*, 543:173–182, 2002.

[109] DELPHI Collaboration. Search for Single Top Production via FCNC at LEP at $\sqrt{s} = 189$ GeV - 208 GeV. *Phys. Lett. B*, 590:21–34, 2004.

[110] OPAL Collaboration. Search for Single Top Quark Production at LEP2. *Phys. Lett. B*, 521:181–194, 2001.

[111] L3 Collaboration. Search for Single Top Production at LEP. *Phys. Lett. B*, 549:290–300, 2002.

[112] LEP Exotica Working Group. Search for Single Top Production via Flavour Changing Neutral Currents: Preliminary Combined Results of the LEP Experiments. Technical Report DELPHI-2001-119-CONF-542, CERN-DELPHI-2001-119-CONF-542, LEP-Exotica-WG-2001-01, ALEPH-2001-055, CERN-ALEPH-CONF-2001-035, L3-2706, OPAL-TN-698, CERN, Geneva, Jul 2001.

[113] H1 Collaboration. Search for Single Top Quark Production at HERA. *Phys. Lett. B*, 678:450–458, 2009.

[114] ZEUS Collaboration. Search for Single-Top Production in *ep* Collisions at HERA. *Phys. Lett. B*, 559:153–170, 2003.

[115] A. A. Ashimova and S. R. Slabospitsky. The Constraint on FCNC Coupling of the Top Quark with a Gluon from *ep* Collisions. *Phys. Lett. B*, 668:282–285, 2008.

[116] H1 Collaboration. Search for Single Top Quark Production in *ep* Collisions at HERA. *Eur. Phys. J. C*, 33:9–22, 2004.

[117] CDF Collaboration. Search for Flavor-Changing Neutral Current Decays of the Top Quark in $p\bar{p}$ Collisions at $\sqrt{s} = 1.8$ TeV. *Phys. Rev. Lett.*, 80:2525–2530, 1998.

[118] D0 Collaboration. Search for Flavor Changing Neutral Currents via Quark-Gluon Couplings in Single Top Quark Production Using 2.3 fb^{-1} of $p\bar{p}$ Collisions. *Phys. Lett. B*, 693:81–87, 2010.

[119] D0 Collaboration. Search for Flavor Changing Neutral Currents in Decays of Top Quarks. *Phys. Lett. B*, 701:313–320, 2011.

[120] CMS Collaboration. Search for flavor changing neutral currents in top quark decays in pp collisions at 7 TeV. 2012. Submitted to JHEP.

[121] Sunghoon Jung, Hitoshi Murayama, Aaron Pierce, and James D. Wells. Top quark forward-backward asymmetry from new t-channel physics. *Phys. Rev. D*, 81:015004, Jan 2010.

[122] CDF Collaboration. Evidence for a Mass Dependent Forward-Backward Asymmetry in Top Quark Pair Production. *Phys. Rev. D*, 83:112003, 2011.

[123] D0 Collaboration. Forward-backward asymmetry in top quark-antiquark production. *Phys. Rev. D*, 84:112005, 2011.

[124] Roberto Contino and Geraldine Servant. Discovering the top partners at the LHC using same-sign dilepton final states. *JHEP*, 0806:026, 2008.

[125] J.A. Aguilar-Saavedra. Identifying top partners at LHC. *JHEP*, 0911:030, 2009.

[126] CMS Collaboration. Search for a Heavy Bottom-like Quark in pp Collisions at $\sqrt{s} = 7$ TeV. *Phys. Lett. B*, 701:204–223, 2011.

[127] CDF Collaboration. Search for New Bottomlike Quark Pair Decays $Q\bar{Q} \rightarrow (tW^{\mp})(\bar{t}W^{\pm})$ in Same-Charge Dilepton Events. *Phys. Rev. Lett.*, 104:091801, 2010.

[128] ATLAS Collaboration. Search for down-type fourth generation quarks with the ATLAS detector in events with one lepton and high transverse momentum hadronically decaying W bosons in $\sqrt{s} = 7$ TeV pp collisions. *Phys. Rev. Lett.*, 109:032001, 2012.

[129] CDF Collaboration. Search for heavy bottom-like quarks decaying to an electron or muon and jets in $p\bar{p}$ collisions at $\sqrt{s} = 1.96$ TeV. *Phys. Rev. Lett.*, 106:141803, 2011.

[130] CMS Collaboration. Search for new physics in events with same-sign dileptons and b-tagged jets in pp collisions at sqrt(s) = 7 TeV. *JHEP*, 1208:110, 2012.

[131] Edmond L. Berger, Qing-Hong Cao, Chuan-Ren Chen, Gabe Shaughnessy, and Hao Zhang. Color sextet scalars in early lhc experiments. *Phys. Rev. Lett.*, 105:181802, Oct 2010.

[132] Hao Zhang, Edmond L. Berger, Qing-Hong Cao, Chuan-Ren Chen, and Gabe Shaughnessy. Color Sextet Vector Bosons and Same-Sign Top Quark Pairs at the LHC. *Phys. Lett. B*, 696:68–73, 2011.

[133] D. Acosta et al. Inclusive search for anomalous production of high p_{T} like-sign lepton pairs in $p\bar{p}$ collisions at $\sqrt{s} = 1.8$ TeV. *Phys. Rev. Lett.*, 93:061802, 2004.

[134] Paul H. Frampton, P.Q. Hung, and Marc Sher. Quarks and leptons beyond the third generation. *Phys. Rept.*, 330:263, 2000.

[135] J.A. Aguilar-Saavedra. Effective four-fermion operators in top physics: A Roadmap. *Nucl. Phys. B*, 843:638–672, 2011.

[136] J.A. Aguilar-Saavedra and M. Perez-Victoria. No like-sign tops at Tevatron: Constraints on extended models and implications for the $t\bar{t}$ asymmetry. *Phys. Lett. B*, 701:93–100, 2011.

[137] ATLAS Collaboration. Search for exotic same-sign dilepton signatures (b' quark, $T_{5/3}$ and four top quarks production) in 4.7/fb of pp collisions at $\sqrt{s} = 7$ TeV with the ATLAS detector. Technical Report ATLAS-CONF-2012-130, CERN, Geneva, Sep 2012.

[138] F.J. Hasert *et al.* Observation of neutrino-like interactions without muon or electron in the gargamelle neutrino experiment. *Phys. Lett. B*, 46:138–140, 1973.

[139] G. Baur *et al.* Production of antihydrogen. *Phys. Lett. B*, 368:251–258, 1996.

[140] V. Fanti et al. A New measurement of direct CP violation in two pion decays of the neutral kaon. *Phys. Lett. B*, 465:335–348, 1999.

[141] G.B. Andresen *et al.* Trapped antihydrogen. *Nature*, 468:673–676, Dec 2010.

[142] G.B. Andresen *et al.* Confinement of antihydrogen for 1,000 seconds. *Nature Physics*, 7:558–564, Jul 2011.

[143] Lyndon Evans and Philip Bryant. LHC Machine. *Journal of Instrumentation*, 3:S08001, 2008.

[144] ATLAS Collaboration. The ATLAS Experiment at the CERN Large Hadron Collider. *Journal of Instrumentation*, 3:S08003, 2008.

[145] ATLAS Collaboration. ATLAS inner detector: Technical design report. Vol. 1. Technical Report CERN-LHCC-97-16, ATLAS-TDR-4, CERN, Geneva, 1997.

[146] ATLAS Collaboration. ATLAS inner detector: Technical design report. Vol. 2. Technical Report CERN-LHCC-97-17, CERN, Geneva, 1997.

[147] ATLAS Collaboration. The ATLAS Inner Detector commissioning and calibration. *Eur. Phys. J. C*, 70:787–821, 2010.

[148] ATLAS Collaboration. ATLAS calorimeter performance Technical Design Report. Technical Report CERN-LHCC-96-40, CERN, Geneva, 1996.

[149] ATLAS Collaboration. ATLAS liquid argon calorimeter: Technical design report. Technical Report CERN-LHCC-96-41, CERN, Geneva, 1996.

[150] ATLAS Collaboration. Readiness of the ATLAS liquid argon calorimeter for LHC collisions. *Eur. Phys. J. C*, 70:723–753, Dec 2010.

[151] ATLAS Collaboration. ATLAS tile calorimeter: Technical design report. Technical Report CERN-LHCC-96-42, CERN, Geneva, 1996.

[152] ATLAS Collaboration. ATLAS muon spectrometer: Technical design report. Technical Report CERN-LHCC-97-22, ATLAS-TDR-10, CERN, Geneva, 1997.

[153] ATLAS Collaboration. Commissioning of the ATLAS Muon Spectrometer with Cosmic Rays. *Eur. Phys. J. C*, 70:875–916, 2010.

[154] ATLAS Collaboration. ATLAS magnet system: Technical design report. Technical Report CERN-LHCC-97-18, CERN, Geneva, 1997.

[155] ATLAS Collaboration. ATLAS first level trigger: Technical design report. Technical Report CERN-LHCC-98-14, ATLAS-TDR-12, CERN, Geneva, 1998.

[156] ATLAS Collaboration. ATLAS high-level trigger, data acquisition and controls: Technical design report. Technical Report CERN-LHCC-2003-022, ATLAS-TRD-016, CERN, Geneva, 2003.

[157] R.W.L. Jones. Atlas computing and the grid. *Nuclear Instruments and Methods in Physics Research Section A: Accelerators, Spectrometers, Detectors and Associated Equipment*, 502(2-3):372–375, 2003.

[158] ATLAS Collaboration. ATLAS computing: Technical design report. Technical Report CERN-LHCC-2005-022, ATLAS-TRD-017, CERN, Geneva, 2005.

[159] Nuno Filipe Castro. *Study of the Wtb vertex structure at the ATLAS experiment.* PhD thesis, University of Coimbra, Coimbra, 2008. CERN-THESIS-2008-083.

[160] Filipe Manuel Almeida Veloso. *Study of ATLAS sensitivity to FCNC top quark decays.* PhD thesis, University of Coimbra, Coimbra, 2008. CERN-THESIS-2008-106.

[161] Miguel Castro Nunes Fiolhais. *Study of ATLAS sensitivity to asymmetries in single top events.* MSc thesis, University of Coimbra, Coimbra, 2008. CERN-THESIS-2009-014.

[162] Inês Ochoa. *Study of ATLAS sensitivity to the single top Wt-channel cross section.* MSc thesis, University of Coimbra, Coimbra, 2010. CERN-THESIS-2010-096.

[163] Susana Patrícia Amor dos Santos. *Study of ATLAS sensitivity to the single top s-channel production.* MSc thesis, University of Coimbra, Coimbra, 2010. CERN-THESIS-2010-252.

[164] F. Spanó. Simulation of the full noise pattern in Tile Calorimeter Front End electronics: a phenomenological approach to coherent effects. Technical Report ATL-TILECAL-PUB-2008-011, CERN, Geneva, Aug 2008.

[165] A. Valero. The ATLAS TileCal Read-Out Drivers Signal Reconstruction. Technical Report ATL-TILECAL-PROC-2009-004, CERN, Geneva, Nov 2009.

[166] W. Lampl *et al.* Calorimeter Clustering Algorithms: Description and Performance. Technical Report ATL-LARG-PUB-2008-002, CERN, Geneva, Apr 2008.

[167] TileCal Collaboration. Testbeam studies of production modules of the atlas tile calorimeter. *Nuclear Instruments and Methods in Physics Research Section A: Accelerators, Spectrometers, Detectors and Associated Equipment*, 606:362–394, 2009.

[168] G. Usai. Signal Reconstruction of the ATLAS Hadronic Tile Calorimeter: implementation and performance. Technical Report ATL-TILECAL-PROC-2010-008, CERN, Geneva, Aug 2010.

[169] ATLAS Collaboration. Charged-particle multiplicities in pp interactions at $\sqrt{s} = 900$ GeV measured with the ATLAS detector at the LHC. *Phys. Lett. B*, 688:21–42, 2010.

[170] Stefano Frixione and Bryan R. Webber. Matching NLO QCD computations and parton shower simulations. *JHEP*, 0206:029, 2002.

[171] F. del Aguila and J.A. Aguilar-Saavedra. Precise determination of the Wtb couplings at CERN LHC. *Phys. Rev. D*, 67:014009, 2003.

[172] Cen Zhang and Scott Willenbrock. Effective-Field-Theory Approach to Top-Quark Production and Decay. *Phys. Rev. D*, 83:034006, 2011.

[173] Luminosity Determination in pp Collisions at $\sqrt{s} = 7$ TeV using the ATLAS Detector in 2011. Technical Report ATLAS-CONF-2011-116, CERN, Geneva, Aug 2011.

[174] ATLAS Collaboration. Luminosity Determination in pp Collisions at sqrt(s)=7 TeV Using the ATLAS Detector at the LHC. *Eur. Phys. J. C*, 71:1630, 2011.

[175] J. Pumplin *et al.* New generation of parton distributions with uncertainties from global QCD analysis. *JHEP*, 0207:012, 2002.

[176] Torbjorn Sjostrand, Stephen Mrenna, and Peter Z. Skands. PYTHIA 6.4 Physics and Manual. *JHEP*, 0605:026, 2006.

[177] Stefano Frixione, Paolo Nason, and Bryan R. Webber. Matching NLO QCD and parton showers in heavy flavor production. *JHEP*, 0308:007, 2003.

[178] Stefano Frixione, Eric Laenen, Patrick Motylinski, and Bryan R. Webber. Single-top production in MC@NLO. *JHEP*, 0603:092, 2006.

[179] Pavel M. Nadolsky, Hung-Liang Lai, Qing-Hong Cao, Joey Huston, Jon Pumplin, et al. Implications of CTEQ global analysis for collider observables. *Phys. Rev. D*, 78:013004, 2008.

[180] Michelangelo L. Mangano, Mauro Moretti, Fulvio Piccinini, Roberto Pittau, and Antonio D. Polosa. ALPGEN, a generator for hard multiparton processes in hadronic collisions. *JHEP*, 0307:001, 2003.

[181] Stefan Hoeche, Frank Krauss, Nils Lavesson, Leif Lonnblad, Michelangelo Mangano, et al. Matching parton showers and matrix elements. 2006. Proceedings of the "HERA and the LHC" workshop, CERN/DESY 2004/2005.

[182] G. Corcella, I.G. Knowles, G. Marchesini, S. Moretti, K. Odagiri, et al. HERWIG 6: An Event generator for hadron emission reactions with interfering gluons (including supersymmetric processes). *JHEP*, 0101:010, 2001.

[183] Stefano Frixione, Eric Laenen, Patrick Motylinski, Bryan R. Webber, and Chris D. White. Single-top hadroproduction in association with a W boson. *JHEP*, 0807:029, 2008.

[184] T. Gleisberg *et al.* Event generation with SHERPA 1.1. *JHEP*, 0902:007, 2009.

[185] J.M. Butterworth, Jeffrey R. Forshaw, and M.H. Seymour. Multiparton interactions in photoproduction at HERA. *Z. Phys. C*, 72:637–646, 1996.

[186] New atlas event generator tunes to 2010 data. Technical Report ATL-PHYS-PUB-2011-008, CERN, Geneva, Apr 2011.

[187] Borut Paul Kersevan and Elzbieta Richter-Was. The Monte Carlo event generator AcerMC version 2.0 with interfaces to PYTHIA 6.2 and HERWIG 6.5. Technical Report TPJU-6-2004, 2004.

[188] Paolo Nason. A New method for combining NLO QCD with shower Monte Carlo algorithms. *JHEP*, 0411:040, 2004.

[189] Stefano Frixione, Paolo Nason, and Carlo Oleari. Matching NLO QCD computations with Parton Shower simulations: the POWHEG method. *JHEP*, 0711:070, 2007.

[190] S. Agostinelli et al. GEANT4: A Simulation toolkit. *Nucl. Instrum. Meth. A*, 506:250–303, 2003.

[191] ATLAS Collaboration. The ATLAS Simulation Infrastructure. *Eur. Phys. J. C*, 70:823–874, 2010.

[192] Sven Moch and Peter Uwer. Theoretical status and prospects for top-quark pair production at hadron colliders. *Phys. Rev. D*, 78:034003, 2008.

[193] U. Langenfeld, S. Moch, and P. Uwer. New results for t bar t production at hadron colliders. Jul 2009. To appear in the proceedings of the XVII International Workshop on Deep-Inelastic Scattering and Related Subjects, DIS 2009, 26-30 April 2009, Madrid.

[194] ATLAS Collaboration. Measurement of the cross section for top-quark pair production in pp collisions at $\sqrt{s} = 7$ TeV with the ATLAS detector using final states with two high-pt leptons. *JHEP*, 1205:059, 2012.

[195] ATLAS Collaboration. Measurement of the charge asymmetry in top quark pair production in pp collisions at $\sqrt{s} = 7$ TeV using the ATLAS detector. *Eur. Phys. J. C*, 72:2039, 2012.

[196] ATLAS Collaboration. Measurement of the top quark-pair production cross section with ATLAS in pp collisions at $\sqrt{s} = 7$ TeV. *Eur. Phys. J. C*, 71:1577, 2011.

[197] A.D. Martin, W.J. Stirling, R.S. Thorne, and G. Watt. Parton distributions for the LHC. *Eur. Phys. J. C*, 63:189–285, 2009.

[198] Chun-Hay Kom and W. James Stirling. Charge asymmetry in W + jets production at the LHC. *Eur. Phys. J. C*, 69:67–73, 2010.

[199] ATLAS Collaboration. Electron performance measurements with the ATLAS detector using the 2010 LHC proton-proton collision data. *Eur. Phys. J. C*, 72:1909, 2012.

[200] ATLAS Collaboration. Muon Momentum Resolution in First Pass Reconstruction of pp Collision Data Recorded by ATLAS in 2010. Technical Report ATLAS-CONF-2011-046, CERN, Geneva, Mar 2011.

[201] Matteo Cacciari, Gavin P. Salam, and Gregory Soyez. The Anti-k(t) jet clustering algorithm. *JHEP*, 0804:063, 2008.

[202] ATLAS Collaboration. Commissioning of the atlas high-performance b-tagging algorithms in the 7 tev collision data. Technical Report ATLAS-CONF-2011-102, CERN, Geneva, Jul 2011.

[203] Peter Zeiler Skands. Tuning Monte Carlo Generators: The Perugia Tunes. *Phys. Rev.*, D82:074018, 2010.

[204] ATLAS Collaboration. Expected Performance of the ATLAS Experiment - Detector, Trigger and Physics. 2009.

[205] TeV4LHC QCD Working Group. Tevatron-for-LHC Report of the QCD Working Group. Technical Report FERMILAB-CONF-06-359, Fermilab, USA, 2006.

[206] Andy Buckley, Hendrik Hoeth, Heiko Lacker, Holger Schulz, and Jan Eike von Seggern. Systematic event generator tuning for the LHC. *Eur. Phys. J. C*, 65:331–357, 2010.

[207] F. A. Berends, H. Kuijf, B. Tausk, and W. T. Giele. On the production of a W and jets at hadron colliders. *Nuclear Physics B*, 357:32–64, June 1991.

[208] John M. Campbell and R. Keith Ellis. Radiative corrections to Z b anti-b production. *Phys. Rev. D*, 62:114012, 2000.

[209] ATLAS Collaboration. Jet energy measurement with the ATLAS detector in proton-proton collisions at $\sqrt{s} = 7$ TeV. Technical Report CERN-PH-EP-2011-191, CERN, Geneva, 2011.

[210] ATLAS Collaboration. Measurement of the rate of collisions from satellite bunches for the april-may 2010 lhc luminosity calibration. Technical Report ATLAS-CONF-2010-102, CERN, Geneva, Dec 2010.

[211] Louis Lyons, Duncan Gibaut, and Peter Clifford. How to combine correlated estimates of a single physical quantity. *Nucl. Instrum. Meth. A*, 270:110, 1988.

[212] A. Valassi. Combining correlated measurements of several different physical quantities. *Nucl. Instrum. Meth. A*, 500:391–405, 2003.

[213] J.A. Aguilar-Saavedra and J. Bernabeu. W polarisation beyond helicity fractions in top quark decays. *Nucl. Phys. B*, 840:349–378, 2010.

[214] Tevatron Electroweak Working Group. Combination of CDF and D0 Measurements of the Single Top Production Cross Section. Technical Report FERMILAB-TM-2440-E, Fermilab, USA, 2009.

[215] CMS Collaboration. Measurement of the single-top-quark t-channel cross section in pp collisions at $\sqrt{s} = 7$ TeV. 2012. Submitted to JHEP.

[216] Allen Caldwell, Daniel Kollar, and Kevin Kroninger. BAT: The Bayesian Analysis Toolkit. *Comput. Phys. Commun.*, 180:2197–2209, 2009.

[217] D0 Collaboration. Combination of searches for anomalous top quark couplings with 5.4 fb^{-1} of $p\bar{p}$ collisions. Technical Report FERMILAB-PUB-12-096-E, Fermilab, USA, 2012.

[218] Jure Drobnak, Svjetlana Fajfer, and Jernej F. Kamenik. Probing anomalous tWb interactions with rare B decays. *Nucl. Phys. B*, 855:82–99, 2012.

[219] Jure Drobnak, Svjetlana Fajfer, and Jernej F. Kamenik. Interplay of $t \to bW$ Decay and B_q Meson Mixing in Minimal Flavor Violating Models. *Phys. Lett. B*, 701:234–239, 2011.

[220] Cen Zhang, Nicolas Greiner, and Scott Willenbrock. Constraints on Non-standard Top Quark Couplings. *Phys. Rev. D*, 86:014024, 2012.

[221] Bohdan Grzadkowski and Zenro Hioki. Energy spectrum of secondary leptons in $e^+e^- \to t\bar{t}$: Nonstandard effects and CP violation. *Nucl. Phys. B*, 484:17–32, 1997.

[222] Bohdan Grzadkowski and Zenro Hioki. Probing top quark couplings at polarized NLC. *Phys. Rev. D*, 61:014013, 2000.

[223] Bohdan Grzadkowski and Zenro Hioki. New hints for testing anomalous top quark interactions at future linear colliders. *Phys. Lett. B*, 476:87–94, 2000.

[224] Bohdan Grzadkowski and Zenro Hioki. Optimal observable analysis of the angular and energy distributions for top quark decay products at polarized linear colliders. *Nucl. Phys. B*, 585:3–27, 2000.

[225] American Linear Collider Working Group. Linear collider physics resource book for Snowmass 2001. Part 3. Studies of exotic and standard model physics. Technical Report SLAC-R-570, SLAC-R-0570, SLAC-570, SLAC-0570, BNL-52627, CLNS-01-1729, FERMILAB-PUB-01-058-E, LBNL-47813, UCRL-ID-143810-DR, LC-REV-2001-074-US, USA, 2001.

[226] Erik Devetak, Andrei Nomerotski, and Michael Peskin. Top quark anomalous couplings at the International Linear Collider. *Phys. Rev. D*, 84:034029, 2011.

[227] J.A. Aguilar-Saavedra, J. Carvalho, N. Castro, A. Onofre, and F. Veloso. ATLAS sensitivity to Wtb anomalous couplings in top quark decays. *Eur. Phys. J. C*, 53:689–699, 2008.

[228] U. Baur, A. Juste, L.H. Orr, and D. Rainwater. Probing electroweak top quark couplings at hadron colliders. *Phys. Rev. D*, 71:054013, 2005.

[229] U. Baur, A. Juste, D. Rainwater, and L.H. Orr. Improved measurement of ttZ couplings at the CERN LHC. *Phys. Rev. D*, 73:034016, 2006.

[230] F. del Aguila, M. Perez-Victoria, and Jose Santiago. Effective description of quark mixing. *Phys. Lett. B*, 492:98–106, 2000.

[231] F. del Aguila, M. Perez-Victoria, and Jose Santiago. Observable contributions of new exotic quarks to quark mixing. *JHEP*, 0009:011, 2000.

[232] ATLAS Collaboration. Measurement of the t-channel single top-quark production cross section in pp collisions at $sqrts = 7$ TeV with the ATLAS detector. 2012.

[233] Philippe Doublet, Francois Richard, Roman Poschl, Thibault Frisson, and Jeremy Rouene. Determination of Top-quark Asymmetries at the ILC. 2012.